

学位論文

**Atmospheric evolution in the Precambrian:
Constraints from water-rock-atmosphere interactions**

(先カンブリア時代の大気進化：水-岩石-大気相互作用からの制約)

平成 25 年 12 月博士（理学）申請

東京大学大学院理学系研究科
地球惑星科学専攻

菅崎良貴

Abstract

Atmospheric evolution of the Earth is considered to be correlated with the physicochemical and biological evolutions of the surface environment, and thus is important for understanding the Earth's system. Special interests have been given for the evolutions of atmospheric O₂, CO₂ and CH₄. From accumulating isotopic and mineralogical data in sediments, it is accepted by most researchers that there were two major events of great increases in oxygen in the Precambrian: the Great Oxidation Event (GOE) at ~2.5–2.0 Ga and the Neoproterozoic Oxygenation Event (NOE) at ~0.8–0.6 Ga. At almost the same timings as the GOE and NOE, there were global glaciation events where greenhouse gases, CO₂ and CH₄, are considered to have fluctuated. Although the timings of these major events and qualitative information on surface environments in the events are becoming clearer than ever, quantitative constraints on atmospheric compositions throughout the Precambrian are still scarce. The present thesis gives constraints on atmospheric compositions, mainly CO₂ and O₂, in the Precambrian from water-rock-atmosphere interactions.

In order to precisely estimate atmospheric CO₂ levels in the Precambrian, I developed a new method that calculates CO₂ levels from the chemical compositions of paleosols. The new method (i) calculates the cation concentrations in porewaters at the time of weathering from those of paleosols, (ii) describes the relationships between partial pressure of atmospheric CO₂ (P_{CO_2}), pH and cation concentrations based on the charge balance between the cations and anions including carbonate species in porewaters, and (iii) finally calculates P_{CO_2} levels at a given temperature constraining pH by thermodynamics of weathering secondary-minerals. By applying the new method to modern weathering profiles, I obtained a good agreement between the calculated and observed P_{CO_2} levels. The weathering rate deduced from the new method was proportional to P_{CO_2} with fractional dependence of 0.18 and the apparent activation energy of weathering was 40–55 kJ mol⁻¹, which is consistent with the laboratory and field results. The application to modern weathering and the formulated characteristics of weathering strongly indicate that the new method is valid and robust. The new method was then applied to eight paleosols formed in the Neoproterozoic. I first made constraints on the local temperatures, at which the paleosols were formed, mainly by the temperature-solute concentration relationships in the literature, because local temperatures should have been different between the paleosols and from the average global surface temperatures. Under the constrained local temperatures, the P_{CO_2} levels were calculated to be 85–510 of the present day atmospheric level (PAL) at ~2.77 Ga ,

78–2500 PAL at ~2.75 Ga, 160–490 PAL at ~2.46 Ga, 30–190 PAL at ~2.15 Ga, 20–620 PAL at ~2.08 Ga and 23–210 PAL at ~1.85 Ga. The estimated P_{CO_2} levels are higher than those to maintain the average global surface temperature of the Earth above the freezing point of water only by CO_2 itself. The newly estimated P_{CO_2} levels imply that atmospheric CO_2 decreased gradually in long term in the Neoproterozoic and that the wide-spread glaciations at ~2.9 and ~2.4–2.2 Ga were differently triggered.

To estimate the partial pressure of atmospheric O_2 (P_{O_2}) in the Precambrian, Fe redistributions recorded in paleosols are useful. To interpret Fe records in paleosols, the relationship between P_{O_2} and Fe(II) oxidation rate is essential according to the previous studies. Because there is no experimental data on Fe(II) oxidation rate under low O_2 conditions ($P_{\text{O}_2} < 10^{-3}$ atm), I first experimentally obtained the Fe(II) oxidation rate law under low O_2 conditions down to 10^{-5} atm of P_{O_2} . All oxidation experiments were carried out in a glove box by introducing Ar gas at $\sim 10^{-5}$ – $\sim 10^{-4}$ atm of P_{O_2} , pH 7.57–8.09 and 22 °C. Luminol chemiluminescence was adopted to measure low Fe(II) concentrations (down to ~2 nM). Combining previous data under higher P_{O_2} conditions (10^{-3} –0.2 atm) with the newly obtained data, the rate law for Fe(II) oxidation over a wide range of P_{O_2} (10^{-5} –0.2 atm) was found to be written as:

$$\frac{d[\text{Fe(II)}]}{dt} = -k[\text{Fe(II)}][\text{O}_2]^x[\text{OH}^-]^2$$

where the exponent of $[\text{O}_2]$, x , and the rate constant, k , change from $x = 0.98$ (± 0.04) and $\log k = 15.46$ (± 0.06) at $\sim 6 \times 10^{-3}$ –0.2 atm of P_{O_2} to $x = 0.58$ (± 0.02) and $\log k = 13.41$ (± 0.03) at 10^{-5} – $\sim 6 \times 10^{-3}$ atm of P_{O_2} . The most plausible mechanism that explains the change in x under low O_2 conditions is that, instead of O_2 , oxygen-derived oxidants, H_2O_2 and to some extent, O_2^- , dominate the oxidation reactions at $< \sim 10^{-3}$ atm of P_{O_2} .

Then, I developed a new weathering model, which considers the steady-state weathering of Fe, in order to constrain P_{O_2} in the Precambrian from paleosols. The model calculates the ratio of the precipitated Fe(III)-(oxyhydr)oxides from dissolved Fe(II) to the total dissolved Fe(II) during weathering (ϕ), as a function of P_{O_2} . For the calculation of the ϕ - P_{O_2} relationship, the kinetic law for Fe(II) oxidation by O_2 obtained above was adapted. The law was further modified to include the effects of both the Fe(II)-hydroxyl and Fe(II)-carbonate species on Fe(II) oxidation from the kinetic data in the literature. The model's validity was confirmed by the consistency of the calculated ϕ - P_{O_2} relationships with those by the weathering model in the literature whose validity has already been verified. Once a ϕ value, and the values for the parameters relevant to weathering, namely, pH of porewater, P_{CO_2} , water flow, temperature and O_2 diffusion into soil, are obtained for a paleosol, the model can estimate P_{O_2} from the paleosol, in

theory. The values for the parameters relevant to weathering were scrutinized for five Paleoproterozoic paleosols. The observed values of ϕ were obtained from the literature on the Paleoproterozoic paleosols. The values of pH, P_{CO_2} and temperature for the Paleoproterozoic paleosols were estimated during the P_{CO_2} estimation from the paleosols, as described above. The parameter value for water flow was estimated for each paleosol based on the mass balance of Si, the relationships between weathering fluxes and runoff and the relationship between water flux and hydraulic conductivity. The parameter value for O_2 diffusion into soil was assumed in a reasonable range. Then, by incorporating the constrained values for the weathering-relevant parameters into the model and applying the model to the Paleoproterozoic paleosols, the P_{O_2} levels in the Paleoproterozoic were estimated: $10^{-6.7}$ – $10^{-5.4}$ atm at ~ 2.46 Ga, $10^{-5.2}$ – $10^{-3.2}$ atm at ~ 2.15 Ga, $10^{-3.9}$ – $10^{-1.2}$ atm at ~ 2.08 Ga and more than $10^{-4.6}$ – $10^{-2.5}$ atm at ~ 1.85 Ga. Comparison of the calculated results to the estimates of P_{O_2} in the literature suggests that a drastic rise of oxygen would not have occurred at ~ 2.4 Ga, supporting a slightly rapid rise of oxygen at ~ 2.4 Ga and a gradual rise of oxygen in the Paleoproterozoic in long term.

Besides the constraints on P_{CO_2} and P_{O_2} in the Precambrian from paleosols, I also considered the theoretical relationships between silicate weathering, atmospheric compositions (CO_2 as well as CH_4 and O_2) and climates (surface temperatures) in the Precambrian. Atmospheric CO_2 is a greenhouse gas and thus regulates the surface temperature of the Earth together with silicate weathering, which is a major sink of CO_2 . The apparent activation energy of natural silicate weathering is thus a determinant factor of the regulation of the surface temperature of the Earth. Although it has long been suggested that the apparent activation energy of silicate weathering can be affected by solution compositions in natural weathering systems, the relationships between the apparent activation energy and solution composition are not fully understood. I formulated the apparent activation energy of silicate weathering, including solution composition effects, in three different scales: (i) each mineral-reaction in a weathering profile, (ii) elemental loss from the profile and (iii) weathering flux, based on the rate expressions in the three scales. It was found that the apparent activation energy of silicate weathering consistent between the three scales is affected by, and thus is a function of, the temperature dependence of atmospheric CO_2 ($\Delta H'_{CO_2}$). By introducing the general rate law for total cation flux by silicate weathering (F_{CO_2}) in the Arrhenius expression and the compensation law, which represents the relationships between the apparent activation energy and the pre-exponential factor, the relationships between $\Delta H'_{CO_2}$, temperature (T) and F_{CO_2} were established. Based on the relationships between

$\Delta H'_{\text{CO}_2}$, T and F_{CO_2} , I discussed the effects of atmospheric CO_2 as well as those of CH_4 and O_2 , on the silicate weathering, and their implications for the atmospheric compositions and surface temperatures in the Precambrian.

The effects of CO_2 on silicate weathering were firstly discussed based on the relationships between $\Delta H'_{\text{CO}_2}$, T and F_{CO_2} and the greenhouse effect of CO_2 . In the global scale, the greenhouse effect of atmospheric CO_2 represents $\Delta H'_{\text{CO}_2}$, and thus determines silicate weathering. From the greenhouse effects of CO_2 in the literature, I calculated the ratio of the change in F_{CO_2} to the corresponding change in P_{CO_2} , as an indicator of the feedback of silicate weathering on CO_2 . The calculation of the feedback indicator revealed that the feedback is negative and independent of both P_{CO_2} and T when $P_{\text{CO}_2} > 10^{-0.5}$ atm. Thus, the conditions of $P_{\text{CO}_2} > 10^{-0.5}$ atm are stable with respect to silicate weathering. On the other hand, when $P_{\text{CO}_2} < 10^{-0.5}$ atm, the feedback is P_{CO_2} -independent but temperature-dependent; at low ($< \sim 30$ °C) and high ($> \sim 30$ °C) temperatures, the feedback is negative and positive, respectively. Due to the positive feedback, the conditions of $P_{\text{CO}_2} < 10^{-0.5}$ atm and $T > \sim 30$ °C are unstable, and immediately change, with a slight change in CO_2 , to either the conditions of $P_{\text{CO}_2} > 10^{-0.5}$ atm or those of $P_{\text{CO}_2} < 10^{-0.5}$ atm and $T < \sim 30$ °C. When $P_{\text{CO}_2} < 10^{-0.5}$ atm and $< \sim 30$ °C, the feedback is not only negative, but also becomes more negative as temperature decreases. Therefore, the global glaciations hardly occur by CO_2 alone. The stable climates in the Precambrian excluding the periods of glaciations (especially the stable climate in the Mesoproterozoic) may be explained by the stability of low CO_2 conditions ($P_{\text{CO}_2} < 10^{-0.5}$ atm and $< \sim 30$ °C) against glaciations.

Atmospheric CH_4 affects the greenhouse effect of CO_2 , and thus the feedback of weathering on CO_2 . I calculated the feedback indicator under the presence of CH_4 , using the relationships between $\Delta H'_{\text{CO}_2}$, T and F_{CO_2} and the greenhouse effects of CH_4 in the literature. It was found that with a limited range of CH_4/CO_2 ratio ($< \sim 0.15$ and $> \sim 0.03$), positive feedback operates at low temperatures ($< \sim 5$ °C). Thus, with such CH_4/CO_2 ratios, global glaciations can occur. The emergence of CH_4 to make such CH_4/CO_2 ratios can be one of the triggers of the glaciations in the Precambrian, especially that in the Mesoarchean.

Atmospheric O_2 , when increasing from extremely low P_{O_2} to $\sim 10^{-6}$ – 10^{-3} atm, changes the apparent activation energy of weathering by involving oxidation reactions in weathering, and can increase F_{CO_2} at low temperatures, according to the general rate law. Thus, it is possible that the P_{O_2} increase from almost nil to $\sim 10^{-6}$ – 10^{-3} atm, can cause global glaciations, which may explain the glaciations in the Paleoproterozoic.

I finally calculated the temperature and P_{CO_2} transitions in the Precambrian based

on the relationships between $\Delta H'_{\text{CO}_2}$, T and F_{CO_2} and the greenhouse effects of CO_2 in the literature. The results show that the temperature can have been maintained at $> 0^\circ\text{C}$ only by CO_2 itself through the Precambrian, confirming that CO_2 was the dominant greenhouse gas in the eon. The argument is supported by the consistency of the calculated results with the P_{CO_2} estimates from paleosols in the Precambrian. From the calculated temperatures, it is also suggested that the Earth might have been hot ($>\sim 40^\circ\text{C}$) until around the end of Archean.

Contents

I. General introduction	1
1. Background	1
1.1. Atmospheric evolution in the Precambrian	1
1.2. Water-rock-atmosphere interactions: Weathering of rocks	3
1.3. Application of water-rock-atmosphere interactions to estimation of atmospheric compositions in the Precambrian	5
2. Objectives	7
References	7
II. Estimates of atmospheric CO₂ in the Neoproterozoic from paleosols	14
1. Introduction	14
2. A new method to estimate <i>P</i>co₂ from weathering profiles	16
2.1. Estimation of cation concentrations in porewater from a remaining weathering profile	17
2.2. Estimation of <i>P</i>co₂ from charge balance in porewater	19
2.3. pH constraints from secondary minerals	21
3. Validity of the present method for the estimation of <i>P</i>co₂	30
3.1. Application of the present method to modern weathering profiles	30
3.2. Weathering formulation deduced from the present method	33
4. Atmospheric CO₂ variation in the Neoproterozoic	36
4.1. <i>P</i>co₂ estimates at different temperatures	37
4.2. Local temperature constraints for the Neoproterozoic paleosols	48
4.3. Atmospheric CO₂ evolution and climate in the Neoproterozoic ..	52
5. Conclusions	56
Appendix A	56

Appendix B	58
Appendix C	59
Appendix D	61
Appendix E	64
References	69
III. Rate law of Fe(II) oxidation under low O₂ conditions	80
1. Introduction	80
2. Experimental methods	82
2.1. Reagents	82
2.2. Fe(II) oxidation experiments	83
2.3. Fe(II) analysis	84
3. Results	85
4. Discussion	89
4.1. pH dependence of oxidation rate	89
4.2. P _{o2} dependence of oxidation rate	91
4.3. Possible mechanisms of Fe(II) oxidation under low O ₂ conditions	93
4.4. Application of the rate law to Fe redistribution during mineral dissolution under low O ₂ conditions	99
5. Conclusions	102
Appendix A	102
Appendix B	103
Appendix C	106
References	107
IV. Estimates of atmospheric O₂ in the Paleoproterozoic from paleosols	112
1. Introduction	112
2. P_{o2} estimation method	113

2.1. Formulation for the calculation of ϕ	114
2.2. Introduction of new Fe(II) oxidation kinetics in the model.....	119
2.3. P_{O_2} estimation equation for paleosols	124
3. Constraints on parameter values for the Paleoproterozoic paleosols.....	124
3.1. Temperature and O_2 diffusion into soil (f).....	124
3.2. pH and P_{CO_2}	125
3.3. Water flow (k_f)	130
4. Atmospheric O_2 evolution in the Paleoproterozoic	138
5. Conclusions	143
Appendix A	143
References.....	149
V. Effects of atmospheric composition on apparent activation energy of silicate weathering: Implications for evolution of atmospheric CO_2 in the Precambrian.....	154
1. Introduction.....	154
2. Formulation of rate and apparent activation energy of silicate weathering.....	156
2.1. Rate formulation	156
2.2. Apparent activation energy.....	168
3. Estimation of apparent activation energy of silicate weathering.....	174
3.1. Estimation of apparent activation energy of elemental loss by silicate weathering	175
3.2. Estimation of apparent activation energy of silicate-weathering flux.....	183
4. Estimation of silicate-weathering flux.....	185
5. Effects of atmospheric compositions on silicate weathering.....	188
5.1. Effects of CO_2	188
5.2. Effects of CH_4	196
5.3. Effects of O_2	200

6. Implication for evolution of atmospheric CO₂ and temperature	202
7. Conclusions	211
Appendix A	212
Appendix B	216
Appendix C	217
References	218
VI. General conclusions	231
Acknowledgements	234

I. General introduction

1. Background

1.1. Atmospheric evolution in the Precambrian

In the Precambrian, there were important innovations of life (Knoll, 2003; Farquhar et al., 2011), which must have been associated with the evolution of surface environments including atmospheric composition (Walker, 1977), sedimentary rocks (Garrels and Mackenzie, 1971), ocean chemistry (Anbar, 2008) and mineral species (Hazen et al., 2008). Atmospheric compositions, especially oxygen (O_2), carbon dioxide (CO_2) and methane (CH_4), in the Precambrian have given intensive attentions, because they can constrain whether the life was possible or not (e.g., Segura et al., 2003) and/or what forms of life can have been possible (e.g., McKay and Hartman, 1991; Lowe and Tice, 2007).

Atmospheric O_2 was negligible in the early Earth due to the absence of O_2 -producing organisms. Before the advent of the photosynthetic organisms which produce O_2 as by-products, the partial pressure of atmospheric O_2 (P_{O_2}) is estimated to have been as low as $\sim 10^{-13}$ atm (Kasting et al., 1979). The O_2 -producing photosynthetic organisms are considered to have evolved as far back as ~ 2.8 Ga (e.g., Farquhar et al., 2011). The first oxygenation of surface environments at the Earth, on the other hand, occurred at ~ 2.5 – 2.0 Ga, called the Great Oxidation Event (GOE) (Holland, 2002). Many lines of evidence from geological records have established the timing of the GOE. Especially, the mass independent fractionation of sulfur (MIF-S where $\Delta^{33}S \cong \delta^{33}S - 0.515 \times \delta^{34}S \neq 0$) has strongly constrained the GOE: $\leq \sim 10^{-6}$ atm of P_{O_2} at ≥ 2.45 Ga, $\geq \sim 10^{-6}$ atm at 2.32 Ga, and to $\geq \sim 10^{-3}$ atm at 2.0 Ga (Farquhar et al., 2000; Pavlov and Kasting, 2002; Farquhar and Wing, 2003; Bekker et al., 2004). After the boring billion where P_{O_2} is considered to have been rather constant (1.85–0.85 Ga) (Holland, 2006), another oxygen increase occurred in the Neoproterozoic (~ 0.8 – 0.6 Ga), called the Neoproterozoic Oxygenation Event (NOE) (Och and Shields-Zhou, 2012). The NOE is also considered to have been related with evolution of organisms (e.g., Och and Shields-Zhou, 2012). Similarity between the GOE and NOE has been pointed out from geological records such as C isotopic data (e.g., Och and Shields-Zhou, 2012). Interestingly, the timings of the GOE and NOE were around those of the global glaciations in the Paleoproterozoic (e.g., Bekker et al., 2005) and Neoproterozoic (e.g.,

Hoffman et al., 1998), respectively. Despite intensive studies on both the GOE and NOE, how oxygen increased and why at these particular times in the Earth's history remain unresolved. The issues of how and why are of crucial importance to understand the evolution of surface redox environment at the Earth (Holland, 2002, 2009; Catling and Claire, 2005; Kasting, 2013).

CO₂ in the atmosphere works as a greenhouse gas, whose concentration influences the surface temperature of the Earth. The luminosity of the Sun was fainter in the older ages (Gough, 1981) and therefore, the concentrations of greenhouse gases are more serious issues in the older ages (Walker, 1982), because the existence of liquid water (and thus the moderate surface temperature where > 0 °C) can go back to as far as 4.4 Ga (e.g., Valley et al., 2002; Nutman, 2006). High values of partial pressure of atmospheric CO₂ (P_{CO_2}) have been proposed to compensate the weak luminosities in the Precambrian (Hart, 1978; Owen et al., 1979; Kasting, 1987). Constraints on P_{CO_2} from geological records, on the other hand, have been inconsistent with one another (e.g., Rye et al., 1995; Ohmoto et al., 2004), and thus whether CO₂ was high enough, or not, to compensate the weak luminosities only by itself in the Precambrian has not yet been settled (Feulner, 2012). Assuming P_{CO_2} in the Precambrian was relatively low, other warming agents for the Earth have been suggested, e.g., NH₃ (Sagan and Mullen, 1972), CH₄ (Pavlov et al., 2000) and N₂ and H₂ (Goldblatt et al., 2009; Wordsworth and Pierrehumbert, 2013). Despite the uncertainty in P_{CO_2} in the Precambrian, P_{CO_2} is important to consider the possible causes of the global glaciations in the Paleoproterozoic and Neoproterozoic and the mechanisms to escape from these glaciated states (e.g., Kirschvink, 1992; Caldeira and Kasting, 1992; Pierrehumbert et al., 2011).

CH₄ is biologically produced and thus the partial pressure of atmospheric CH₄ (P_{CH_4}) in the Precambrian must have been affected by the organisms (Kharecha et al., 2005). Because of the redox reaction with O₂, the evolution of P_{CH_4} is considered to have been related to that of P_{O_2} : in the early Earth, P_{CH_4} can have been high due to negligibly low P_{O_2} (Kharecha et al., 2005); in the vicinity of the GOE, P_{CH_4} is suggested to have been reduced to significantly lower levels (Papineau et al., 2005, 2007; Claire et al., 2006; Zahnle et al., 2006). In addition, because CH₄ is a greenhouse gas, P_{CH_4} also affects the surface temperature of the Earth, together with P_{CO_2} . In contrast to CO₂, too much of CH₄ ($CH_4/CO_2 > \sim 0.1$) creates organic haze in the atmosphere, which cools the Earth, complicating the greenhouse effect of CH₄ (Trainer et al., 2006; Haqq-Misra et al., 2008). Accordingly, P_{CH_4} is another important factor to consider the surface environments in the Precambrian. Unfortunately, P_{CH_4} is hardly recorded in any

geological records, and therefore there have been no constraints on P_{CH_4} from geological records in the Precambrian.

The correlation of the transitions of the three gases (O_2 , CO_2 and CH_4) through ages are emphasized especially in the GOE, because in the GOE, P_{O_2} increased and P_{CH_4} decreased and in the vicinity of the GOE, there were possibly global scale multiple glaciations (e.g., Evans et al., 1997) where greenhouse gases, including CO_2 and CH_4 , must have fluctuated. Although the correlations between P_{O_2} , P_{CO_2} and P_{CH_4} have been suggested by many researchers as described above (e.g., Bekker and Kaufman, 2007; Papineau et al., 2007), there have been almost no quantitative, synchronous constraints on P_{O_2} , P_{CO_2} and P_{CH_4} from geological records during the GOE.

Paleosols, fossil weathering profiles, in the Precambrian can be of use to give quantitative constraints on P_{O_2} and P_{CO_2} , because paleosols are the vestiges of in-situ reactions of rocks with atmosphere via water at the time of the reactions (Murakami et al., 2011). It may be also possible to deduce the constraints on P_{CH_4} from the constrained P_{O_2} and P_{CO_2} from paleosols. The knowledge of water-rock-atmosphere interactions, i.e., weathering processes of rocks, is essential for the quantification of P_{O_2} and P_{CO_2} from paleosols.

1.2. Water-rock-atmosphere interactions: Weathering of rocks

Weathering of rocks occurs at the interface between rock, water and atmosphere, which has been called the Critical Zone (Brantley et al., 2007). Weathering involves several physicochemical phenomena such as mineral dissolution/precipitation, transport of dissolved elements by water flow and diffusion, and physical erosion of weathering profiles (e.g., White and Brantley, 1995). Chemical dissolution/precipitation of minerals are important factors in weathering processes because they are the chemical reactions of minerals that affect the atmospheric composition, namely, atmospheric O_2 and CO_2 . O_2 is consumed by oxidative dissolution of sulfide minerals and by oxidation of reduced elements like Fe(II) dissolved from primary minerals (Holland, 1978). During oxidation of reduced minerals/elements in weathering processes, O_2 is reduced to H_2O . CO_2 is consumed during dissolution of minerals where proton, supplied from carbonic acid, is consumed to release cations, leaving bicarbonate/carbonate ions in porewater of weathering profiles (Holland, 1978). The consumption of O_2 by weathering of rocks can affect O_2 budgets in the global scale (Garrels and Perry, 1974; Holland, 1978), while weathering of rocks regulates atmospheric CO_2 (Walker, 1977). Therefore, intensive studies for chemical dissolution/precipitation of minerals have been conducted both in

the laboratory and field.

The effects of P_{O_2} on mineral dissolution have been studied for Fe(II)-bearing silicate minerals (Murakami et al., 2004; Sugimori et al., 2009, 2012). Although the observation of redox-insensitive elements (e.g., Mg and Si) released during dissolution of the minerals has revealed that dissolution rates of minerals are not affected by P_{O_2} , the amounts of released Fe are strongly dependent on P_{O_2} : Fe is less released at higher P_{O_2} (Murakami et al., 2004; Sugimori et al., 2009, 2012). The apparently low rate of Fe dissolution at high P_{O_2} levels has been attributed to oxidation of dissolved Fe(II) to Fe(III) and immediate precipitation of Fe(III)-(oxyhydr)oxides (Murakami et al., 2004; Sugimori et al., 2009, 2012). Therefore, it is essential to understand the mechanisms of Fe(II) oxidation by O_2 for understanding Fe behaviors during mineral dissolution. The relationships between other redox sensitive elements (e.g., Mn) and P_{O_2} in mineral dissolution are less understood (c.f., Junta and Hochella, 1994).

The effects of P_{CO_2} on dissolution rates of minerals may appear principally in three ways: by changing solution pH (e.g., Berner, 1992), by forming metal-carbonate complexes at mineral-water interfaces (e.g., Pokrovsky and Schott, 2000) or by changing temperature as the greenhouse effect of CO_2 (e.g., Brady, 1991). The relationships between pH and dissolution rates of minerals are well established (e.g., Sverdrup, 1990; Palandri and Kharaka, 2004; Schott et al., 2009). However, pH of porewater in weathering profiles is determined not only by P_{CO_2} , but also by cation concentrations (Holland, 1978). Thus, it is not certain how the change in P_{CO_2} affects pH of porewater and weathering rate (e.g., Godd ris et al., 2009). The effects of the formation of metal-carbonate complexes on mineral dissolution are not well understood, either. Laboratory experiments have reported that the dissolution rates of some minerals (e.g., anorthite) are increased by metal-carbonate complexes (Berg and Banwart, 2000) while the dissolution rates of some others (e.g., olivine and pyroxene) are not at all affected or even decreased (Wogelius and Walther, 1991; Pokrovsky and Schott, 2000; Golubev et al., 2005). On the other hand, the temperature change induced by a CO_2 change affects mineral dissolution rates significantly (e.g., Brady and Carroll, 1994). The significance of the temperature effects depends on the apparent activation energy of mineral dissolution, which has been reported to be affected by solution composition (e.g., Cama et al., 1999). Because the relationship between the apparent activation energy and solution composition is not yet fully understood, it is not certain how mineral dissolution rate changes when temperature changes with CO_2 . Thus, the effects of temperature change with CO_2 in natural weathering systems have not yet been well established, either (e.g., Brady, 1991). The analysis of the P_{CO_2} effects become much

more complicated by the fact that the dissolution rates of minerals in the field are slower by orders of magnitude than those in the laboratory due to other factors such as saturation degrees of porewater with respect to dissolving minerals, surface roughness of minerals, water flow rates in weathering profiles (e.g., White and Brantley, 2003). Nevertheless, it is certain that the cations in porewater of weathering profiles are charge-balanced by atmosphere-derived bicarbonate/carbonate ions (Holland, 1978).

To deduce atmospheric composition from paleosols at the time of weathering, the knowledge on water-rock-atmosphere interactions as described above must be taken into account.

1.3. Application of water-rock-atmosphere interactions to estimation of atmospheric compositions in the Precambrian

It has been attempted to apply theories of water-rock-atmosphere interactions to the estimation of atmospheric compositions in the Precambrian. P_{CO_2} has been estimated from the CO_2 consumption by dissolution of silicate minerals. From the equilibrium calculations between silicate minerals, atmospheric CO_2 and carbonates, Urey (1952) suggested that P_{CO_2} was low (as low as 10^{-8} atm) and P_{CH_4} was high in the early Earth. However, it is kinetics, but not equilibrium, of weathering that controls atmospheric composition (e.g., Lasaga, 1981; Berner et al., 1983), and thus the results from simple equilibrium calculation are not always correct (Holland, 1978). Rye et al. (1995) applied siderite ($Fe(II)CO_3$)/greenalite ($Fe(II)_3Si_2O_5(OH)_4$) phase equilibrium to the estimation of P_{CO_2} ; they interpreted the absence of siderite in paleosols of ages > 2.2 Ga as $P_{CO_2} < 10^{-1.5}$ atm at > 2.2 Ga. The estimates given by Rye et al. (1995) were criticized by Sheldon (2006) because greenalite is unlikely to occur as a weathering product and because the thermodynamic data for greenalite adopted in Rye et al. (1995) are not correct. Sheldon (2006, 2013), on the other hand, calculated CO_2 consumption rates from paleosols using a mass balance method, and estimated $\sim 10^{-3.5} - 10^{-1.5}$ atm of P_{CO_2} in the Proterozoic. However, Sheldon's method (2006) considers only the kinetics of CO_2 transport into soil, but not the reaction kinetics of weathering itself (Holland and Zbinden, 1988; Sheldon, 2006). In addition, the validity of Sheldon's method (2006) has not yet been confirmed.

The estimation of P_{O_2} in the Precambrian based on water-rock-atmosphere interactions has yielded different results between researchers. Sverjensky and Lee (2010) estimated extremely low P_{O_2} at $> \sim 2.4$ Ga ($\sim 10^{-60} - 10^{-70}$ atm) based on the phase equilibria of siderite, pyrite and uraninite, detrital minerals in ages prior to the GOE.

However, such application of phase equilibrium requires to assume that the detrital minerals had been exposed to the atmosphere at $>\sim 2.4$ Ga for infinite time. On the other hand, Grandstaff (1980) suggested that the survival of detrital uraninites requires P_{O_2} to be $< \sim 10^{-3} - 10^{-7}$ atm using uraninite dissolution kinetics (Grandstaff, 1976). Holland (1984) further included the effects of P_{CO_2} on the kinetics of uraninite dissolution, and suggested that the survival of detrital uraninites indicates $(P_{O_2} \cdot P_{CO_2}) < 10^{-4.9}$. The significant difference of P_{O_2} constraints by Sverjensky and Lee (2010) from those by Grandstaff (1980) and Holland (1984) indicates the importance of the kinetics of water-rock-atmosphere interactions to estimate P_{O_2} from geological records.

Holland further developed a method for constraining P_{O_2} from paleosols (Holland, 1984; Holland and Zbinden, 1988; Pinto and Holland, 1988), which is based on the transport kinetics of O_2 and CO_2 , the mole numbers of O_2 and CO_2 demanded for the consumption of parent rocks of paleosols and the retention levels of Fe in paleosols. The summary of P_{O_2} estimates by his method is given by Rye and Holland (1998): $P_{O_2} \leq 10^{-3.1}$ atm at > 2.245 Ga and $P_{O_2} \geq 10^{-1.5}$ atm at < 2.203 Ga. The P_{O_2} constraints from paleosols by Holland's method are dependent on P_{CO_2} , and thus the estimates in Rye and Holland (1998), where P_{CO_2} was assumed as $< 10^{-1.7}$ atm, change significantly with assumed P_{CO_2} . In addition, his method considers only the transport kinetics of CO_2 and O_2 , and does not take into account the reaction kinetics of rocks (Holland, 1984; Holland and Zbinden, 1988; Pinto and Holland, 1988). Recently, Murakami et al. (2011) applied Fe(II) oxidation kinetics to Fe behaviors in paleosols in the Paleoproterozoic, and estimated P_{O_2} in the era. Their estimates were based on the assumed kinetic law for Fe(II) oxidation (i.e., not experimentally obtained one) and the constraints on P_{O_2} from MIF-S.

To improve the method given by Murakami et al. (2011), Yokota et al. (2013) developed a weathering model which considers dissolution of Fe(II)-bearing minerals, oxidation of dissolved Fe(II) to Fe(III) (and immediate precipitation of Fe(III)-(oxyhydr)oxides) and transport of Fe(II) by water flow. The model of Yokota et al. (2013) incorporates Fe(II) oxidation kinetic expression obtained from experiments given by Sugimori et al. (2011) and predicts Fe redistribution during weathering as a function of P_{O_2} . The validity of their model has been confirmed by the fact that their model can reproduce the Fe redistributions reported in olivine dissolution experiments at different P_{O_2} levels by Sugimori et al. (2012). Because paleosols retain different Fe redistributions at different P_{O_2} levels at the time of weathering, the model of Yokota et al. (2013) can in turn calculate P_{O_2} from the Fe redistributions in paleosols. However, to estimate P_{O_2} by their model, the values for the parameters relevant to weathering (e.g.,

pH of porewater, P_{CO_2} , water flow rate, temperature and O_2 diffusion into soil) are required as inputs that have large uncertainties. In addition, Fe(II) oxidation kinetic data used by Yokota et al. (2013) are those obtained at $> \sim 10^{-3}$ atm of P_{O_2} (Sugimori et al., 2011) and thus the estimation of P_{O_2} by Yokota et al.'s model (2013) may not be accurate at $< \sim 10^{-3}$ atm.

The estimates of both P_{CO_2} and P_{O_2} from theory and its application of water-rock-atmosphere interactions given in the literature so far are not conclusive as described above. To constrain P_{O_2} and P_{CO_2} from paleosols, a weathering model with its validity verified must be applied to paleosols. It is also necessary that the effects of both P_{O_2} and P_{CO_2} are included in such model, so that the estimates of P_{O_2} and P_{CO_2} are consistent with one another.

2. Objectives

The objective of this thesis is to give the constraints on atmospheric compositions, mainly CO_2 and O_2 , in the Precambrian from water-rock-atmosphere interactions. I utilized paleosols as geological records because paleosols are the vestiges of in-situ water-rock-atmosphere interactions and thus retain direct information on atmospheric compositions at the time of weathering. To estimate P_{O_2} and P_{CO_2} from paleosols, I constructed two different weathering models. The model for the estimation of P_{CO_2} was developed so that the model can be applied to any modern- and paleo-weathering profiles, by which the validity of the model can be confirmed. To estimate P_{O_2} from paleosols, Fe(II) oxidation kinetics under low O_2 conditions ($P_{O_2} < \sim 10^{-3}$ atm) is required (Section 1.3 in this chapter). Thus, I first conducted experiments to establish Fe(II) oxidation kinetics under low O_2 conditions. Then, the model for estimating P_{O_2} from paleosols was constructed, which incorporates the experimentally obtained relationship between Fe(II) oxidation kinetics and P_{O_2} , and includes the other weathering-relevant parameters (P_{CO_2} , pH, water flow rate etc.). To estimate P_{CO_2} without geological records including paleosols, the third model was developed. The third model calculates the effects of atmospheric composition (CO_2 , O_2 and CH_4) on the activation energy of silicate weathering in a theoretical framework, which leads to a better understanding of atmospheric evolution as well as surface-temperature variation in the Precambrian.

References

- Anbar A. D. (2008) Elements and evolution. *Science* **322**, 1481–1483.
- Bekker A., Holland H. D., Wang P. -L., Rumble III D., Stein H. J., Hannah J. L., Coetzee L. L. and Beukes N. J. (2004) Dating the rise of atmospheric oxygen. *Nature* **427**, 117–120.
- Bekker A., Kaufman A. J., Karhu J. A. and Eriksson K. A. (2005) Evidence for Paleoproterozoic cap carbonates in North America. *Precambrian Res.* **137**, 167–206.
- Bekker A. and Kaufman A. J. (2007) Oxidative forcing of global climate change: A biogeochemical record across the oldest Paleoproterozoic ice age in North America. *Earth Planet Sci. Lett.* **258**, 486–499.
- Berg A. and Banwart S. A. (2000) Carbon dioxide mediated dissolution of Ca-fekdspar: implications for silicate weathering. *Chem. Geol.* **163**, 25–42.
- Berner R. A., Lasaga A. C. and Garrels R. M. (1983) The carbonate-silicate geochemical cycle and its effect on atmospheric carbon dioxide over the past 100 million years. *Am. J. Sci.* **283**, 641–683.
- Berner R. A. (1992) Weathering, plants, and the long-term carbon cycle. *Geochim. Cosmochim. Acta* **56**, 3225–3231.
- Brady P. V. (1991) The effect of silicate weathering on global temperature and atmospheric CO₂. *J. Geophys. Res.* **B11**, 18101–180106.
- Brady P. V. and Carroll S. A. (1994) Direct effects of CO₂ and temperature on silicate weathering: Possible implications for climate control. *Geochim. Cosmochim. Acta* **58**, 1853–1856.
- Brantley S. L., Goldhaber M. B. and Ragnarsdottir K. V. (2007) Crossing disciplines and scales to understand the Critical Zone. *Elements* **3**, 307–314.
- Caldeira K. and Kasting J. F. (1992) Susceptibility of the early Earth to irreversible glaciation caused by carbon dioxide clouds. *Nature* **359**, 226–228.
- Cama J., Ayora C. and Lasaga A. C. (1999) The derivation-from-equilibrium effect on dissolution rate and on apparent variations in activation energy. *Geochim. Cosmochim. Acta* **17**, 2481–2486.
- Claire M. W., Catling D. C. and Zahnle K. J. (2006) Biogeochemical modelling of the rise in atmospheric oxygen. *Geobiol.* **4**, 239–269.
- Evans D. A., Beukes N. J. and Kirschvink J. L. (1997) Low-latitude glaciation in the Paleoproterozoic era. *Nature* **386**, 262–266.
- Farquhar J., Bao T. H. and Thiemens M. H. (2000) Atmospheric influence of earth's earliest sulfur cycle. *Science* **289**, 756–759.
- Farquhar J. and Wing B. A. (2003) Multiple sulfur isotopes and the evolution of the

- atmosphere. *Earth Planet. Sci. Lett.* **213**, 1–13.
- Farquhar J., Zerkle A. L. and Bekker A. (2011) Geological constraints on the origin of oxygenic photosynthesis. *Photosyn. Res.* **107**, 11–37.
- Feulner G. (2012) The faint young Sun problem. *Rev. Geophys.* **50**, RG2006.
- Junta J. L. and Hochella M. F. Jr. (1994) Manganese (II) oxidation at mineral surfaces: A microscopic and spectroscopic study. *Geochim. Cosmochim. Acta* **22**, 4985–4999.
- Garrels R. M. and Mackenzie F. T. (1971) *Evolution of Sedimentary Rocks*. W. W. Norton & Company, New York, 397 pp.
- Garrels R. M. and Perry E. A. Jr. (1974) Cycling of carbon, sulfur, and oxygen through geologic time. In *The Sea* (ed. E. Goldberg), vol. **5**, pp. 303–336.
- Goddéris Y., Roelandt C., Schott J., Pierret M-C. and François L. M. (2009) Towards and integrated model of weathering, climate and biosphere processes. *Rev. Mineral. Geochem.* **70**, 411–434.
- Goldblatt C., Claire M. W., Lenton T. M., Mathews A. J., Watson A. J. and Zahnle K. J. (2009) Nitrogen-enriched greenhouse warming on early Earth. *Nat. Geosci.* **2**, 891–896.
- Golubev S. V., Pokrovsky O. S. and Schott J. (2005) Experimental determination of the effect of dissolved CO₂ on the dissolution kinetics of Mg and Ca silicates at 25 °C. *Chem. Geol.* **217**, 227–238.
- Gough D. O. (1981) Solar interior structure and luminosity variations. *Solar Phys.* **74**, 21–34.
- Grandstaff D. E. (1976) A kinetic study of the dissolution of uraninite. *Econ. Geol.* **71**, 1493–1506.
- Grandstaff D. E. (1980) Origin of uraniferous conglomerates at Elliot Lake, Canada and Witwatersrand, South Africa: Implications for oxygen in the Precambrian atmosphere. *Precambrian Res.* **13**, 1–26.
- Haqq-Misra J. D., Domagal-Goldman S. D., Kasting P. J. and Kasting J. F. (2008) A revised, hazy methane greenhouse for the Archean Earth. *Astrobiology* **8**, 1127–1137.
- Hart M. H. (1978) The evolution of the atmosphere of the Earth. *Icarus* **33**, 23–39.
- Hazen R. M., Papineau D., Bleeker W., Downs R. T., Frey J. M., McCoy T. J., Sverjensky D. A. and Yang H. (2008) Mineral evolution. *Am. Mineral.* **93**, 1693–1720.
- Hoffman P. F., Haufman A. J., Halverson G. P. and Schrag D. P. (1998) A Neoproterozoic Snowball Earth. *Science* **281**, 1342–1346.

- Holland H. D. (1978) *The Chemistry of the Atmosphere and Oceans*. John Wiley & Sons, New York, 351pp.
- Holland H. D. (1984) *The Chemical Evolution of the Atmosphere and Oceans*. Princeton University Press, Princeton, NJ, 582 pp.
- Holland H. D. and Zbinden E. A. (1988) Paleosols and the evolution of atmosphere: Part I. In *Physical and Chemical weathering in Geochemical cycles* (eds. A. Larman and M. Meybeck). Reidel Dordrecht, pp. 61–82.
- Holland H. D. (2002) Volcanic gases, black smokers, and the Great Oxidation Event. *Geochim. Cosmochim. Acta* **66**, 3811–3826.
- Holland H. D. (2006) The oxygenation of the atmosphere and oceans. *Philos. Trans. R. Soc. B* **361**, 903–915.
- Holland H. D. (2009) Why the atmosphere became oxygenated: A proposal. *Geochim. Cosmochim. Acta* **73**, 5241–5255.
- Kasting J. F., Liu S. C. and Donahue T. M. (1979) Oxygen levels in the prebiological atmosphere. *J. Geophys. Res.* **84**, 3097–3107.
- Kasting J. F. (1987) Theoretical constraints on oxygen and carbon dioxide concentrations in the Precambrian atmosphere. *Precambrian Res.* **34**, 205–229.
- Kasting J. F. (2013) What caused the rise of atmospheric O₂? *Chem. Geol.* **362**, 13–25.
- Kharecha P., Kasting J. F. and Siefert J. (2005) A coupled atmosphere-ecosystem model of the early Archean Earth. *Geobiol.* **3**, 53–76.
- Kirschvink J. L. (1992) Late Proterozoic low-latitude global glaciations: the Snowball Earth. In *The Proterozoic Biosphere: A Multidisciplinary Study* (eds. J. W. Schopf and C. Klein), p. 51–52. Cambridge University Press, Cambridge.
- Knoll A. H. (2003) The geological consequences of evolution. *Geobiol.* **1**, 3–14.
- Konhauser K. O., Lalonde S. V., Planavsky N. J., Pecoits E., Lyons T. W., Mojzsis S. J., Rouzel O. J., Barley M. E., Rosière C., Fralick P. W., Kump L. R. and Bekker A. (2011) Aerobic bacterial pyrite oxidation and acid rock drainage during the Great Oxidation Event. *Nature* **478**, 369–373.
- Lasaga A. C. (1981) Dynamic treatment of geochemical cycles: Global kinetics. *Rev. Mineral.* **8**, 69–110.
- Lowe D. R. and Tice M. M. (2007) Tectonic controls on atmospheric, climatic, and biological evolution 3.5–2.4 Ga. *Precambrian Res.* **158**, 177–197.
- McKay C. P. and Hartman H. (1991) Hydrogen peroxide and the evolution of oxygenic photosynthesis. *Orig. Life Evol. Biosph.* **21**, 157–163.
- Murakami, T., Ito, J., Utsunomiya, S., Kasama, T., Kozai N. and Ohnuki T. (2004) Anoxic dissolution processes of biotite: Implications for Fe behavior during

- Archean weathering. *Earth Planet Sci. Lett.* **224**, 117–129.
- Murakami T., Sreenivas B., Das Sharma S. and Sugimori H. (2011) Quantification of atmospheric oxygen levels during the Paleoproterozoic using paleosol compositions and iron oxide kinetics. *Geochim. Cosmochim. Acta* **75**, 3982–4004.
- Nutman A. P. (2006) Antiquity of the oceans and continents. *Elements* **2**, 223–227.
- Och L. M. and Shields-Zhou G. A. (2012) The Neoproterozoic oxygenation event: Environmental perturbations and biogeochemical cycling. *Earth-Sci. Rev.* **110**, 26–57.
- Ohmoto H., Watanabe Y. and Kumazawa K. (2004) Evidence from massive siderite beds for a CO₂-rich atmosphere before ~1.8 billion years ago. *Nature* **429**, 395–399.
- Owen T., Cess R. D. and Ramanathan V. (1979) Enhanced CO₂ greenhouse to compensate for reduced solar luminosity on early Earth. *Nature* **277**, 640–642.
- Palandri J. L. and Kharaka Y. K. (2004) A compilation of rate parameters of water-mineral interaction kinetics for application to geochemical modeling. US Geol. Surv. Open File Report 2004–1068, 64 pp.
- Papineau D., Mojzsis S. J., Coath C. D., Karhu J. A. and McKeegan K. D. (2005) Multiple sulfur isotopes of sulfides from sediments in the aftermath of Paleoproterozoic glaciations. *Geochim. Cosmochim. Acta* **69**, 5033–5060.
- Papineau D., Mojzsis S. J. and Schmitt A. K. (2007) Multiple sulfur isotopes from Paleoproterozoic Huronian interglacial sediment and the rise of atmospheric oxygen. *Earth Planet Sci. Lett.* **255**, 188–212.
- Pavlov A. A., Kasting J. F., Brown, L. L., Rages K. A. and Freedman R. (2000) Greenhouse warming by CH₄ in the atmosphere of early Earth. *J. Geophys. Res.* **105**, 11981–11990.
- Pavlov A. A. and Kasting J. F. (2002) Mass-independent fractionation of sulfur isotopes in Archean sediments: Strong evidence for an anoxic Archean atmosphere. *Astrobiology* **2**, 27–41.
- Pierrehumbert R. T., Abbot D. S., Voigt A. and Knoll D. (2011) Climate of the Neoproterozoic. *Annu. Rev. Earth Planet. Sci.* **39**, 417–460.
- Pinto J. P. and Holland H. D. (1988) Paleosols and the evolution of the atmosphere; part II. In *Paleosols and Weathering through Geologic Time* (eds. J. Reinhardt and W. Silgeo). Spec. Pap. Geol. Soc., America, pp. 21–34.
- Pokrovsky O. S. and Schott J. (2000) Kinetics and mechanism of forsterite dissolution at 25°C and pH from 1 to 12. *Geochim. Cosmochim. Acta* **64**, 3313–3325.
- Rye R., Kuo P. H. and Holland H. D. (1995) Atmospheric carbon dioxide concentrations

- before 2.2 billion years ago. *Nature* **378**, 603–605.
- Rye R. and Holland H. D. (1998) Paleosols and the atmospheric oxygen: A critical review. *Am. J. Sci.* **298**, 621–672.
- Sagan C. and Mullen G. (1972) Earth and Mars: Evolution of atmospheres and surface temperatures. *Science* **177**, 52–56.
- Segura A., Krelow K., Kasting J. F., Sommerlatt D., Meadows V., Crisp D., Cohen M. and Mlawer E. (2003) Ozone concentrations and ultraviolet fluxes on Earth-like planets around other stars. *Astrobiology* **3**, 689–708.
- Schott J., Pokrovsky O. S. and Oelkers E. H. (2009) The link between mineral dissolution/precipitation kinetics and solution chemistry. *Rev. Mineral. Geochem.* **70**, 207–258.
- Sheldon N. D. (2006) Precambrian paleosols and atmospheric CO₂ levels. *Precambrian Res.* **147**, 148–155.
- Sheldon N. D. (2013) Causes and consequences of low atmospheric pCO₂ in the Late Mesoproterozoic. *Chem. Geol.* **362**, 224–231.
- Sugimori H., Yokoyama T. and Murakami T. (2009) Kinetics of biotite dissolution and Fe behavior under low O₂ conditions and their implications for Precambrian weathering. *Geochim. Cosmochim. Acta* **73**, 3767–3781.
- Sugimori H., Kanzaki Y., Yokota K. and Murakami T. (2011) Nonlinear dependence of the oxidation rate of Fe(II) on dissolved oxygen under low-O₂ conditions in aqueous solutions. *J. Mineral. Petrol. Sci.* **106**, 142–152.
- Sugimori H., Kanzaki Y. and Murakami T. (2012) Relationship between Fe redistribution and P_{O₂} during mineral dissolution under low O₂ conditions. *Geochim. Cosmochim. Acta* **84**, 29–46.
- Sverdrup H. U. (1990) *The Kinetics of Base Cation Release due to Chemical Weathering*. Lund University Press, Lund, Sweden, 246 p.
- Sverjensky D. A. and Lee N. (2010) The Great Oxidation Event and mineral diversification. *Elements* **6**, 31–36.
- Trainer M. G., Pavlov A. A., Dewitt H. L., Jimenez J. L., McKay C. P., Toon O. B. and Tolbert M. A. (2006) Organic haze on Titan and the early Earth. *Proc. Natl. Acad. Sci.* **103**, 18035–18042.
- Urey H. C. (1952) On the early chemical history of the Earth and the origin of life. *Proc. Natl. Acad. Sci. U.S.A.* **38**, 351–363.
- Valley J. W., Peck W. H., King E. M. and Wilde S. A. (2002) A cool early Earth. *Geology* **30**, 351–354.
- Walker J. C. G. (1977) *Evolution of the Atmosphere*. Macmillan, New York.

- Walker J. C. G. (1982) Climatic factors on the Archean earth. *Palaeogeography Palaeoclimatol. Palaeoecol.* **40**, 1–11.
- White A. F. and Brantley S. L. (1995) Chemical weathering rates of silicate minerals: an overview. *Rev. Mineral.* **31**, 1–22.
- White A. F. and Brantley S. L. (2003) The effect of time on the weathering of silicate minerals: Why do weathering rates differ in the laboratory and field? *Chem. Geol.* **202**, 479–506.
- Wogelius R. A. and Walther J. V. (1991) Olivine dissolution at 25°C: Effects of pH, CO₂ and organic acids. *Geochim. Cosmochim. Acta* **55**, 943–954.
- Wordsworth R. and Pierrehumbert R. (2013) Hydrogen-Nitrogen greenhouse warming in Earth's early atmosphere. *Science* **339**, 64–67.
- Yokota K., Kanzaki Y. and Murakami T. (2013) Weathering model for the quantification of atmospheric oxygen evolution during the Paleoproterozoic. *Geochim. Cosmochim. Acta* **117**, 332–347.
- Zahnle K. J., Claire M. and Catling D. (2006) The loss of mass-independent fractionation in sulfur due to a Paleoproterozoic collapse of atmospheric methane. *Geobiology* **4**, 271–283.

II. Estimates of atmospheric CO₂ in the Neoproterozoic-Paleoproterozoic from paleosols

1. Introduction

Evolution of atmospheric CO₂ through the whole history of the Earth has been correlated with the surface environments, especially surface temperatures. While the levels of partial pressure of atmospheric CO₂ (P_{CO_2}) in the Phanerozoic are elaborately reconstructed (Berner et al., 1983; Berner, 1991; 2006), those in the Precambrian are less established because of scarce geological records for atmospheric CO₂. The Precambrian Earth should have been a “Snowball” if the atmospheric composition at the time had not had greater greenhouse effects than the present one due to the significantly weak luminosity from the young Sun (“faint young Sun” problem; Sagan and Mullen (1972); see Feulner (2012) for a recent review of the issue). Indeed, the wide-spread glaciation events occurred at ~2.9 Ga (Wiebols, 1955; von Brunn and Gold, 1993; Young et al., 1998) and at ~2.4–2.2 Ga (Coleman, 1907; Young, 1970; Bekker et al., 2001, 2005), and some of them could have been “Snowball” events (Evans et al., 1997). Atmospheric CO₂ can work as an effective greenhouse-effect gas (Hart, 1978; Owen et al., 1978; Kasting, 1987; Haqq-Misra et al., 2008; von Paris et al., 2008) along with other potential greenhouse-effect gases to compensate the weak luminosity in the Precambrian Earth. It is thus important to understand the variation of P_{CO_2} levels in the Neoproterozoic (2.8–2.5 Ga) and the Paleoproterozoic (2.5–1.6 Ga).

The above glaciations are considered to have been related to the transition of greenhouse-effect gases, especially CO₂ and CH₄, because another greenhouse gas NH₃ (Sagan and Mullen, 1972) should have been vulnerable to intense UV in the above eras (Kuhn and Atreya, 1979). Although CH₄ can serve as complementary greenhouse-effect gas to CO₂ (Kasting et al., 1983; Kiehl and Dickinson, 1987; Kasting, 1993; Pavlov et al., 2000), too much of atmospheric CH₄ makes organic haze that conversely cools the Earth (Pavlov et al., 2001a; see, on the other hand, the minimal anti-greenhouse effects by fractal organic haze, Wolf and Toon (2010)). Organic haze formation depends on the ratio of CH₄/CO₂ (Pavlov et al., 2001b; Trainer et al., 2006; Haqq-Misra et al., 2008; Zerkle et al., 2012); the atmosphere is haze free when CH₄/CO₂ < 0.1 and with thin haze when CH₄/CO₂ \cong 0.2 (Zerkle et al., 2012). The ratio and contents of CH₄ and CO₂ in the atmosphere are key factors to determine the surface temperature in the Neoproterozoic-Paleoproterozoic (Lowe and Tice, 2004, 2007; Domagal-Goldman et al.,

2008; Haqq-Misra et al., 2008).

Furthermore, the early Paleoproterozoic is also the era of evolution of atmospheric oxygen (the Great Oxidation Event, Holland (2006)) and possibly evolution of oxygenic photosynthesis (e.g., Knoll, 2003; Kopp et al., 2005; Liang et al., 2006). The evolution of atmosphere and early organisms and the wide-spread glaciations in the early Paleoproterozoic are considered to have been correlated (Knoll, 2003; Papineau et al., 2005; Kopp et al., 2005; Clare et al., 2006; Liang et al., 2006; Zahnle et al., 2006; Bekker and Kaufman, 2007; Domagal-Goldman et al., 2008; Sekine et al., 2011; Hoffman, 2013). The variation of P_{CO_2} levels in the Neoproterozoic-Paleoproterozoic is also a crucial key for understanding the evolution of early organisms and atmospheric O_2 .

The P_{CO_2} levels have been estimated by utilizing chemical weathering of continental rocks, formation of carbonates, metamorphism of sedimentary rocks and mantle degassing (Holland, 1978, 1984; Lasaga, 1981; Tajika and Matsui, 1992; Sleep and Zahnle, 2001). The utilization of paleosol, fossil weathering profile, as a geological record for reconstruction of P_{CO_2} focuses solely on the chemical weathering process. The estimation of P_{CO_2} from paleosols in the Neoproterozoic-Paleoproterozoic has been made by two different methods. One is a thermodynamic method using siderite ($Fe(II)CO_3$)/greenalite ($Fe(II)_3Si_2O_5(OH)_4$) phase equilibrium (Rye et al., 1995). Because of the absence of siderite as a secondary mineral in the paleosols at > 2.2 Ga, Rye et al. (1995) estimated < 100 of the present day atmospheric level (PAL) of P_{CO_2} at the time of weathering. However, the occurrence of greenalite as a secondary mineral in a weathering profile was criticized by Sheldon (2006). The other is a mass balance method proposed by Sheldon (2006) as a more accurate way of reconstructing P_{CO_2} from paleosols; this method calculates the amounts of CO_2 consumed by cations released from paleosols and converts the amounts to P_{CO_2} . This method has estimated 7–70 PAL of P_{CO_2} at 2.5–1.8 Ga (Sheldon, 2006) and 10–50 PAL at 2.69 Ga (Driese et al., 2011). Importantly, P_{CO_2} levels have been used either directly or indirectly as a parameter for the estimation of P_{O_2} levels from paleosols (Holland, 1984; Murakami et al., 2011a; Yokota et al., 2013). Therefore, the estimated P_{CO_2} levels should be sufficiently precise to understand the atmospheric evolution in the Neoproterozoic-Paleoproterozoic. I have developed a new method to more precisely estimate P_{CO_2} levels from 2.8–1.8 Ga paleosols.

The effects of CO_2 on mineral dissolution have been examined; the dissolution rate of feldspar is increased with increase in CO_2 (e.g., Sverdrup, 1990), while those of some other minerals such as olivine and pyroxene are not affected by CO_2 (e.g.,

Wogelius and Walther, 1991; Golubev et al., 2005). For feldspar dissolution, the rate is proportionally related to $P_{\text{CO}_2}^n$ where $n = 0.2\text{--}0.5$ (e.g., Sverdrup, 1990; Utsunomiya et al., 1999; Berg and Banwart, 2000; Navarre-Sitchler and Thyne, 2007). However, such quantitative relationships between mineral dissolution rates and P_{CO_2} may not be directly applied to paleosols for the quantitative estimation of P_{CO_2} levels at the time of weathering because of several orders of magnitude difference in mineral dissolution rates between the laboratory and field (e.g., Paces, 1983; Yokoyama and Banfield, 2002; White and Brantley, 2003). On the other hand, CO_2 in porewater in a weathering profile function as a dominant charge-balancing agent (Holland, 1978), and thus, is useful to deduce P_{CO_2} levels from porewater chemistries. While the cation concentrations in porewaters are different between weathering systems depending on temperature, evapotranspiration, precipitation and so on (e.g., Drever and Zobrist, 1992; White and Blum, 1995), the porewater compositions usually terminate near the equilibrium between kaolinite and smectite (Garrels, 1967; Nesbitt, 1977; Nesbitt and Young, 1984; 1989; Nesbitt and Wilson, 1992), which is useful to estimate P_{CO_2} levels.

This chapter has been undertaken to estimate P_{CO_2} levels in the Neoproterozoic-Paleoproterozoic from the chemical compositions of paleosols. My new method firstly calculates the cation concentrations in porewaters at the time of weathering from those of solid, weathering profiles (Section 2.1). Then, the new method introduces an equation describing the relationships between P_{CO_2} , pH and cation concentrations based on the charge balance between the cations and anions including carbonate species in porewaters (Section 2.2). Thermodynamics of possible secondary minerals gives pH constraints (Section 2.3), which allows me to estimate P_{CO_2} levels. The new method is validated by applying it to the chemical compositions of modern weathering profiles (Section 3.1). The characteristics of the weathering rate law derived from the present method also argue the validity of the method (Section 3.2). Finally, P_{CO_2} levels in the Neoproterozoic-Paleoproterozoic are calculated based on the chemical compositions of paleosols (Section 4).

2. A new method to estimate P_{CO_2} from weathering profiles

I here introduce general equations that describe cation concentrations in porewater, charge balance between cations and anions in porewater, and relationships between P_{CO_2} , pH and cation concentrations. The general equations can be applicable to weathering profiles including the modern. All calculations in this section were made at the condition of 15°C , unless otherwise described, according to $10\text{--}20^\circ\text{C}$ of the

suggested surface-temperature since the Paleoproterozoic onwards (Tajika and Matsui, 1993). The P_{CO_2} estimates considering temperature variation will be discussed below in Section 4.

2.1. Estimation of cation concentrations in porewater from a remaining weathering profile

The cation concentrations in porewater in a weathering profile at the time of weathering were estimated by considering the mass balance of each cation between solid and water phases. I consider elemental transport only along a certain water flow path in a weathering profile for simplicity (e.g., Holland and Zbinden, 1988; Pinto and Holland, 1988; Maher, 2010). Differential equation for the time evolution of cation X in porewater is given by

$$\frac{d[X]}{dt} = R_X([X]) - P_X([X]) - \frac{F}{V}[X] - D_X \frac{\partial^2[X]}{\partial z^2} \quad (1)$$

where $[X]$ and t denote the concentration of X dissolved in porewater (mol L^{-1}) and the time (yr), respectively. The first term in the right hand side of Eq. (1), $R_X([X])$ ($\text{mol L}^{-1} \text{yr}^{-1}$), is the rate of X supplied by the dissolution of minerals that contain X, expressed by some function, R_X , of $[X]$. The second term, $P_X([X])$ ($\text{mol L}^{-1} \text{yr}^{-1}$), represents the rate of X removed by the precipitation of secondary minerals that contain X, expressed by some precipitation function, P_X , of $[X]$. The third term, $(F/V) \times [X]$, is the rate of X removed by water flow with F and V representing the volumetric water flow (L yr^{-1}) and the water volume in pore space (L), respectively. The last term represents the loss rate of X by diffusion, with D_X and z denoting the diffusion coefficient for X ($\text{m}^2 \text{yr}^{-1}$) and the length of water flow path (m), respectively. In most weathering profiles, diffusion effects are negligible compared to those of water flow (Maher, 2010), and then Eq. (1) can be simplified as

$$\frac{d[X]}{dt} = R_X([X]) - P_X([X]) - k_f[X] \quad (2)$$

where k_f is defined here as the rate constant of X removed by water flow ($k_f \equiv F/V$ (yr^{-1}), c.f., Berner, 1978).

Differential equation for the time evolution of the concentration of X in the rock phase, $[X\text{-rock}]$ (mol m^{-3}), can be written as

$$\frac{d[X\text{-rock}]}{dt} = -\theta\sigma\{R_X([X]) - P_X([X])\} \quad (3)$$

where θ and σ represent the porosity ($\text{m}^3 \text{m}^{-3}$) and the water saturation ratio (L m^{-3}) of

the weathering profile, respectively. When the water phase becomes in steady state,

$$\frac{d[X]}{dt} = 0 = R_X([X]_{ss}) - P_X([X]_{ss}) - k_f[X]_{ss} \quad (4)$$

where $[X]_{ss}$ represents the steady-state concentration of X in porewater (mol L^{-1}). The cation concentrations in porewater are reported to reach to those in steady state in a significantly short period of time compared with total weathering duration in modern weathering systems (e.g., Stonestrom et al., 1998; Brantley and White, 2009; White et al., 2009). Therefore, I can substitute Eq. (4) into Eq. (3), giving

$$\frac{d[X - \text{rock}]}{dt} = -\theta\sigma k_f [X]_{ss} \quad (5)$$

Although θ , σ and k_f are a function of time, I can regard them as constants for the further calculation (see Appendix A). In addition, $[X]$ remains as $[X]_{ss}$ for most of the total weathering time. Then, integration of Eq. (5) for the whole weathering time, t_{tot} (yr), yields

$$[X - \text{rock}]_{\text{loss}} = \theta\sigma k_f [X]_{ss} t_{\text{tot}} \quad (6)$$

where $[X - \text{rock}]_{\text{loss}}$ is the concentration of the total loss of X from parent rock (mol m^{-3}). Using Eq. (6), I can estimate $[X]_{ss}$ from $[X - \text{rock}]_{\text{loss}}$ (i.e., cation concentration in porewater from the chemical composition of a weathering profile) if the values of θ , σ , k_f and t_{tot} are given:

$$[X]_{ss} = \frac{[X - \text{rock}]_{\text{loss}}}{\theta\sigma k_f t_{\text{tot}}} \quad (7)$$

However, it is practically difficult to estimate the values of θ , σ , k_f and t_{tot} . To solve Eq. (7), I use Si as a reference element because its concentration in porewater of a weathering profile can be constrained in a relatively small range (e.g., Rye et al., 1995; White, 1995; Ohmoto et al., 2004; Appelo and Postma, 2005). From Eq. (6) for Si,

$$[\text{Si} - \text{rock}]_{\text{loss}} = \theta\sigma k_f [\text{Si}]_{ss} t_{\text{tot}} \quad (8)$$

From Eq. (8),

$$\theta\sigma k_f t_{\text{tot}} = \frac{[\text{Si} - \text{rock}]_{\text{loss}}}{[\text{Si}]_{ss}} \quad (9)$$

Substituting Eq. (9) into Eq. (7) yields

$$[X]_{ss} = \frac{[X - \text{rock}]_{\text{loss}}}{[\text{Si} - \text{rock}]_{\text{loss}}} [\text{Si}]_{ss} \quad (10)$$

I can calculate any cation concentrations in porewaters according to Eq. (10), once $[X - \text{rock}]_{\text{loss}}$, $[\text{Si} - \text{rock}]_{\text{loss}}$ and $[\text{Si}]_{ss}$ are given.

I calculate $[X - \text{rock}]_{\text{loss}}$ and $[\text{Si} - \text{rock}]_{\text{loss}}$ from the concentration depth-profiles of X and Si, respectively. $[\text{Si}]_{ss}$ in porewater, which is required to calculate $[X]_{ss}$ from Eq.

(10), usually falls between the solubilities of quartz and amorphous silica (Appelo and Postma, 2005). Then, $[\text{Si}]_{\text{ss}}$ is in the range of $10^{-3.9}$ – $10^{-2.8}$ mol L⁻¹ at 15°C. The solubilities of quartz, K_{quartz} , and amorphous silica, $K_{\text{amorphous_silica}}$, were obtained from Gunnarsson and Arnórsson (2000). Based on the values of $[\text{X-rock}]_{\text{loss}}/[\text{Si-rock}]_{\text{loss}}$ obtained from the chemical compositions of a weathering profile and the above range of $[\text{Si}]_{\text{ss}}$ values, the $[\text{X}]_{\text{ss}}$ values for Fe, Mg, Ca, Na and K are calculated for the weathering profile. To demonstrate the steps from the calculations of the values of $[\text{X-rock}]_{\text{loss}}/[\text{Si-rock}]_{\text{loss}}$ and $[\text{X}]_{\text{ss}}$ to those of pH (see below), I take one paleosol and one modern weathering profile as examples, Pronto/NAN (Table 1; G-Farrow and Mossman, 1988) and SCT1 profile at Santa Cruz (Table 2; White et al., 2008, 2009), respectively. See Appendix B for the calculation of $[\text{X-rock}]_{\text{loss}}$ and Section 4.1 for $[\text{K-rock}]_{\text{loss}}$ of paleosols. The $[\text{X}]_{\text{ss}}$ values of the SCT1 profile and the Pronto/NAN paleosol are plotted against $[\text{Si}]_{\text{ss}}$ (Figs. 1a and b). The new method is thus characterized by its calculation of steady-state cation concentrations in porewater from the chemical compositions of a weathering profile without knowing the total weathering time.

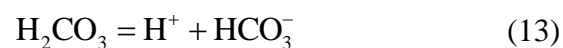
2.2. Estimation of P_{CO_2} from charge balance in porewater

Using the steady-state cation concentrations estimated for weathering profiles in the previous section, I here establish the relationships between the cation concentrations, pH and P_{CO_2} estimated from charge balance in porewater. Equation for charge balance in porewater is given by

$$\sum_{\text{X}} Z_{\text{X}} [\text{X}^{\text{Z}_{\text{X}}+}] + [\text{H}^+] = [\text{HCO}_3^-] + 2[\text{CO}_3^{2-}] + [\text{OH}^-] \quad (11)$$

where Z_{X} denotes the valence number of cation X. $[\text{HCO}_3^-]$, $[\text{CO}_3^{2-}]$, $[\text{OH}^-]$ and $[\text{H}^+]$ represent the concentrations (mol L⁻¹) of bicarbonate ion, carbonate ion, hydroxyl ion and proton, respectively, and at steady state, $[\text{X}^{\text{Z}_{\text{X}}+}] = [\text{X}]_{\text{ss}}$. In Eq. (11), I assumed only bicarbonate and carbonate ions derived from gaseous CO₂ are the predominant anions (Holland, 1978). The contributions of other possible anions to charge balance in porewater had negligible effects on charge balance and therefore were ignored (see Appendix C for the detail).

Bicarbonate and carbonate ions are in equilibrium with gaseous CO₂ through the following reactions:





Using equilibrium constants of K_H , K_1 and K_2 for Reactions (12), (13) and (14), respectively, the concentrations of bicarbonate and carbonate ions can be calculated as

$$[\text{HCO}_3^-] = \frac{K_1 K_H P_{\text{CO}_2}}{[\text{H}^+]} \quad (15)$$

$$[\text{CO}_3^{2-}] = \frac{K_1 K_2 K_H P_{\text{CO}_2}}{[\text{H}^+]^2} \quad (16)$$

where $\log K_H = -1.34$ ($\text{mol L}^{-1} \text{atm}^{-1}$), $\log K_1 = -6.42$ (mol L^{-1}) and $\log K_2 = -10.43$ (mol L^{-1}). The H^+ and OH^- concentrations are related to one another by the water dissociation constant, K_w :

$$[\text{OH}^-] = \frac{K_w}{[\text{H}^+]} \quad (17)$$

where $\log K_w = -14.35$ $\text{mol}^2 \text{L}^{-2}$. The values of K_H , K_1 , K_2 and K_w are those at 15°C and obtained from Stumm and Morgan (1996).

Substituting Eqs. (15)–(17) into Eq. (11) gives

$$\sum_{\text{X}} Z_{\text{X}} [\text{X}^{Z_{\text{X}}+}] + [\text{H}^+] = \frac{K_1 K_H P_{\text{CO}_2}}{[\text{H}^+]} + 2 \frac{K_1 K_2 K_H P_{\text{CO}_2}}{[\text{H}^+]^2} + \frac{K_w}{[\text{H}^+]} \quad (18)$$

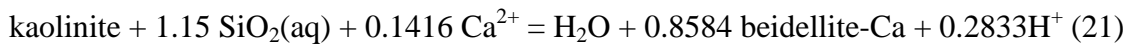
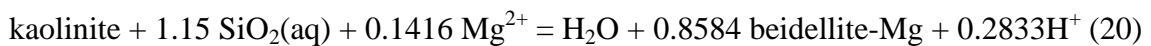
Because $[\text{OH}^-]$ is negligible compared to $[\text{HCO}_3^-]$ and $[\text{CO}_3^{2-}]$ at $\text{pH} < 10$ and $P_{\text{CO}_2} > 0.1$ PAL and because the proton concentration is similarly negligible compared to the total cation concentrations at $\text{pH} > 4$, Eq. (18) is simplified as

$$\sum_{\text{X}} Z_{\text{X}} [\text{X}^{Z_{\text{X}}+}] = \frac{K_1 K_H P_{\text{CO}_2}}{[\text{H}^+]} + 2 \frac{K_1 K_2 K_H P_{\text{CO}_2}}{[\text{H}^+]^2} \quad (19)$$

Eq. (19) clearly indicates that I only need the chemical compositions and pH of porewater of a weathering profile for the estimation of P_{CO_2} at a given temperature. I have confirmed that, in the range of pH from 4 to 10, Eqs. (18) and (19) yield the same calculated value of P_{CO_2} at a given total cation concentration and pH (data not shown). The porewater pH is reasonably assumed to be < 10 . At 1000 PAL of P_{CO_2} , pH ~ 4 is expected for rainwater (i.e., for simple $\text{H}_2\text{O}-\text{CO}_2$ system), and weathering will increase the pH to $> \sim 4.5$ in the range of $10^{-3.9}$ – $10^{-2.8}$ mol L^{-1} of $[\text{Si}]_{\text{ss}}$ (Section 2.1) by releasing cations into porewater. Therefore, Eq. (19) in the range of $4 < \text{pH} < 10$ will be used for the further discussion. Eqs. (10) and (19) show that larger $[\text{Si}]_{\text{ss}}$ values give larger pH values at a given P_{CO_2} and larger P_{CO_2} values at a given pH. Because the values of $\sum Z_{\text{X}} [\text{X}^{Z_{\text{X}}+}]$ can be obtained (Section 2.1), the pH values should be constrained to estimate P_{CO_2} values with smaller uncertainties.

2.3. pH constraints from secondary minerals

Co-existent secondary minerals can constrain pHs in porewaters of weathering profiles. The porewater compositions usually terminate near the equilibrium boundary between kaolinite and smectite (Garrels, 1967; Nesbitt, 1977; Nesbitt and Young, 1984; 1989; Nesbitt and Wilson, 1992), which is consistent with the presence of co-existent secondary kaolinite and smectite (Nesbitt and Wilson, 1992). Although the mineralogical compositions of paleosols are obscured by later geological events such as diagenesis, kaolinite and smectite are considered to have been present as secondary minerals at the time of weathering (Retallack, 1991; Retallack and Krinsley, 1993; Rye and Holland, 2000; Murakami et al., 2004; 2011b). Then I can reasonably assume that the porewater compositions of weathering profiles including paleosols were near the boundary of kaolinite/smectite. Thermodynamics of beidellites-Mg, -Ca and -Na ((Mg_{0.165})(Al₂)(Si_{3.67}Al_{0.33})O₁₀(OH)₂, (Ca_{0.165})(Al₂)(Si_{3.67}Al_{0.33})O₁₀(OH)₂, and (Na_{0.33})(Al₂)(Si_{3.67}Al_{0.33})O₁₀(OH)₂, respectively) were used for those of smectites. The equilibria of kaolinite/beidellite-Mg, kaolinite/beidellite-Ca and kaolinite/beidellite-Na are expressed by the following respective reactions:



Because K is involved in the equilibrium of kaolinite and muscovite, the equilibrium can further constrain pHs of porewaters. I, therefore, consider the kaolinite/muscovite boundary:



Equilibrium constants for Reactions (20)–(23) are defined here as K_{Mg} , K_{Ca} , K_{Na} and K_{K} , respectively, and obtained from the Lawrence Livermore National Laboratory thermodynamic dataset, thermo.com.v8r6+.dat (Delany and Lundeen, 1990) (Table 3).

The relationships between cation concentrations, $[\text{H}^+]_{\text{ss}}$ and $[\text{Si}]_{\text{ss}}$ at the phase boundaries can be obtained using the equilibrium constants for Reactions (20)–(23). For example, the porewater composition at the kaolinite/beidellite-Mg boundary (Reaction (20)) is expressed as

$$0.1416 \times \log [\text{Mg}^{2+}]_{\text{ss}} + 1.15 \times \log [\text{Si}]_{\text{ss}} - 0.2833 \times \log [\text{H}^+]_{\text{ss}} = -\log K_{\text{Mg}} \quad (24)$$

which gives a range of $[\text{H}^+]_{\text{ss}}$ values because $[\text{Mg}^{2+}]_{\text{ss}}$ is obtained as a function of $[\text{Si}]_{\text{ss}}$, $10^{-3.9}$ – $10^{-2.8}$ mol L⁻¹ at 15 °C for instance (Section 2.1). Similarly, $[\text{H}^+]_{\text{ss}}$ values (or pHs) at the kaolinite/the other smectites and kaolinite/muscovite boundaries can be plotted against $[\text{Si}]_{\text{ss}}$ for a weathering profile. Because kaolinite and smectite are present

as secondary minerals in weathering profiles, the porewater pHs are near the kaolinite/smectites boundaries that are limited by the kaolinite/muscovite boundary. The step for pH constraint is demonstrated by the shaded areas in Figs. 1c and d for the SCT1 profile (pH of 5.9–7.5) and the Pronto/NAN paleosol (pH of 5.8–7.7), respectively.

I can further constrain pH from saturation states of carbonate minerals during weathering under the conditions of the presence of the clay minerals. When a porewater is supersaturated with respect to the clay minerals, the porewater should have high concentrations of cations such as Ca and Mg (Garrels, 1967; Nesbitt, 1977; Nesbitt and Young, 1984; 1989; Nesbitt and Wilson, 1992). Under such conditions, a porewater with carbonate saturation does not reach smectite saturation because of the fast precipitation rates of carbonates (e.g., Busenberg and Plummer, 1986; Pokrovsky and Schott, 2002). Indeed, carbonate precipitation is usually correlated with specific conditions such as large amounts of carbonates in host rocks, degassing of CO₂ from solution and temporal, intense evaporation (Wang et al., 1994; Berner and Berner, 1996; Capo et al., 2000). Thus, porewater compositions are close to the saturation of clay minerals (Lasaga et al., 1994). I can also assume that Fe-carbonates did not occur in the paleosols used (Rye et al., 1995). Even when calcite is contained in a parent rock as in the case for the Flin Flon paleosol (Holland et al., 1989), the porewater compositions are calculated only from silicate weathering.

Consequently, I can give pH constraints from the undersaturation of carbonates at the kaolinite/smectite boundary; I use solubilities of five carbonate minerals, calcite (CaCO₃), magnesite (MgCO₃), siderite (FeCO₃), dolomite (CaMg(CO₃)₂) and ankerite (CaFe(CO₃)₂):

$$[\text{Ca}^{2+}][\text{CO}_3^{2-}] = K_{\text{calcite}} \quad (25)$$

$$[\text{Mg}^{2+}][\text{CO}_3^{2-}] = K_{\text{magnesite}} \quad (26)$$

$$[\text{Fe}^{2+}][\text{CO}_3^{2-}] = K_{\text{siderite}} \quad (27)$$

$$[\text{Ca}^{2+}][\text{Mg}^{2+}][\text{CO}_3^{2-}]^2 = K_{\text{dolomite}} \quad (28)$$

$$[\text{Ca}^{2+}][\text{Fe}^{2+}][\text{CO}_3^{2-}]^2 = K_{\text{ankerite}} \quad (29)$$

where K_{calcite} , $K_{\text{magnesite}}$, K_{siderite} , K_{dolomite} and K_{ankerite} are the solubilities of calcite, magnesite, siderite, dolomite and ankerite, respectively (Table 3, data from Stumm and

Morgan (1996), Shock et al. (1997) and Holland and Powell (1998)). $[\text{CO}_3^{2-}]$ in Eqs. (25)–(29) can be obtained from equations for charge balance (Section 2.2). From the dissociation of bicarbonate ion (Reaction (14)),

$$[\text{HCO}_3^-] = \frac{[\text{H}^+][\text{CO}_3^{2-}]}{K_2} \quad (30)$$

I have already discussed that I can ignore the concentrations of H^+ and OH^- in Eq. (11) (Section 2.2), and then, I substitute Eq. (30) into Eq. (11):

$$\sum_X Z_X [\text{X}^{Z_X+}] = \frac{[\text{H}^+][\text{CO}_3^{2-}]}{K_2} + 2[\text{CO}_3^{2-}] \quad (31)$$

Thus, $[\text{CO}_3^{2-}]$ is expressed by

$$[\text{CO}_3^{2-}] = \sum_X Z_X [\text{X}^{Z_X+}] \left(\frac{[\text{H}^+]}{K_2} + 2 \right)^{-1} \quad (32)$$

Substituting Eq. (32) into Eqs. (25)–(29) yields the following respective equations:

$$[\text{H}^+] = K_2 \left(\frac{[\text{Ca}^{2+}]}{K_{\text{calcite}}} \sum_X Z_X [\text{X}^{Z_X+}] - 2 \right) \quad (33)$$

$$[\text{H}^+] = K_2 \left(\frac{[\text{Mg}^{2+}]}{K_{\text{magnesite}}} \sum_X Z_X [\text{X}^{Z_X+}] - 2 \right) \quad (34)$$

$$[\text{H}^+] = K_2 \left(\frac{[\text{Fe}^{2+}]}{K_{\text{siderite}}} \sum_X Z_X [\text{X}^{Z_X+}] - 2 \right) \quad (35)$$

$$[\text{H}^+] = K_2 \left(\sqrt{\frac{[\text{Ca}^{2+}][\text{Mg}^{2+}]}{K_{\text{dolomite}}}} \sum_X Z_X [\text{X}^{Z_X+}] - 2 \right) \quad (36)$$

$$[\text{H}^+] = K_2 \left(\sqrt{\frac{[\text{Ca}^{2+}][\text{Fe}^{2+}]}{K_{\text{ankerite}}}} \sum_X Z_X [\text{X}^{Z_X+}] - 2 \right) \quad (37)$$

Because the steady-state concentrations of $[\text{Ca}^{2+}]_{\text{ss}}$, $[\text{Mg}^{2+}]_{\text{ss}}$, $[\text{Fe}^{2+}]_{\text{ss}}$ and $\sum_X Z_X [\text{X}^{Z_X+}]$ are represented as a function of $[\text{Si}]_{\text{ss}}$ (Eq. (10)), pHs at carbonate equilibria can be plotted against $[\text{Si}]_{\text{ss}}$ for a weathering profile. The example curves shown in Figs. 1e and f represent the lower limits of pHs at which the carbonates precipitate. Then, the undersaturation of the carbonates gives the upper limits of pHs of porewaters at the time of weathering. Figs. 1e and f demonstrate that calcite and siderite are the carbonates that precipitate at the lowest pH at any given $[\text{Si}]_{\text{ss}}$ values for the SCT1 profile at Santa Cruz

and the Pronto/NAN paleosol, respectively. Finally, the presence of kaolinite and smectite and the undersaturation of carbonates give pH constraints as demonstrated in Figs. 1g and h; pH = 5.9–7.5 and 5.8–6.1 for the SCT1 profile and the Pronto/NAN paleosol, respectively. At this stage, I can calculate the P_{CO_2} levels at the time of weathering for the SCT1 profile at Santa Cruz and the Pronto/NAN paleosol according to Eq. (19).

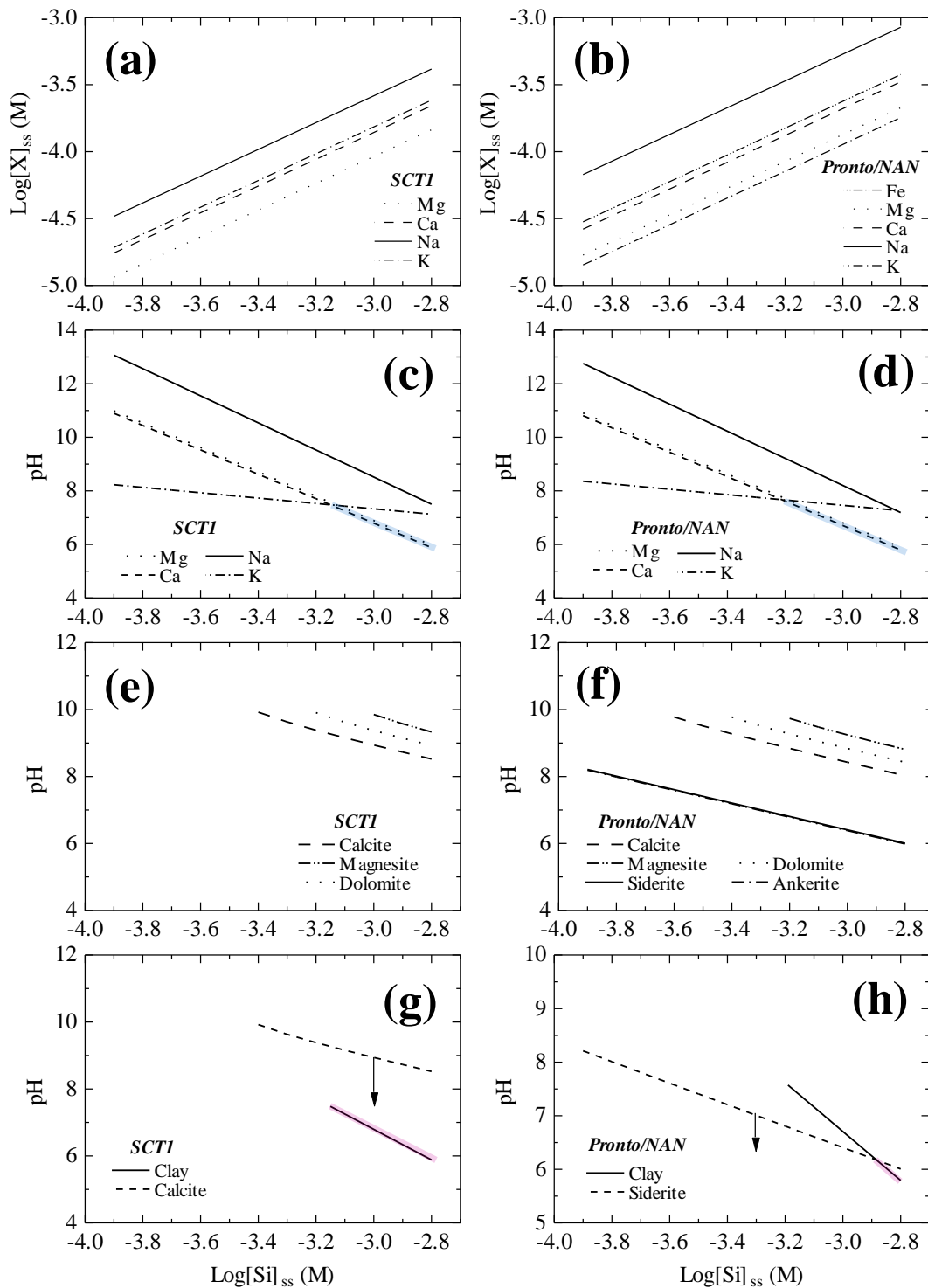


Figure 1. Steps from the calculation of $[X]_{ss}$ to constraint of porewater pH of weathering profiles.

For the demonstration of the steps, I used one modern weathering profile (SCT1 profile at Santa

Cruz, left column, (a), (c), (e) and (g), White et al., 2008; 2009) and one paleosol (Pronto/NAN paleosol, right column, (b), (d), (f) and (h), G-Farrow and Mossman, 1988) as examples. (a) and (b) Steady-state cation concentrations based on Eq. (10), plotted against $[\text{Si}]_{\text{ss}}$ in log unit. (c) and (d) Kaolinite/smectites and kaolinite/muscovite equilibria in the pH- $[\text{Si}]_{\text{ss}}$ plots, indicating porewater pH constraints (shaded areas). The lines with marks of Mg, Ca, Na and K represent the kaolinite/beidellite-Mg, kaolinite/beidellite-Ca, kaolinite/beidellite-Na and kaolinite/muscovite equilibria. Note that the kaolinite/beidellite-Mg (dotted line) and the kaolinite/beidellite-Ca (dashed line) equilibria lines are almost entirely overlapped in both the figures. (e) and (f) Carbonate saturation equilibria in the pH- $[\text{Si}]_{\text{ss}}$ plots. Calcite and siderite are calculated to be the carbonates to precipitate in the lowest pH regions in the SCT1 profile and the Pronto/NAN paleosol, respectively. In the final step, (g) and (h) pH regions in the pH- $[\text{Si}]_{\text{ss}}$ plots constrained from both smectite precipitation (“clay”) and carbonate unsaturation as shown by the shaded areas. Note that the kaolinite/muscovite equilibrium constrains pH along with the siderite unsaturation for the Pronto/NAN paleosol but carbonate saturation does not constrain pH for the SCT1 profile.

Table 1. $[X\text{-rock}]_{\text{loss}}/[Si\text{-rock}]_{\text{loss}}$ values and formation ages for the Neoproterozoic-Paleoproterozoic paleosols.

Paleosol profile	Age ^a (Ga)	$[X\text{-rock}]_{\text{loss}}/[Si\text{-rock}]_{\text{loss}}^b$					Ref. ^c
		Fe	Mg	Ca	Na	K ^d	
Mt. Roe1	2.775–2.755	0.136	0.114	0.175	0.045	0.102	1
Mt. Roe2	2.775–2.755	0.250	0.166	0.026	0.100	0.029	1
Bird	2.8–2.7	0.240	0.357	0.212	0.144	0.004	2
Cooper Lake	2.475–2.440	0.463	0.235	0.049	0.307	0.075	3
Pronto/NAN	2.475–2.440	0.237	0.134	0.209	0.535	0.113	4
Gaborone	2.245–2.059	0.022 (± 0.007) ^e	0.262	0.157	0.196	0.020	5
Drakenstein	2.222–1.928	0.028 (± 0.019) ^e	0.271	0.316	0.188	0.017	6
Flin Flon	1.9–1.8	≤ 0.022 ^f	0.658 (± 0.114) ^e	0.860 ^g (± 0.186) ^e	0.076	0.006	7

^a From Rye and Holland (1998).

^b Calculated based on the retention fractions of elements (see Appendix B).

^c 1—Macfarlane et al. (1994); 2—Palmer et al. (1989); 3—Utsunomiya et al. (2003); 4—G-Farrow and Mossman (1988); 5—Yang and Holland (2003); 6—Wiggering and Beukes (1990); 7—Holland et al. (1989)

^d Calculated using the retention fractions of Na for all respective paleosols except for the Pronto/NAN paleosol for which two times of the retention fraction of Na was used (see Appendix B).

^e Errors more than 10% are only shown in parentheses. The errors were calculated from the errors in the retention fractions.

^f Only the upper limit is shown because of almost complete retention of Fe in the Flin Flon paleosol (Murakami et al., 2011a).

^g Calcium loss associated with silicates is obtained by subtracting CO₂ loss (mol m⁻³) from the total calcium loss (mol m⁻³).

Table 2. Parameters for modern weathering profiles and observed and calculated pH and P_{CO_2} .

Locality name	[X-rock] _{loss} /[Si-rock] _{loss} ^a				Temperature ^b (°C)	Calc. pH	Obs. pH ^b	Calc. soil P_{CO_2} (atm)	Obs. soil P_{CO_2} ^b (atm)	Ref. ^c	
	Mg	Ca	Na	K							
SCT1	0.092	0.139	0.261	0.153	15	5.9–7.5	5.7–7.0	1.2×10^{-3} –0.11	1×10^{-2} –0.1	1,2	
SCT2	0.116	0.604	0.929	0.220	15	5.6–7.4	5.4–6.8	4.1×10^{-3} –0.64	1×10^{-2} –0.1	1,2	
Santa Cruz ^d	SCT3	0.068	0.070	0.160	0.036	15	6.0–8.2	5.4–7.3	8.0×10^{-5} – 4.0×10^{-2}	1×10^{-2} –0.1	1,2
	SCT4	0.144	0.432	0.769	0.082	15	5.6–7.9	5.6–7.3	7.5×10^{-4} – 4.2×10^{-2}	1×10^{-2} –0.1	1,2
	SCT5	0.089	0.140	0.284	0.039	15	5.9–8.2	5.5–7.3	1.5×10^{-2} –0.85	1×10^{-2} –0.1	1,2
Riverbank		0.007	0.060	0.059	0.109	16	6.1–7.6	6.5–8.3	2.7×10^{-4} – 3.0×10^{-2}	1×10^{-2}	3
Belbex		0.523	0.275	0.179	0.124	10	5.7–7.8	n.a. ^e	8.2×10^{-4} –0.27	n.a.	4,5
Baynton		0.382	0.288	0.187	0.062	25	5.4–7.9	n.a.	6.5×10^{-4} –0.81	n.a.	6,7
	E	0.123	0.177	0.304	0.065	20	5.7–7.9	6.9–7.9	4.3×10^{-4} –0.18	n.a.	8
	I	0.089	0.131	0.286	0.059	18	5.9–8.0	6.0–7.1	2.6×10^{-4} –0.11	n.a.	8
Hawaii	J	0.072	0.134	0.274	0.050	18	5.8–8.1	5.9–6.4	2.0×10^{-4} –0.11	n.a.	8
	L	0.116	0.137	0.220	0.047	17	5.9–8.2	3.6–5.6	3.1×10^{-4} –0.21	n.a.	8
	M	0.101	0.137	0.222	0.041	17	5.9–8.1	4.4–5.3	3.0×10^{-4} –0.17	n.a.	8

^a [X-rock]_{loss} and [Si-rock]_{loss} are given for Santa Cruz by White et al. (2008), and calculated based on the retention fractions of elements for the other profiles (see Appendix B).

^b Values of temperature, observed pH and observed soil P_{CO_2} are from the references given in the last column.

^c 1—White et al. (2008); 2—White et al. (2009); 3—White et al. (2005); 4—Chesworth et al. (1981); 5—Tardy (1971); 6—Nesbitt and Wilson (1992); 7—Price et al. (1991); 8—Chadwick et al. (2003).

^d Obs. soil P_{CO_2} was obtained from reference 2, and the other parameters from reference 1.

^e Not available.

Table 3. Equilibrium constants (log unit) at various temperatures.

Equilibrium constant	Temperature (°C)					Ref. ^a
	0	5	15	25	40	
K_H	-1.10	-1.19	-1.34	-1.47	-1.62	1
K_1	-6.58	-6.52	-6.42	-6.35	-6.30	1
K_2	-10.63	-10.55	-10.43	-10.33	-10.22	1
K_{quartz}	-4.07	-4.00	-3.87	-3.75	-3.57	2
$K_{\text{amorphous_silica}}$	-2.95	-2.90	-2.80	-2.71	-2.59	2
K_{calcite}	-8.38	-8.39	-8.43	-8.48	-8.58	1
$K_{\text{magnesite}}^b$	-7.56	-7.66	-7.85	-8.03	-8.28	3,4
K_{siderite}^c	-10.28	-10.32	-10.39	-10.45	-10.54	1
K_{dolomite}^c	-15.80	-15.96	-16.26	-16.54	-16.93	1
K_{ankerite}^b	-20.73	-20.78	-20.87	-20.96	-21.08	3,4
K_{Mg}	2.15	2.12	2.07	2.03	2.00	5
K_{Ca}	2.18	2.14	2.07	2.02	1.96	5
K_{Na}	2.58	2.16	2.05	1.97	1.86	5
K_K	-2.44	-2.41	-2.34	-2.28	-2.19	5

^a 1—Stumm and Morgan (1996); 2—Gunnarsson and Arnórsson (2000); 3—Holland and Powell (1998); 4—Shock et al. (1997); 5—Lawrence Livermore National Laboratory thermodynamic dataset, thermo.com.v8r6+.dat (Delany and Lundeen, 1990).

^b $K_{\text{magnesite}}$ and K_{ankerite} were calculated using thermodynamic data for magnesite and ankerite given by Holland and Powell (1998) and those for aqueous species given by Shock et al. (1997) (c.f., Gysi and Stefánsson, 2011).

^c K_{dolomite} and K_{siderite} are those for disordered dolomite and precipitated siderite, respectively, and they were obtained using the van't Hoff temperature relationship from equilibrium constants at 25°C and the enthalpy changes for reactions, ΔH° . Because ΔH° for precipitated siderite is not available in Stumm and Morgan (1996), I used ΔH° for crystalline siderite instead (c.f., Jesen et al., 2002).

3. Validity of the present method for the estimation of P_{CO_2}

3.1. Application of the present method to modern weathering profiles

The validity of the present method can be assessed by applying it to the chemical compositions of modern weathering profiles. I compared the values of pH and P_{CO_2} calculated by the present method to those observed. I also applied the method by Sheldon (2006) (see Appendix D) to modern weathering profiles for comparison. The modern weathering profiles selected here were Santa Cruz chronosequence (SCTs 1–5, White et al., 2008; 2009) and Riverbank formation (White et al., 2005) developed on granitic rocks, and Belbex (Chesworth et al., 1981), Baynton (Nesbitt and Wilson, 1992) and Hawaii (soils E, I, J, L and M, Chadwick et al., 2003) profiles developed on basaltic rocks. For these weathering profiles, detailed information is reported, sufficient to test the present method and Sheldon's method (2006); the information includes total weathering duration time, annual rainfall, temperature, concentration depth-profiles of major cations and, though only for two sites (Santa Cruz and Riverbank), "soil P_{CO_2} ". The word "soil P_{CO_2} " is used in this section because "soil P_{CO_2} " $\neq P_{CO_2}$ for modern weathering profiles due to vegetation. Nonetheless, "soil P_{CO_2} " is partial pressure of CO_2 that is equilibrated with porewater, and my method can calculate "soil P_{CO_2} ". All modern weathering profiles listed above contain smectite as precipitated or dissolving state and authigenic kaolinite. The calculated and observed values of pH and P_{CO_2} as well as parameters for these weathering profiles are summarized in Table 2.

I used $[Al\text{-rock}]_{\text{loss}}$ for some Hawaiian soils to include the charge contribution of $[Al]_{\text{ss}}$ in addition to those by major cations, because significant amounts of Al dissolve at relatively low pH in some soils at Hawaii (Chadwick et al., 2003); I used hydrolysis constants of Al in Stumm and Morgan (1996) and observed pH in Table 2 to determine the valence of $[Al]_{\text{ss}}$ for the Hawaiian soils (data not shown). The calculations were made at the temperatures given in Table 2. The calculated ranges of pH constrained by the presence of secondary kaolinite and smectite and the undersaturation of secondary carbonates (Section 2.3) are mostly in good agreement with the observed pH ranges except for those of the L and M soils of the Hawaii profiles (Table 2). The present method for pH constraints will be also applicable to paleosols.

Observed "soil P_{CO_2} " levels are available for Santa Cruz and Riverbank (overwritten circle and triangle in Fig. 2, respectively) but not for the profiles developed on basaltic rocks. "Soil P_{CO_2} " in modern weathering profiles is higher than the

atmospheric level ($10^{-3.5}$ atm) and has an average of $\sim 10^{-2}$ atm (overwritten square in Fig. 2) because of plant respiration (e.g., Holland, 1978; White et al., 2001; Maher et al., 2009). For the calculated P_{CO_2} values by the present method, I take a geometric mean of the maximum and minimum values of “soil P_{CO_2} ” for each profile (open symbols with error bars in Fig. 2). Fig. 2 reveals that my estimates of P_{CO_2} are reasonably in good agreement with the observed “soil P_{CO_2} ” values. Out of the calculated P_{CO_2} values, those for SCTs 3 and 5 of Santa Cruz and possibly for Riverbank underestimate “soil P_{CO_2} ”. Even in such cases, the observed “soil P_{CO_2} ” values are within the errors of the calculated P_{CO_2} values. The reasonable agreement between the calculated and observed “soil P_{CO_2} ” values confirms that my method is valid and can be applied to paleosols. On the other hand, Sheldon’s method (2006) significantly and uniformly underestimates “soil P_{CO_2} ” (half-filled symbols in Fig. 2). This indicates that Sheldon’s equation does not correctly formulate the relationship of (cation release rate) = (CO₂ supply rate) (Eq. (D1) in Appendix D). The P_{CO_2} values calculated by Sheldon’s method tend to be smaller than corresponding observed P_{CO_2} values (Appendix D).

Although the calculated and observed “soil P_{CO_2} ” values are in reasonably good agreement, there are large uncertainties for the calculated “soil P_{CO_2} ” values (± 1 to ± 1.5 in log unit). The large uncertainties are probably attributed to the wide range of $[\text{Si}]_{\text{ss}}$ and possible inaccuracy of the thermodynamic data set of clay minerals, which in turn affects the estimates of the steady-state cation concentrations and pH of porewaters (Sections 2.1 and 2.3, and Appendix E). The large uncertainties indicate that I will have similar uncertainties when the present method is applied to paleosols. Nonetheless, the geometric means of my estimated P_{CO_2} values (open symbols in Fig. 2) are generally in good agreement with the observed “soil P_{CO_2} ” values (overwritten symbols in Fig. 2; see above for the overwritten square), which should be considered when I apply the present method to paleosols.

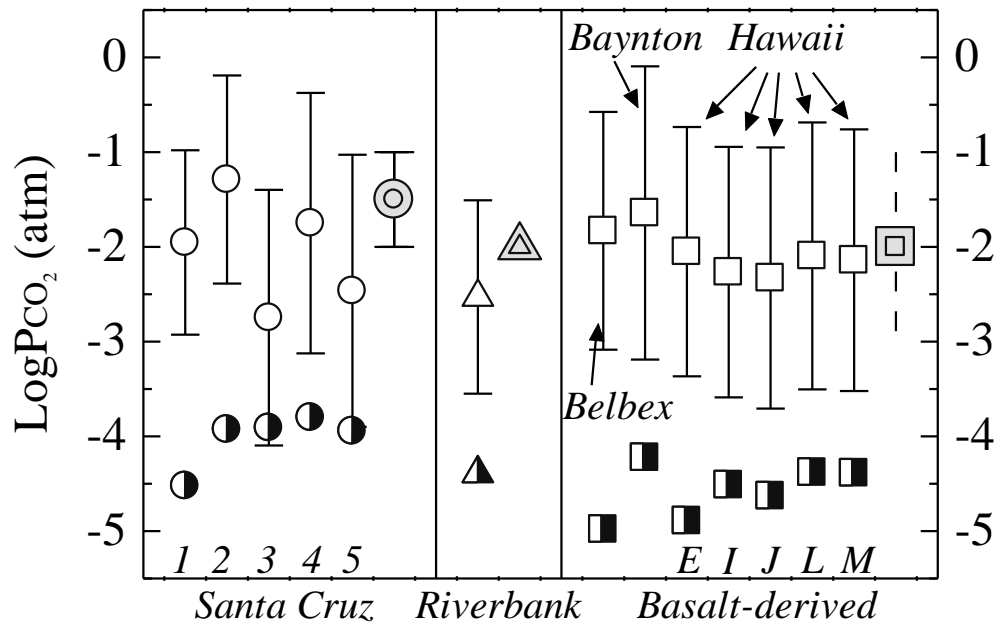


Figure 2. Comparison of calculated P_{CO_2} levels (open symbols, the present method; half-filled symbols, Sheldon's (2006)); and overwritten symbols, observed P_{CO_2} levels for the modern weathering profiles (Table 2). Because "soil P_{CO_2} " is not available for the basaltic weathering profiles, I used assumed "soil P_{CO_2} " (see Section 3.1).

3.2. Weathering formulation deduced from the present method

3.2.1. P_{CO_2} dependence of weathering

The validity of the present method can be also shown by the similarity in P_{CO_2} dependence of weathering between the rate formulated by the present method and those in the laboratory and field. The weathering rate by the present method can be deduced from the presence of secondary kaolinite and smectite (Section 2.3). I here consider the kaolinite/beidellite-Mg boundary; the boundaries of kaolinite/beidellite-Ca and kaolinite/beidellite-Na yield almost the same conclusion. From Reaction (20),

$$\frac{[H^+]_{ss}^{0.2833}}{[Si]_{ss}^{1.15} [Mg^{2+}]_{ss}^{0.1416}} = K_{Mg} \quad (38)$$

Then,

$$[H^+]_{ss} = K_{Mg}^{3.53} [Si]_{ss}^{4.06} [Mg^{2+}]_{ss}^{0.50} \quad (39)$$

$[H^+]_{ss}$ is related to P_{CO_2} in charge balance equation (Section 2.2). Eq. (19) can be further simplified at pH of 4 to 9 where $[HCO_3^-] \gg [CO_3^{2-}]$:

$$\sum_X Z_X [X^{Z_X+}]_{ss} = \frac{K_1 K_H P_{CO_2}}{[H^+]_{ss}} \quad (40)$$

Substituting Eq. (39) into Eq. (40) yields

$$\sum_X Z_X [X^{Z_X+}]_{ss} = \frac{K_1 K_H P_{CO_2}}{K_{Mg}^{3.53} [Si]_{ss}^{4.06} [Mg^{2+}]_{ss}^{0.50}} \quad (41)$$

Here I define $\beta_X \equiv [X\text{-rock}]_{\text{loss}}/[Si\text{-rock}]_{\text{loss}}$ for simplicity. Then, Eq. (10) can be rewritten as

$$[X]_{ss} = \beta_X [Si]_{ss} \quad (42)$$

Using Eq. (42), Eq. (41) can be expressed by

$$[Si]_{ss} \sum_X Z_X \beta_X = \frac{K_1 K_H P_{CO_2}}{K_{Mg}^{3.53} [Si]_{ss}^{4.56} \beta_{Mg}^{0.50}} \quad (43)$$

Then,

$$[Si]_{ss} = \left[\frac{K_1 K_H}{K_{Mg}^{3.53} \beta_{Mg}^{0.50}} \left(\sum_X Z_X \beta_X \right)^{-1} \right]^{0.18} P_{CO_2}^{0.18} \quad (44)$$

From Eqs. (5) and (42),

$$\frac{d[X - \text{rock}]}{dt} = -\theta\sigma k_f \beta_X [\text{Si}]_{ss} \quad (45)$$

Defining the total concentration of cations in a solid, weathering profile as [Rock] (mol m⁻³), [Rock] is given by

$$[\text{Rock}] = \sum_X [\text{X} - \text{rock}] \quad (46)$$

The differential equation for [Rock] is written as

$$\frac{d[\text{Rock}]}{dt} = -\theta\sigma k_f \left(\sum_X \beta_X \right) [\text{Si}]_{ss} \quad (47)$$

Then substituting Eq. (44) into (47) gives the weathering rate law deduced from the present method:

$$\frac{d[\text{Rock}]}{dt} = -\theta\sigma k_f \left[\frac{K_1 K_H}{K_{\text{Mg}}^{3.53} \beta_{\text{Mg}}^{0.50}} \left(\sum_X Z_X \beta_X \right)^{-1} \right]^{0.18} \left(\sum_X \beta_X \right) P_{\text{CO}_2}^{0.18} \quad (48)$$

This equation clearly indicates that the weathering rate depends on P_{CO_2} with fractional dependence of 0.18. The fractional dependence of the weathering rate on CO_2 in Eq. (48) is consistent with that in the laboratory and field, $P_{\text{CO}_2}^n$, where $n = 0.2\text{--}0.5$ for feldspars and $n \cong 0$ for basic silicates (Sverdrup, 1990; Wogelius and Walther, 1991; Utsunomiya et al., 1999; Berg and Banwart, 2000; Golubev et al., 2005; Navarre-Sitchler and Thyne, 2007). Consequently, the present method is valid in the viewpoint of P_{CO_2} dependence of weathering rate. In contrast to the present method, Sheldon's method indicates the first order dependence of the weathering rate law on P_{CO_2} (Eq. (D1) in Appendix D).

3.2.2. Apparent activation energy of weathering

I here examine apparent activation energy of weathering deduced from the present method to further confirm the validity of the present method. Apparent activation energies of weathering are generally different between elements because the activation energy based on a certain element is approximately equal to that of dissolution of a specific mineral which dominantly dissolves the element (e.g., White et al., 1999; Dalai et al., 2002). Accordingly, I consider the apparent activation energy of Si dissolution in weathering because Si dissolution is representative of weathering of silicate minerals. The dissolution rate of Si can be obtained from Eq. (45) with Si for X:

$$\frac{d[\text{Si} - \text{rock}]}{dt} = -\theta\sigma k_f [\text{Si}]_{ss} \quad (49)$$

Eq. (49) can be written in the Arrhenius expression (e.g., White and Blum, 1995):

$$\frac{d[\text{Si - rock}]}{dt} = -A \exp\left(-\frac{E_{\text{app}}}{R_g T}\right) \quad (50)$$

where A and E_{app} are the pre-exponential factor ($\text{mol m}^{-3} \text{yr}^{-1}$) and the apparent activation energy (kJ mol^{-1}), respectively, for Si dissolution in weathering. R_g and T denote the gas constant ($8.3 \times 10^{-3} \text{kJ K}^{-1} \text{mol}^{-1}$) and the absolute temperature (K), respectively. Then, from Eqs. (49) and (50),

$$\begin{aligned} E_{\text{app}} &= -R_g \frac{d}{d(1/T)} \left(\ln \left| \frac{d[\text{Si - rock}]}{dt} \right| \right) \\ &= -R_g \frac{d(\ln \theta \sigma k_f)}{d(1/T)} - R_g \frac{d(\ln [\text{Si}]_{\text{ss}})}{d(1/T)} \end{aligned} \quad (51)$$

Because $\theta \sigma k_f = \theta \sigma F/V$ (Section 2.1) and $V/\theta \sigma$ is equal to the total volume of the weathering system, only F is temperature dependent in the first term of Eq. (51). Assuming the temperature dependence of F is similar to that of continental runoff, the first term in Eq. (51) gives an approximate value of 30kJ mol^{-1} at $< 40 \text{ }^\circ\text{C}$ of temperature (e.g., Berner et al., 1983; Le Hir et al., 2009). The second term in Eq. (51) represents the temperature dependence of $[\text{Si}]_{\text{ss}}$. $[\text{Si}]_{\text{ss}}$ is constrained by thermodynamics of amorphous silica, clay and carbonate minerals in the present method (Figs. 1g and h). Consequently, the temperature dependence of thermodynamic constants of the minerals determine that of $[\text{Si}]_{\text{ss}}$. Using the thermodynamic data listed in Table 3, the value of the second term was calculated to be $10\text{--}25 \text{kJ mol}^{-1}$ in the temperature range of $0\text{--}40 \text{ }^\circ\text{C}$. Then, $E_{\text{app}} = 40\text{--}55 \text{kJ mol}^{-1}$, in good agreement with $\sim 50 \text{kJ mol}^{-1}$ obtained from Si fluxes/concentrations in granitic rock weathering and Si concentrations in dissolution experiments (White and Blum, 1995; White et al., 1999; Dalai et al., 2002; Oliva et al., 2003), and also with 42kJ mol^{-1} obtained from HCO_3^- concentrations in basaltic rock weathering (Dessert et al., 2001). The good agreement in the E_{app} value further grants the validity of the present method.

4. Atmospheric CO₂ variation in the Neoproterozoic-Paleoproterozoic

The estimation of P_{CO_2} levels was made using the chemical compositions of paleosols in the Neoproterozoic-Paleoproterozoic. The Neoproterozoic-Paleoproterozoic paleosols used were those passing through a screening test of the absence and presence of significant physical and chemical disturbances (Murakami et al., 2011a): Mt. Roe (1), Mt. Roe (2), Bird, Cooper Lake, Pronto/NAN, Gaborone, Drakenstein and Flin Flon paleosols (Table 1). The paleosols are of mafic origin except for the Pronto/NAN paleosol which was developed on felsic rock.

As indicated in Section 2, the P_{CO_2} estimation by the present method requires temperature as an input parameter. In the calculation of cation concentrations (Eq. (10), Section 2.1), $[Si]_{ss}$ is constrained between the solubilities of quartz and amorphous silica, i.e., thermodynamic parameters which are temperature dependent (Table 3). pH constraints in Section 2.3 also require temperature because the constraints are given by the clay and carbonates thermodynamics (Table 3). The charge balance equation, which calculates P_{CO_2} from estimated cation concentrations and constrained pH (Eq. (19), Section 2.2), also requires temperature due to the thermodynamic parameters, K_H , K_1 and K_2 (Eq. (19)). Although temperatures are given for the modern weathering profiles (Table 2, Section 3), they are unknown at the time of weathering of the paleosols (Table 1).

The eight paleosols used in this chapter were possibly weathered at respective local temperatures, different from the respective, average global surface temperatures (hereafter, referred to as global temperatures simply) which possibly varied with age. Even if two paleosols were formed at the same age, their local temperatures may be different as modern weathering occurs at different temperatures (e.g., 10–25 °C, Table 2). It is also possible that some of the paleosols were affected by extreme temperatures during or after the glaciation events at ~2.9 and ~2.4–2.2 Ga (e.g., Young et al., 1998; Bekker et al., 2001; 2005), which resulted in large deviation of global temperature from 15 °C (Caldeira and Kasting, 1992; Claire et al., 2006; Bao et al., 2008; Le Hir et al., 2009). Even if there are two paleosols formed at different local temperatures but at the same age, the P_{CO_2} levels for the two paleosols estimated by the present method must be the same. Therefore, once a local temperature for a paleosol is determined, my method allows me to estimate the P_{CO_2} level without knowing global temperature at the time of weathering in theory.

In this section, I first calculate P_{CO_2} levels at different temperatures for the

paleosols (Section 4.1) and then, constrain the local temperatures for the paleosols (Section 4.2). Finally, the P_{CO_2} levels in the Neoproterozoic-Paleoproterozoic are estimated taking account of the local temperatures (Section 4.3).

4.1. P_{CO_2} estimates at different temperatures

I calculated P_{CO_2} levels at 0, 5, 15, 25 and 40 °C for each paleosol using the reaction constants listed in Table 3. First, I demonstrate below the detailed results of the steady-state cation concentrations and constrained pH only at 15 °C for the eight paleosols, which are required to calculate P_{CO_2} levels (Eq. (19)).

4.1.1. Steady-state cation concentrations at 15 °C

As shown in Section 2.1, I calculated $[\text{X-rock}]_{\text{loss}}$ and $[\text{Si-rock}]_{\text{loss}}$ from the concentration depth-profiles of cation X and Si, respectively, for each paleosol according to the method by Murakami et al. (2011a) (see Appendix B for the calculation details). The values of $[\text{X-rock}]_{\text{loss}}/[\text{Si-rock}]_{\text{loss}}$ are listed in Table 1 for Fe, Mg, Ca, Na, and K for the Neoproterozoic-Paleoproterozoic paleosols. As for K, the amounts of loss cannot be obtained directly from the profiles of the paleosols due to K-metasomatism (Nesbitt and Young, 1989; Kimberley and Holland, 1992). I assumed the same mobility of K as that of Na for the paleosols of mafic origin (Sheldon, 2006). Chesworth et al. (1981) reported similar mobilities of Na and K for long-term weathering of basalt. Because less mobility of K than Na is expected for felsic rock weathering (Holland, 1978), I used a half of Na mobility as the K mobility for the Pronto/NAN paleosol which is of felsic origin.

Based on the values of $[\text{X-rock}]_{\text{loss}}/[\text{Si-rock}]_{\text{loss}}$ in Table 1 and the assumed $[\text{Si}]_{\text{ss}}$ values (Section 2.1), the $[\text{X}]_{\text{ss}}$ values for Fe, Mg, Ca, Na and K were calculated for each paleosol (Eq. (10)) and plotted against $[\text{Si}]_{\text{ss}}$ (Fig. 3). $[\text{Mg}]_{\text{ss}}$, and sometimes both $[\text{Mg}]_{\text{ss}}$ and $[\text{Ca}]_{\text{ss}}$, are prominently high for all paleosols except for the Pronto/NAN paleosol (Fig. 3), reflecting mafic origin of the paleosols (Holland, 1978), while $[\text{Na}]_{\text{ss}}$ and $[\text{Ca}]_{\text{ss}}$ are significant in the Pronto/NAN paleosol, reflecting its felsic parent rock (Holland, 1978). Because Fe^{3+} is very low in solubility, calculated $[\text{Fe}]_{\text{ss}}$ is all attributed to $[\text{Fe}^{2+}]_{\text{ss}}$. $[\text{Fe}]_{\text{ss}}$ is significant ($> \sim 10^{-5} \text{ mol L}^{-1}$) at $\geq 2.45 \text{ Ga}$ (i.e., for the Mt. Roe (1), Mt. Roe (2), Bird, Cooper Lake and Pronto/NAN paleosols) and less so ($< \sim 10^{-5} \text{ mol L}^{-1}$) at $< \sim 2.2 \text{ Ga}$ (i.e., for the Gaborone, Drakenstein and Flin Flon paleosols), resulting from slower and faster rates of Fe^{2+} oxidation, respectively, which is greatly affected by P_{O_2} levels

(Murakami et al., 2011a; Yokota et al., 2013).

4.1.2. Constraints of pH at 15 °C

According to Section 2.3, the $[H^+]_{ss}$ values (or pHs) at the kaolinite/smectites and kaolinite/muscovite boundaries are constrained, and plotted against $[Si]_{ss}$ for each paleosol in Fig. 4. Because kaolinite and smectite were present as secondary minerals in the paleosols, the porewater pHs are near the kaolinite/smectites boundaries that are limited by the kaolinite/muscovite boundary (shaded areas in Fig. 4). The presence of kaolinite and smectite as secondary minerals constrains porewater pHs as follows: pH = 5.8–7.7, 5.9–8.4, 5.7–9.6, 5.8–7.9, 5.8–7.7, 5.8–8.6, 5.7–8.7 and 5.5–9.4 for the Mt. Roe (1), Mt. Roe (2), Bird, Cooper Lake, Pronto/NAN, Gaborone, Drakenstein and Flin Flon paleosols, respectively.

Also according to Section 2.3, pHs at the carbonate equilibria are constrained, and plotted against $[Si]_{ss}$ for each paleosol in Fig. 5. The curves shown in Fig. 5 represent the lower limits of pHs at which the carbonates precipitate. Then, the undersaturation of the carbonates gives the upper limits of pHs of the porewaters at the time of weathering. Fig. 5 indicates that siderite or ankerite is the carbonate that precipitates at the lowest pH at any given $[Si]_{ss}$ values for all paleosols except for the Flin Flon paleosol. Therefore, the pH constraints from carbonates are given by the equilibrium of siderite or ankerite for the paleosols except for the Flin Flon paleosol. For the Flin Flon paleosol, the siderite and ankerite boundaries shown in Fig. 5 are those for the maximum $[Fe]_{ss}$ because Fe is almost completely retained in the paleosol (Holland et al., 1989; Murakami et al., 2011a). Then, it is possible that the actual boundaries are located at higher pH sides (arrows in Fig. 5). For conservative estimation, therefore, I take the calcite solubility for the pH constraint for the Flin Flon paleosol.

The carbonate equilibria are found to give stronger pH constraints than the kaolinite/muscovite boundaries for all paleosols when combined with the kaolinite/smectite boundaries (Figs. 4 and 5). Consequently, pHs of the porewaters in the paleosols are constrained by the presence of secondary kaolinite and smectites and the undersaturation of secondary carbonates. In Fig. 6, pHs at the kaolinite/smectite boundaries and at equilibria of the carbonates, easiest to precipitate among the five carbonates, are plotted against $\log [Si]_{ss}$ for the paleosols. As discussed above, because the porewater compositions are indicated by those along the kaolinite/smectite boundaries, pHs of the porewaters range from the upper limits posed by the carbonate equilibria to the solubility of amorphous silica along the kaolinite/smectite boundaries

(shaded areas in Fig. 6). The estimated pH ranges were: 5.8–6.8 for Mt. Roe (1), 5.9–6.5 for Mt. Roe (2), 5.7–6.2 for Bird, 5.8–6.1 for Pronto/NAN, 5.8–7.6 for Gaborone, 5.7–7.0 for Drakenstein, and 5.5–8.4 for Flin Flon (Table 4). These pH ranges are not much different from those observed in the modern weathering profiles (Table 2). The pH range at 15 °C for Cooper Lake were not determined; any pH or $[\text{Si}]_{\text{ss}}$ could not satisfy the conditions of the presence of kaolinite and smectite and the undersaturation of carbonates at the same time (Fig. 6).

4.1.3. P_{CO_2} estimates at different temperatures for the paleosols

The procedures shown in Sections 4.1.1 and 4.1.2 were also taken at 0, 5, 25 and 40 °C, using the thermodynamic data at the respective temperatures in Table 3. The values of constrained pH and $[\text{Si}]_{\text{ss}}$ obtained at these temperatures are summarized in Table 4 along with those at 15 °C. Based on Eqs. (10) and (19), and the data in Tables 1, 3 and 4, the P_{CO_2} levels for the eight paleosols were estimated at 0, 5, 15, 25 and 40 °C and are listed in Table 5 and illustrated in Fig. 7.

For the Cooper Lake paleosol, the consistent pHs with the secondary minerals were not obtained at 25 and 40 °C like those at 15 °C, and therefore, P_{CO_2} estimation was not made either at these temperatures (Tables 4 and 5 and Fig. 7). The estimated P_{CO_2} levels have large uncertainties for all paleosols at most temperatures (Table 5). The uncertainties in the P_{CO_2} estimates are mainly attributed to those in pH, and in turn to those in $[\text{Si}]_{\text{ss}}$ (Fig. 6 and Table 4). The estimated P_{CO_2} values were not affected by the assumed $[\text{K}]_{\text{ss}}$ (Section 4.1.1); even with 0 mol L⁻¹ of $[\text{K}]_{\text{ss}}$, the P_{CO_2} values changed by < 10%. The little effect of K is due to the relatively, low contribution of K to the total cation concentration (Table 1) and to no involvement of K in the kaolinite/smectite boundary or carbonate equilibria by which the pH constraints are given (Section 4.1.2). Because the geometric means of my calculated P_{CO_2} values are in good agreement with those observed P_{CO_2} values for the modern weathering profiles (Fig. 2), the geometric means can give more probable P_{CO_2} values for the paleosols. Thus, the geometric means of the estimated P_{CO_2} levels are plotted in Fig. 7 by open squares with vertical bars representing the ranges of the minimum and maximum values. Fig. 7 shows that the higher the temperature is, the higher the P_{CO_2} level is required for a paleosol to form the secondary minerals, kaolinite and smectite. For example, the geometric means of P_{CO_2} levels estimated for the Mt. Roe (1) paleosol are 16 and 300 PAL at 0 and 25 °C of local temperatures, respectively. That is, temperature affects P_{CO_2} estimates largely. Accordingly, unless the local temperatures at the time of weathering for the paleosols

are constrained, as discussed in the next section, I have large uncertainties even in the geometric-mean P_{CO_2} levels.

I compare my P_{CO_2} estimates to those by Sheldon's method (2006). Because Sheldon's method does not include temperature as a parameter (Appendix D), my P_{CO_2} estimates at 15 °C of local temperature are used. The geometric means of my estimates are: ~100–160 PAL at ~2.77 Ga, ~500 PAL at ~2.75 Ga, ~490 PAL at ~2.46 Ga, ~42 PAL at ~2.15 Ga, ~130 PAL at ~2.08 Ga and ~42 PAL at ~1.85 Ga (squares at 15 °C in Fig. 7). Note that the range of P_{CO_2} at ~2.77 Ga is due to the values taken from two paleosols. These estimates are generally larger than those by Sheldon's method, 10–50 PAL at 2.69 Ga (Driese et al., 2011) and 7–70 PAL at 2.5–1.8 Ga (Sheldon, 2006), like the estimates for the modern weathering profiles (Fig. 2 and Section 3.1). This is because the P_{CO_2} values calculated by Sheldon's method are underestimated ones (Appendix D).

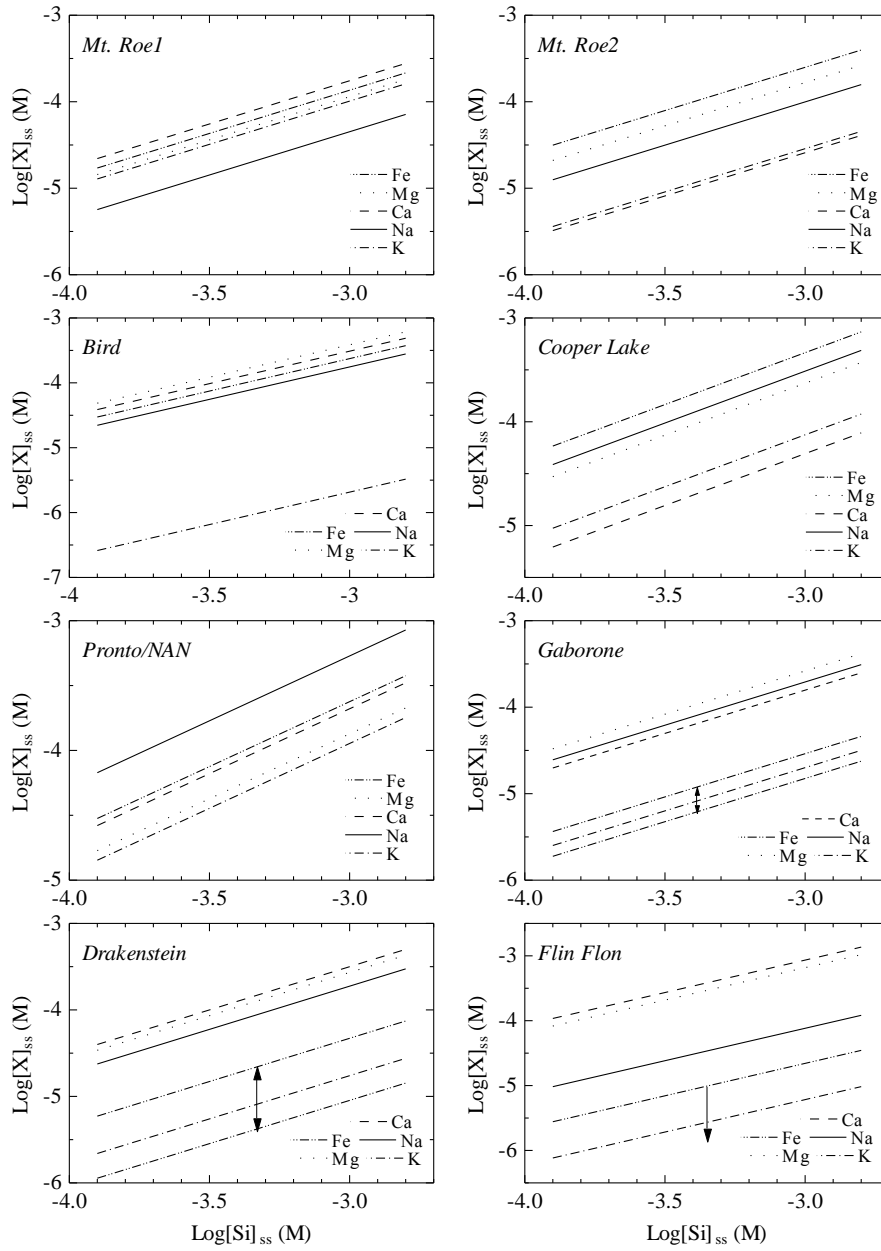


Figure 3. Steady-state cation concentrations, $[X]_{ss}$, plotted against that of Si, $[Si]_{ss}$, in the logarithmic scale for the Neoproterozoic-Paleoproterozoic paleosols. The $[X]_{ss}$ values for Fe (double-dotted and dashed lines), Mg (dotted lines), Ca (dashed lines), Na (solid lines) and K (dotted and dashed lines) were calculated from Eq. (10), with $[Si]_{ss}$ in the range of $10^{-3.9}$ – $10^{-2.8}$ mol L⁻¹. Only the $[Fe]_{ss}$ values (double-dotted and dashed lines) of the Gaborone, Drakenstein and Flin Flon paleosols have significant errors. Uncertainties of $[Fe]_{ss}$ for the Gaborone and Drakenstein are represented by the range between pairs of double-dotted and dashed lines with double-headed arrows. In the Flin Flon paleosol, only the upper limits of $[Fe]_{ss}$ were obtained (arrow).

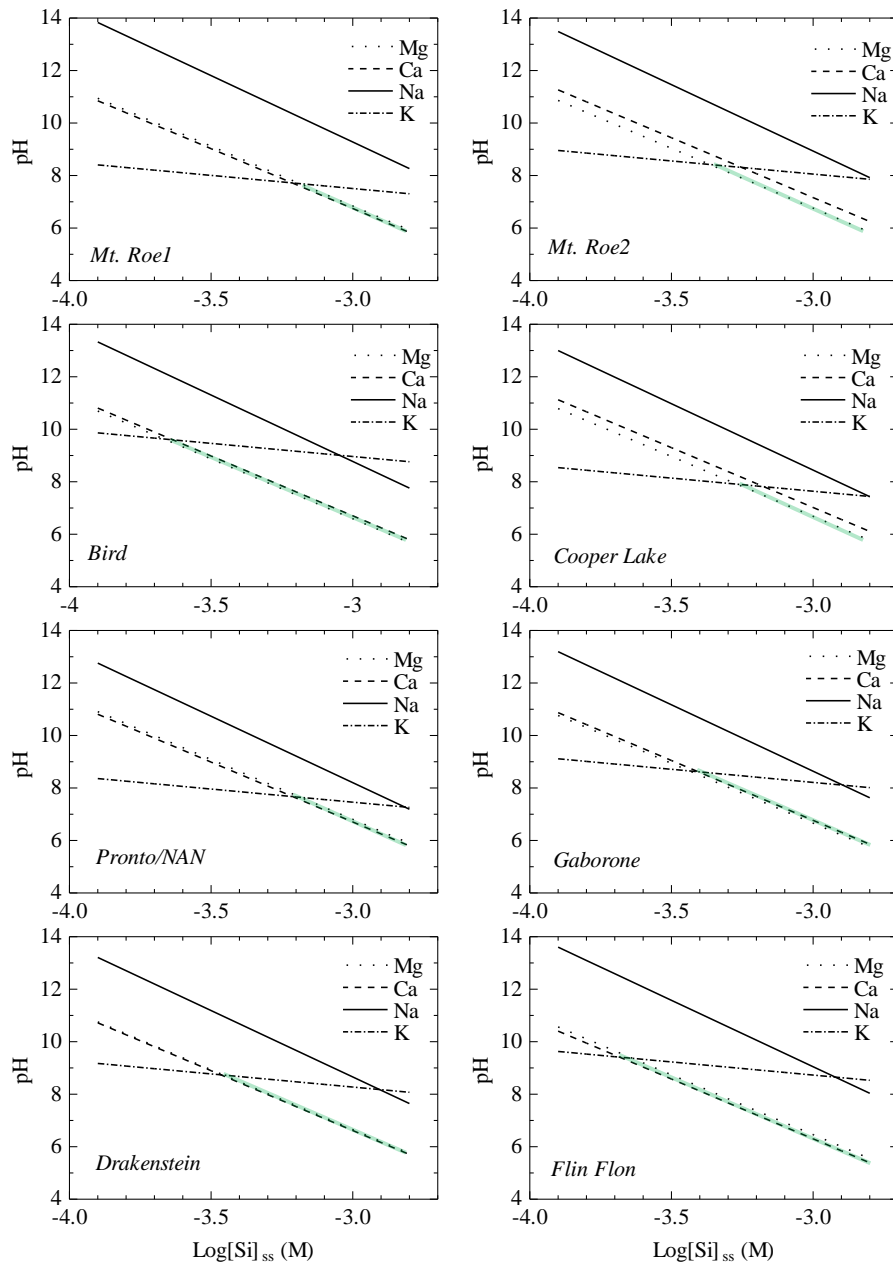


Figure 4. Porewater pHs at kaolinite/smectites and kaolinite/muscovite boundaries against $\log [\text{Si}]_{\text{ss}}$ for the Neoproterozoic-Paleoproterozoic paleosols. Dotted lines (with the notation “Mg”) are pHs in equilibrium with kaolinite/beidellite-Mg, dashed lines (“Ca”) with kaolinite/beidellite-Ca, solid lines (“Na”) with kaolinite/beidellite-Na and dotted and dashed lines (“K”) with kaolinite/muscovite. Note that the dotted line and dashed line are almost completely superimposed for the Drakenstein paleosol, and only the dashed line can be seen. The ranges of the porewater pHs constrained by kaolinite, beidellite-Mg or -Ca, and muscovite are shown by the shaded areas.

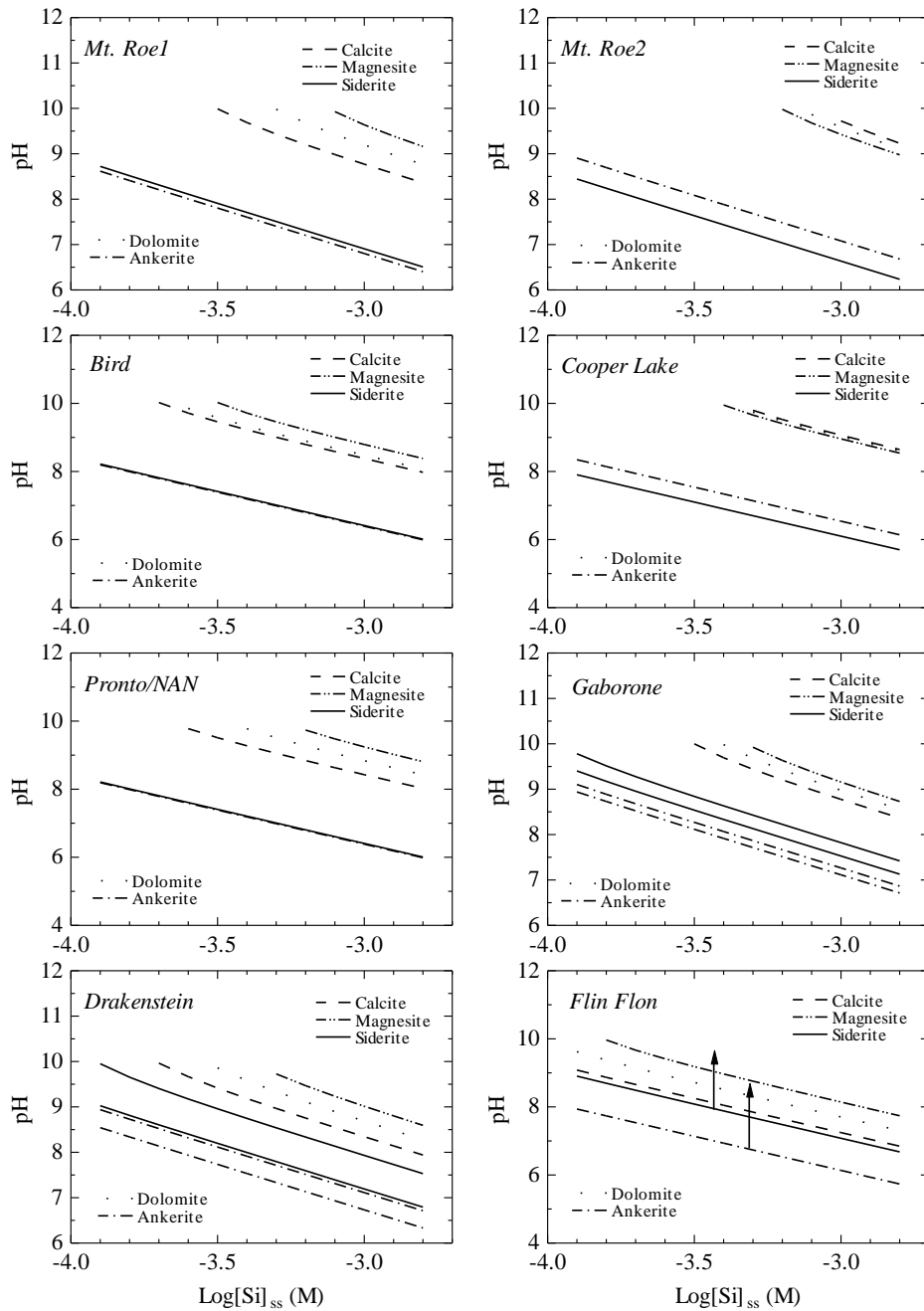


Figure 5. Porewater pHs at carbonate equilibria plotted against $\log [\text{Si}]_{\text{ss}}$ for the Neoproterozoic-Paleoproterozoic paleosols. Calculations at $\text{pH} > 10$ were not made (see Section 2.2). For the Gaborone and Drakenstein paleosols, the siderite equilibrium is given by the range between the two solid curves because of the range of the $[\text{Fe}]_{\text{ss}}$ values (Table 1); the ankerite equilibrium is also given similarly. Because only the maximum value of $[\text{Fe}]_{\text{ss}}$ is given for the Flin Flon paleosol (Table 1), the equilibrium curves of siderite and ankerite should be shifted at higher pH sides (arrows).

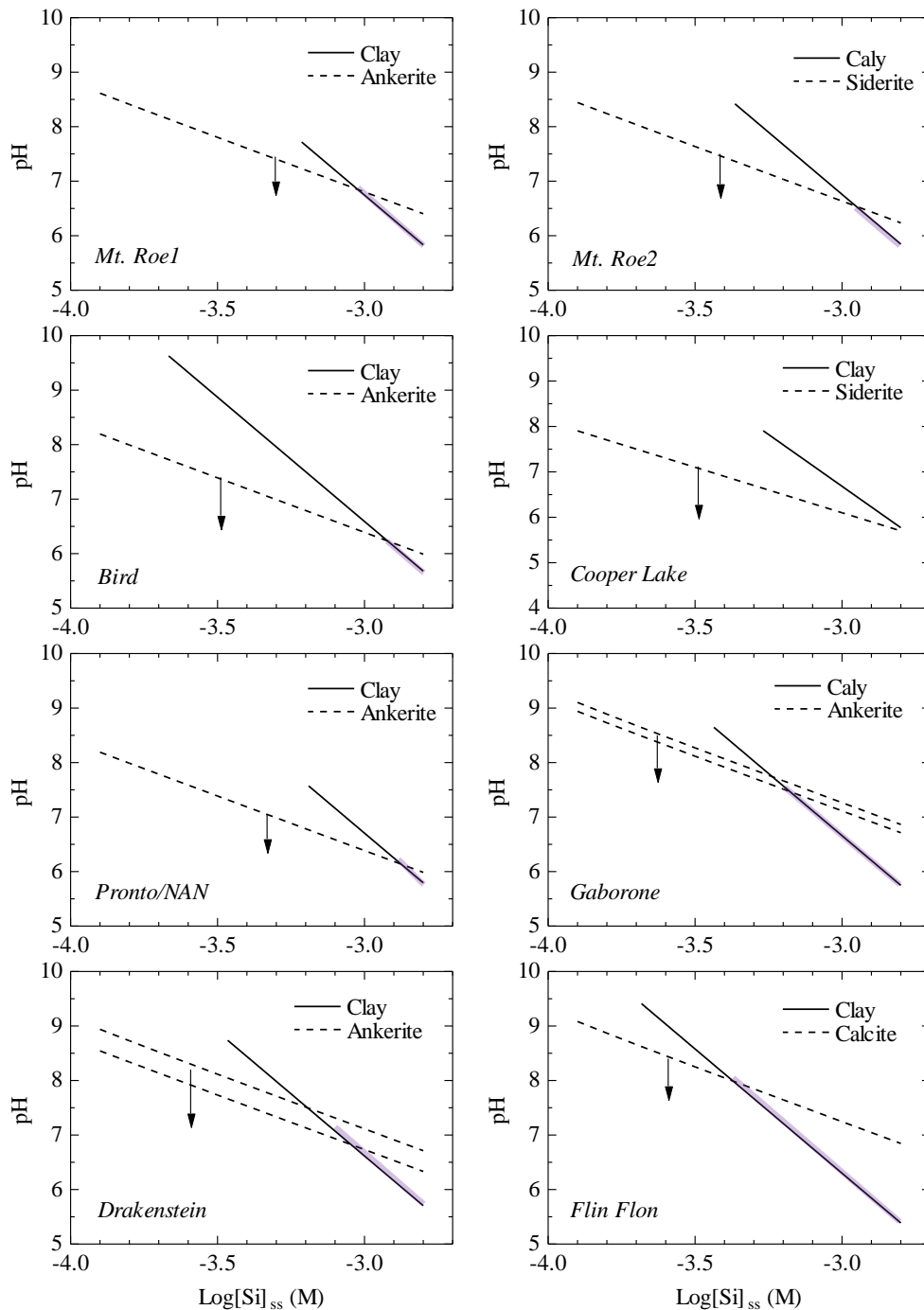


Figure 6. Porewater pH constraints from Figs. 4 and 5 in the pH-log $[Si]_{ss}$ plots for the Neoproterozoic-Paleoproterozoic paleosols. The constraints are finally made from the kaolinite/smectites boundaries (solid lines) and the carbonate equilibria (dashed curves), and shown by shaded areas along the kaolinite/smectites boundaries. See the caption of Fig. 5 for a pair of two curves for the Gaborone and Drakenstein paleosols.

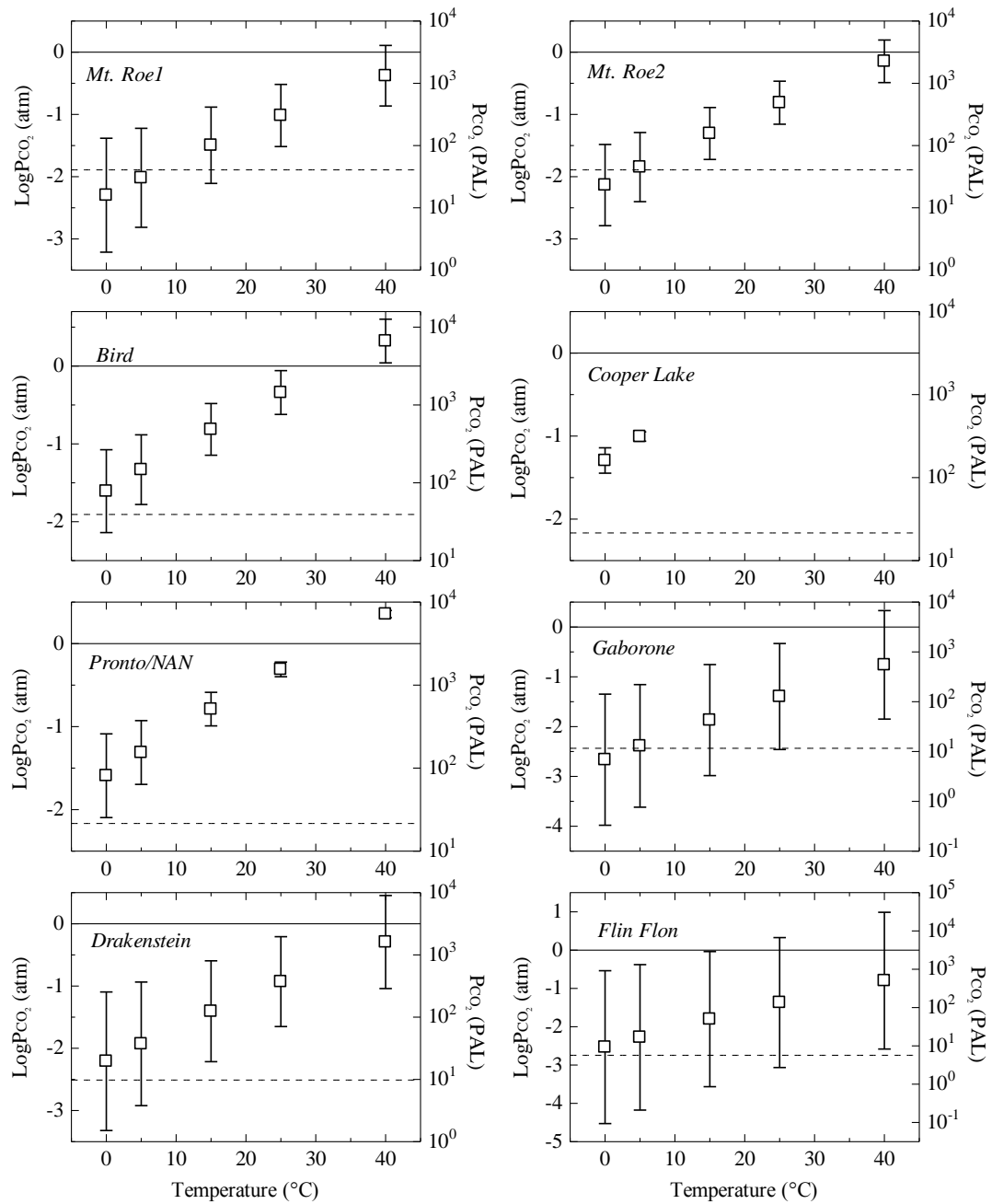


Figure 7. Estimates of P_{CO_2} at different temperatures for the Neoproterozoic paleosols.

Estimated ranges of P_{CO_2} are plotted against temperatures (0, 5, 15, 25 and 40°C) for each paleosol with the geometric means and the ranges represented as open squares and vertical bars, respectively. Horizontal solid lines denote 1 atm of P_{CO_2} , the upper constraint of P_{CO_2} at 2.7 Ga from Som et al. (2012) and horizontal dashed lines the lower constraint to maintain the surface global temperature at 0°C only with CO_2 .

Table 4. Calculated pH and [Si]_{ss} at various temperatures for the Neoproterozoic paleosols.

Paleosol profile	Age (Ga) ^a	Estimated pH					Estimated [Si] _{ss} in log unit (mol L ⁻¹)				
		0 (°C)	5 (°C)	15 (°C)	25 (°C)	40 (°C)	0 (°C)	5 (°C)	15 (°C)	25 (°C)	40 (°C)
Mt. Roe1	2.775–2.755	6.1–7.6	6.0–7.3	5.8–6.8	5.6–6.4	5.2–6.0	-(2.95–3.28)	-(2.90–3.18)	-(2.80–3.02)	-(2.71–2.89)	-(2.59–2.77)
Mt. Roe2	2.775–2.755	6.2–7.3	6.1–7.0	5.9–6.5	5.9–6.1	5.1–5.7	-(2.95–3.18)	-(2.90–3.10)	-(2.80–2.95)	-(2.71–2.83)	-(2.59–2.71)
Bird	2.8–2.7	6.1–6.9	5.9–6.7	5.7–6.2	5.4–5.9	5.0–5.4	-(2.95–3.14)	-(2.90–3.06)	-(2.80–2.92)	-(2.71–2.81)	-(2.59–2.69)
Cooper Lake	2.475–2.440	6.2–6.4	6.0–6.1	n.c. ^b	n.c.	n.c.	-(2.95–3.00)	-(2.90–2.92)	n.c.	n.c.	n.c.
Pronto/NAN	2.475–2.440	6.1–6.9	6.0–6.6	5.8–6.1	5.6–5.7	5.2–5.3	-(2.95–3.13)	-(2.90–3.04)	-(2.80–2.87)	-(2.71–2.75)	-(2.59–2.61)
Gaborone	2.245–2.059	6.1–8.3	6.0–8.0	5.8–7.6	5.5–7.2	5.0–6.8	-(2.95–3.42)	-(2.90–3.34)	-(2.80–3.20)	-(2.71–3.10)	-(2.59–2.98)
Drakenstein	2.222–1.928	6.0–7.8	5.9–7.5	5.7–7.0	5.5–6.7	5.0–6.3	-(2.95–3.35)	-(2.90–3.25)	-(2.80–3.09)	-(2.71–2.97)	-(2.59–2.86)
Flin Flon	1.9–1.8	5.8–9.0	5.7–8.4	5.5–8.4	5.3–8.1	4.8–7.8	-(2.95–3.66)	-(2.90–3.58)	-(2.80–3.44)	-(2.71–3.32)	-(2.59–3.23)

^a From Rye and Holland (1998).

^b Not calculated because any pH or [Si]_{ss} cannot satisfy the conditions of the presence of kaolinite and smectite and the undersaturation of carbonates at the same time (see Sections 4.1.2 and 4.1.3).

Table 5. Estimated P_{CO_2} at various temperatures and local temperature constraints for the Neoproterozoic-Paleoproterozoic paleosols.

Paleosol profile	Age (Ga) ^a	Estimated P_{CO_2} (PAL)					Constraints on local temperature (°C)		
		0 (°C)	5 (°C)	15 (°C)	25 (°C)	40 (°C)	Fig. 7 ^b	Eqs. (52)-(54) ^c	Adopted in Fig. 9
Mt. Roe1	2.775–2.755	1.9–130	4.8–190	25–410	96–960	430–4100 ^d	n.g. ^e	12–39	12–30 ^f
Mt. Roe2	2.775–2.755	5.2–100	13–160	60–410	220–1100	1000–5000 ^d	n.g.	10–41	10–30 ^f
Bird	2.8–2.7	23–270	53–410	230–1000	760–2800	3500–13000 ^d	0–~32	≤53	0–30 ^f
Cooper Lake	2.475–2.440	110–230	270–360	n.c. ^g	n.c.	n.c.	0–~9	≤61	0–9
Pronto/NAN	2.475–2.440	25–260	64–370	320–820	1300–1900	6500–7900 ^d	0–~32	n.g.	0–30 ^f
Gaborone	2.245–2.059	0.33–140	0.76–220	3.3–560	11–1500	45–6800 ^d	n.g.	12–29	12–29
Drakenstein	2.222–1.928	1.5–250	3.8–370	19–800	71–2000	290–9000 ^d	0<	≤42	0–30 ^f
Flin Flon	1.9–1.8	0.094–920	0.21–1300	1.2–2900	2.7–6700 ^d	8.3–31000 ^d	0<	8–54	8–30 ^f

^a From Rye and Holland (1998).

^b Constraints given by Fig. 7 (see Section 4.2.1).

^c Eqs. (52)–(54) (Dessert et al., 2003) assume a temperature range of 2–27 °C.

^d Values of > 3200 PAL exceed 1 atm of the total pressure (see Section 4.2.1 and Fig. 7).

^e Not given by Fig. 7 or Eqs. (52)–(54).

^f Upper and lower constraints, 30 and 0 °C, respectively, are included (see Section 4.2.3).

^g Not calculated because the estimates of pH were not available (see Section 4.2.1 and Table 4).

4.2. Local temperature constraints for the Neoproterozoic-Paleoproterozoic paleosols

Because the P_{CO_2} levels estimated by my method are affected by temperature, I should constrain local temperatures for the paleosols and reduce the uncertainties in P_{CO_2} estimates. The constraints on the local temperatures are made from (1) temperature dependence of P_{CO_2} and (2) empirical relationships between temperature and solute compositions. Then I discuss local temperatures for the paleosols, which is applied to the P_{CO_2} estimation in the Neoproterozoic-Paleoproterozoic.

4.2.1. Constraints from temperature dependence of P_{CO_2}

The P_{CO_2} levels at different temperatures shown in Fig. 7 also give local-temperature constraints for the paleosols; the upper constraint is given by Som et al. (2012) (< 1 atm of P_{CO_2} , horizontal, solid lines in Fig. 7) and the other constraint is the P_{CO_2} levels to retain the global temperature at ≥ 0 °C from Kasting (2010) (dashed lines in Fig. 7). The Bird and Pronto/NAN paleosols yielded > 1 atm of P_{CO_2} at 40 °C, inconsistent with the upper constraint (horizontal, solid lines in Fig. 7). Therefore the Bird and Pronto/NAN paleosols should have been weathered at < 40 °C, possibly $< \sim 32$ °C (Fig. 7 and Table 5). The geometric means of P_{CO_2} levels at 0 °C for the Bird, Cooper Lake, Pronto/NAN, Drakenstein and Flin Flon paleosols are larger than the respective, required P_{CO_2} levels to maintain the global temperature at 0 °C (dashed lines in Fig. 7), and therefore these paleosols should have been formed at > 0 °C (Table 5). Note that I assumed haze-free atmosphere in the above local temperature constraints (i.e., $CH_4/CO_2 < 0.1$, Zerkle et al., 2012). The geometric means of P_{CO_2} levels at 0 °C for the Mt. Roe (1), Mt. Roe (2) and Gaborone paleosols are smaller than the respective required P_{CO_2} levels (dashed lines in Fig. 7), and in theory, there should have been other greenhouse-effect gases than CO_2 . Nonetheless, the Mt. Roe (1), Mt. Roe (2) and Gaborone paleosols were also formed probably at > 0 °C because significant amounts of cations were removed from those paleosols (Macfarlane et al., 1994; Yang and Holland, 2003). There is no pH range that satisfies the conditions of both the presence of kaolinite and smectite and the undersaturation of the carbonates at 15, 25 and 40°C for the Cooper Lake paleosol (Sections 4.1.2 and 4.1.3). Therefore, the Cooper Lake paleosols would have been weathered at $< \sim 15$ °C, possibly $< \sim 9$ °C (Fig. 7).

4.2.2. Constraints from temperature dependence of solute compositions

To further constrain local temperatures for the Neoproterozoic-Paleoproterozoic paleosols, I utilized the empirical relationships between temperature and solute compositions reported for modern weathering systems. The difference in P_{CO_2} between the present and the Neoproterozoic-Paleoproterozoic can be assumed to have much less effects on water compositions than the temperature difference (e.g., Brady and Carroll, 1994). Dessert et al. (2003) reported the empirical relations of local temperature (T_c , °C) to bicarbonate concentration ($[HCO_3^-]$, mol L⁻¹), cation concentration (TDS_{cat} , g L⁻¹) and total dissolved elements (TDS_w , g L⁻¹) in various rivers draining modern basalt watersheds. TDS_{cat} is the sum of concentrations of Ca, Mg, Na and K corrected for atmospheric inputs and TDS_w is the total concentration of weathering-derived SiO₂, Ca, Mg, Na, K and SO₄. Therefore, $[HCO_3^-]$, TDS_{cat} and TDS_w are of basalt-weathering origin. The empirical relations are represented by the following equations:

$$[HCO_3^-] = 3.2436 \times 10^{-4} \times \exp(0.0638 T_c) \quad (52)$$

$$TDS_{cat} = 6.7 \times 10^{-3} \times \exp(0.0673 T_c) \quad (53)$$

$$TDS_w = 1.842 \times 10^{-2} \times \exp(0.0551 T_c) \quad (54)$$

The concentrations of HCO_3^- , TDS_{cat} and TDS_w can also give local temperatures for the paleosols of mafic origin. I assume one standard deviation for the six constants in Eqs. (52)–(54) (Dessert et al., 2003), which gives three zones, instead of three lines, in the plots of the concentration and temperature.

Independently from Eqs. (52)–(54), the present method can calculate $[HCO_3^-]$, TDS_{cat} and TDS_w values for each paleosol at a given temperature using the reaction constants in Table 3 and the estimated pH, $[Si]_{ss}$ and P_{CO_2} in Tables 4 and 5 (Section 4.1), which gives three curves in the plots of the concentration and temperature. Then, the intersected range of temperature by the method of Dessert et al. (2003) and the present one will give a constrained local temperature range for each paleosol. The TDS_{cat} and TDS_w values were obtained from the cation concentrations (Eq. (10)) based on $[Si]_{ss}$ constrained by pH (Fig. 6 and Table 4), and the $[HCO_3^-]$ values from Eq. (15) based on pH (Fig. 6 and Table 4) and P_{CO_2} (Fig. 7 and Table 5). I included Fe in TDS_{cat} and TDS_w but did not include SO₄ in TDS_w for the calculations (Section 2.2 and Appendix C). Note that my estimates of $[HCO_3^-]$, TDS_{cat} and TDS_w for the paleosols are those for the porewaters. On the other hand, Eqs. (52)–(54) are derived from river waters draining basaltic watersheds. Therefore, the imaginary riverine water

compositions draining paleosols are necessary to compare $[\text{HCO}_3^-]$, TDS_{cat} and TDS_{w} values between Dessert et al. (2003) and mine. Assuming that mixing of porewater and rainwater makes river water (e.g., Johnson et al., 1969), I calculated the imaginary riverine composition of a paleosol by diluting the porewater composition. Note that rainwater is treated as purewater in the calculation.

The actual steps to constrain a local temperature range are demonstrated for the Mt. Roe (1) paleosol in Fig. 8. Figs. 8a–c compare the $[\text{HCO}_3^-]$, TDS_{cat} and TDS_{w} values of the Mt. Roe (1) paleosol (open, overwritten and half-filled circles, respectively) to those obtained from Eqs. (52)–(54) (three zones limited by pairs of solid, dashed and dotted lines) with dilution of the porewater of the Mt. Roe (1) paleosol by factors of 1 (i.e., without dilution; Fig. 8a), 2 (Fig. 8b) and 2.5 (Fig. 8c). For the porewater without dilution (Fig. 8a), three temperature ranges are obtained from the superimposed ranges for the $[\text{HCO}_3^-]$, TDS_{cat} and TDS_{w} variations separately (three double-headed arrows in Fig. 8a). Then, the temperature range that satisfies the above three ranges at the same time is the local temperature range for the Mt. Roe (1) paleosol, 30–39 °C (shaded area in Fig. 8a). Similar procedures are taken for the imaginary riverine compositions with dilution factors of 2 and 2.5 (Figs. 8b and 8c, respectively), resulting in 13–15 °C of local temperature range (shaded area in Fig. 8b) and no consistent local temperature (Fig. 8c), respectively. Fig. 8d summarizes the local temperature range as a function of dilution factor and shows that any local temperatures obtained from the riverine compositions with dilution factors of $> \sim 2.2$ are not consistent with those from Eqs. (52)–(54). Fig. 8d finally reveals that the local temperature for the Mt. Roe (1) paleosol ranges from 12 to 39 °C.

In the same way, the ranges of local temperatures for the other mafic paleosols were obtained: 10–41 °C for Mt. Roe (2), ≤ 53 °C for Bird, ≤ 61 °C for Cooper Lake, 12–29 °C for Gaborone, ≤ 42 °C for Drakenstein and 8–54 °C for Flin Flon (Table 5). Eqs. (52)–(54) were also applied to modern weathering profiles (Belbex, Baynton and Hawaiian soils in Table 2), yielding ≤ 41 °C for Belbex, ≤ 34 °C for Baynton and 4–31, 18–23, 13–25, 5–29 and 7–28 °C for Hawaiian soils E, I, J, L and M, respectively. Note that I included Al in TDS_{cat} and TDS_{w} for Hawaiian soils because Al dissolves and flows out of the profiles significantly (Chadwick et al., 2003). The estimated local temperatures for the modern weathering profiles are consistent with those observed (Table 2). The application to the modern weathering profiles indicates that the above estimated local temperatures for the paleosols are sufficiently reasonable.

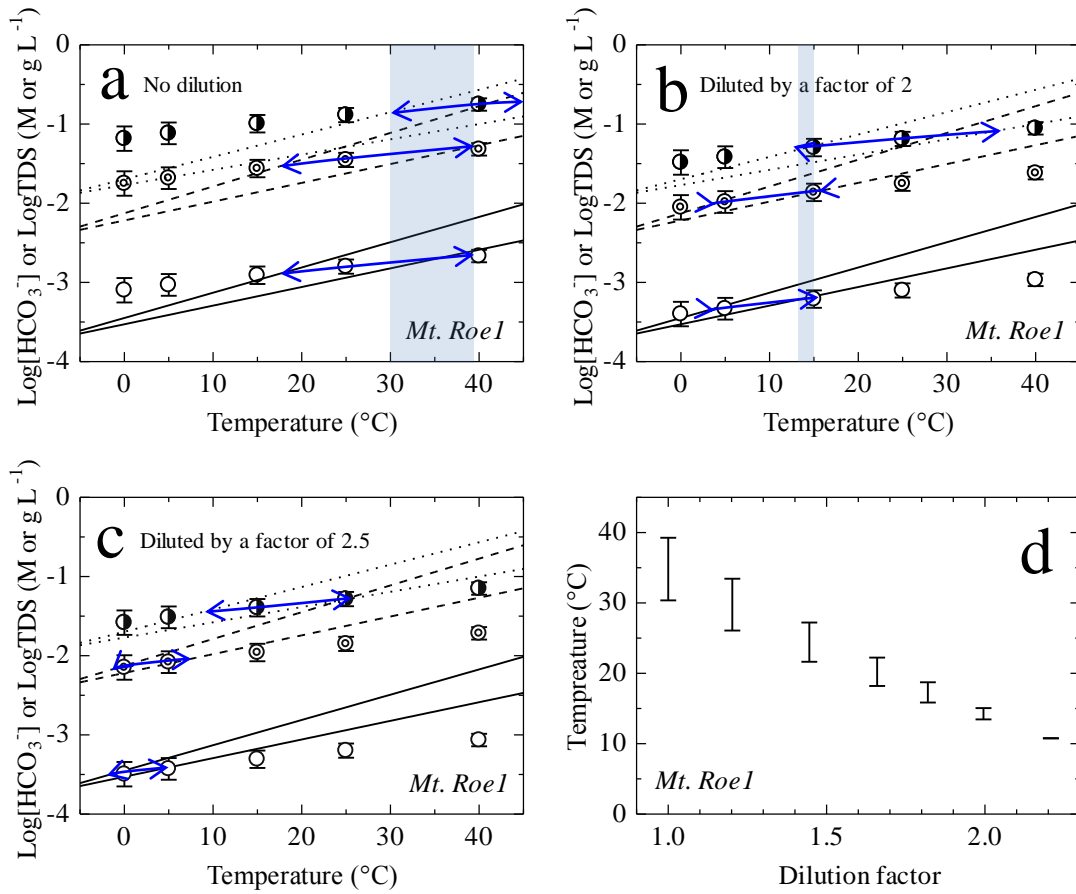


Figure 8. Steps to determine local temperatures of mafic paleosols using the relationships between solution concentrations and temperatures. The steps are demonstrated only for the Mt. Roe (1) paleosol. (a)-(c) Imaginary riverine compositions calculated from the porewater composition of the paleosol with no dilution (a) and with dilution by a factor of 2 (b) and 2.5 (c). (d) Possible local temperature ranges against dilution factor. Open, overwritten and half-filled circles represent [HCO₃⁻], TDS_{cat} and TDS_w values, respectively, calculated by the present method (see Section 4.2.2). Each pair of solid, dashed and dotted lines are from Eqs. (52), (53) and (54), respectively, with one standard deviation. No consistent local temperature is obtained at dilution factor > ~2.2.

4.2.3. Local temperatures for the Neoproterozoic-Paleoproterozoic paleosols

I gave the local temperature ranges for the eight Neoproterozoic-Paleoproterozoic paleosols in Sections 4.2.1 and 4.2.2 (Table 5). The lower constraints reveal that all the paleosols should have been weathered at > 0 °C of local temperature, which is consistent with significant weathering indicated by depletion of cations from the profiles (e.g., Murakami et al., 2011a; Yokota et al., 2013). On the other hand, the Mt. Roe (1), Mt. Roe (2), Bird, Drakenstein and Flin Flon paleosols still have high upper constraints (Table 5). Silicon dissolution is representative of that of silicate minerals, and thus, I can assume that it is proportional to the intensity of weathering. The Si depth profiles of the above five paleosols do not show strong depletion of Si in the weathering profiles (Murakami et al., 2011a) and are not largely different from those in modern weathering, either (e.g., White et al., 2001). Consequently, any of the five paleosols did not form during very hot periods which generate intense weathering, for instance, just after glaciation, but formed under rather moderate conditions (Yokota et al., 2013). Therefore, I can assume the upper constraint of local temperature as 30 °C (Holland, 1978) for the five paleosols. The assumption is consistent with some analyses of Archean geological records (≤ 40 °C at 3.4 Ga, Hren et al., 2009; 26–35 °C at 3.2–3.5 Ga, Blake et al., 2010). The rightmost column in Table 5 shows local temperature ranges for the paleosols used in the present study: 12–30 °C for Mt. Roe (1), 10–30 °C for Mt. Roe (2), 0–30 °C for Bird, 0–9 °C for Cooper Lake, 0–30 °C for Pronto/NAN, 12–29 °C for Gaborone, 0–30 °C for Drakenstein and 8–30 °C for Flin Flon paleosol. The local temperatures for the Cooper Lake and Pronto/NAN paleosols are probably similar to one another because of their similar location (~60 km distant from one another) and coeval formation-age (e.g., Murakami et al., 2011b). However, I use the conservative estimate, 0–30 °C, for the local temperature range for the Pronto/NAN paleosol because possible difference in altitude could give a difference in local temperature.

4.3. Atmospheric CO₂ evolution and climate in the Neoproterozoic-Paleoproterozoic

Applying the lowest and highest local temperatures for the paleosols (the rightmost column in Table 5) to the estimated P_{CO_2} levels in Section 4.1.3 (Table 5), I give a P_{CO_2} variation with age in Fig. 9. The P_{CO_2} levels at 8, 9, 10, 12, 29 and 30 °C, not given in Table 5, were obtained from the interpolation of the temperatures in those

listed in Table 5, using quadratic or cubic fitting functions ($R^2 > 0.999$). The dashed curves in Fig. 9 are the P_{CO_2} levels required for global temperatures to be 0 and 15 °C (Kasting, 2010). The P_{CO_2} -age relationships given by Kasting (2010) are based on the P_{CO_2} -luminosity relationships at 0 and 15 °C of global temperatures (von Paris et al., 2008) and the luminosity-age relationships (Gough, 1981). I also give an upper constraint of 1 atm of P_{CO_2} in the Neoproterozoic-Paleoproterozoic (horizontal, dashed and dotted line in Fig. 9; Som et al., 2012). The geometric means of P_{CO_2} levels at the lowest and highest local-temperatures for the paleosols are given by solid circles, and the uncertainties of P_{CO_2} levels and formation ages by boxes in Fig. 9.

The geometric means of P_{CO_2} levels are most likely (Section 3.1); the P_{CO_2} levels corrected for the local temperatures are 85–510, 78–2500, 160–490, 30–190, 20–620 and 23–210 PAL at ~2.77, ~2.75, ~2.46, ~2.15, ~2.08 Ga and ~1.85 Ga, respectively. Note that the P_{CO_2} levels at ~2.77 and ~2.46 Ga listed above are the intersections for the two coeval paleosols at respective ages (Table 5). Although the P_{CO_2} level determined at a given local temperature is a global one, the large uncertainties of local temperatures make me difficult to accurately show how atmospheric CO_2 evolved and fluctuated. Nevertheless, Fig. 9 indicates that the higher CO_2 scenario in the Neoproterozoic-early Paleoproterozoic (Haqq-Misra et al., 2008) is likely than previously thought regardless of the fluctuation of atmospheric CO_2 . Fig. 9 reveals that the above estimated P_{CO_2} levels are sufficient to retain the global temperature at > 0 °C (lower dashed curve in Fig. 9). Therefore, the P_{CO_2} levels in the Neoproterozoic-Paleoproterozoic, except for the glacial periods, should have been high enough to at least prevent the whole surface of the Earth from freezing water without any other greenhouse-effect gases. Fig. 9 suggests the secular variation of atmospheric CO_2 , the gradual decrease in P_{CO_2} in long term in the Neoproterozoic-Paleoproterozoic.

I here consider the variation of atmospheric CO_2 between 3.0 and 1.8 Ga including the glaciation periods at ~2.9 and ~2.4–2.2 Ga qualitatively. Because it is not certain how the Earth was covered with ice at ~2.9 and ~2.4–2.2 Ga (e.g., Evans et al., 1997; Williams et al., 1998; Young et al., 1998; Bekker et al., 2005), I assume that the global temperature was 0 °C (or less) during the glaciation periods. Because of small signatures of mass-independent fractionation of sulfur isotopes (MIF-S) at ~2.9 Ga, an ephemeral oxidation event occurred ($P_{O_2} > 10^{-5}$ PAL), which destabilized a CH_4 -rich atmosphere and triggered the ~2.9 Ga Pongola glaciation (e.g., Ono et al., 2006). This scenario was criticized because $> 10^{-5}$ PAL of P_{O_2} would cause all sulfur to be oxidized to sulfate, thereby eliminating the MIF signal (Domagal-Goldman et al., 2008). Then, I can assume the P_{O_2} level was $< 10^{-5}$ PAL at ~2.9 Ga, which can allow the atmosphere to

contain some amount of CH₄. Haqq-Misra et al. (2008) have suggested that $\sim 10^{-1.3}$ atm of P_{CO_2} with $\sim 10^{-2}$ atm of P_{CH_4} is sufficient to bring the global temperature at 0 °C. Accordingly, the ~ 2.9 Ga Pongola glaciation could have been triggered by the anti-greenhouse effect of organic haze of atmospheric CH₄, which was possibly accompanied by slight drawdown of CO₂ as suggested by Domagal-Goldman et al. (2008). The drawdown of CO₂ is not inconsistent with my estimates of P_{CO_2} (Fig. 9). This organic haze disappeared, that is, the P_{CH_4} level decreased until the time of weathering of the ~ 2.77 -Ga Mt. Roe paleosols developed under moderate climate (Table 5 and Fig. 9).

The two ~ 2.46 -Ga paleosols (Cooper Lake and Pronto) were overlain by the Matinenda, McKim, Ramsey Lake, Pecors, Mississagi, Bruce, Espanola, Serpent and Gowganda Formations in the upward order; evidence for the ~ 2.4 – 2.2 Ga Huronian glaciations was found in the Ramsey Lake, Bruce and Gowganda Formations (e.g., Bekker et al., 2006 and references therein). The climate at the time of weathering of the ~ 2.46 -Ga paleosols should have been moderate based on the analysis of cation depth-profiles (G-Farrow and Mossman, 1988; Utsunomiya et al., 2003) and my analysis in Fig. 9. MIF-S signals were observed in the McKim and Pecors Formations but not in the Espanola Formation that is almost coeval with the Timeball Hill Formation of the Transvaal Supergroup, South Africa formed at ~ 2.3 Ga (Bekker et al., 2004; Papineau et al., 2007). The increase in atmospheric O₂ as indicated by the MIF-S signals suggests a decrease in P_{CH_4} (also see above), and thus, atmospheric CH₄ functioned as greenhouse-effect gas but not as anti-greenhouse-effect gas at least since the time of weathering of the ~ 2.46 -Ga paleosols. The estimates of P_{CO_2} (Fig. 9) and the greenhouse effect of atmospheric CH₄ suggest that the Ramsey Lake glaciation was triggered by the drawdown of both CO₂ and CH₄. The Bruce glaciation might have been similarly triggered. Because no MIF-S signal was observed in the Espanola Formation (Papineau et al., 2007), the P_{O_2} level increased at the time period and accordingly the P_{CH_4} level further decreased compared to the time period of the Pecors Formation. Thus, the trigger of the Gowganda glaciation might be different from those of the two preceding glaciations. The drawdown of CO₂ is indispensable as inferred from Fig. 9. On the other hand, it is not certain whether or not the drawdown of CH₄ is necessary. If the P_{O_2} level increased greatly at ~ 2.3 Ga as suggested by Bekker and Holland (2012), the P_{CH_4} level must have decreased accordingly, which could have immediately triggered the Gowganda glaciation. If the decrease of the P_{CH_4} level was not significant, the drawdown of both CO₂ and CH₄ occurred for the Gowganda glaciation, and if the P_{CH_4} level was already small, the drawdown of only CO₂ was sufficient for the

glaciation. After the Gowganda glaciation, the P_{CO_2} level was roughly 20–300 PAL at least until 1.8 Ga (Fig. 9).

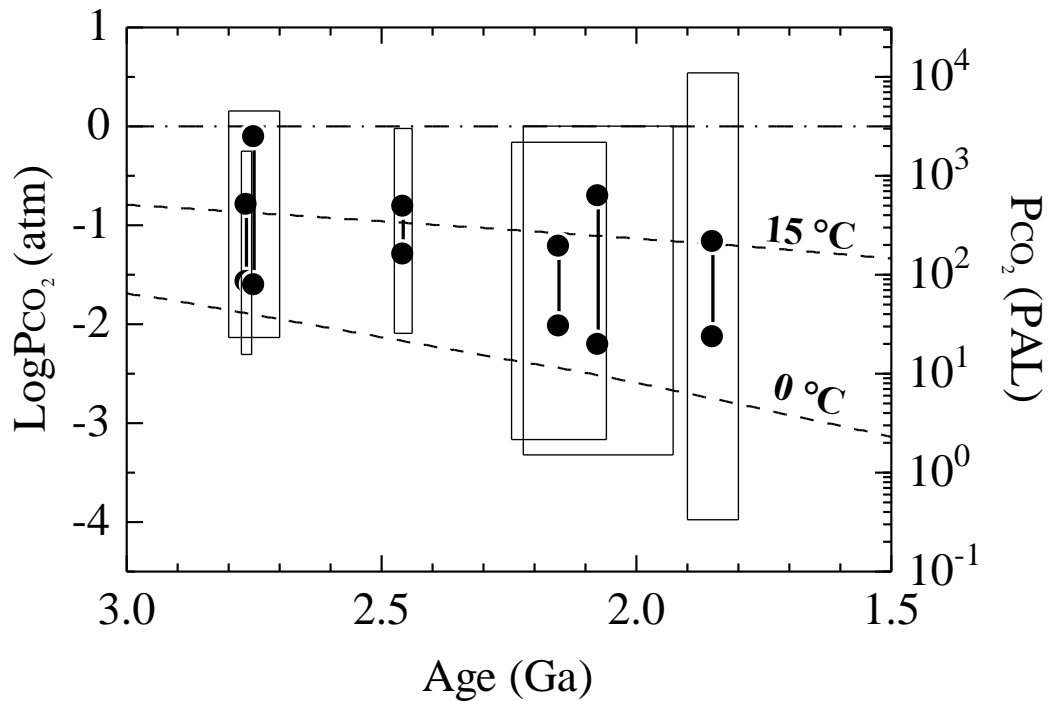


Figure 9. Variation of P_{CO_2} level with age in the Neoproterozoic-Paleoproterozoic considering local temperatures for the paleosols. Boxes represent the formation ages (Table 1) and possible ranges of P_{CO_2} levels (Table 5) of the paleosols. A pair of solid circles for each paleosol denotes the geometric-mean P_{CO_2} levels at the maximum and minimum local temperatures at the time of weathering of the paleosol (Section 4.2.3). The geometric-mean P_{CO_2} levels at ~2.77 and ~2.46 Ga are the intersections for the Mt. Roe 1 and 2 paleosols and for the Cooper Lake and Pronto/NAN paleosols, respectively. Dashed curves are the P_{CO_2} levels that maintain the average global surface-temperature of the Earth at 0 and 15 °C from Kasting (2010). Horizontal, dashed and dotted line represents 1 atm of P_{CO_2} , the upper constraint of P_{CO_2} at 2.7 Ga from Som et al. (2012).

5. Conclusions

I developed a new method for the estimation of P_{CO_2} from paleosols. The method estimates cation concentrations in porewater at the time of weathering of paleosols, assuming clay minerals as weathering secondary-minerals. Based on the relationships between pH, cation concentrations and CO_2 and the relationships between pH and secondary minerals, the method can estimate P_{CO_2} levels. The method was found to properly estimate P_{CO_2} levels by the comparison of calculated and observed P_{CO_2} levels in modern weathering profiles. The weathering rate law deduced from my method was consistent with that in the laboratory and field. The new method is valid and robust as revealed by the good agreement in P_{CO_2} levels and the deduced characteristics of the weathering rate law. However, the uncertainties in the steady-state Si concentration and temperature were found to result in large uncertainties in P_{CO_2} estimates.

The P_{CO_2} levels estimated by the present method are affected by local temperatures at the time of weathering of paleosols because the parameters such as pH constrained from thermodynamics of secondary minerals are temperature dependent; higher local temperatures require higher P_{CO_2} levels to keep the equilibria of the secondary minerals. Applying my method to Neoproterozoic-Paleoproterozoic paleosols with considering their local temperatures, I estimated P_{CO_2} levels at 2.8–1.8 Ga. The constraints on the local temperatures were made by utilizing the upper constraint on P_{CO_2} (1 atm) and the temperature-solute concentration relationships reported in the literature. Under the constrained local temperatures, P_{CO_2} was calculated; the estimated P_{CO_2} levels were higher than previously thought and high enough to maintain the average global surface temperature of the Earth above the freezing point of water in the Neoproterozoic-Paleoproterozoic except for the wide-spread glaciation periods.

Furthermore, the P_{CO_2} estimates suggested a gradual decrease in P_{CO_2} in long term in the Neoproterozoic-Paleoproterozoic. Based on the present results along with implications from the other geological records like MIF-S, I concluded that the multiple glaciations at ~2.9 and ~2.4–2.2 Ga might be differently triggered: the Pongola glaciation by CH_4 accumulation, the Ramsey Lake and Bruce glaciations by the collapse of both CO_2 and CH_4 and the Gowganda glaciation by the collapse of both CO_2 and CH_4 or only CO_2 .

Appendix A

In Section 2, I have assumed θ , σ and k_f as constants for the whole weathering

duration time, and calculated the $[X]_{ss}$ values. However, the values of θ , σ and k_f change as weathering proceeds (e.g., Maher, 2010; Rossi and Graham, 2010). Accordingly, the $[X]_{ss}$ value may also change with time. Because I obtain a P_{CO_2} value from Eq. (19) that requires a value of $[X]_{ss}$ from Eq. (10), I must confirm that Eq. (10) is valid even if θ , σ and k_f are variables.

I here consider $[X]_{ss}$, θ , σ and k_f are time-dependent parameters, $[X]_{ss}(t)$, $\theta(t)$, $\sigma(t)$ and $k_f(t)$, respectively. $[X]_{ss}(t)$ is then expressed by

$$[X]_{ss}(t) = [X]_{ss} \times f_X(t) \quad (A1)$$

where $f_X(t)$ is some function describing the time dependency of $[X]_{ss}$. Then, Eq. (5) is rewritten as

$$\frac{d[X - \text{rock}]}{dt} = -\theta(t)\sigma(t)k_f(t)[X]_{ss}f_X(t) \quad (A2)$$

Integrating Eq. (A2) for the total weathering duration time,

$$[X - \text{rock}]_{\text{loss}} = [X]_{ss} \int_{t=0}^{t=t_{\text{wt}}} f_X(t)\theta(t)\sigma(t)k_f(t)dt \quad (A3)$$

Applying Eqs. (A1) and (A3) to Si yields the following respective equations:

$$[Si]_{ss}(t) = [Si]_{ss} \times f_{Si}(t) \quad (A4)$$

$$[Si - \text{rock}]_{\text{loss}} = [Si]_{ss} \int_{t=0}^{t=t_{\text{wt}}} f_{Si}(t)\theta(t)\sigma(t)k_f(t)dt \quad (A5)$$

From Eqs. (A3) and (A5),

$$[X]_{ss} = \frac{[X - \text{rock}]_{\text{loss}}}{[Si - \text{rock}]_{\text{loss}}} [Si]_{ss} \frac{\int_{t=0}^{t=t_{\text{wt}}} f_{Si}(t)\theta(t)\sigma(t)k_f(t)dt}{\int_{t=0}^{t=t_{\text{wt}}} f_X(t)\theta(t)\sigma(t)k_f(t)dt} \quad (A6)$$

Similarly, combining Eqs. (A1), (A4) and (A6) yields

$$[X]_{ss}(t) = \frac{[X - \text{rock}]_{\text{loss}}}{[Si - \text{rock}]_{\text{loss}}} [Si]_{ss}(t) \frac{f_X(t) \int_{t=0}^{t=t_{\text{wt}}} f_{Si}(t)\theta(t)\sigma(t)k_f(t)dt}{f_{Si}(t) \int_{t=0}^{t=t_{\text{wt}}} f_X(t)\theta(t)\sigma(t)k_f(t)dt} \quad (A7)$$

Congruent weathering can be assumed from the consistent cation ratios reported for

modern silicates-draining rivers (e.g., Bluth and Kump, 1994; Gaillardet et al., 1999; Dalai et al., 2002; Das et al., 2005). Therefore, $f_X(t) = f_{Si}(t)$. Then, Eqs. (A6) and (A7) are rewritten as the following respective equations:

$$[X]_{ss} = \frac{[X - \text{rock}]_{\text{loss}}}{[Si - \text{rock}]_{\text{loss}}} [Si]_{ss} \quad (\text{A8})$$

$$[X]_{ss}(t) = \frac{[X - \text{rock}]_{\text{loss}}}{[Si - \text{rock}]_{\text{loss}}} [Si]_{ss}(t) \quad (\text{A9})$$

Eq. (A8) is exactly the same as Eq. (10). The range of $[Si]_{ss}$ value is between the solubilities of quartz and amorphous silica (Section 2.1, Appelo and Postma, 2005), and the $[Si]_{ss}(t)$ value should be in the same range even if $[Si]_{ss}(t)$ varies with time. Therefore, the calculation of $[X]_{ss}$ from Eq. (10) is valid for the estimation of P_{CO_2} from Eq. (19).

Appendix B

The total loss of element X from a paleosol, $[X - \text{rock}]_{\text{loss}}$ (mol m^{-3}), was calculated according to Murakami et al. (2011a). Paleosols have suffered compaction due to burial (Retallack, 1991; Sheldon and Retallack, 2001). The observed concentrations of elements in paleosols must be corrected for compaction to obtain $[X - \text{rock}]_{\text{loss}}$. A compaction factor of a paleosol, CF , is calculated using immobile elements such as Al, Ti and Zr:

$$CF = \frac{L_{PS}}{L_{PR}} = \frac{C_{i,PR} \times \rho_{PR}}{C_{i,PS} \times \rho_{PS}} \quad (\text{B1})$$

where L and ρ denote the thickness (m) and the density (g m^{-3}) of a paleosol (denoted by subscript PS) or the corresponding parent rock (denoted by subscript PR), respectively. C_i represents the concentration of immobile element, i (mol m^{-3}), for a whole weathering profile. For paleosols, $\rho_{PR} = \rho_{PS}$ can be assumed (Murakami et al., 2011a). Then Eq. (B1) can be simplified as

$$CF = \frac{L_{PS}}{L_{PR}} = \frac{C_{i,PR}}{C_{i,PS}} \quad (\text{B2})$$

I obtained a CF value using Eq. (B2) and assuming Al and Ti as immobile elements. A retention fraction, a mass ratio of paleosol to parent rock, of element X, RET_X , is defined as (Murakami et al., 2011a)

$$RET_X = \frac{CF \times C_{X,PS}}{C_{X,PR}} \quad (\text{B3})$$

where $C_{X,PS}$ and $C_{X,PR}$ represent the concentrations of element X (mol m^{-3}) in a whole

paleosol and parent rock, respectively. From the definition of $[X\text{-rock}]_{\text{loss}}$ (Section 2.1),

$$\begin{aligned} [X\text{-rock}]_{\text{loss}} &= C_{X,\text{PR}} - CF \times C_{X,\text{PS}} \\ &= C_{X,\text{PR}} (1 - RET_X) \end{aligned} \quad (\text{B4})$$

The values in Table 1 were calculated using Eq. (B4) except for $[K\text{-rock}]_{\text{loss}}/[Si\text{-rock}]_{\text{loss}}$. The values of $[K\text{-rock}]_{\text{loss}}$ were obtained using the values of RET_{Na} for all paleosols but the Pronto/NAN paleosol, for which $[K\text{-rock}]_{\text{loss}}$ was calculated using 2 times of RET_{Na} (see Section 4.1.1).

Appendix C

The charge balance in porewater in Eq. (11) considers water species, species derived from gaseous CO_2 and weathering-derived cations; I have ignored two other possible contributions: (1) anions released from a parent rock during weathering and (2) input of ions from rainwater. Firstly, I examined weathering-derived anions, HCO_3^- , CO_3^{2-} , NO_3^- , F^- , H_2PO_4^- , HPO_4^{2-} , PO_4^{3-} , SO_4^{2-} and Cl^- . Because, except for P, C, N, F, S and Cl have not been usually measured for Neoproterozoic-Paleoproterozoic paleosols, I estimated possible concentrations of the above anions. My assumptions were: each parent rock of the Neoproterozoic-Paleoproterozoic paleosols had the average anion composition of granite or basalt given by Taylor (1964), and the anions were all dissolved into porewater and finally flowed out of the profile completely. The assumptions allow me to calculate the total loss of an anion, Y (Y = C, N, F, S and Cl), from a parent rock ($[Y\text{-rock}]_{\text{loss}}$ (mol m^{-3})) because a $C_{Y,\text{PR}}$ value can be obtained from Taylor (1964) and RET_Y is equal to 0 (see Appendix B). Then, the estimated $[Y\text{-rock}]_{\text{loss}}$ value will be a maximum one (Eq. (B4)). A steady-state concentration of Y in porewater, $[Y]_{\text{ss}}$ (mol L^{-1}), can be calculated in a similar way as in Eq. (10):

$$[Y]_{\text{ss}} = \frac{[Y\text{-rock}]_{\text{loss}}}{[Si\text{-rock}]_{\text{loss}}} [Si]_{\text{ss}} \quad (\text{C1})$$

Then, defining Z_Y as the valence number of anion Y, I can calculate the ratio of the total anion concentration against the total cation concentration as

$$\sum_Y Z_Y [Y^{Z_Y-}] / \sum_X Z_X [X^{Z_X+}] = \sum_Y Z_Y [Y\text{-rock}]_{\text{loss}} / \sum_X Z_X [X\text{-rock}]_{\text{loss}} \quad (\text{C2})$$

HCO_3^- , NO_3^- , F^- , H_2PO_4^- , SO_4^{2-} and Cl^- were assumed to be the dominant species of C, N, F, P, S and Cl, respectively. The calculated ratios based on Eq. (C2) for the Neoproterozoic-Paleoproterozoic paleosols were in the range of 1–3%. These figures are

certainly overestimated because P and some of the other anions in the paleosols are not completely depleted (see the above assumption). Then, the values of $\leq 1-3\%$ indicate that I do not need to consider weathering-derived anions in Eq. (11).

I next consider the effects of rainwater on charge balance in porewater. If rainwater has significantly different charge of cations and anions, excluding those derived from atmospheric CO_2 , from the charge of porewater, the rainwater contributes significantly to the charge balance in porewater. The residual charge in rainwater, $\varepsilon_{\text{rain}}$ (eq L^{-1}), is defined as a difference obtained by subtracting the total equivalent of anions excluding the carbonate species from that of cations. The ions in rainwater are usually more condensed due to evapotranspiration when the rainwater is mixed with porewater. The resultant residual charge of rainwater origin in porewater, $\varepsilon_{\text{pore}}$ (eq L^{-1}), is expressed by

$$\varepsilon_{\text{pore}} = \frac{100}{100 - ET} \varepsilon_{\text{rain}} \quad (\text{C3})$$

where ET is the evapotranspiration factor (%). Then, Eq. (11) is rewritten as

$$\sum_{\text{X}} Z_{\text{X}} [\text{X}^{\text{Z}_{\text{X}}+}] + [\text{H}^+] + \varepsilon_{\text{pore}} = [\text{HCO}_3^-] + 2[\text{CO}_3^{2-}] + [\text{OH}^-] \quad (\text{C4})$$

Although ET has a large range, I can assume $< 90\%$ of ET (Holland, 1978; White and Blum, 1995) for the paleosols. Actually, $ET = \sim 80\%$ in Riverbank with an annual rainfall of 0.30 m yr^{-1} (White et al., 2005) and $ET = 60-80\%$ in Santa Cruz with an annual rainfall of $0.37-0.69 \text{ m yr}^{-1}$ (White et al., 2009). The larger the ET value is, the larger the $|\varepsilon_{\text{pore}}|$ value is. Then, the effects of rainwater on the charge balance (Eq. (C4)) can be assessed by evaluating the $|\varepsilon_{\text{pore}}|/\sum Z_{\text{X}}[\text{X}^{\text{Z}_{\text{X}}+}]$ value at $< 90\%$ of ET . From Eqs. (C3) and (10),

$$\begin{aligned} & \left| \varepsilon_{\text{pore}} \right| / \sum_{\text{X}} Z_{\text{X}} [\text{X}^{\text{Z}_{\text{X}}+}] \\ &= \frac{|\varepsilon_{\text{rain}}|}{\sum_{\text{X}} Z_{\text{X}} [\text{X - rock}]_{\text{loss}} / [\text{Si - rock}]_{\text{loss}}} \times \left(\frac{100}{100 - ET} \right) \times [\text{Si}]_{\text{ss}}^{-1} \quad (\text{C5}) \end{aligned}$$

In the right-hand side of Eq. (C5), $|\varepsilon_{\text{rain}}|$, the numerator of the first term, is $10^{-4.56 (\pm 0.53)}$ eq L^{-1} according to Berner and Berner (1996) (number of data = 99). The denominator of the first term ($\sum Z_{\text{X}}[\text{X-rock}]_{\text{loss}}/[\text{Si-rock}]_{\text{loss}}$) is 1.0–3.2 for the Neoproterozoic-Paleoproterozoic paleosols (Table 1) and 0.3–2.6 for the modern weathering profiles (Table 2). Then, I can assume the first term is roughly equal to $|\varepsilon_{\text{rain}}|$, $10^{-4.56}$. The second term, $100/(100 - ET)$, and the third term, $[\text{Si}]_{\text{ss}}^{-1}$, are related to one another; as ET becomes larger, $[\text{Si}]_{\text{ss}}$ becomes larger (e.g., Tardy, 1971; White and Blum,

1995). Therefore, the change in $|\varepsilon_{\text{pore}}|/\sum Z_X[X^{Zx+}]$ with increasing ET caused by the increase in value of the second term $100/(100 - ET)$ ($= 1-10$ at ≤ 90 % of ET) is mitigated by the decrease in $[\text{Si}]_{\text{ss}}^{-1}$ ($10^{3.9}-10^{2.8} \text{ M}^{-1}$, at 15°C). In other words, the value of $\{100/(100 - ET)\} \times [\text{Si}]_{\text{ss}}^{-1}$ in Eq. (C5) is almost constant at various ET (≤ 90 %). Assuming that $[\text{Si}]_{\text{ss}}$ is $10^{-2.8} \text{ M}$ at $ET = 90$ %, $\{100/(100 - ET)\} \times [\text{Si}]_{\text{ss}}^{-1} = 10^{3.8} \text{ M}^{-1}$. Then, from Eq. (C5), $|\varepsilon_{\text{pore}}|/\sum Z_X[X^{Zx+}]$ is calculated to be $10^{-0.76 (\pm 0.53)}$. The average value, $10^{-0.76}$, shifts the charge-balanced pH at a given P_{CO_2} only by -0.07 or $+0.08$. The possible greatest effect is expected when $|\varepsilon_{\text{pore}}|/\sum Z_X[X^{Zx+}]$ is maximum, i.e., $10^{-0.23}$, but even in this case, the resultant pH shift is -0.20 or $+0.39$, not significant. The calculations showed that $|\varepsilon_{\text{pore}}|$ does not have significant effects on charge balance equation in porewater and I can ignore the input of ions from rainwater in Eq. (11).

Appendix D

Sheldon (2006) has utilized the relationship of (cation release rate) = (CO_2 supply rate) for the estimation of P_{CO_2} , which is formulated by

$$\frac{M}{t_{\text{tot}}} = P_{\text{CO}_2} \left(10^3 \times K_{\text{H}} q + 45 \times \alpha \frac{D_{\text{CO}_2}}{L} \right) \quad (\text{D1})$$

M denotes the total cation loss from a weathering profile or paleosol (eq m^{-2}) and t_{tot} the total weathering time (yr). Then, the left hand side of Eq. (D1) is the cation release rate per unit area of the weathering profile or paleosol ($\text{eq m}^{-2} \text{ yr}^{-1}$). In the right hand side of Eq. (D1), the first term expresses the supply rate of CO_2 by rainwater, where 10^3 is the unit conversion figure (L m^{-3}) and K_{H} and q denote the Henry's constant for gaseous CO_2 dissolution into water ($\text{mol L}^{-1} \text{ atm}^{-1}$) (i.e., the equilibrium constant of Reaction (12) in Section 2.2) and the annual rainfall (m yr^{-1}), respectively. The second term describes the supply rate of CO_2 by diffusion, where 45 is the amount of gas molecules in unit air volume (mol m^{-3}) and α , D_{CO_2} and L represent the ratio of diffusion coefficient of CO_2 in soil against that in air (including porosity and water saturation factors (Holland and Zbinden, 1988)), the diffusion coefficient of CO_2 in air ($\text{m}^2 \text{ yr}^{-1}$) and the thickness of weathering profile (m), respectively. $\alpha = 0.1$ and $D_{\text{CO}_2} = 511 \text{ m}^2 \text{ yr}^{-1}$ were given by Sheldon (2006). Then once M , q , L and t_{tot} are given, P_{CO_2} can be calculated according to

$$P_{\text{CO}_2}^{\text{S}} = \frac{M}{t_{\text{tot}}} \left(10^3 \times K_{\text{H}} q + 45 \times \alpha \frac{D_{\text{CO}_2}}{L} \right)^{-1} \quad (\text{D2})$$

where $P_{\text{CO}_2}^{\text{S}}$ is the P_{CO_2} value calculated by Sheldon's method. The values of M , q , L and t_{tot} used for Eq. (D2) are given in Table D1.

The application of Sheldon's method (2006) to the modern weathering profiles clearly indicates that the calculated $P_{\text{CO}_2}^{\text{S}}$ values are much lower than the observed ones by up to three orders of magnitude (Fig. 2). Eq. (D1) assumes a CO_2 concentration gradient with depth and the CO_2 concentration of zero at the bottom of a weathering profile (Holland and Zbinden, 1988; Sheldon, 2006), which requires rather high cation release rate and corresponding high CO_2 supply rate (e.g., Dörr and Münnich, 1990). A higher CO_2 supply rate results in underestimation of P_{CO_2} as observed in Fig. 2. The large difference between the calculated $P_{\text{CO}_2}^{\text{S}}$ and observed "soil P_{CO_2} " values is caused mainly by inaccurate estimation of the CO_2 concentration gradient with depth. Atmospheric CO_2 indeed modulates its supply rate to balance the release rate of cations (e.g., Lasaga, 1984). Accordingly, the right hand side of Eq. (D1) does not appropriately estimate the supply rate of CO_2 at a given atmospheric CO_2 level. Overestimation of the supply rate of CO_2 leads to underestimation of P_{CO_2} (Eq. (D2)), which results in $P_{\text{CO}_2} \geq P_{\text{CO}_2}^{\text{S}}$.

Table D1. Parameters for modern weathering profiles and P_{CO_2} estimated by Sheldon's method (2006).

Locality name	M^a (10^4 eq m^{-2})	q^b (m yr^{-1})	L^b (m)	t_{tot}^b (10^3 yr)	Calc. $P_{\text{CO}_2}^s$ ^a (atm)	Obs. soil $P_{\text{CO}_2}^b$ (atm)	Ref. ^c	
SCT1	0.17	0.37	2.7	65	3.0×10^{-5}	1×10^{-2} –0.1	1,2	
SCT2	0.621	0.52	4.1	90	1.2×10^{-4}	1×10^{-2} –0.1	1,2	
Santa Cruz ^d	SCT3	0.926	0.61	4.4	137	1.2×10^{-4}	1×10^{-2} –0.1	1,2
	SCT4	1.854	0.69	4	194	1.6×10^{-4}	1×10^{-2} –0.1	1,2
	SCT5	1.541	0.59	4	226	1.1×10^{-4}	1×10^{-2} –0.1	1,2
Riverbank	0.438	0.3	5.5	250	4.1×10^{-5}	1×10^{-2}	3	
Belbex ^e	3.952	1	4.5	6900	1.0×10^{-5}	n.a. ^f	4,5	
Baynton	5.407	0.71	4	2000	6.0×10^{-5}	n.a.	6,7	
	E	0.903	0.57	1	310	1.3×10^{-5}	n.a.	8
	I	1.601	1.26	1.3	290	3.1×10^{-5}	n.a.	8
Hawaii	J	1.295	1.38	1.3	290	2.3×10^{-5}	n.a.	8
	L	1.98	1.25	1.2	230	4.2×10^{-5}	n.a.	8
	M	1.901	1.2	1.2	230	4.1×10^{-5}	n.a.	8

^a Total cation loss (M) and $P_{\text{CO}_2}^s$ were calculated according to Sheldon (2006) (Appendix D).

^b Annual rainfall (q), thickness of weathering profile (L), total weathering time (t_{tot}) and observed soil P_{CO_2} are from the references given in the last column unless otherwise described below.

^c 1—White et al. (2008); 2—White et al. (2009); 3—White et al. (2005); 4—Chesworth et al. (1981); 5—Tardy (1971); 6—Nesbitt and Wilson (1992); 7—Price et al. (1991); 8—Chadwick et al. (2003).

^d Observed soil P_{CO_2} was obtained from reference 2, and the other parameters from reference 1.

^e Annual rainfall and temperature are from reference 5, and the others from reference 4.

^f Not available

Appendix E

The thermodynamic data for smectites are not fully established (e.g., Gailhanou et al., 2012), and different thermodynamic data have been proposed for smectites (e.g., Helgeson, 1969; Norton, 1974; Nesbitt, 1977; Robie et al., 1979; Mattigod and Sposito, 1978; Chermak and Rimstidt, 1989; Tardy and Duplay, 1992; Vieillard, 2000). I used the thermodynamic data by Delany and Lundeen (1990) for smectites for the present study. I here examine how the estimates of P_{CO_2} change with other thermodynamic data. Among various thermodynamic data, I chose those given by Helgeson (1969), Norton (1974) and Nesbitt (1977) for the examination because their data have been proposed based on the observations of natural weathering systems.

Because the kaolinite/beidellite-Mg or -Ca phase boundaries controls solution pH (Section 2.3), I consider the thermodynamic data of K_{Mg} and K_{Ca} at 25 °C (Table E1). If I redefine K_{Mg} and K_{Ca} by Delany and Lundeen (1990) (Table 3) as $K_{\text{Mg}}^{\text{DL}}$ and $K_{\text{Ca}}^{\text{DL}}$, respectively, K_{Mg} and K_{Ca} of the other thermodynamic data are defined as

$$K_{\text{Mg}} = \delta_{\text{Mg}} K_{\text{Mg}}^{\text{DL}} \quad (\text{E1})$$

and

$$K_{\text{Ca}} = \delta_{\text{Ca}} K_{\text{Ca}}^{\text{DL}} \quad (\text{E2})$$

where $\delta_{\text{Mg}} = 0.76\text{--}2.53$ and $\delta_{\text{Ca}} = 0.72\text{--}4.42$ (Table E1). Following the steps for the estimation of P_{CO_2} demonstrated in Section 2, I can show how the thermodynamic data of smectites affect the estimates of P_{CO_2} .

I take beidellite-Mg as an example of smectite (Reaction (20)), and then, pH is constrained by

$$\frac{[\text{H}^+]_{\text{ss}}^{0.2833}}{[\text{Si}]_{\text{ss}}^{1.115} [\text{Mg}^{2+}]_{\text{ss}}^{0.1416}} = K_{\text{Mg}} \quad (\text{E3})$$

Using Eq. (10) and $\beta_{\text{X}} (= [\text{X-rock}]_{\text{loss}}/[\text{Si-rock}]_{\text{loss}}$, Section 3.2.1), Eq. (E3) is rewritten as

$$[\text{H}^+]_{\text{ss}} = K_{\text{Mg}}^{3.53} [\text{Si}]_{\text{ss}}^{4.56} \beta_{\text{Mg}}^{0.5} \quad (\text{E4})$$

or

$$\text{pH} = -4.56 \log[\text{Si}]_{\text{ss}} - 0.5 \log \beta_{\text{Mg}} - 3.53 \log K_{\text{Mg}} \quad (\text{E5})$$

$[\text{H}^+]_{\text{ss}}$ is related to P_{CO_2} by charge balance equation (Section 2.2). Eq. (19) in Section

2.2 can be even further simplified at $4 < \text{pH} < 9$ where $[\text{HCO}_3^-] \gg [\text{CO}_3^{2-}]$:

$$\sum_X Z_X [\text{X}^{Z_X+}] = \frac{K_1 K_H P_{\text{CO}_2}}{[\text{H}^+]} \quad (\text{E6})$$

Then,

$$[\text{Si}]_{\text{ss}} \sum_X Z_X \beta_X = \frac{K_1 K_H P_{\text{CO}_2}}{[\text{H}^+]_{\text{ss}}} \quad (\text{E7})$$

Substituting Eqs. (E4) into (E7) and solving for P_{CO_2} ,

$$P_{\text{CO}_2} = \frac{K_{\text{Mg}}^{3.53} \beta_{\text{Mg}}^{0.5} [\text{Si}]_{\text{ss}}^{5.56}}{K_1 K_H} \sum_X Z_X \beta_X \quad (\text{E8})$$

Because I examine how P_{CO_2} values estimated by the other thermodynamic data deviate from those by Delany and Lundeen's (1990), I can take a ratio instead of absolute values for simplicity. Because β_{Mg} , Z_X , β_X , K_1 and K_H do not depend on the thermodynamic data of smectites, from Eqs. (E1) and (E8),

$$\frac{P_{\text{CO}_2}^{\text{A}}}{P_{\text{CO}_2}^{\text{DL}}} = \delta_{\text{Mg-A}}^{3.53} \times \left(\frac{[\text{Si}]_{\text{ss}}^{\text{A}}}{[\text{Si}]_{\text{ss}}^{\text{DL}}} \right)^{5.56} \quad (\text{E9})$$

where the parameters with sub- and superscripts of DL and A are those calculated based on the thermodynamic data by Delany and Lundeen (1990) and those by one of the others (i.e., Helgeson (1969), Norton (1974) or Nesbitt (1977)), respectively. The concentration term of Si remains in Eq. (E9) because $[\text{Si}]_{\text{ss}}$ is affected by thermodynamic data as discussed below. Using Eq. (E8) or (E9), I can calculate possible shifts in estimated P_{CO_2} resulting from uncertainties in smectite thermodynamics.

Because I have used geometric means of maximum and minimum P_{CO_2} values (Sections 3.1, 4.1 and 4.3), possible shifts in estimated P_{CO_2} should be firstly determined at maximum and minimum P_{CO_2} values. For an individual set of the thermodynamic data, Eq. (E8) indicates that the maximum and minimum P_{CO_2} values are given when $[\text{Si}]_{\text{ss}}$ is maximum and minimum, respectively, because β_{Mg} , Z_X , β_X , K_1 and K_H do not depend on the thermodynamic data of smectites as discussed just above. The maximum $[\text{Si}]_{\text{ss}}$ value is determined uniquely to be $K_{\text{amorphous_silica}}$ while the minimum $[\text{Si}]_{\text{ss}}$ value depends on the thermodynamic data (Figs. 4 and 6). Accordingly, at maximum P_{CO_2} values, $[\text{Si}]_{\text{ss}}^{\text{A}} = [\text{Si}]_{\text{ss}}^{\text{DL}} = K_{\text{amorphous_silica}}$, and then, $P_{\text{CO}_2}^{\text{A}}/P_{\text{CO}_2}^{\text{DL}} = \delta_{\text{Mg-A}}^{3.53}$ (Eq. (E9)) which is directly obtained from Table E1.

The minimum $[\text{Si}]_{\text{ss}}$ value is given by the intersection between kaolinite/beidellite-Mg and kaolinite/muscovite boundaries (referred to as "muscovite-limited" case) or the intersection between kaolinite/beidellite-Mg and

carbonate-saturation boundaries (referred to as “carbonate-limited” case) (see Fig. 4 or 6, respectively). Firstly, I consider the “muscovite-limited” case. From Reaction (23),

$$\text{pH} = -\log[\text{Si}]_{\text{ss}} - \log \beta_{\text{K}} - (1/0.6667)\log K_{\text{K}} \quad (\text{E10})$$

By applying the thermodynamic data of Delany and Lundeen (1990) and A separately to Eqs. (E5) and (E10), $[\text{Si}]_{\text{ss}}^{\text{A}}/[\text{Si}]_{\text{ss}}^{\text{DL}} = \delta_{\text{Mg-A}}^{-0.99}$, and then, $P_{\text{CO}_2}^{\text{A}}/P_{\text{CO}_2}^{\text{DL}} = \delta_{\text{Mg-A}}^{-1.99}$. In the “carbonate-limited” case, any equation of Eqs. (33)–(37) results in

$$\text{pH} = -2\log[\text{Si}]_{\text{ss}} + \text{“const”} \quad (\text{E11})$$

where “const” is the constant that varies depending on Eqs. (33)–(37). Similarly to the “muscovite-limited” case, from Eqs. (E5) and (E11), $[\text{Si}]_{\text{ss}}^{\text{A}}/[\text{Si}]_{\text{ss}}^{\text{DL}} = \delta_{\text{Mg-A}}^{-1.38}$, and then, $P_{\text{CO}_2}^{\text{A}}/P_{\text{CO}_2}^{\text{DL}} = \delta_{\text{Mg-A}}^{-4.14}$. Consequently, at geometric-mean P_{CO_2} values, $P_{\text{CO}_2}^{\text{A}}/P_{\text{CO}_2}^{\text{DL}} = \delta_{\text{Mg-A}}^{0.77}$ and $\delta_{\text{Mg-A}}^{-0.31}$ for the “muscovite-limited” and “carbonate-limited” cases, respectively.

For beidellite-Ca as the smectite (Reaction (21)), the calculations were similarly made: $P_{\text{CO}_2}^{\text{A}}/P_{\text{CO}_2}^{\text{DL}} = \delta_{\text{Ca-A}}^{3.53}$ at maximum P_{CO_2} values, and $P_{\text{CO}_2}^{\text{A}}/P_{\text{CO}_2}^{\text{DL}} = \delta_{\text{Ca-A}}^{-1.99}$ and $\delta_{\text{Ca-A}}^{-4.14}$ for the “muscovite-limited” and “carbonate-limited” cases, respectively, at minimum P_{CO_2} values. At geometric-mean P_{CO_2} values, $P_{\text{CO}_2}^{\text{A}}/P_{\text{CO}_2}^{\text{DL}} = \delta_{\text{Ca-A}}^{0.77}$ and $\delta_{\text{Ca-A}}^{-0.31}$ for the “muscovite-limited” and “carbonate-limited” cases, respectively.

To demonstrate how the difference in the thermodynamic data of the smectites affect the estimates of P_{CO_2} (Eq. (E9)), I here assume that $P_{\text{CO}_2}^{\text{DL}} = 10^{-2.0 \pm 1.5}$ atm, i.e., the maximum, geometric mean and minimum P_{CO_2} levels are $10^{-0.5}$, $10^{-2.0}$ and $10^{-3.5}$ atm, respectively. The above range of the $P_{\text{CO}_2}^{\text{DL}}$ levels was chosen because it is approximately the same as the calculated range for the modern weathering profiles (Fig. 2), which allows me to compare the $P_{\text{CO}_2}^{\text{DL}}$ and $P_{\text{CO}_2}^{\text{A}}$ levels to the observed “soil P_{CO_2} ” levels of the modern weathering profiles. Fig. E1 indicates that the P_{CO_2} levels using the geometric means (solid circles) are not significantly affected by the difference in the thermodynamic data: the geometric-mean P_{CO_2} level changes by factors of 0.63–3.14 (Table E1), or -0.2 to $+0.5$ in log unit. Accordingly, the differences in the thermodynamic data of smectites give relatively small differences as long as the geometric-mean P_{CO_2} levels are used for P_{CO_2} estimation (Fig. 9). On the other hand, at the maximum and minimum of P_{CO_2} levels (i.e., $P_{\text{CO}_2}^{\text{DL}} = 10^{-0.5}$ and $10^{-3.5}$ atm, respectively), the differences in the thermodynamic data greatly affect P_{CO_2} estimates: the deviation from corresponding $P_{\text{CO}_2}^{\text{DL}}$ values is by ± 0.5 to $\sim \pm 3$ in log unit (triangles and reverse triangles in Fig. E1). A good agreement between the observed and calculated geometric-mean “soil P_{CO_2} ” values has been discussed (Fig. 2 and Section 3.1) where I applied the present method to modern weathering profiles, using the thermodynamic data by Delany and Lundeen (1990). Although the whole uncertainties are still large (Figs. 2 and E1), the geometric-mean P_{CO_2} values with the thermodynamic data by

Delany and Lundeen (1990) are useful to estimate P_{CO_2} levels with less uncertainties.

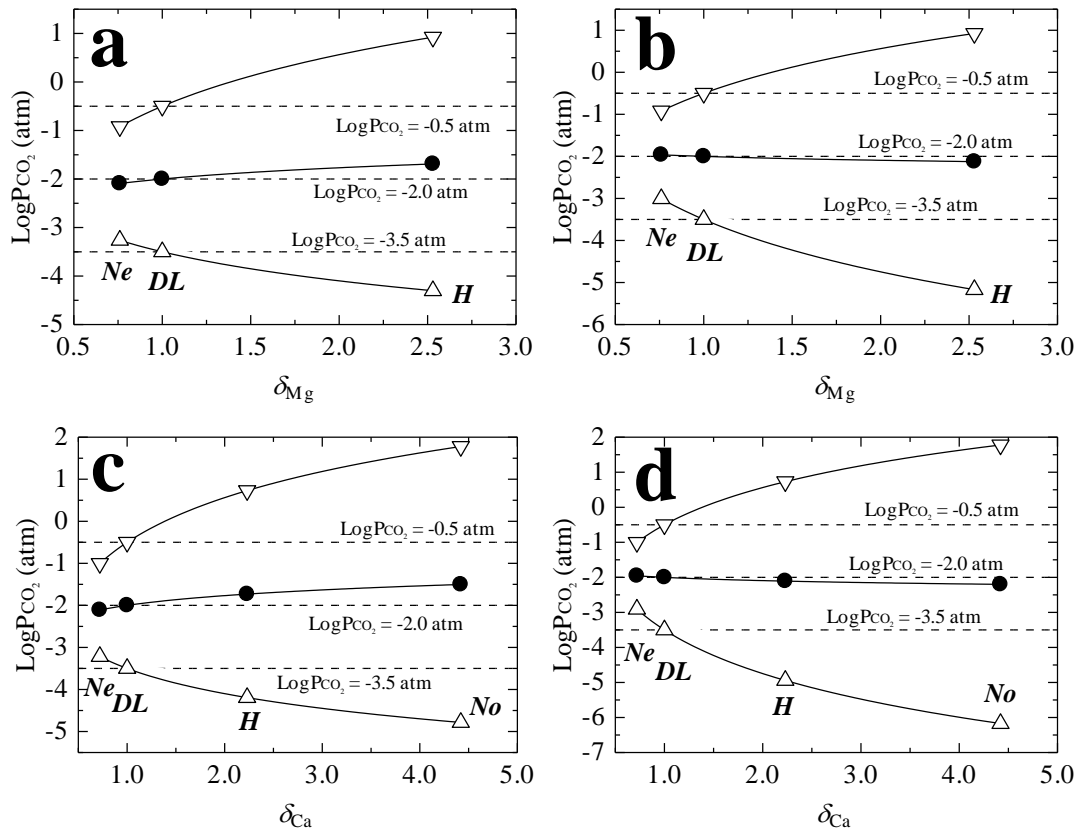


Figure E1. Changes of P_{CO_2} levels with difference in thermodynamic data of beidellite-Mg and -Ca. (a) P_{CO_2} levels with different thermodynamic data of beidellite-Mg in the “muscovite-limited” case; (b) P_{CO_2} levels with different thermodynamic data of beidellite-Mg in the “carbonate-limited” case; (c) P_{CO_2} levels with different thermodynamic data of beidellite-Ca in the “muscovite-limited” case; and (d) P_{CO_2} levels with different thermodynamic data of beidellite-Ca in the “carbonate-limited” case. See Appendix E for the details. The maximum, geometric-mean and minimum P_{CO_2} levels with the thermodynamic data by Delany and Lundeen (1990) are assumed to be $10^{-0.5}$, $10^{-2.0}$ and $10^{-3.5}$ atm, respectively (dotted lines). Reverse triangles, circles and triangles denote the data points at maximum, geometric-mean and minimum P_{CO_2} levels, respectively, with the thermodynamic data by Nesbitt (1977) (*Ne*), Delany and Lundeen (1990) (*DL*), Helgeson (1969) (*H*) and Norton (1974) (*No*).

Table E1. Various thermodynamic data for beidellite-Mg and -Ca and their effects on P_{CO_2} level.

Reference	Log K_{Mg}	log K_{Ca}	Ratio in geometric-mean P_{CO_2} level ^a			
			"Muscovite-limited" ^b		"Carbonate-limited" ^c	
			Beidellite-Mg ^d	Beidellite-Ca ^e	Beidellite-Mg ^d	Beidellite-Ca ^e
Delany and Lundeen (1990)	2.03	2.02	1.00	1.00	1.00	1.00
Helgeson (1969)	2.44	2.37	2.05	1.86	0.75	0.78
Norton (1974)	-	2.66	-	3.14	-	0.63
Nesbitt (1977)	1.92	1.88	0.81	0.78	1.09	1.11

^a Ratio of a calculated geometric-mean P_{CO_2} level to that using the thermodynamic data of Delany and Lundeen (1990) (Eq. (E9)).

^b The case when the maximum pH is determined at the intersection between kaolinite/smectite and kaolinite/muscovite boundaries.

^c The case when the maximum pH is determined at the intersection between kaolinite/smectite and carbonate saturation boundaries.

^d The case when the smectite is represented by beidellite-Mg.

^e The case when the smectite is represented by beidellite-Ca.

References

- April R., Newton R. and Coles L. T. (1986) Chemical weathering in two Adirondack watersheds: Past and present day rates. *Geol. Soc. Am. Bull.* **97**, 1232–1238.
- Appelo C. A. J. and Postma D. (2005) *Geochemistry, groundwater and pollution*, second ed. Balkema Publ., 649pp.
- Bao H., Lyons L. R. and Zhou C. (2008) Triple oxygen isotope evidence for elevated CO₂ levels after a Neoproterozoic glaciation. *Nature* **453**, 504–506.
- Bekker A. and Holland H. D. (2012) Oxygen overshoot and recovery during the early Paleoproterozoic. *Earth Planet Sci. Lett.* **317-318**, 295–304.
- Bekker A., Kaufman A. J., Karhu J. A., Beukes N. J., Swart Q. D., Coetzee L. L. and Eriksson K. A. (2001) Chemostratigraphy of the Paleoproterozoic Duitschland Formation, South Africa: Implication for coupled climate change and carbon cycling. *Am. J. Sci.* **301**, 261–285.
- Bekker A., Holland H. D., Wang P. -L., Rumble III D., Stein H. J., Hannah J. L., Coetzee L. L. and Beukes N. J. (2004) Dating the rise of atmospheric oxygen. *Nature* **427**, 117–120.
- Bekker A., Kaufman A. J., Karhu J. A. and Eriksson K. A. (2005) Evidence for Paleoproterozoic cap carbonates in North America. *Precambrian Res.* **137**, 167–206.
- Bekker A. and Kaufman A. J. (2007) Oxidative forcing of global climate change: A biogeochemical record across the oldest Paleoproterozoic ice age in North America. *Earth Planet Sci. Lett.* **258**, 486–499.
- Berg A. and Banwart S. A. (2000) Carbon dioxide mediated dissolution of Ca-fekdspar: implications for silicate weathering. *Chem. Geol.* **163**, 25–42.
- Berner E. K. and Berner R. A. (1996) *Global Environment: Water, Air and Geochemical Cycles*. Prince Hall, New Jersey.
- Berner R. A. (1978) Rate control of mineral dissolution under Earth surface conditions. *Am. J. Sci.* **278**, 1235–1252.
- Berner R. A., Lasaga A. C. and Garrels R. M. (1983) The carbonate-silicate geochemical cycle and its effect on atmospheric carbon dioxide over the past 100 million years. *Am. J. Sci.* **283**, 641–683.
- Berner R. A. (1991) A model for atmospheric CO₂ over Phanerozoic time. *Am. J. Sci.* **291**, 339–376.
- Berner R. A. (2006) GEOCARBSULF: A combined model for Phanerozoic atmospheric O₂ and CO₂. *Geochim. Cosmochim. Acta* **70**, 5653–5664.
- Blake R. E., Chang S. J. and Lepland A. (2010) Phosphate oxygen isotope evidence for

- a temperate biologically active Archean ocean. *Nature* **464**, 1029–1032.
- Bluth G. J. S. and Kump L. R. (1994) Lithologic and climatologic controls of river chemistry. *Geochim. Cosmochim. Acta* **58**, 2341–2359.
- Brady P. V. and Carroll S. A. (1994) Direct effects of CO₂ and temperature on silicate weathering: Possible implications for climate control. *Geochim. Cosmochim. Acta* **58**, 1853–1856.
- Brantley S. L. and White A. F. (2009) Approaches to modeling weathered regolith. *Rev. Mineral. Geochem.* **70**, 435–484.
- Busenberg E. and Plummer L. N. (1986). A comparative study of the dissolution and crystal growth kinetics of calcite and aragonite. In *Studies in Diagenesis* (ed. F. A. Mumpton). USGS Bulletin 1578. Washington, DC, U. S. Government Printing Office, pp. 139–168.
- Caldeira K. and Kasting J. F. (1992) Susceptibility of the early Earth to irreversible glaciation caused by carbon dioxide clouds. *Nature* **359**, 226–228.
- Capo R. C., Whipkey C. E., Blachère J. R. and Chadwick O. A. (2000) Pedogenic origin of dolomite in a basaltic weathering profile, Kohala peninsula, Hawaii. *Geology* **28**, 271–274.
- Chadwick O. A., Gavenda R. T., Kelly E. F., Ziegler K., Olson C. G., Elliott W. C. and Hendricks D. M. (2003) The impact of climate on the biogeochemical functioning of volcanic soils. *Chem. Geol.* **202**, 195–223.
- Chermak J. A. and Rimstidt J. D. (1989) Estimating the thermodynamic properties (ΔG_f° and ΔH_f°) of silicate minerals at 298 K from the sum of polyhedral contributions. *Am. Mineral.* **74**, 1023–1031.
- Chesworth W., Dejou J. and Larroque P. (1981) The weathering of basalt and relative mobilities of the major elements at Belbex, France. *Geochim. Cosmochim. Acta* **45**, 1235–1243.
- Claire M. W., Catling D. C. and Zahnle K. J. (2006) Biogeochemical modelling of the rise in atmospheric oxygen. *Geobiol.* **4**, 239–269.
- Coleman A. P. (1907) A lower Huronian ice age. *Am. J. Sci.* **23**, 187–192.
- Dalai T. K., Krishnaswami S. and Sarin M. M. (2002) Major ion chemistry in the headwaters of the Yamuna river system: Chemical weathering, its temperature dependence and CO₂ consumption in the Himalaya. *Geochim. Cosmochim. Acta* **66**, 3397–3416.
- Das A., Krishnaswami A. D., Sarin M. M. and Pande K. (2005) Chemical weathering in Krishna Basin and Western Ghats of the Deccan Traps, India: Rates of basalt weathering and their controls. *Geochim. Cosmochim. Acta* **69**, 2067–2084.

- Delany J. M. and Lundeen S. R. (1990) The LLNL thermochemical database. Lawrence Livermore National Laboratory Report UCRL-21658. Lawrence Livermore National Laboratory.
- Dessert C., Dupré B., François L. M., Schott J., Gaillardet J., Chakrapani G. and Bajpai S. (2001) Erosion of Decan Traps determined by river geochemistry: impact on the global climate and the $^{87}\text{Sr}/^{86}\text{Sr}$ ratio of seawater. *Earth Planet. Sci. Lett.* **188**, 459–474.
- Dessert C., Dupré B., Gaillardet J., François L. M. and Allègre C. J. (2003) Basalt weathering laws and the impact of basalt weathering on the global carbon cycle. *Chem. Geol.* **202**, 257–273.
- Domagal-Goldman S. D., Kasting J. F., Johnston D. T. and Farquhar J. (2008) Organic haze, glaciations and multiple sulfur isotopes in the Mid-Archean Era. *Earth Planet Sci. Lett.* **269**, 29–40.
- Dörr H. and Münnich K. O. (1990) ^{222}Rn flux and soil air concentration profiles in West-Germany. Soil ^{222}Rn as tracer for gas transport in the unsaturated soil zone. *Tellus* **42B**, 20–28.
- Drever J. I. (1988) *The Geochemistry of Natural Waters*, second ed. Prentice Hall. p437.
- Drever J. I. and Zobrist J. (1992) Chemical weathering of silicate rocks as a function of elevation in the southern Swiss Alps. *Geochim. Cosmochim. Acta* **56**, 3209–3216.
- Driese S. G., Jirsa M. A., Ren M., Brantley S. L., Sheldon N. D., Parker D. and Schmitz M. (2011) Neoproterozoic paleoweathering of tonalite and metabasalt: Implications for reconstructions of 2.69 Ga early terrestrial ecosystems and paleoatmospheric chemistry. *Precambrian Res.* **189**, 1–17.
- Evans D. A., Beukes N. J. and Kirschvink J. L. (1997) Low-latitude glaciation in the Paleoproterozoic era. *Nature* **386**, 262–266.
- Farquhar J., Bao H. and Thieme M. (2000) Atmospheric influence of Earth's earliest sulfur cycle. *Science* **289**, 756–758.
- Farquhar J. and Wing B. A. (2003) Multiple sulfur isotopes and the evolution of the atmosphere. *Earth Planet Sci. Lett.* **213**, 1–13.
- Feulner G. (2012) The faint young Sun problem. *Rev. Geophys.* **50**, RG2006.
- Gailhanou H., Blanc P., Rogez J., Mikaelian G., Kawaji H., Olives J., Amouric M., Denoyel R., Burrelly S., Montouillout V., Vieillard P., Fialips C. I., Michau N. and Gaucher E. C. (2012) Thermodynamic properties of illite, smectite and beidellite by calorimetric methods: Enthalpies of formation, heat capacities, entropies and Gibbs free energies of formation. *Geochim. Cosmochim. Acta* **89**, 279–301.
- Gaillardet L., Dupré B., Louvat P. and Allègre C. J. (1999) Global silicate weathering

- and CO₂ consumption rates deduced from the chemistry of large rivers. *Chem. Geol.* **159**, 3–30.
- Garrels R. M. (1967) Genesis of some ground waters from igneous rocks. In *Researches in Geochemistry* (ed. P. H. Ableson), pp. 405–420. Wiley.
- G-Farrow C. E. and Mossman D. J. (1988) Geology of Precambrian paleosols at the base of the Huronian supergroup, Elliot Lake, Ontario, Canada. *Precambrian Res.* **42**, 107–139.
- Golubev S. V., Pokrovsky O. S. and Schott J. (2005) Experimental determination of the effect of dissolved CO₂ on the dissolution kinetics of Mg and Ca silicates at 25 °C. *Chem. Geol.* **217**, 227–238.
- Golubev S. V., Bauer A. and Pokrovsky O. S. (2006) Effect of pH and organic ligands on kinetics of smectite dissolution at 25 °C. *Geochim. Cosmochim. Acta* **70**, 4436–4451.
- Gough D. O. (1981) Solar interior structure and luminosity variations. *Solar Phys.* **74**, 21–34.
- Gunnarsson I. and Arnórsson S. (2000) Amorphous silica solubility and the thermodynamic properties of H₄SiO₄⁰ in the range of 0° to 350°C at P_{sat}. *Geochim. Cosmochim. Acta* **64**, 2295–2307.
- Gysi A. P. and Stefánsson A. (2011) CO₂-water-basalt interaction. Numerical simulation of low temperature CO₂ sequestration into basalts. *Geochim. Cosmochim. Acta* **75**, 4728–4751.
- Haqq-Misra J. D., Domagal-Goldman S. D., Kasting P. J. and Kasting J. F. (2008) A revised, hazy methane greenhouse for the Archean Earth. *Astrobiology* **8**, 1127–1137.
- Hart M. H. (1978) The evolution of the atmosphere of the Earth. *Icarus* **33**, 23–39.
- Helgeson H. C. (1969) Thermodynamics of hydrothermal systems at elevated temperatures and pressures. *Am. J. Sci.* **267**, 729–804.
- Hoffman P. F. (2013) The Great Oxidation and a Siderian snowball Earth: MIF-S based correlation of Paleoproterozoic glaciation epochs. *Chem. Geol.* **362**, 143–156.
- Holland H. D. (1978) *The Chemistry of the Atmosphere and Oceans*. John Wiley & Sons, New York, 351pp.
- Holland H. D. (1984) *The Chemical Evolution of the Atmosphere and Oceans*. Princeton University Press, Princeton, NJ, 582 pp.
- Holland H. D. and Zbinden E. A. (1988) Paleosols and the evolution of atmosphere: Part I. In *Physical and Chemical weathering in Geochemical cycles* (eds. A. Larman and M. Meybeck). Reidel Dordrecht, pp. 61–82.

- Holland H. D., Feakes C. R. and Zbinden E. A. (1989) The Flin Flon paleosol and the composition of the atmosphere 1.8 bybp. *Am. J. Sci.* **289**, 362–389.
- Holland T. J. B. and Powell R. (1998) An internally consistent thermodynamic data set for phases of petrological interest. *J. Metamorph. Geol.* **16**, 309–343.
- Hren M. T., Tice M. M. and Chamberlain C. P. (2009) Oxygen and hydrogen isotope evidence for a temperate climate 3.42 billion years ago. *Nature* **462**, 205–208.
- Jensen D. L., Boddum J. K., Tjell J. C. and Christensen T. H. (2002) The solubility of rhodochrosite (MnCO₃) and siderite (FeCO₃) in anaerobic aquatic environments. *Appl. Geochem.* **17**, 503–511.
- Johnson N. M., Likens G. E., Bormann F. H., Fisher D. W. and Pierce R. S. (1969) A working model for the variation in stream water chemistry at the Hubbard Brook Experimental Forest, New Hampshire. *Water Res. Res.* **5**, 1353–1363.
- Kasting J. F., Zahnle K. J. and Walker J. C. G. (1983) Photochemistry of methane in the Earth's early atmosphere. *Precambrian Res.* **20**, 121–148.
- Kasting J. F. (1987) Theoretical constraints on oxygen and carbon dioxide concentrations in the Precambrian atmosphere. *Precambrian Res.* **34**, 205–229.
- Kasting J. F. (1993) Earth's early atmosphere. *Science* **259**, 920–926.
- Kasting J. F. (2010) Faint young Sun redux. *Nature* **464**, 687–689.
- Kiehle J. T. and Dickinson R. E. (1987) A study of the radiative effects of enhanced atmospheric CO₂ and CH₄ on early Earth surface temperatures. *J. Geophys. Res.* **92**, 2991–2998.
- Kimberley M. M. and Holland H. D. (1992) Introduction to Precambrian weathering and paleosols. In *Early Organic Evolution — Implications for Mineral and Energy Resources* (eds. M. Schidlowski, S. Golubic, M. M. Kimberley, D. M. McKirdy and P. A. Trundinger). Springer-Verlag, Berlin, pp. 9–15.
- Knoll A. H. (2003) The geological consequences of evolution. *Geobiol.* **1**, 3–14.
- Kopp R. E., Kirschvink J. L., Hilburn I. A. and Nash C. Z. (2005) The Paleoproterozoic snowball Earth: A climate disaster triggered by the evolution of oxygenic photosynthesis. *Proc. Natl. Acad. Sci.* **102**, 11131–11136.
- Kuhn W. R. and Atreya S. K. (1979) Ammonia photolysis and the greenhouse effect in the primordial atmosphere of the Earth. *Icarus* **37**, 207–213.
- Kump L. R., Brantley S. L. and Arthur M. A. (2000) Chemical weathering, atmospheric CO₂, and climate. *Annu. Rev. Earth Planet. Sci.* **28**, 611–667.
- Lasaga A. C. (1981) Dynamic treatment of geochemical cycles: Global kinetics. *Rev. Mineral.* **8**, 69–110.
- Lasaga A. C. (1984) Chemical kinetics of water-rock interactions. *J. Geophys. Res.* **89**,

4009–4025.

- Lasaga A. C., Soler J. M., Ganor J., Burch T. E. and Nagy K. (1994) Chemical weathering rate laws and global geochemical cycles. *Geochim. Cosmochim. Acta* **58**, 2361–2386.
- Le Hir G., Donnadiou Y., Godd ris Y., Pierrehumbert R. T., Halverson G. P., Macouin M., N d lec A. and Ramstein G. (2009) The snowball Earth aftermath: Exploring the limits of continental weathering process. *Earth Planet Sci. Lett.* **277**, 453–463.
- Liang M.-C., Hartman H., Kopp R. E., Kirschvink J. L. and Yung Y. L. (2006) Production of hydrogen peroxide in the atmosphere of a Snowball Earth and the origin of oxygenic photosynthesis. *Proc. Natl. Acad. Sci.* **103**, 18896–18899.
- Lowe D. R. and Tice M. M. (2004) Geological evidence for Archean atmospheric and climatic evolution: Fluctuating levels of CO₂, CH₄, and O₂ with an overriding tectonic control. *Geology* **32**, 493–496.
- Lowe D. R. and Tice M. M. (2007) Tectonic controls on atmospheric, climatic, and biological evolution 3.5–2.4 Ga. *Precambrian Res.* **158**, 177–197.
- Macfarlane A. W., Danielson A. and Holland H. D. (1994) Geology and major and trace element chemistry of late Archean weathering profiles in the Fortescue Group, Western Australia: Implications for atmospheric Po₂. *Precambrian Res.* **65**, 297–317.
- Maher K., Steefel C. I., White A. F. and Stonestrom D. A. (2009) The role of reaction affinity and secondary minerals in regulating chemical weathering rates at the Santa Cruz Soil Chronosequence, California. *Geochim. Cosmochim. Acta* **73**, 2804–2831.
- Maher K. (2010) The dependence of chemical weathering rates on fluid residence time. *Earth Planet Sci. Lett.* **294**, 101–110.
- Mattigod S. V. and Sposito G. (1978) Improved method for estimating the standard free energies of formation ($\Delta G^{\circ}_{f,298.15}$) of smectites. *Geochim. Cosmochim. Acta* **42**, 1753–1762.
- Murakami, T., Ito, J., Utsunomiya, S., Kasama, T., Kozai N. and Ohnuki T. (2004) Anoxic dissolution processes of biotite: Implications for Fe behavior during Archean weathering. *Earth Planet Sci. Lett.* **224**, 117–129.
- Murakami T., Sreenivas B., Das Sharma S. and Sugimori H. (2011a) Quantification of atmospheric oxygen levels during the Paleoproterozoic using paleosol compositions and iron oxide kinetics. *Geochim. Cosmochim. Acta* **75**, 3982–4004.
- Murakami T., Kasama T. and Utsunomiya S. (2011b) Early Proterozoic weathering processes under low O₂ conditions reconstructed from a 2.45 Ga paleosol in Pronto, Canada. *Am. Mineral.* **96**, 1613–1623.

- Navarre-Sitchler A. and Thyne G. (2007) Effects of carbon dioxide on mineral weathering rates at earth surface conditions. *Chem. Geol.* **243**, 53–63.
- Nesbitt H. W. (1977) Estimation of the thermodynamic properties of Na- Ca- and Mg-beidellites. *Canadian Mineral.* **15**, 22–30.
- Nesbitt H. W. and Young G. M. (1984) Prediction of some weathering trends of plutonic and volcanic rocks based on thermodynamic and kinetic considerations. *Geochim. Cosmochim. Acta* **48**, 1523–1534.
- Nesbitt H. W. and Young G. M. (1989) Formation and diagenesis of weathering profiles. *J. Geol.* **97**, 129–147.
- Nesbitt H. W. and Wilson R. E. (1992) Recent chemical weathering of basalts. *Am. J. Sci.* **292**, 740–777.
- Norton D. (1974) Chemical mass transfer in the Rio Tanama system, west-central Puerto Rico. *Geochim. Cosmochim. Acta* **38**, 267–277.
- Oliva P., Viers J. and Dupré B. (2003) Chemical weathering in granitic environments. *Chem. Geol.* **202**, 225–256.
- Ono S., Beukes N. J., Rumble D. and Fogel M. L. (2006) Early evolution of atmospheric oxygen from multiple-sulfur and carbon isotope records of the 2.9 Ga Mozaan Group of the Pongola Supergroup, Southern Africa. *S. Afr. J. Geol.* **109**, 97–108.
- Owen T., Cess R. D. and Ramanathan V. (1979) Enhanced CO₂ greenhouse to compensate for reduced solar luminosity on early Earth. *Nature* **277**, 640–642.
- Paces T. (1983) Rate constants of dissolution derived from the measurements of mass balance in hydrological catchments. *Geochim. Cosmochim. Acta* **47**, 1855–1863.
- Palmer J. A., Phillips, G. N. and McCarthy T. S. (1989) Paleosols and their relevance to Precambrian atmosphere composition. *J. Geol.* **97**, 77–92.
- Papineau D., Mojzsis S. J., Coath C. D., Karhu J. A. and McKeegan K. D. (2005) Multiple sulfur isotopes of sulfides from sediments in the aftermath of Paleoproterozoic glaciations. *Geochim. Cosmochim. Acta* **69**, 5033–5060.
- Papineau D., Mojzsis S. J. and Schmitt A. K. (2007) Multiple sulfur isotopes from Paleoproterozoic Huronian interglacial sediment and the rise of atmospheric oxygen. *Earth Planet Sci. Lett.* **255**, 188–212.
- Pavlov A. A., Kasting J. F., Brown, L. L., Rages K. A. and Freedman R. (2000) Greenhouse warming by CH₄ in the atmosphere of early Earth. *J. Geophys. Res.* **105**, 11981–11990.
- Pavlov A. A., Brown L. L. and Kasting J. F. (2001a) UV shielding of NH₃ and O₂ by organic hazes in the Archean atmosphere. *J. Geophys. Res.* **106**, 23267–23287.
- Pavlov A. A., Kasting J. F., Eigenbrode J. L. and Freeman K. H. (2001b) Organic haze

- in Earth's early atmosphere: Source of low- ^{13}C Late Archaean kerogens? *Geology* **29**, 1003–1006.
- Pavlov A. A., Hurtgen M. T., Kasting J. F. and Arthur M. A. (2003) Methane-rich Proterozoic atmosphere? *Geology* **31**, 87–90.
- Pokrovsky O. S. and Schott J. (2002) Surface chemistry and dissolution kinetics of divalent metal carbonates. *Environ. Sci. Technol.* **36**, 426–432.
- Pinto J. P. and Holland H. D. (1988) Paleosols and the evolution of the atmosphere; part II. In *Paleosols and Weathering through Geologic Time* (eds. J. Reinhardt and W. Silgeo). Spec. Pap. Geol. Soc., America, pp. 21–34.
- Price R. C., Gray C. M., Wilson R. E., Frey F. A. and Taylor S. R. (1991) The effects of weathering on rare-earth element, Y and Ba abundances in Tertiary basalts from southern Australia. *Chem. Geol.* **93**, 245–265.
- Retallack G. J. (1991) Untangling the effects of burial alteration and ancient soil formation. *Annu. Rev. Earth Planet. Sci.* **19**, 183–206.
- Retallack G. J. and Krinsley D. H. (1993) Metamorphic alteration of a Precambrian (2.2Ga) paleosol from South Africa revealed by backscattered electron imaging. *Precambrian Res.* **63**, 27–41.
- Robie R. A., Hemingway B. S. and Fisher J. R. (1979) Thermodynamic properties of minerals and related substances at 289.15 K and 1 bar (10⁵ pascals) pressure and at higher temperatures. *U. S. Geol. Survey Bull.* **1452**.
- Rossi A. M. and Graham R. C. (2010) Weathering and porosity formation in subsoil granitic clasts, Bishop Creek moraines, California. *Soil Sci. Soc. Am. J.* **74**, 172–185.
- Rye R., Kuo P. H. and Holland H. D. (1995) Atmospheric carbon dioxide concentrations before 2.2 billion years ago. *Nature* **378**, 603–605.
- Rye R. and Holland H. D. (1998) Paleosols and the atmospheric oxygen: A critical review. *Am. J. Sci.* **298**, 621–672.
- Rye R. and Holland H. D. (2000) Geology and geochemistry of paleosols developed on the Hekpoort basalt, Pretoria group, South Africa. *Am. J. Sci.* **300**, 85–141.
- Sagan C. and Mullen G. (1972) Earth and Mars: Evolution of atmospheres and surface temperatures. *Science* **177**, 52–56.
- Sekine Y., Tajika E., Tada R., Hirai T., Goto K. T., Kuwatani T., Goto K., Yamamoto S., Tachibana S., Isozaki Y. and Kirschvink J. L. (2011) Manganese enrichment in the Gowganda Formation of the Huronian Supergroup: A highly oxidizing shallow-marine environment after the last Huronian glaciation. *Earth Planet Sci. Lett.* **307**, 201–210.

- Sheldon N. D. and Retallack G. J. (2001) Equation for compaction of paleosols due to burial. *Geology* **29**, 247–250.
- Sheldon N. D. (2006) Precambrian paleosols and atmospheric CO₂ levels. *Precambrian Res.* **147**, 148–155.
- Shock E. L., Sassani D. C., Willis M. and Sverjensky D. A. (1997) Inorganic species in geologic fluids: Correlations among standard molar thermodynamic properties of aqueous ions and hydroxide complexes. *Geochim. Cosmochim. Acta* **61**, 907–950.
- Sleep N. H. and Zahnle K. (2001) Carbon dioxide cycling and implications for climate on ancient Earth. *J. Geophys. Res.* **106**, 1373–1399.
- Som S. M., Catling D. C., Harnmeijer J. P., Polivka P. M. and Buick R. (2012) Air density 2.7 billion years ago limited to less than twice modern levels by fossil raindrop imprints. *Nature* **484**, 359–362.
- Stonestrom D. A., White A. F. and Akstin K. (1998) Determining rates of chemical weathering in soils — Solute transport versus profile evolution. *J. Hydrol.* **209**, 331–345.
- Stumm W. and Morgan J. J. (1996) *Aquatic Chemistry*, third ed. John Wiley & Sons, New York, 780p.
- Sverdrup H. U. (1990) *The Kinetics of Base Cation Release due to Chemical Weathering*. Lund University Press, Lund, Sweden, 246 p.
- Tajika E. and Matsui T. (1992) Evolution of terrestrial proto-CO₂ atmosphere coupled with thermal history of the earth. *Earth Planet Sci. Lett.* **113**, 251–266.
- Tajika E. and Matsui T. (1993) Degassing history and carbon cycle of the Earth: From an impact-induced steam atmosphere to the present atmosphere. *Lithos* **30**, 267–280.
- Tardy Y. (1971) Characterization of the principal weathering types by the geochemistry of waters from some European and African crystalline massifs. *Chem. Geol.* **7**, 253–271.
- Tardy Y. and Duplay J. (1992) A method of estimating the Gibbs free energies of formation of hydrate and dehydrated clay minerals. *Geochim. Cosmochim. Acta* **56**, 3007–3029.
- Taylor S. R. (1964) Abundance of chemical elements in the continental crust: A new table. *Geochim. Cosmochim. Acta* **28**, 1273–1285.
- Trainer M. G., Pavlov A. A., Dewitt H. L., Jimenez J. L., McKay C. P., Toon O. B. and Tolbert M. A. (2006) Organic haze on Titan and the early Earth. *Proc. Natl. Acad. Sci.* **103**, 18035–18042.
- Utsunomiya S., Murakami T., Kadohara H. and Tsukimura K. (1999) The effect of partial pressure of carbon dioxide on anorthite dissolution. *Mineral. J.* **21**, 1–8.

- Utsunomiya S., Murakami T., Nakada M. and Kasama T. (2003) Iron oxidation state of a 2.45-Byr-old paleosol developed on mafic volcanics. *Geochim. Cosmochim. Acta* **67**, 213–221.
- Vieillard P. (2000) A new method for the prediction of Gibbs free energies of formation of hydrated clay minerals based on the electronegativity scale. *Clays Clay Miner.* **48**, 459–473.
- von Brunn V. and Gold D. J. C. (1993) Diamictite in the Archean Pongola sequence of southern Africa. *J. Afr. Earth Sci.* **16**, 367–374.
- von Paris P., Rauer H., Grenfell J. L., Patzer B., Hedelt P., Stracke B., Trautmann T. and Schreier F. (2008) Warming the early earth—CO₂ reconsidered. *Planet Space Sci.* **56**, 1244–1259.
- Wang Y., Nahon D. and Merino E. (1994) Dynamic model of genesis of calcretes replacing silicate rocks in semi-arid regions. *Geochim. Cosmochim. Acta* **58**, 5131–5145.
- White A. F. (1995) Chemical weathering rates of silicate minerals in soils. *Rev. Mineral.* **31**, 407–461.
- White A. F. and Blum A. E. (1995) Effects of climate on chemical weathering in watersheds. *Geochim. Cosmochim. Acta* **59**, 1729–1747.
- White A. F., Blum A. E., Bullen T. D., Vivit D. V., Schultz M. and Fitzpatrick J. (1999) The effect of temperature on experimental and natural chemical weathering rates of granitoid rocks. *Geochim. Cosmochim. Acta* **63**, 3277–3291.
- White A. F., Bullen T. D., Schultz M. S., Blum A. E., Huntington T. G. and Peters N. E. (2001) Differential rates of feldspar weathering in granitic regoliths. *Geochim. Cosmochim. Acta* **65**, 847–869.
- White A. F. and Brantley S. L. (2003) The effect of time on the weathering of silicate minerals: Why do weathering rates differ in the laboratory and field? *Chem. Geol.* **202**, 479–506.
- White A. F., Schultz M. S., Vivit D. A., Blum A. E., Stonestrom D. A. and Harden J. W. (2005) Chemical weathering rates of a soil chronosequence on granitic alluvium: III. Hydrochemical evolution and contemporary solute fluxes and rates. *Geochim. Cosmochim. Acta* **69**, 1975–1996.
- White A. F., Schulz M. S., Vivit D. V., Blum A. E., Stonestrom D. A. and Anderson S. P. (2008) Chemical weathering of a marine terrace chronosequence, Santa Cruz, California I: Interpreting rates and controls based on soil concentration–depth profiles. *Geochim. Cosmochim. Acta* **72**, 36–68.
- White A. F., Schulz M. S., Stonestrom D. A., Vivit D. V., Fitzpatrick J., Bullen T. D.,

- Maher K. and Blum A. E. (2009) Chemical weathering of a marine terrace chronosequence, Santa Cruz, California. Part II: Solute profiles, gradients and the comparisons of contemporary and long-term weathering rates. *Geochim. Cosmochim. Acta* **73**, 2769–2803.
- Wiggering H. and Beukes N. J. (1990) Petrography and geochemistry of a 2000–2200-Ma-old hematitic paleo-alteration profile on Ongeluk basalt of the Transvaal Supergroup, Griqualand West, South Africa. *Precambrian Res.* **46**, 241–258.
- Williams D. M., Kasting J. F. and Frakes L. A. (1998) Low-latitude glaciation and rapid changes in the Earth's obliquity explained by obliquity-oblateness feedback. *Nature* **396**, 453–455.
- Wogelius R. A. and Walther J. V. (1991) Olivine dissolution at 25°C: Effects of pH, CO₂, and organic acids. *Geochim. Cosmochim. Acta* **55**, 943–954.
- Wolf E. T. and Toon O. B. (2010) Fractal organic hazes provided an ultraviolet shield for early Earth. *Science* **328**, 1266–1268.
- Yang L. and Steefel C. I. (2008) Kaolinite dissolution and precipitation at 22 °C and pH 4. *Geochim. Cosmochim. Acta* **72**, 99–116.
- Yang W. and Holland H. D. (2003) The Hekpoort paleosol profile in strata 1 at Gaborone, Botswana: Soil formation during the Great Oxidation Event. *J. Am. Sci.* **303**, 187–220.
- Yokota K., Kanzaki Y. and Murakami T. (2013) Weathering model for the quantification of atmospheric oxygen evolution during the Paleoproterozoic. *Geochim. Cosmochim. Acta*. <http://dx.doi.org/10.1016/j.gca.2013.03.015>.
- Yokoyama T. and Banfield J. F. (2002) Direct determinations of the rates of rhyolite dissolution and clay formation over 52,000 years and comparison with laboratory measurements. *Geochim. Cosmochim. Acta* **66**, 2665–2681.
- Young G. M. (1970) An extensive Proterozoic glaciation in North America? *Palaeogeography Palaeoclimatol. Palaeoecol.* **7**, 85–101.
- Young G. M., von Brunn V., Gold D. J. C., and Minter W. E. L. (1998) Earth's oldest reported glaciation: Physical and chemical evidence from the Archean Mozaan Group (~2.9 Ga) of South Africa. *J. Geol.* **106**, 523–538.
- Zahnle K. J., Claire M. and Catling D. (2006) The loss of mass-independent fractionation in sulfur due to a Paleoproterozoic collapse of atmospheric methane. *Geobiol.* **4**, 271–283.
- Zerkle A. L., Claire M. W., Domagal-Goldman S. D., Farquhar J. and Poulton S. W. (2012) A bistable organic-rich atmosphere on the Neoproterozoic Earth. *Nature Geosci.* **5**, 359–363.

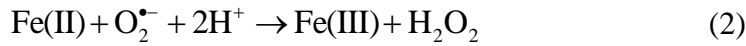
III. Rate law of Fe(II) oxidation under low O₂ conditions

1. Introduction

Many geological signatures point to a great rise of atmospheric oxygen in the Paleoproterozoic (the Great Oxidation Event, GOE) (see recent reviews, Canfield, 2005; Catling and Claire, 2005; Sreenivas and Murakami, 2005; Holland, 2006; Kasting and Ono, 2006). Mass independent fractionation of sulfur isotopes (MIF-S where $\Delta^{33}\text{S} \cong \delta^{33}\text{S} - 0.515 \times \delta^{34}\text{S} \neq 0$) and some other geological records indicate that oxygen increased from $\leq \sim 10^{-6}$ atm of partial pressure of the atmospheric oxygen (P_{O_2}) at ≥ 2.45 Ga, $\geq \sim 10^{-6}$ atm at 2.32 Ga, and to $\geq \sim 10^{-3}$ atm at 2.0 Ga (Farquhar et al., 2000; Pavlov and Kasting, 2002; Farquhar and Wing, 2003; Bekker et al., 2004). The Fe contents of paleosols (soils formed by ancient weathering) formed during the Precambrian can be also used as a barometer of P_{O_2} levels because Fe is sensitive to redox state: Fe(II) in water is oxidized to Fe(III) which readily precipitates as Fe(III) (hydr)oxides and remains in a weathering profile at high P_{O_2} levels, while Fe(II) flows out of the profile, saved from oxidation, at low P_{O_2} levels (Murakami et al., 2011). Then, redox-sensitive elements such as Fe retained in a weathering profile should reflect the P_{O_2} level at the time of weathering. Indeed, some authors have extracted strong constraints on the transition of P_{O_2} levels, e.g., from $< \sim 10^{-3}$ to $> \sim 10^{-2}$ atm of P_{O_2} at ~ 2.2 Ga (e.g., Holland, 1984; Rye and Holland, 1998). Such transition is reflected by Fe kinetics but not by Fe thermodynamics because Fe(III) (hydr)oxides are thermodynamically stable at $> 10^{-60}$ atm of P_{O_2} in the range of weakly-acidic to neutral pH (e.g., Ohmoto et al., 2004). A quantitative pattern of the GOE has been recently estimated taking account of the Fe oxidation kinetics, proposing a gradual rise of atmospheric oxygen in the Paleoproterozoic (Murakami et al., 2011). However, the Fe oxidation rates under low O₂ conditions used by Murakami et al. (2011) were assumed rates, and therefore, the rate law should be determined experimentally for more accurate estimation of P_{O_2} levels. Even in the modern Earth's surface, there are some O₂-limited environments, such as oxygen minimum zones in the ocean and redox fronts in lakes and groundwaters (e.g., Teutsch et al., 2005; 2009; Paulmier and Ruiz-Pino, 2009; Keeling et al., 2010) where Fe(II) oxidation kinetics as a function of O₂ is important.

There are few experiments that elucidate the relationships between the Fe(II) oxidation rate and P_{O_2} . On the other hand, the rate of Fe(II) oxidation in modern surface environments (high O₂ conditions) has been studied in-depth by numerous researchers.

The most accepted mechanisms of Fe(II) oxidation by dissolved O₂ (DO) are described by (e.g., Stumm and Lee, 1961; King et al., 1995; Emmenegger et al., 1998; Santana-Casiano et al., 2005)



where Reactions (1) and/or (3) are the rate determining steps. Stumm and Lee (1961) have established a rate law for Fe(II) oxidation by DO in natural water at > pH 5:

$$\frac{d[\text{Fe(II)}]}{dt} = -k[\text{Fe(II)}][\text{O}_2][\text{OH}^-]^2 \quad (5)$$

where [Fe(II)], [O₂] and [OH⁻] are the concentrations of total Fe(II), DO and OH⁻, respectively, in solution (mol L⁻¹) and *k* is the rate constant (L³ mol⁻³ min⁻¹). DO can be substituted by *P*_{O₂} under the equilibrium of gas and liquid, applying Henry's law, and [OH⁻] can be substituted by pH. Then, Eq. (5) indicates the rate of Fe(II) oxidation is a function of pH and *P*_{O₂}. The effects of pH on the oxidation rate have been scrutinized along with the effects of other solution factors, such as temperature and ionic strength, and Fe(II) interactions with anions and organic materials (e.g., Tamura et al., 1976a; Theis and Singer, 1974; Millero et al., 1987; King, 1998; Santana-Casiano et al., 2000, 2004; Rose and Waite, 2002; Craig et al., 2009; Burns et al., 2010, 2011a, b; González et al., 2010; Mao et al., 2011). Singer and Stumm (1970) have shown that the exponent of [OH⁻] is smaller than 2 at pH < 5, and the rate is independent of pH at pH < 3.5. In contrast, the effects of oxygen on the oxidation rate have not been tested over a wide range of *P*_{O₂}. Stumm and Lee (1961) have established Eq. (5) by varying *P*_{O₂} from 0.107 to 0.195 atm and Tamura et al. (1976a; b) have confirmed the validity of Eq. (5) at *P*_{O₂} = 0.308–0.903 atm. These oxygen levels were within one order of the present atmospheric oxygen level (*P*_{O₂} = 0.2 atm). On the other hand, Liang et al. (1993) have examined oxidation rates down to *P*_{O₂} = 5×10⁻³ atm and indicated that “at low DO, the rate appeared to deviate from the theoretical prediction”. Sugimori et al. (2011) have performed oxidation experiments at 9.6×10⁻⁴–0.2 atm of *P*_{O₂}, indicated deviation from Eq. (5) at low *P*_{O₂}, and suggested the possibility of further deviation under even lower O₂ conditions. Sugimori et al. (2012) have conducted dissolution experiments of olivine

at $\sim 10^{-4}$ –0.2 atm of P_{O_2} and demonstrated a possible change in the Fe(II) oxidation rate law as a function of P_{O_2} . The results by Liang et al. (1993) and Sugimori et al. (2011; 2012) prompt me to establish a revised Fe(II) oxidation rate law over a wide range of P_{O_2} .

In the context of both the precise interpretation of geologic records of Fe and the elucidation of the Fe(II) oxidation mechanism itself, it is indispensable to fully comprehend the relationships between P_{O_2} and the Fe(II) oxidation rate. In this chapter, Fe(II) oxidation rates at the inferred, low P_{O_2} levels during the GOE ($P_{O_2} = 10^{-5}$ – 10^{-4} atm) were examined. Following the method of Sugimori et al. (2011), the general oxidation rate law is represented by

$$\frac{d[\text{Fe(II)}]}{dt} = -k[\text{Fe(II)}][\text{O}_2]^x[\text{OH}^-]^y \quad (6)$$

where x and y are variables. The variables, x and y , were determined as a function of DO by a series of experiments at $P_{O_2} = \sim 10^{-5}$ – $\sim 10^{-4}$ atm. All experiments were conducted in a glove box where DO concentrations were controlled by introducing Ar gas and monitored by DO and $\text{O}_2(\text{gas})$ meters. Sugimori et al. (2011) have shown that when $[\text{Fe(II)}]$ is larger than the $[\text{O}_2]$ supplied to the system, Fe(II) oxidation does not follow the pseudo-first-order reaction, suggesting that the rate of DO consumption is faster than that of O_2 supply, and the actual DO concentration in the exact reaction area is lower than the supplied $[\text{O}_2]$. Although the stoichiometric Fe(II)/ O_2 ratio of 4:1 (Reactions (1)–(4)) means that $[\text{Fe(II)}]$ has to be lower than $4 \times [\text{O}_2]$ on the molar scale (King et al., 1995), whether the inflow rate of O_2 is stoichiometrically sufficient to fully oxidize Fe(II) depends on time required for Fe(II) to consume O_2 . Indeed, even when the monitored DO concentration is stoichiometrically insufficient, the reaction resulting in pseudo-first order is observed (Sugimori et al., 2011). Under low O_2 conditions, Fe(II) must be reacted in low concentration, and therefore, I adopted Fe(II)-luminol chemiluminescence (e.g., King et al. 1995), which can measure Fe(II) on the nanomolar level. This chapter aims (1) to determine the Fe(II) oxidation rates under low O_2 conditions and establish a new Fe(II) oxidation rate law over a wide range of P_{O_2} , (2) to suggest possible mechanisms of the oxidation, and (3) to consider the applicability of the rate law to the Precambrian paleosols.

2. Experimental methods

2.1. Reagents

All solutions were prepared using 18.2 MΩ Milli-Q water. Chemicals were all reagent-grade and used as received; tris(hydroxymethyl)aminomethane (Tris) ($C_4H_{11}NO_3$; purity >99.0%, Wako Pure Chemical Industries, Ltd., Japan), hydrochloric acid (HCl; assay 35–37%, Wako Pure Chemical Industries, Ltd., Japan), ferrous ammonium sulfate hexahydrate ($Fe(NH_4)_2(SO_4)_2 \cdot 6H_2O$; purity >99.5%, Wako Pure Chemical Industries, Ltd., Japan), oxalic acid dihydrate ($((COOH)_2 \cdot 2H_2O$; purity >99.5%, Wako Pure Chemical Industries, Ltd., Japan), citric acid monohydrate ($C_6H_8O_7 \cdot H_2O$; purity >99.5%, Wako Pure Chemical Industries, Ltd., Japan), potassium hydroxide (KOH; purity >85.0%, Wako Pure Chemical Industries, Ltd., Japan), luminol (5-amino-2,3-dihydro-1,4-phthalazinedione) ($C_8H_7N_3O_2$; purity >99.0%, Wako Pure Chemical Industries, Ltd., Japan), boric acid (H_3BO_3 ; purity >99.5%, Kanto Chemical Co., Inc.) and hydrogen peroxide (H_2O_2 ; assay 30.0–35.5%, Wako Pure Chemical Industries, Ltd., Japan). Ar gases used were >99.99% or >99.9999% purity (Suzuki Shokan Co., Ltd., Japan) depending on the concentrations of DO.

2.2. Fe(II) oxidation experiments

Fe(II) oxidation experiments at $\sim 10^{-5}$ – $\sim 10^{-4}$ atm of P_{O_2} were conducted in the glove box at room temperature (22 ± 1 °C). The detailed procedures to reach low P_{O_2} in the glove box are described by Sugimori et al. (2009). The Fe(II) oxidation proceeded in buffer solutions prepared with 0.04 M Tris and 0.04 M HCl in polypropylene containers, at pH 7.57–8.09 and ionic strength ~ 0.03 . The experimental conditions except for P_{O_2} were the same as those used by Sugimori et al. (2011) so that a comparison between the two studies can be performed. The Fe(II) stock solution (0.5–100 μ M), prepared by dissolving $Fe(NH_4SO_4)_2 \cdot 6H_2O$ in 2 mM HCl solution, was put into the glove box together with the buffer solutions. When P_{O_2} reached the expected value, the Fe(II) stock solution (~ 1 mL) was delivered to the buffer solution (100 mL) and the oxidation experiment was started. At appropriate intervals, ~ 3 mL of solution sample was removed for the Fe(II) concentration measurement and was transferred directly through a Teflon tube to the sample injector of the Fe(II) measurement apparatus, which enabled nearly in-situ measurements with the measurements of Fe(II) conducted without further oxidation of Fe(II) (see next section for the detail).

The initial Fe(II) concentrations with approximately one-order difference were used for the oxidation experiments at $\sim 10^{-5}$ and $\sim 10^{-4}$ atm of P_{O_2} to confirm little effect of the initial Fe(II) concentration on Fe(II) oxidation (Sugimori et al., 2011): 5.7×10^{-8} – 1.1×10^{-6} M at $\sim 10^{-4}$ atm and 5.8×10^{-9} – 4.0×10^{-8} M at $\sim 10^{-5}$ atm. Measurements of the

pH and DO/ P_{O_2} were conducted in the glove box. For the pH measurements, an F-21 pH meter (Horiba, Japan) was used; calibrations were performed on the free hydrogen scale at pH 6.86 (phosphate buffer) and pH 9.18 (borate buffer) at 22 °C. The error in the pH value was ± 0.02 . The pH variations throughout the oxidation experiments were within 0.02 of the initial pH values.

The oxygen concentrations in the solution and/or gas were measured by a DO meter (Toko Chemical Laboratories, DO Meter TOX-02H; detection limit, 5×10^{-6} atm of P_{O_2}) for the $\sim 10^{-4}$ atm experiments (runs of series 4 in Table 1) and by an O_2 (gas) meter (Toray Engineering Co., Ltd., zirconia oxygen analyzer LC-850KS; detection limit: 2×10^{-10} atm of P_{O_2}) for the $\sim 10^{-5}$ atm experiments (runs of series 5 in Table 1). The two O_2 meters showed consistent values within the experimental errors at $\sim 10^{-4}$ atm of P_{O_2} , but the DO meter did not show stable values at $\sim 10^{-5}$ atm. Ar gas was introduced to the solution in the glove box directly. The solution was bubbled with Ar gas throughout the experiment to ensure the equilibrium between the gaseous and dissolved aqueous phase oxygen and the O_2 concentration was monitored during the entire experiment. To reach the expected values of P_{O_2} , the gas flow rate was controlled at 50 mL/min – 2 L/min using > 99.99% purity Ar gas for the $\sim 10^{-4}$ atm experiments, and at 500 mL/min – 2 L/min using > 99.9999% purity Ar gas for the $\sim 10^{-5}$ atm experiments.

All experimental conditions are listed in Table 1. To distinguish one experimental run from another, run numbers are assigned according to the P_{O_2} levels (4 for $\sim 10^{-4}$ atm and 5 for $\sim 10^{-5}$ atm), the pH values (A for ~ 7.7 and S for ~ 8.0) and the initial concentrations of Fe(II) ($[Fe(II)]_0$) (L for $[Fe(II)]_0$ ~one order magnitude larger; see Section 3 for the explanation of the actual $[Fe(II)]_0$ values). For similar experimental conditions, a prime mark was added to one of the two corresponding runs.

2.3. Fe(II) analysis

The Fe(II) concentrations of the collected samples delivered from the glove box through a Teflon tube were measured by a flow-injection system (FIS) utilizing Fe(II)-luminol chemiluminescence (King et al., 1995). In the FIS, a carrier solution consisting of 6 mM oxalic acid and 3 mM citric acid was adjusted to pH 4.1 by adding potassium hydroxide solution (~ 2 M). The luminol solution was prepared by dissolving luminol in a 0.15 M boric acid solution and adjusting the pH to 11.0 with a potassium hydroxide solution. The luminol concentration was 0.1 mM for the measurements of the higher concentrations of Fe(II) (for the experiments at ~ 50 – 900 nM of $[Fe(II)]_0$) and

was 0.05 mM for the lower concentrations of Fe(II) (~5–50 nM of $[\text{Fe(II)}]_0$). The luminol concentrations were chosen based on the reported sensitivity increase (O’Sullivan et al., 1995). The hydrogen peroxide solution was prepared with 10 mM of H_2O_2 in 0.1 M Tris. The two solutions of luminol and hydrogen peroxide were pumped by a high performance liquid chromatography pump (JASCO PU-2080i) and were made to react with the sample that was carried in the carrier solution by a Shimadzu LC-10Ai. The mixed solution was measured by a luminescent detector (JASCO TM-2027). The relationships between the Fe(II)-induced chemiluminescence intensities and the Fe(II) concentrations (fitted by a quadratic curve ($R^2 > 0.999$)) were obtained from Fe(II) standard solutions. The standard solutions were prepared in the glove box under the same conditions as those for the Fe(II) oxidation experiments which were subsequently carried out. Therefore, the matrix effects of O_2 , Tris, HCl and pH on luminol chemiluminescence (Rose and Waite, 2001; Xiao et al., 2002) can be ignored. Due to the low O_2 conditions in the glove box, there was insignificant or no Fe(II) oxidation during sampling and measurement (Rose and Waite, 2001), which was confirmed by 2–3 times measurements of Fe(II) for the same samples and standards (done within 5 min for the whole procedure). The effect of Fe(III) on the luminosity was checked for different Fe(III) concentrations (20–70 nM) and found to be negligible compared to the effect of Fe(II) (data not shown). Therefore, all luminosity changes during the oxidation experiments were attributed to changes in the Fe(II) concentration. The quantitative detection limit of the Fe(II) concentration by this method is 0.9 nM. The low detection limit of $[\text{Fe(II)}]$ in FIS enables the Fe(II) oxidation experiments at P_{O_2} levels lower than the previous studies ($<10^{-3}$ atm, e.g., Liang et al., 1993; Sugimori et al., 2011) (Section 1).

3. Results

The rate law of Fe(II) oxidation (Eq. (6)) is simplified as

$$\frac{d[\text{Fe(II)}]}{dt} = -\lambda[\text{Fe(II)}] \quad (7)$$

where

$$\lambda = k[\text{O}_2]^x[\text{OH}^-]^y \quad (8)$$

Eq. (7) is then integrated to:

$$\ln \frac{[\text{Fe(II)}]}{[\text{Fe(II)}]_0} = -\lambda t \quad (9)$$

or

$$\ln[\text{Fe(II)}] = -\lambda t + \ln[\text{Fe(II)}]_0 \quad (10)$$

where $[\text{Fe(II)}]_0$ is the initial Fe(II) concentration (mol L^{-1}) and t is the elapsed time (min).

For an experiment at a given P_{O_2} , pH, $[\text{Fe(II)}]_0$, ionic strength, and temperature, the value of λ can be obtained as the slope of the line drawn by plotting $\ln\{[\text{Fe(II)}]/[\text{Fe(II)}]_0\}$ against time (Eq. (9)) or by plotting the $\ln[\text{Fe(II)}]$ -time variations (Eq. (10)). The addition of the Fe(II) stock solution to the buffer solution was the start of an oxidation experiment in the glove box. It took at most a few days before the addition because of the difficulty to reach the expected P_{O_2} values. This delay must have decreased the accuracy in calculating $[\text{Fe(II)}]_0$ from the concentration of Fe(II) in the stock solution. To evaluate the $[\text{Fe(II)}]_0$ values accurately, the $[\text{Fe(II)}]_0$ values were obtained from the intercepts of regression lines at the $\ln[\text{Fe(II)}]$ axis (Fig. 1) according to Eq. (10). Thus, all $[\text{Fe(II)}]_0$ values listed in Table 1 were those obtained in the above way and not the as-prepared concentrations. The Fe(II) oxidation profiles at $P_{\text{O}_2} = \sim 10^{-5}$ to $\sim 10^{-4}$ atm are given in Fig. 1. Fitted to the linear regression, the λ values were determined (Table 1), and the correlation coefficients (R^2) were 0.97 for run number 5SL, 0.98 for series 4, 5AL' and 5S', and 0.99 for 5AL and 5S. Therefore, the Fe(II) oxidation rate law adheres to pseudo-first order down to 10^{-5} atm of P_{O_2} .

I here define k_{app} as $\lambda = k_{\text{app}}[\text{O}_2][\text{OH}^-]^2$. Then, k_{app} is equal to the rate constant of the classic rate law (Eq. (5)). If the Fe(II) oxidation adhered to the classic rate law even under low O_2 conditions, the values of k_{app} calculated from the λ values would be constant. However, Table 1 reveals that the values of k_{app} change significantly and are smaller at $\sim 10^{-4}$ atm of P_{O_2} (run numbers of series 4 in Table 1) than at $\sim 10^{-5}$ atm of P_{O_2} (series 5). The faster Fe(II) oxidation rate under low O_2 conditions than expected from the classic rate law is also known from the half-life time of Fe(II) ($\equiv (\ln 2)/\lambda$). The half-life times are ~ 270 and ~ 1000 minutes at pH 8.04 (4S) and 7.74 (4A), respectively, at $P_{\text{O}_2} = \sim 7 \times 10^{-5}$ atm, and ~ 700 and ~ 4500 minutes at pH 8.09 (5SL) and 7.57 (5AL), respectively, at $P_{\text{O}_2} = \sim 10^{-5}$ atm. However, the half-life times calculated from the rate law of Stumm and Lee (1961) (Eq. (5); $k = 1.5 \times 10^{13} \text{ mol}^{-2} \text{ L}^2 \text{ atm}^{-1} \text{ min}^{-1}$) are ~ 570 (corresponding to run number 4S), ~ 2160 (4A), ~ 3000 (5SL) and ~ 30000 (5AL) minutes. The examinations of half-life time and k_{app} reveal that the Fe(II) oxidation rate cannot be expressed by the classic rate law (Eq. (5)) under low O_2 conditions. In addition, the lower the O_2 concentration becomes, the faster the Fe(II) oxidation rate is compared to the expected rate from the classic rate law.

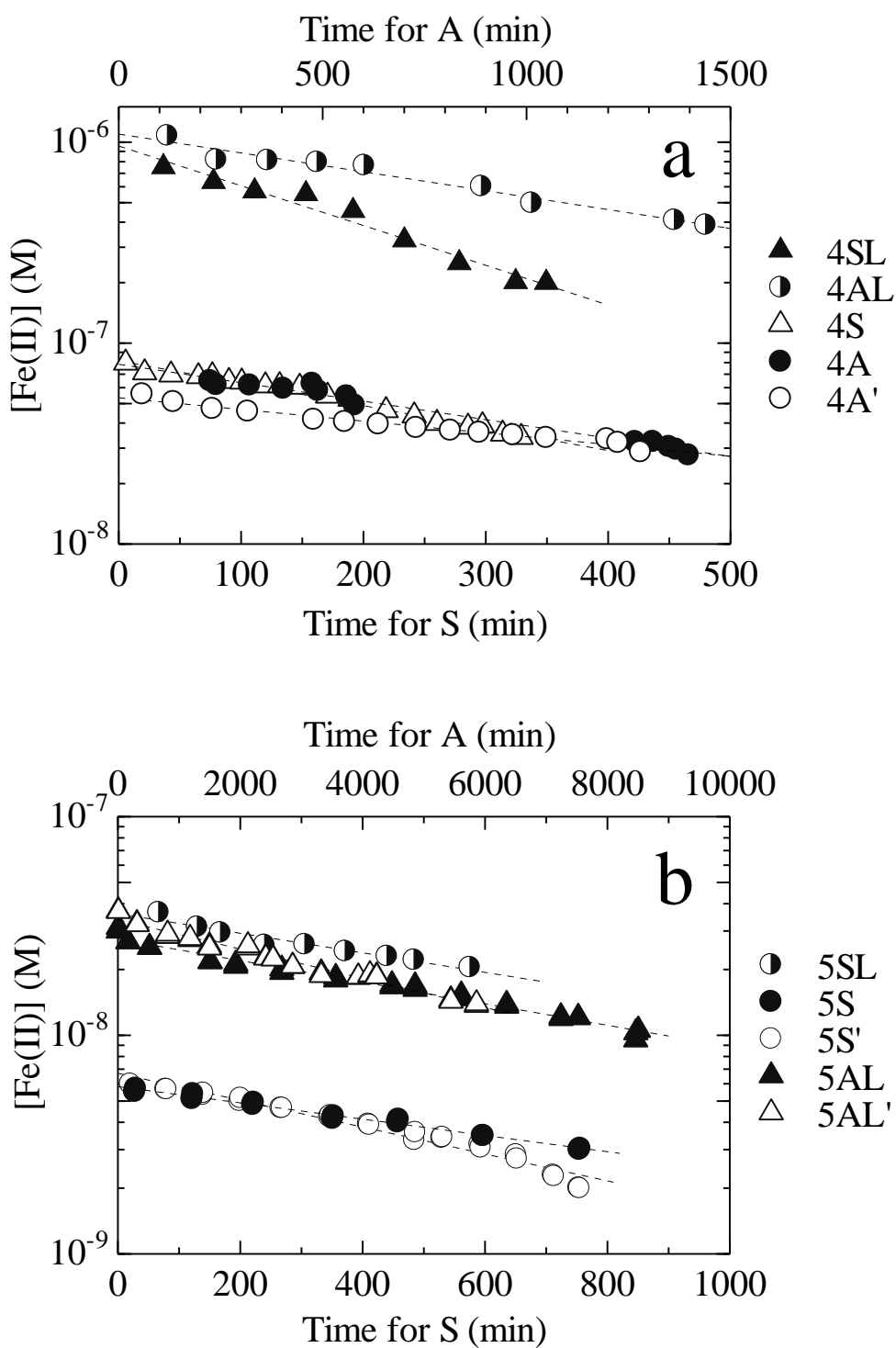


Figure 1. Logarithmic plot of [Fe(II)] (M) against time (minutes) at (a) $\sim 10^{-4}$ and (b) $\sim 10^{-5}$ atm of P_{O_2} . Dashed lines represent the linear regression of the experimental data. Note the different horizontal axes between the A and S series.

Table 1. Summary of the experimental conditions.

Run number	P_{O_2} ^a [atm]	$[O_2]$ ^b [M]	pH	$[Fe(II)]_0$ [ppb]	$[Fe(II)]_0$ [M]	Ionic strength [M]	$\log \lambda$ ^c [min ⁻¹]	$\log k_{app}$ ^d [M ⁻³ min ⁻¹]	$\log k''$ ^e [M ⁻¹ min ⁻¹]	$\log k'$ ^f [M ⁻² min ⁻¹]
4AL	1.2 (0.8) ^g ×10 ⁻⁴	1.6 (1.1)×10 ⁻⁷	7.70 (0.02)	61.0 (4.9)	1.1 (0.09)×10 ⁻⁶	0.033 (0.001)	-3.15 (0.06)	16.91 (0.35)	3.69 (0.35)	9.44 (0.07)
4SL	2.1 (0.6)×10 ⁻⁴	2.8 (0.8)×10 ⁻⁷	8.05 (0.02)	53.4 (7.1)	9.6 (1.3)×10 ⁻⁷	0.028 (0.001)	-2.34 (0.06)	16.69 (0.14)	4.21 (0.13)	9.54 (0.07)
4A	7.1 (1.4)×10 ⁻⁵	9.1 (2.0)×10 ⁻⁸	7.74 (0.02)	4.38 (0.25)	7.89 (0.44)×10 ⁻⁸	0.035 (0.001)	-3.15 (0.04)	17.01 (0.11)	3.87 (0.10)	9.27 (0.06)
4A'	6.8 (3.3)×10 ⁻⁵	9.5 (4.5)×10 ⁻⁸	7.71 (0.02)	3.17 (0.12)	5.71 (0.21)×10 ⁻⁸	0.035 (0.001)	-3.30 (0.04)	16.94 (0.22)	3.74 (0.22)	9.37 (0.06)
4S	6.7 (2.0)×10 ⁻⁵	9.0 (2.7)×10 ⁻⁸	8.04 (0.02)	4.56 (0.17)	8.21 (0.30)×10 ⁻⁸	0.031 (0.001)	-2.59 (0.04)	16.96 (0.14)	4.45 (0.14)	9.32 (0.06)
5AL	1.1 (0.2)×10 ⁻⁵	1.5 (0.2)×10 ⁻⁸	7.57 (0.02)	1.42 (0.07)	2.56 (0.1)×10 ⁻⁸	0.035 (0.001)	-3.81 (0.04)	17.30 (0.07)	3.81 (0.06)	8.82 (0.06)
5AL'	2.7 (0.5)×10 ⁻⁵	3.6 (0.6)×10 ⁻⁸	7.58 (0.02)	1.88 (0.06)	3.39 (0.14)×10 ⁻⁸	0.035 (0.001)	-3.81 (0.03)	17.11 (0.09)	3.63 (0.08)	9.02 (0.05)
5SL	1.0 (0.2)×10 ⁻⁵	1.4 (0.2)×10 ⁻⁸	8.09 (0.02)	2.22 (0.14)	4.00 (0.25)×10 ⁻⁸	0.029 (0.001)	-2.99 (0.09)	17.24 (0.11)	4.83 (0.11)	8.84 (0.10)
5S	1.1 (0.2)×10 ⁻⁵	1.5 (0.2)×10 ⁻⁸	8.01 (0.02)	0.32 (0.02)	5.8 (0.2)×10 ⁻⁹	0.029 (0.001)	-3.07 (0.04)	17.29 (0.08)	4.78 (0.07)	8.90 (0.06)
5S'	1.1 (0.1)×10 ⁻⁵	1.5 (0.1)×10 ⁻⁸	8.04 (0.02)	0.37 (0.01)	6.7 (0.1)×10 ⁻⁹	0.029 (0.001)	-2.91 (0.03)	17.41 (0.06)	4.91 (0.04)	8.99 (0.05)

^aConversion of $[O_2]$ according to Henry's law at 22 °C for 4 series.

^bConversion of P_{O_2} according to Henry's law at 22 °C for 5 series.

^c λ was obtained from the data in Fig.1 assuming pseudo-first-order regression.

^d k_{app} was obtained from λ , $[O_2]$ and $[OH^-]$ in the table according to $\lambda = k_{app}[O_2][OH^-]^2$.

^e k'' was obtained from λ and $[O_2]$ in the table according to $\lambda = k''[O_2]$.

^f k' was obtained from λ and $[OH^-]$ in the table according to $\lambda = k'[OH^-]^2$.

^gFigure in parentheses denotes standard deviation, σ , or 2σ .

4. Discussion

4.1. pH dependence of oxidation rate

The effects of pH on Fe(II) oxidation are assessed by scrutinizing y behavior in Eq. (6) under various experimental conditions. Each set of experimental conditions such as P_{O_2} and pH yields an individual λ value, and y at a given P_{O_2} can be obtained if the parameter $[O_2]$ can be excluded from Eq. (6) by introducing the rate constant, k'' :

$$\frac{d[\text{Fe(II)}]}{dt} = -k''[\text{Fe(II)}][O_2] \quad (11)$$

$$\text{where } k'' = \frac{\lambda}{[O_2]} = k[\text{OH}^-]^y \quad (12)$$

Note that k'' includes a shift from the oxidation rate assuming $x = 1$ (larger k'' value at smaller P_{O_2} for a given pH in Fig. 2). Eq. (12) is rewritten as

$$\log k'' = \log k + y \log[\text{OH}^-] \quad (13)$$

The k'' values can be calculated from the λ and $[O_2]$ values (Eq. (12)), and are listed in Table 1. By plotting the k'' values against $[\text{OH}^-]$ in the logarithmic scale, y can be estimated from the slopes (Fig. 2). The y values were 1.90 (± 0.32) and 2.00 (± 0.23) at $P_{O_2} = \sim 10^{-4}$ and $\sim 10^{-5}$ atm, respectively (solid lines in Fig. 2). Sugimori et al. (2011) showed that $y = 2.08$ (± 0.07) and 2.00 (± 0.06) at $\sim 10^{-2}$ and $\sim 10^{-3}$ atm of P_{O_2} , respectively (dashed lines in Fig. 2). The slightly larger y value at 0.2 atm of P_{O_2} (dotted line in Fig. 2, Sugimori et al., 2011) is ascribed to the back reaction of Fe(III) by superoxide, O_2^- , at lower pH (Rose and Waite, 2002; Santana-Casiano et al., 2005; Sugimori et al., 2011). However, the effect of the back reaction of Fe(III) is not observed at pH 6.89 at both $\sim 10^{-2}$ and $\sim 10^{-3}$ atm of P_{O_2} , which indicates that the rates of Fe(III) hydrolysis and precipitation are sufficiently faster than the oxidation rate and Fe(III) cannot compete with Fe(II) for O_2^- (Reaction (2)) because of the slower Fe(II) oxidation rates under lower O_2 conditions. This is the same for the oxidation rates at $\sim 10^{-4}$ and $\sim 10^{-5}$ atm of P_{O_2} . Consequently, the y values (1.90 and 2.00) at $\sim 10^{-4}$ and $\sim 10^{-5}$ atm of P_{O_2} are almost certain although the data points are located at almost two pH values for each P_{O_2} condition (Fig. 2). Therefore, over a wide range of P_{O_2} , 10^{-5} – 10^{-2} atm, y can be equal to 2.

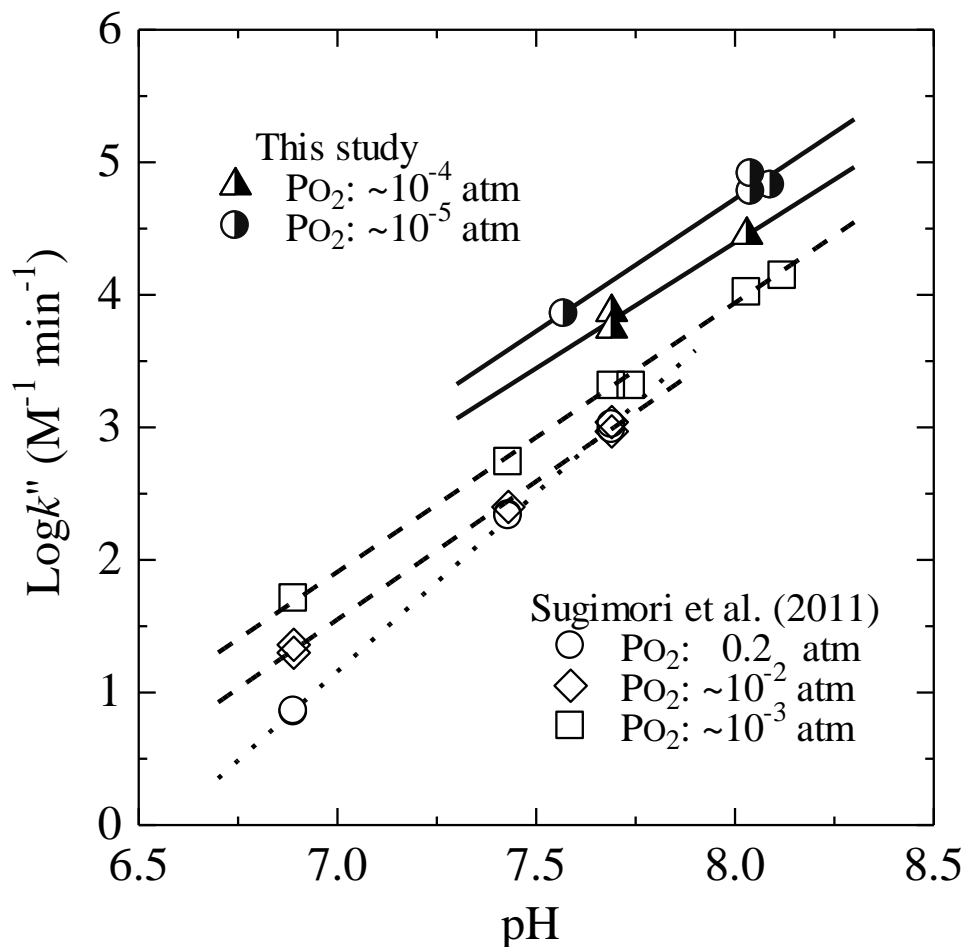


Figure 2. Plot of $\log k''$ against pH. Half-filled triangles and circles are the data points at $\sim 10^{-4}$ (run numbers 4A, 4A' and 4S) and $\sim 10^{-5}$ (5AL, 5SL, 5S and 5S') atm of P_{O_2} , respectively. Experimental runs with similar P_{O_2} values were chosen for each set (Table 1) because a minor change in $[\text{O}_2]$ has an effect on the k'' value and thus the y estimation (Eq. (12)). Solid lines correspond to linear regression of the experimental data at $\sim 10^{-4}$ and $\sim 10^{-5}$ atm of P_{O_2} . The slopes of the regression lines, i.e., the y values, are 1.90 and 2.00 at $\sim 10^{-4}$ and $\sim 10^{-5}$ atm of P_{O_2} , respectively. Also shown are the experimental results of Sugimori et al. (2011): open circles, diamonds and squares represent the data points at 0.2, $\sim 10^{-2}$ and $\sim 10^{-3}$ atm of P_{O_2} , respectively, and dashed lines correspond to the linear regression of the experimental data at $\sim 10^{-2}$ and $\sim 10^{-3}$ atm of P_{O_2} , which show values of 2.08 and 2.00 for y , respectively. The regression shown by dotted line indicates that $y = 2.69$ at $P_{\text{O}_2} = 0.2$ atm.

4.2. P_{O_2} dependence of oxidation rate

Similarly to the previous section, the effects of P_{O_2} on Fe(II) oxidation are examined from Eq. (6); x at a given pH can be obtained if the parameter $[OH^-]$ can be excluded from Eq. (6). Using the y value of 2 and the rate constant, k' , Eq. (6) can be rewritten as

$$\frac{d[Fe(II)]}{dt} = -k'[Fe(II)][OH^-]^2 \quad (14)$$

$$\text{where } k' = \frac{\lambda}{[OH^-]^2} = k[O_2]^x \quad (15)$$

$$\text{or } \log k' = \log k + x \log [O_2] \quad (16)$$

The k' values can be calculated from the λ and pH (or $[OH^-]$) values (Eq. (15)) and are listed in Table 1. By plotting the k' values against $[O_2]$ on a logarithmic scale (or $\log P_{O_2}$), the x values are estimated from the slopes (Fig. 3). The $\log k'$ values at $0.2 \sim 10^{-3}$ atm of P_{O_2} (Sugimori et al., 2011) are also plotted in Fig. 3 where I can observe the k' values against P_{O_2} to comprehensively understand the oxidation rate dependence on P_{O_2} over a wide range of P_{O_2} . Fig. 3 reveals unambiguously that both x and k (Eqs. (6) and (16)) change, depending on the range of P_{O_2} : $x = 0.98 (\pm 0.04)$ and $\log k = 15.46 (\pm 0.06)$ (defined as $\log k_{\text{high}}$) at $\sim 6 \times 10^{-3} \sim 0.2$ atm of P_{O_2} (dotted line in Fig. 3) and $x = 0.58 (\pm 0.02)$ and $\log k = 13.41 (\pm 0.03)$ (defined as $\log k_{\text{low}}$) at $10^{-5} \sim 6 \times 10^{-3}$ atm of P_{O_2} (dashed line in Fig. 3). The threshold value of P_{O_2} , 6×10^{-3} atm ($8 \mu\text{M}$ of $[O_2]$), is calculated at the point where $k_{\text{high}}[O_2]^{0.98} = k_{\text{low}}[O_2]^{0.58}$ (the point of intersection of the dotted and dashed lines in Fig. 3), and the threshold value has a range of $1.6 \times 10^{-3} \sim 1.3 \times 10^{-2}$ atm of P_{O_2} ($2 \sim 17 \mu\text{M}$ of $[O_2]$), resulting from the errors in x and k . The value of x remains ~ 1 down to $\sim 6 \times 10^{-3}$ atm of P_{O_2} , which validates the results of previous studies conducted at $> \sim 6 \times 10^{-3}$ atm of P_{O_2} assuming $x = 1$ (e.g., González-Dávila et al., 2006; Trapp and Millero, 2007). On the other hand, Liang et al. (1993) and Sugimori et al. (2011) have pointed out that the Fe(II) oxidation rate deviates from the linear dependence on P_{O_2} at $1 \times 10^{-3} \sim 5 \times 10^{-3}$ atm of P_{O_2} although the deviations suggested by the two studies are opposite to one another, slower and faster than those expected from the classic rate law (Eq. (5)). The x value of 0.58 at $< \sim 6 \times 10^{-3}$ atm of P_{O_2} clearly indicates that the oxidation rate dependence on P_{O_2} changes under low O_2 conditions, and the rates are faster than those expected from the classic rate law. This change of x as well as that of k strongly suggest that the oxidation mechanisms change at $< \sim 6 \times 10^{-3}$ atm of P_{O_2} from those at higher P_{O_2} levels. Furthermore, little deviation of the data

points from the two regression lines in Fig. 3 confirms that the initial Fe(II) concentration has little effect on Fe(II) oxidation over a wide range of P_{O_2} .

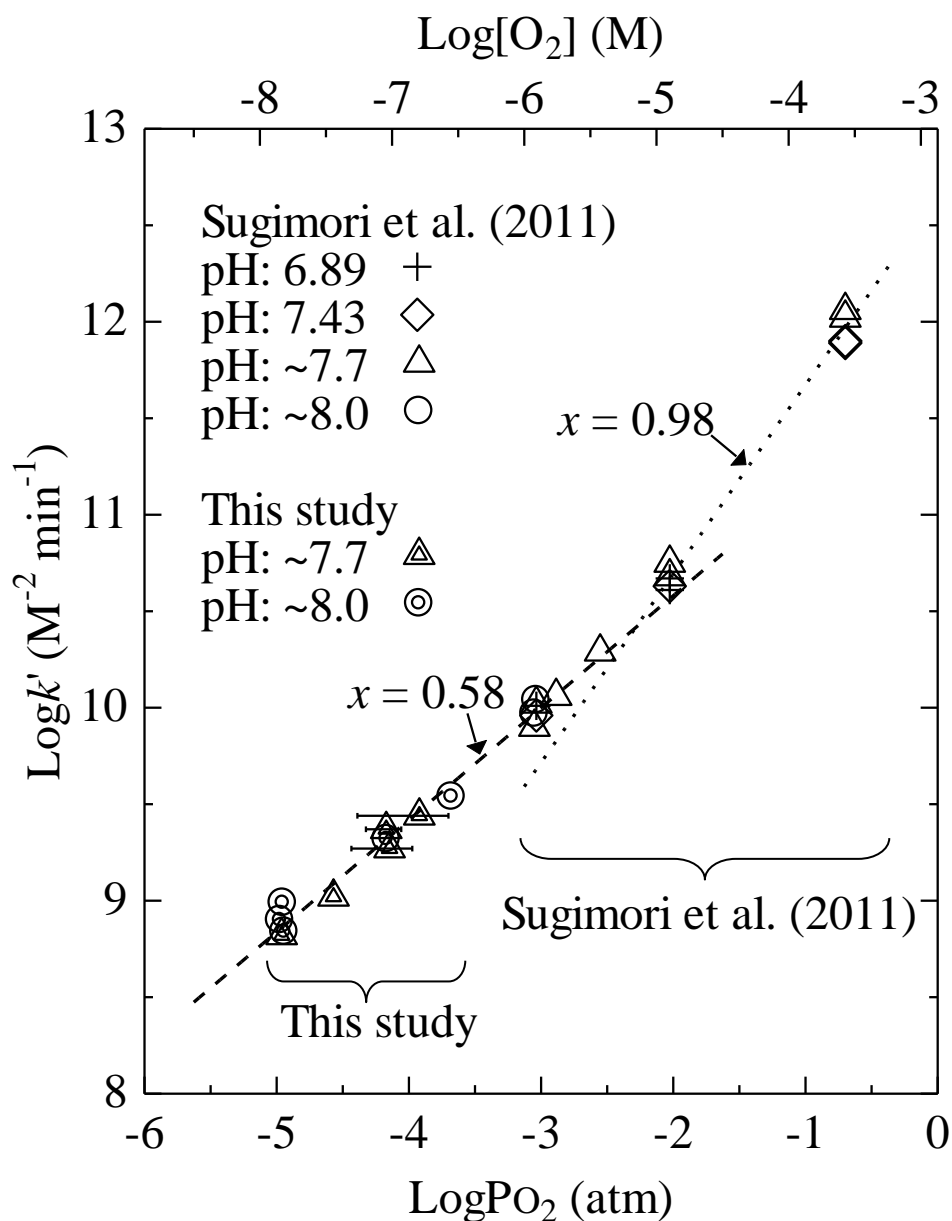


Figure 3. Plot of $\log k'$ against $\log P_{O_2}$ and $\log [O_2]$. Overwritten symbols at $\sim 10^{-5}$ – $\sim 10^{-4}$ atm of P_{O_2} , this study; open symbols at $\sim 10^{-3}$ – 0.2 atm of P_{O_2} , Sugimori et al. (2011). Lines are fitted functions of $k' = k[O_2]^x$; dotted line at $\sim 10^{-2}$ – 0.2 atm of P_{O_2} ($\log k = 15.46$ and $x = 0.98$ ($R^2 = 0.991$)) and dashed line at $10^{-5} \leq P_{O_2} < 10^{-2}$ atm ($\log k = 13.41$ and $x = 0.58$ ($R^2 = 0.988$)). When error bars are not shown in the figure, they are less than the size of the symbols.

4.3. Possible mechanisms of Fe(II) oxidation under low O₂ conditions

As mentioned above, the Fe(II) oxidation rate law can be expressed by

$$\frac{d[\text{Fe(II)}]}{dt} = -k_{\text{high}}[\text{Fe(II)}][\text{O}_2]^{0.98}[\text{OH}^-]^2 \quad (\sim 6 \times 10^{-3} < P_{\text{O}_2} < 0.2 \text{ atm}) \quad (17)$$

and

$$\frac{d[\text{Fe(II)}]}{dt} = -k_{\text{low}}[\text{Fe(II)}][\text{O}_2]^{0.58}[\text{OH}^-]^2 \quad (10^{-5} < P_{\text{O}_2} < \sim 6 \times 10^{-3} \text{ atm}) \quad (18)$$

When P_{O_2} is relatively high ($\sim 6 \times 10^{-3} < P_{\text{O}_2} < 0.2 \text{ atm}$), the rate law is essentially the same as the classic rate law (Eq. (5)). The mechanisms that formulate the classic rate law have been investigated by Millero and coworkers; when O₂ is the dominant oxidant of Fe(II), $x = 1$ can be assumed (Millero, 1985; Millero et al., 1987). The y variation with pH is explained by the dominant Fe(II) species that are determined by the reactivity and amounts of Fe(II) species (Millero, 1985; Millero et al., 1987; King, 1998; Santana-Casiano et al., 2005; Trapp and Millero, 2007).

The value of x , 0.58, indicates less involvement of O₂ in the dominant oxidation reaction(s) at $< \sim 6 \times 10^{-3} \text{ atm}$ of P_{O_2} than at higher P_{O_2} : the contribution of O₂ to the overall oxidation rate is approximately 0.3, 0.2 and 0.07 at 10^{-3} , 10^{-4} and 10^{-5} atm of P_{O_2} , respectively (from the log k' values for the lines of $x = 0.98$ and 0.58 in Fig. 3). In addition to an x of 0.58, the mechanisms of Fe(II) oxidation under low O₂ conditions must be consistent with a y of 2 and the first order with respect to Fe(II) (Eq. (18)). Furthermore, the mechanisms must explain the faster Fe(II) oxidation rate than that predicted by the classic rate law (Fig. 3).

For possible mechanisms, I first consider Fe(II) oxidation by additional O₂ species. To meet the above constraints, additional electron acceptors produced by O₂ should be present. These additional electron acceptors can be O₂ species, such as O₂⁻, H₂O₂ and OH^{*}, because of their reactivity with Fe(II) and strong relation to iron redox cycles (e.g., Burns et al., 2011a). Note that the O₂ species formed by Fe(II) oxidation with O₂ (Reactions (1)–(4)) are not the “additional” electron acceptors; they do not cause any deviation of x predicted by the classic rate law. The possible reductants of O₂ to yield the additional O₂ species are confined to H₂O, Tris and Cl⁻ in my experimental solutions, but none of them are as easily oxidized by O₂ as Fe(II). Therefore Fe ions including Fe(IV) should serve as catalysts in these O₂ reduction processes (Koppenol and Liebman, 1984; Miller et al., 1990; Schaich, 1992; Ensing et al., 2003; Koppenol et al., 2010). Because I here consider only O₂ species as the possible oxidants of Fe(II), the

reductant of O₂ is H₂O (see below for cases where the reductants of O₂ are Tris and Cl⁻).



Reactions (19)–(21) are in a pseudo-steady state where the reactions are apparently in a steady state but only transiently (during Fe(II) oxidation). I use the prefix “pseudo” because I cannot yet formulate Reactions (19)–(21) from elementary reactions in the way King et al. (1995) have done (Appendix A). The pseudo-steady-state constants may differ from the corresponding thermodynamic equilibrium constants, and their pH-dependences are not necessarily the same as those expected from the above reaction formulas. Once Reactions (19)–(21) are in pseudo-steady state,

$$[\text{H}_2\text{O}_2] = \alpha[\text{O}_2]^{0.5}[\text{OH}^-] \quad (22)$$

$$[\text{O}_2^{\bullet-}] = \alpha'[\text{O}_2]^{0.75}[\text{OH}^-]^2 \quad (23)$$

$$[\text{OH}^\bullet] = \alpha''[\text{O}_2]^{0.25}[\text{OH}^-]^2 \quad (24)$$

where α , α' and α'' are the pseudo-steady-state constants of Reactions (19)–(21), respectively, and the pH dependences are assumed so that $y = 2$ can be explained (see below). The assumed pH dependences are, indeed, not inconsistent with those calculated for steady-state O₂ species by King et al. (1995) (Appendix A).

Including Fe(II) oxidation by these additionally produced O₂ species, the total Fe(II) oxidation rate is expressed as

$$\begin{aligned} & \frac{d[\text{Fe(II)}]}{dt} \\ &= -4k_1[\text{Fe(II)}][\text{O}_2] - k_2[\text{Fe(II)}][\text{O}_2^{\bullet-}] - 2k_3[\text{Fe(II)}][\text{H}_2\text{O}_2] - k_4[\text{Fe(II)}][\text{OH}^\bullet] \\ &= -4k_1'[\text{Fe(II)}][\text{O}_2][\text{OH}^-]^2 - k_2[\text{Fe(II)}][\text{O}_2^{\bullet-}] \\ & \quad - 2k_3'[\text{Fe(II)}][\text{H}_2\text{O}_2][\text{OH}^-] - k_4[\text{Fe(II)}][\text{OH}^\bullet] \quad (25) \end{aligned}$$

where k_1 , k_2 , k_3 and k_4 are the rate constants of Reactions (1)–(4), respectively, and k_1' and k_3' are the rate constants modified from k_1 and k_3 , respectively, considering [OH⁻] dependence (Millero et al., 1987; Millero and Sotolongo, 1989). The stoichiometric

numbers of Fe(II)/O₂ and Fe(II)/H₂O₂ are 4 and 2, respectively, from Reactions (1)–(4). Fe(II) oxidation by O₂⁻ and OH^{*} (Reactions (2) and (4), respectively) is pH independent over the pH range examined in the present study (Rush and Bielski, 1985; Stuglik and Zagórski, 1981). Substituting Eqs. (22)–(24) for Eq. (25), I obtain

$$\begin{aligned} \frac{d[\text{Fe(II)}]}{dt} &= -4k_1'[\text{Fe(II)}][\text{O}_2][\text{OH}^-]^2 - \alpha'k_2[\text{Fe(II)}][\text{O}_2]^{0.75}[\text{OH}^-]^2 \\ &\quad - 2\alpha k_3'[\text{Fe(II)}][\text{O}_2]^{0.5}[\text{OH}^-]^2 - \alpha''k_4[\text{Fe(II)}][\text{O}_2]^{0.25}[\text{OH}^-]^2 \\ &= -[\text{Fe(II)}][\text{OH}^-]^2(4k_1'[\text{O}_2] + \alpha'k_2[\text{O}_2]^{0.75} \\ &\quad + 2\alpha k_3'[\text{O}_2]^{0.5} + \alpha''k_4[\text{O}_2]^{0.25}) \end{aligned} \quad (26)$$

Eq. (26) satisfies $y = 2$, and can be expressed as a function of $[\text{O}_2]^{0.58}$ by linear combination of $[\text{O}_2]^x$ where $x = 1, 0.75, 0.5$ and 0.25 in the parentheses (Appendix B). As mentioned earlier, the contribution of $[\text{O}_2]^1$ to the total Fe(II) oxidation is low. The x value of 0.58 suggests that H₂O₂ ($x = 0.5$, Eq. (22)) is the dominant oxidant under low O₂ conditions as discussed below. The slight deviation of $x (= 0.58)$ from 0.5 can be explained by a slight contribution of O₂⁻ ($x = 0.75$, Eq. (23)). OH^{*} ($x = 0.25$, Eq. (24)) is scavenged by Tris and Cl⁻ in my experimental conditions (Appendix A). Fe(II) can be oxidized indirectly by intermediates produced from the reactions of Tris and Cl⁻ with OH^{*} (Folkes et al., 1995; King et al., 1995; Truong et al., 2004; Deborde and von Gunten, 2008), and the OH^{*} scavenged by Tris and Cl⁻ hardly oxidizes Fe(II) directly. Then, the stoichiometric numbers of Fe(II)/O₂ and Fe(II)/H₂O₂ remain 4 and 2, respectively (Reactions (1)–(4)).

The effects of Fe(II)-Tris complexes on the Fe(II) oxidation were also examined. Because the formation constants of the Fe(II)-Tris complexes have not been reported, I utilized those of Ni(II)- and Cu(II)-Tris complexes (Bologni et al., 1983), assuming that Fe(II) can form Tris complexes less easily than Ni(II) and Cu(II) (Stumm and Morgan, 1996). In the case where Fe(II)-Tris complexes behave like Ni(II)-Tris complexes, none of the Fe(II)-Tris complexes (using the data for Ni(II)) can explain 2 for the y value observed in the present study. In the case where Fe(II)-Tris complexes behave like Cu(II)-Tris complexes, some of the Fe(II)-Tris complexes (using the data for Cu(II)) can explain 2 for the y value. However, the concentrations of those Fe(II)-Tris complexes were calculated to be very low. Consequently, the rate constants of the reactions of the complexes with O₂ and H₂O₂ must be larger than that for the diffusion control reaction (e.g., Pham and Waite, 2008), if the complexes should explain the

observed Fe(II) oxidation rates. Therefore, it is very unlikely that Fe(II)-Tris complexes are significant for the rate-determining reaction under both high and low O₂ conditions. It has been also reported that Fe(II)-Tris complexes are relatively inert with respect to oxidation by O₂ (Millero et al., 1987; Yang and Chasteen, 1999), consistent with the above discussion. Fe(II)-carbonate complexes are very small in concentration because the P_{CO₂} level is very low in the glove box ($\leq 10^{-5}$ atm). Therefore, their contributions to the total Fe(II) oxidation rate are also insignificant (kinetic data given by King (1998) and King and Farlow (2000)). In addition, the FeCl⁺ and FeSO₄⁰ species are reported to be non-reactive (e.g., Millero et al., 1987; Santana-Casiano et al., 2005).

Comparison of the semi-theoretical rate law (Eq. (26)) with the empirical rate law (Eq. (18)) gives me the pseudo-steady-state constants in Eqs. (22) and (23) (Appendix B), and I can then calculate the concentrations of H₂O₂ and O₂⁻ as a function of P_{O₂}. The concentration of H₂O₂ calculated from Eq. (22) with the pseudo-steady-state constant, α (Appendix B), at pH 8 and 0.2 atm of P_{O₂} is in good agreement with those calculated and measured by King et al. (1995) at the same pH and P_{O₂} (Fig. B1 in Appendix B), supporting the validity of the present model.

The contributions of O₂, H₂O₂ and O₂⁻, to the total Fe(II) oxidation can be calculated based on the present model over a wide range of P_{O₂} (10⁻⁵-0.2 atm). Excluding the contribution of OH^{*} from Eq. (26), the semi-theoretical rate law of Fe(II) oxidation is rewritten as

$$\frac{d[\text{Fe(II)}]}{dt} = -4k_1'[\text{Fe(II)}][\text{O}_2][\text{OH}^-]^2 - \alpha'k_2[\text{Fe(II)}][\text{O}_2]^{0.75}[\text{OH}^-]^2 - 2\alpha k_3'[\text{Fe(II)}][\text{O}_2]^{0.5}[\text{OH}^-]^2 \quad (27)$$

The corresponding empirical rate law is obtained from Eqs. (17) and (18):

$$\frac{d[\text{Fe(II)}]}{dt} = -k_{\text{high}}[\text{Fe(II)}][\text{O}_2]^{0.98}[\text{OH}^-]^2 - k_{\text{low}}[\text{Fe(II)}][\text{O}_2]^{0.58}[\text{OH}^-]^2 \quad (28)$$

I can calculate a ratio, R_{wide} , of the Fe(II) oxidation rates between the semi-theoretical and empirical laws (Eqs. (27) and (28), respectively) over a wide range of P_{O₂}:

$$\begin{aligned} R_{\text{wide}} &= \frac{-4k_1'[\text{Fe(II)}][\text{O}_2][\text{OH}^-]^2 - \alpha'k_2[\text{Fe(II)}][\text{O}_2]^{0.75}[\text{OH}^-]^2 - 2\alpha k_3'[\text{Fe(II)}][\text{O}_2]^{0.5}[\text{OH}^-]^2}{-k_{\text{high}}[\text{Fe(II)}][\text{O}_2]^{0.98}[\text{OH}^-]^2 - k_{\text{low}}[\text{Fe(II)}][\text{O}_2]^{0.58}[\text{OH}^-]^2} \\ &= \frac{4k_1'[\text{O}_2] + \alpha'k_2[\text{O}_2]^{0.75} + 2\alpha k_3'[\text{O}_2]^{0.5}}{k_{\text{high}}[\text{O}_2]^{0.98} + k_{\text{low}}[\text{O}_2]^{0.58}} \quad (29) \end{aligned}$$

From Eq. (29), I can derive the fractional contributions of O_2 , O_2^- and H_2O_2 (X_{O_2} , $X_{O_2^-}$ and $X_{H_2O_2}$, respectively) to the Fe(II) oxidation rate over a wide range of P_{O_2} :

$$X_{O_2} = \frac{4k_1'[O_2]}{k_{high}[O_2]^{0.98} + k_{low}[O_2]^{0.58}} \quad (30)$$

$$X_{O_2^-} = \frac{\alpha k_2[O_2]^{0.75}}{k_{high}[O_2]^{0.98} + k_{low}[O_2]^{0.58}} \quad (31)$$

$$X_{H_2O_2} = \frac{2\alpha k_3'[O_2]^{0.5}}{k_{high}[O_2]^{0.98} + k_{low}[O_2]^{0.58}} \quad (32)$$

where $k_1' = k_{high}/4$ and k_{high} , k_{low} , α and α' are 15.46, 13.41, 1.82 and 5.33, respectively, in log units (see Appendix B). The R_{wide} value and fractional contributions of O_2 , H_2O_2 and O_2^- are plotted against $\log [O_2]$ and $\log P_{O_2}$ in Fig. 4. The R_{wide} values (0.94–1.02) of approximately 1 and the change of the dominant oxidant from O_2 to H_2O_2 at $\sim 2 \times 10^{-3}$ atm of P_{O_2} are consistent with the mechanism under low O_2 conditions as discussed above. Further studies are required to confirm the Fe(II) oxidation mechanism at low P_{O_2} shown above including experiments to measure the H_2O_2 concentrations at low P_{O_2} .

The other possible mechanisms that can explain the rate law (Eq. (18)) are chain reaction and heterogeneously catalyzed reaction, which are described briefly below. The chain reaction must be initiated by the reaction of O_2 with reductants other than Fe(II) (H_2O , Tris and Cl^- in the present experiments), and Fe(II) must be oxidized in the propagation steps (e.g., Laidler, 1987). Because it is difficult for the initiation reaction to proceed, Fe catalysis may be required for the initiation step (Koppenol and Liebman, 1984; Miller et al., 1990; Schaich, 1992; Ensing et al., 2003; Koppenol et al., 2010). The chain reaction makes the Fe(II) oxidation rate proportional to $[O_2]^{0.5}$, $[Fe(II)]$ and $[OH^-]^2$ (equations not shown), which explains Eq. (18) at low P_{O_2} . On the other hand, the stoichiometric ratio of $[Fe(II)]/[O_2]$ deviates from 4 for the chain reaction. When $[O_2]$ is stoichiometrically insufficient with respect to $[Fe(II)]$, Fe(II) oxidation becomes significantly slower (Sugimori et al., 2011), which is not observed in the present study even for different initial Fe(II) concentrations (Fig. 1). Accordingly, the Fe(II) oxidation mechanism by the chain reaction at low P_{O_2} is less likely than that by water oxidation described above.

For the heterogeneously catalyzed reaction, I consider O_2 adsorbed on material surfaces (e.g., on ferric hydroxides or container of experimental solution in the present study), described by a Freundlich isotherm (e.g., Williamson and Rimstidt, 1994). The rate law of pyrite oxidation by O_2 is reported to be a fractional order with respect to O_2

(rate $\propto \sim [\text{O}_2]^{0.5}$ at 6×10^{-4} – 21 atm of P_{O_2} , e.g., Williamson and Rimstidt, 1994; Holmes and Crundwell, 2000; Rimstidt and Vaughan, 2003); the fractional order is caused by O_2 adsorption on the pyrite surface with a Freundlich isotherm (Williamson and Rimstidt, 1994). Therefore, if O_2 adsorbed on the material surfaces in the present study is more reactive than DO, the Fe(II) oxidation rate can be proportional to $[\text{O}_2]^{0.5}$, which can explain Eq. (18) at least partly. However, the heterogeneous reaction usually deviates from the first-order rate law with respect to $[\text{Fe(II)}]$ (e.g., Tamura et al., 1976b) and is surface-dependent, which is not consistent with my experimental results.

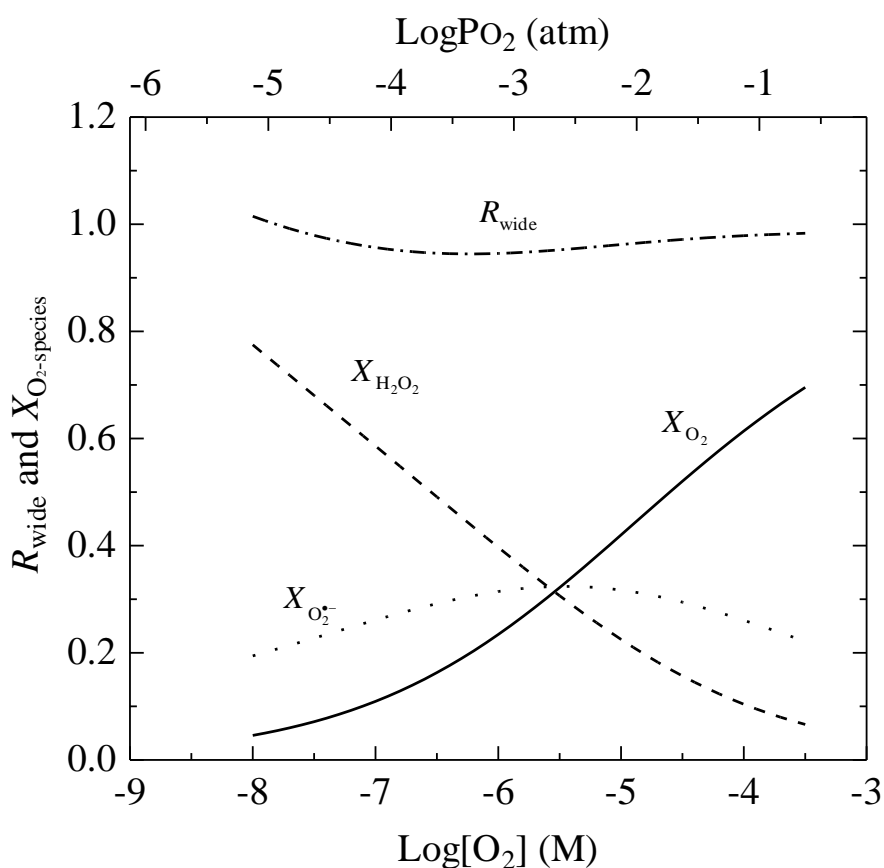


Figure 4. Variations of R_{wide} (dashed and dotted curve), X_{O_2} (solid curve), $X_{\text{H}_2\text{O}_2}$ (dashed curve) and $X_{\text{O}_2^-}$ (dotted curve) with O_2 or P_{O_2} over a wide range of P_{O_2} . See text for the definitions of R_{wide} , X_{O_2} , $X_{\text{H}_2\text{O}_2}$ and $X_{\text{O}_2^-}$. The R_{wide} value is close to 1. The contribution of O_2 (solid curve) is the highest among the three oxidants at $\sim 2 \times 10^{-3} < P_{\text{O}_2} < 0.2$ atm whereas the contribution of H_2O_2 (dashed curve) is the highest at $10^{-5} < P_{\text{O}_2} < \sim 2 \times 10^{-3}$ atm. The contribution of O_2^- (dotted curve) does not change significantly over a wide range of P_{O_2} .

4.4. Application of the rate law to Fe redistribution during mineral dissolution under low O₂ conditions

I discuss here the applicability of the newly found rate law of Fe(II) oxidation to Fe behavior during mineral dissolution. Based on the observed data of Fe(II)/Fe(III) redistribution during olivine dissolution at different P_{O_2} , Sugimori et al. (2012) have calculated the decrease of x in Eq. (6) by their kinetic model considering mineral dissolution, water flow and Fe(II) oxidation rates. Sugimori et al. (2012) have concluded that their experimental results under low O₂ conditions cannot be explained by the classic rate law (Eq. (5)) and that the x value should decrease at low P_{O_2} , namely, $x = 1.0, 0.86, 0.81$ and 0.76 at $0.20, 8.9 \times 10^{-3}, 9.4 \times 10^{-4}$ and 8.7×10^{-5} atm of P_{O_2} , respectively; their x values are apparently different from those in the present study. Because $y = 2$, corrected values (see below) of x and k for the Fe(II) oxidation rate should be compared between the study of Sugimori et al. (2012) and the present study to examine the applicability of the rate law of the present study to Fe behavior during mineral dissolution. Before making a comparison of the values of x and k between this study and Sugimori et al. (2012), I calculated the supply rate of O₂ against that of Fe(II) in the experiment at 8.7×10^{-5} atm of P_{O_2} , the lowest O₂ condition of Sugimori et al. (2012), and confirmed that there was stoichiometrically sufficient O₂ to fully oxidize Fe(II) (i.e., $4 \times [O_2] > [Fe(II)]$, see Appendix C).

The comparison is made according to Eq. (15). I calculated the k' values from the λ and $[OH^-]$ values and obtained two sets of x and k values at higher and lower P_{O_2} by fitting the data to $k' = k[O_2]^x$. On the other hand, by comparing their observed and calculated data, Sugimori et al. (2012) determined x values from $k[O_2]^x$ using the k value of Millero et al. (1987) (defined here as k_M which is $15.78 \text{ M}^{-3} \text{ min}^{-1}$ on the logarithmic scale under their experimental conditions) and measured $[O_2]$; k_M was assumed to be constant for all P_{O_2} conditions. For given k' and $[O_2]$ values, x can change once the k value changes (Eq. (15)). Therefore, I calculated k' values from the x , $[O_2]$ and k_M values given by Sugimori et al. (2012) (open squares in Fig. 5). I compare the x values and $\log k$ values between this study and Sugimori et al. (2012) in the $\log k'$ - $\log P_{O_2}$ plane in Fig. 5. The x value is 1 or nearly 1 at 0.2 atm of P_{O_2} . Consequently, lines with a slope of 1 intersecting respective data points at 0.2 atm of P_{O_2} should give similar values of $\log k'$ at 0 of $\log [O_2]$, i.e., $\log k' = \log k$ in Eq. (16). The values of $\log k$ are 15.78 and 15.46 (± 0.06) for Sugimori et al. (2012) and the present study, respectively, which are similar to one another (Fig. 5). The slightly lower value of $\log k$ in the present

study (15.46) may be attributed to the formation of Fe(II)-Tris complexes, which are inert with respect to oxidation by O₂ (Millero et al., 1987; Yang and Chasteen, 1999). Sugimori et al. (2012) have given only three data points at $< \sim 6 \times 10^{-3}$ atm of P_{O_2} . At $10^{-5} \sim 6 \times 10^{-3}$ atm of P_{O_2} , the olivine dissolution system (Sugimori et al. 2012) yields 0.51 for the x value, which is similar to 0.58 for the present study. On the other hand, the Fe(II) oxidation rates for Sugimori et al. (2012) are higher than those for the present study at $< 10^{-2}$ atm of P_{O_2} . The higher rate for Sugimori et al. (2012) may be partly explained by the presence and concentrations of dissolved Mg (Millero, 1987) and Si (González et al., 2010), which are absent in the present study and/or by the absence of Tris (Millero et al., 1987; Yang and Chasteen, 1999) which is present in the present study. However, it is not certain whether these effects are valid under low O₂ conditions (Sugimori et al., 2011). Because of the faster rates, the log k' value at 0 of log [O₂] at $10^{-5} \sim 6 \times 10^{-3}$ atm of P_{O_2} for Sugimori et al. (2012) (defined as log $k_{low(S)}$), $14.05 \text{ M}^{-3} \text{ min}^{-1}$, is higher than the log k_{low} value for the present study, $13.41 \text{ M}^{-3} \text{ min}^{-1}$ (Fig. 5).

The above similarities indicate that the Fe behavior under low O₂ conditions observed by Sugimori et al. (2012) is well explained by the newly found rate law. Therefore, the rate law found in the present study will be important for considerations of Fe redistribution during the dissolution of Fe-bearing minerals at low P_{O_2} . Fe redistribution during mineral dissolution is a fundamental process that determines the Fe contents in weathering profiles (Murakami et al., 2011). By applying the rate laws over a wide range of P_{O_2} values established in the present study to the Fe contents in paleosols, it is possible to give a deeper understanding of the evolution of atmospheric oxygen in the Precambrian.

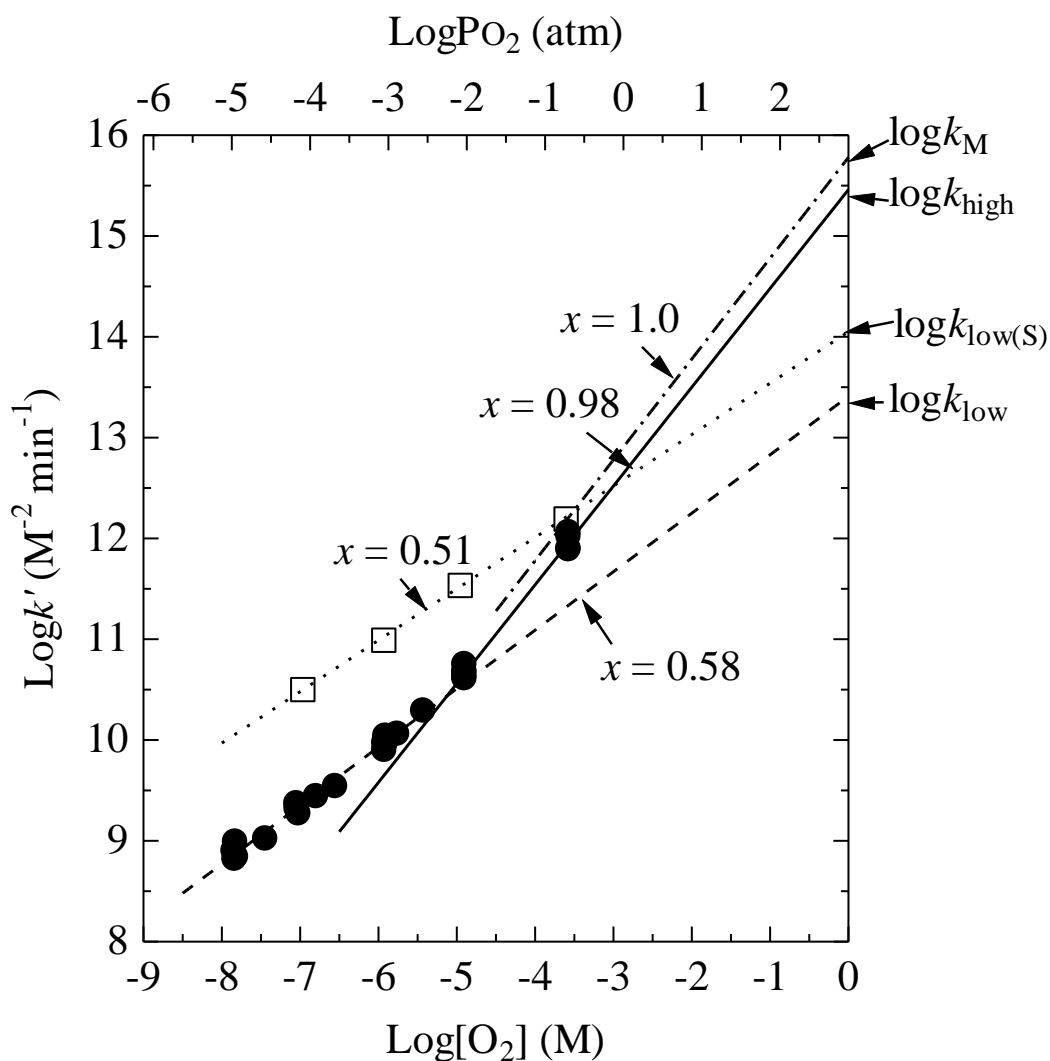


Figure 5. Comparison of the relationships between $\log k'$ and $\log [\text{O}_2]$ (or $\log P_{\text{O}_2}$). Solid circles, the data from the Fe(II) oxidation experiments (this study; Sugimori et al., 2011); open squares, the data from the olivine dissolution experiments (Sugimori et al., 2012). Lines are fitted function of $k' = k[\text{O}_2]^x$: for the present study, solid line at $\sim 10^{-2}$ – 0.2 atm of P_{O_2} ($\log k = 15.46$ ($= \log k_{\text{high}}$) and $x = 0.98$) and dashed line at $10^{-5} \leq P_{\text{O}_2} < 10^{-2} \text{ atm}$ ($\log k = 13.41$ ($= \log k_{\text{low}}$) and $x = 0.58$), and for the olivine dissolution experiments (Sugimori et al., 2012), dashed and dotted line drawn from the data at 0.2 atm of P_{O_2} assuming $x = 1$ and dotted line fitted to the three data points at $< 6 \times 10^{-3} \text{ atm}$ of P_{O_2} ($\log k = 14.05$ ($= \log k_{\text{low(S)}}$) and $x = 0.51$).

5. Conclusions

I conducted Fe(II) oxidation experiments at $\sim 10^{-5}$ – $\sim 10^{-4}$ atm of P_{O_2} and pH 7.57–8.09. These data, combined with the data of Sugimori et al. (2011) at $\sim 10^{-3}$ –0.2 atm of P_{O_2} , lead to a comprehensive understanding of the relationship between O_2 and the Fe(II) oxidation rate over a wide range of P_{O_2} , $\sim 10^{-5}$ atm $< P_{O_2} < 0.2$ atm. The pH dependence of the Fe(II) oxidation rate was expressed as a function of $[OH^-]^2$, as widely accepted, when the pH varied from 6.89 to 8.12 at 10^{-5} –0.2 atm of P_{O_2} . On the other hand, the P_{O_2} dependence of the Fe(II) oxidation rate changes at $\sim 6 \times 10^{-3}$ atm of P_{O_2} ; when $P_{O_2} = \sim 6 \times 10^{-3}$ –0.2 atm, the rate law is essentially the same as originally derived by Stumm and Lee (1961), whereas the oxidation reactions were found to obey a hitherto unknown rate law at 10^{-5} – 6×10^{-3} atm of P_{O_2} where the rate is proportional to $[O_2]^{0.58}$. The mechanism causing this change in rate order with respect to O_2 was possibly attributed to the change of the dominant oxidation pathway from O_2 to the steadily produced H_2O_2 with a minor contribution from O_2^- . Further experimental study is required to explicitly confirm this issue.

The newly derived rate equations can explain the Fe behavior during mineral dissolution under low O_2 conditions reported in a recent study (Sugimori et al., 2012). Therefore, the newly found rate law will be useful for the interpretation of the Fe behavior of paleosols and thus for the estimation of P_{O_2} levels in the Paleoproterozoic.

Appendix A

King et al. (1995) give the steady-state concentrations of H_2O_2 and O_2^- :

$$\frac{d[H_2O_2]}{dt} = 0 = k_1'[Fe(II)][O_2][OH^-]^2 - k_3'[Fe(II)][H_2O_2][OH^-] \quad (A1)$$

$$\frac{d[O_2^{\bullet-}]}{dt} = 0 = k_1'[Fe(II)][O_2][OH^-]^2 - k_2[Fe(II)][O_2^{\bullet-}] \quad (A2)$$

Fe(II) oxidation by O_2^- (Reaction (2)) is pH independent at pH $> \sim 6$ (Rush and Bielski, 1985). From Eqs. (A1) and (A2),

$$[H_2O_2] = \frac{k_1'[O_2][OH^-]}{k_3'} \quad (A3)$$

$$[O_2^{\bullet-}] = \frac{k_1'[O_2][OH^-]^2}{k_2} \quad (A4)$$

The steady-state concentration of OH[•] is not given by King et al. (1995) but can be derived similarly by considering the dependency on various sinks for OH[•] other than Fe(II) (e.g., Cl⁻ and HCO₃⁻/CO₃²⁻, King et al. (1995)):

$$[\text{OH}^{\bullet}] = \frac{k_1'[\text{Fe(II)}][\text{O}_2][\text{OH}^-]^2}{k_{\text{sink}}} \quad (\text{A5})$$

where k_{sink} is the total loss rate of OH[•] by its scavenging agents. The scavenging agents in the present study can be Cl⁻ and Tris due to their high reactivity with OH[•] (e.g., King et al., 1995; Hicks and Gebicki, 1986). King et al. (1995) measured a steady-state concentration of H₂O₂ at 0.2 atm of P_{O_2} and confirmed the validity of Eq. (A3) (see Appendix B).

Appendix B

Fitting of the semi-theoretical rate law (Eq. (26)) to the empirical rate law (Eq. (18)) yields the pseudo-steady-state constants of Eqs. (22) and (23). Because O₂ contribution is low (Section 4.3) and direct oxidation of Fe(II) by OH[•] is not likely (Section 4.3), H₂O₂ and O₂⁻ are considered to be the dominant oxidants under low O₂ conditions. Then, from Eq. (26),

$$\frac{d[\text{Fe(II)}]}{dt} = -(2\alpha k_3'[\text{O}_2]^{0.5} + \alpha'k_2[\text{O}_2]^{0.75})[\text{Fe(II)}][\text{OH}^-]^2 \quad (\text{B1})$$

When Eq. (B1) is equivalent to Eq. (18),

$$\begin{aligned} k_{\text{low}}[\text{O}_2]^{0.58} &= 2\alpha k_3'[\text{O}_2]^{0.5} + \alpha'k_2[\text{O}_2]^{0.75} \\ &= \left(\frac{2\alpha k_3'}{\alpha'k_2}[\text{O}_2]^{0.5} + [\text{O}_2]^{0.75}\right)\alpha'k_2 \end{aligned} \quad (\text{B2})$$

To fit $\{(2\alpha k_3'/\alpha'k_2)[\text{O}_2]^{0.5} + [\text{O}_2]^{0.75}\}$ to a linear function of $[\text{O}_2]^{0.58}$ under the experimental conditions (i.e., $\sim 10^{-5}$ – $\sim 10^{-3}$ atm of P_{O_2}), $(2\alpha k_3')/(\alpha'k_2)$ must be ~ 0.04 . Then,

$$\frac{2\alpha k_3'}{\alpha'k_2}[\text{O}_2]^{0.5} + [\text{O}_2]^{0.75} \cong 0.04[\text{O}_2]^{0.5} + [\text{O}_2]^{0.75} \cong 0.2 \times [\text{O}_2]^{0.58} \quad (\text{B3})$$

From Eqs. (B2) and (B3), $k_{\text{low}} = 0.2 \times \alpha' \times k_2$. Because $\log k_2 = 8.78$ (Rush and Bielski, 1985) and $\log k_3' = 10.59$ (calculated from Millero and Sotolongo (1989)), $\log \alpha' = 5.33$, and then, $\log \alpha = 1.82$.

Then, I can calculate the H₂O₂ and O₂⁻ concentrations as functions of pH and P_{O_2} according to Eqs. (22) and (23), respectively. Fig. B1 plots the concentrations of O₂ (DO), H₂O₂ and O₂⁻ as a function of P_{O_2} at pH 8 (solid, dashed and dotted lines, respectively). Because the exponent of $[\text{O}_2]$ is 0.75 (equation 23), the O₂⁻ concentration

variation shows a similar decrease to that of O_2 . On the other hand, because of the exponent, 0.5, the concentration of H_2O_2 shows a slower decrease and is lower than that of O_2 by a few and a half orders of magnitude at 6×10^{-3} and 10^{-6} atm of P_{O_2} , respectively (Fig. B1). There are no available observed concentrations of H_2O_2 under low O_2 conditions. King et al. (1995) measured H_2O_2 concentrations at 0.2 atm of P_{O_2} and proposed a model for the steady-state concentration of H_2O_2 (i.e., Eq. (A3) in Appendix A) (open square and dashed and dotted line in Fig. B1, respectively). At 0.2 atm of P_{O_2} , the observed H_2O_2 concentration by King et al. (1995) and the calculated H_2O_2 concentration by the present model are very similar (Fig. B1). Therefore, Eq. (22) with $\log \alpha = 1.82$ is not inconsistent with the H_2O_2 concentration measured by King et al. (1995).

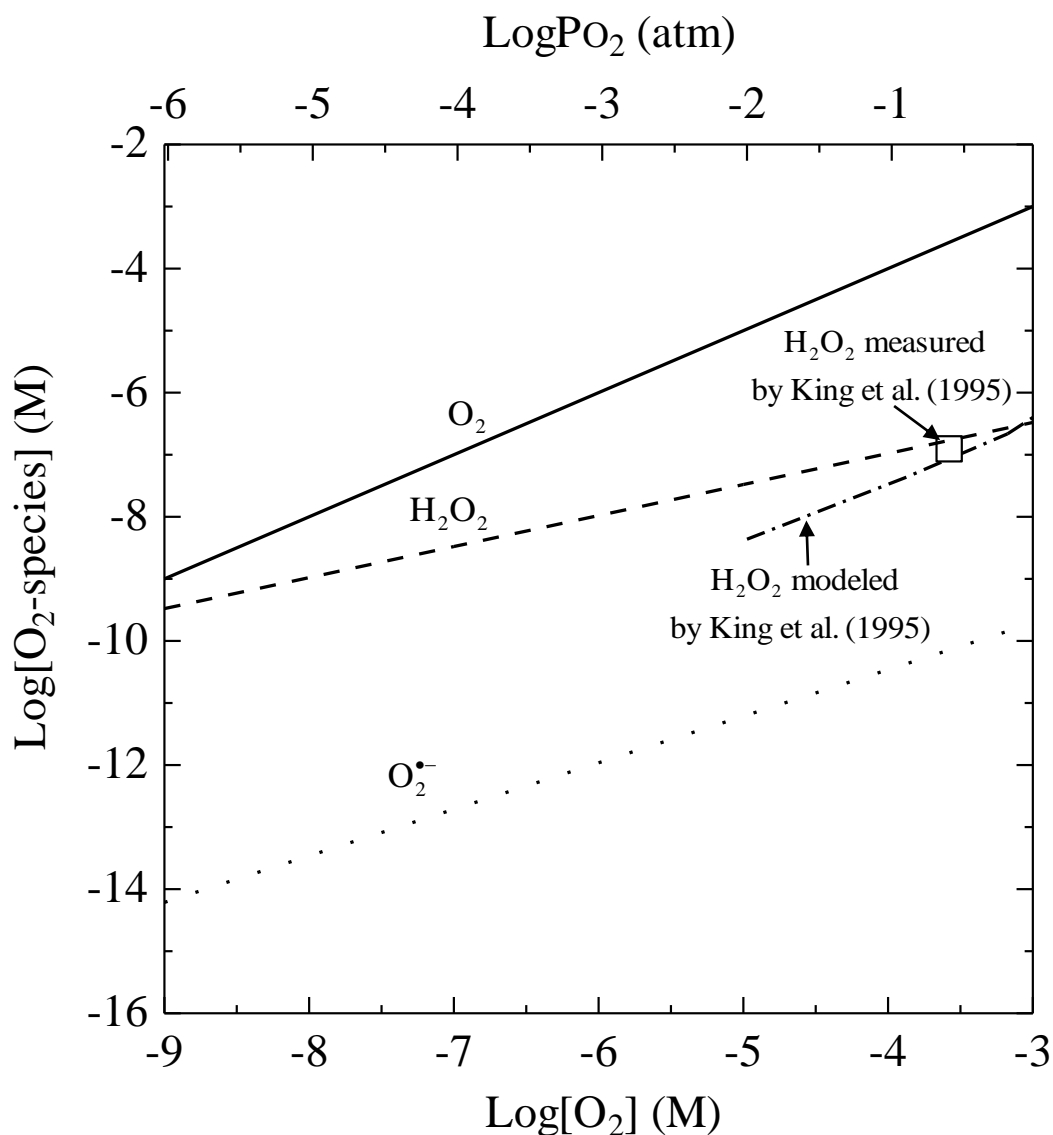


Figure B1. Concentration variations of O₂, H₂O₂ and O₂^{•-} against O₂ or P_O₂. The pseudo-steady-state concentrations of H₂O₂ and O₂^{•-} are calculated from Eqs. (22) and (23) for the present study (dashed and dotted lines, respectively) and that of H₂O₂ from Eq. (A3) for King et al. (1995) (dashed and dotted line). Because King et al. (1995) measured the concentration of H₂O₂ at 25 °C and ionic strength (*I*) 0.7 (open square), all calculations were performed accordingly and at pH 8 (or [OH⁻] = 10⁻⁶ M). Log *k*₁' and log *k*₃' were calculated based on the equation given by Millero et al. (1987) and Millero and Sotolongo (1989), respectively, and log *k*₂ was obtained from Rush and Bielski (1985). The values of α and α' are shown in Appendix B.

Appendix C

In contrast to the Fe(II) oxidation experiments which were performed in a batch system, the olivine dissolution experiments were carried out in a flow system where a solution flows and a mineral dissolves (or Fe(II) dissolves into solution) at constant rates (Sugimori et al., 2012). Accordingly, it is not certain whether the O₂ supply is stoichiometrically sufficient with respect to Fe(II) in the olivine dissolution system to follow the rate law. The supply rates of both O₂ and Fe(II) were calculated for the experiment of Sugimori et al. (2012) at 8.7×10^{-5} atm of P_{O_2} , the lowest P_{O_2} level for their experiments. Note that the supply rate of Fe(II) is almost the same at any P_{O_2} level (Sugimori et al., 2012).

Using the gas exchange constant, K_g (8.3×10^{-4} m min⁻¹ from Liss (1973)), the O₂ supply rate, r_{O_2} (mol min⁻¹), can be represented by

$$r_{O_2} = 10^3 \times K_g ([O_2]_{\text{sat}} - [O_2]_{\text{int}}) S_{\text{int}} \quad (\text{C1})$$

where $[O_2]_{\text{sat}}$, $[O_2]_{\text{int}}$ and S_{int} denote the DO concentration in equilibrium with O₂ gas (mol L⁻¹), the DO concentration at the interface between water and atmosphere (mol L⁻¹), and the area of the interface (m²), respectively. A factor of 10³ (L m⁻³) is the conversion value from m³ to L. $[O_2]_{\text{sat}}$ is 1.1×10^{-7} mol L⁻¹ at 8.7×10^{-5} atm of P_{O_2} (Henry's law at 25°C). $S_{\text{int}} = 1 \times 10^{-3}$ m² (Sugimori et al., 2012) and $[O_2]_{\text{int}}$ is assumed to be 99% of $[O_2]_{\text{sat}}$ due to the loss of O₂ by the reaction with Fe(II). Then, $r_{O_2} = 9.2 \times 10^{-11}$ mol min⁻¹ at 8.7×10^{-5} atm of P_{O_2} .

The Fe(II) supply rate, $r_{\text{Fe(II)}}$ (mol min⁻¹), is given by:

$$r_{\text{Fe(II)}} = \delta_{\text{ol}} \beta_{\text{Fe(II)}} S_{\text{ol}} m_{\text{ol}} \quad (\text{C2})$$

where δ_{ol} , $\beta_{\text{Fe(II)}}$, S_{ol} and m_{ol} denote the dissolution rate of olivine (mol m⁻² min⁻¹), the mole number of Fe(II) in one mole of olivine, the surface area of olivine (m² g⁻¹) and the mass of olivine used in the experiments (g), respectively. All of the parameters are given by Sugimori et al. (2012): $\delta_{\text{ol}} = 6 \times 10^{-9}$ mol m⁻² min⁻¹, $\beta_{\text{Fe(II)}} = 0.16$, $S_{\text{ol}} = 0.076$ m² g⁻¹ and $m_{\text{ol}} = 0.12$ g. Then, $r_{\text{Fe(II)}}$ is calculated to be 8.8×10^{-12} mol min⁻¹.

Consequently, $r_{O_2} \approx 10 \times r_{\text{Fe(II)}}$ even at 8.7×10^{-5} atm of P_{O_2} , indicating that there was stoichiometrically sufficient O₂ to fully oxidize Fe(II), i.e., $4 \times [O_2] > [Fe(II)]$ (see Introduction), in the olivine dissolution experiments of Sugimori et al. (2012).

References

- Bekker A., Holland H. D., Wang P. -L., Rumble III D., Stein H. J., Hannah J. L., Coetzee L. L. and Beukes N. J. (2004) Dating the rise of atmospheric oxygen. *Nature* **427**, 117–120.
- Bologni, L., Sabatini A. and Vacca A. (1983) Complex formation equilibria between 2-amino-2(hydroxymethyl)-1,3,-propanediol (tris, tham) and nickel(II), copper(II), zinc(II) and hydrogen ions in aqueous solutions. *Inorg. Chim. Acta* **69**, 71–75.
- Burns J. M., Craig P. S., Shaw T. J. and Ferry J. L. (2010) Multivariate examination of Fe(II)/Fe(III) cycling and consequent hydroxyl radical generation. *Environ. Sci. Technol.* **44**, 7226–7231.
- Burns J. M., Craig P. S., Shaw T. J. and Ferry J. L. (2011a) Short-term Fe cycling during Fe(II) oxidation: Exploring joint oxidation and prediction with a combinatorial system. *Environ. Sci. Technol.* **45**, 2663–2669.
- Burns J. M., Craig P. S., Shaw T. J. and Ferry J. L. (2011b) Combinatorial parameter space as an empirical tool for predicting water chemistry: Fe(II) oxidation across a watershed. *Environ. Sci. Technol.* **45**, 4023–4029.
- Canfield D. E. (2005) The early history of atmospheric oxygen: Homage to Robert M. Garrels. *Ann. Rev. Earth Planet. Sci.* **33**, 1–36.
- Catling D. C. and Claire M. W. (2005) How Earth's atmosphere evolved to an oxic state: A status report. *Earth Planet. Sci. Lett.* **237**, 1–20.
- Craig P. S., Shaw T. J., Miller P. L., Pellechia P. J. and Ferry, J.L. (2009) Use of multiparametric techniques to quantify the effects of naturally occurring ligands on the kinetics of Fe(II) oxidation. *Environ. Sci. Technol.* **43**, 337–342.
- Deborde M. and von Gunten U. (2008) Reactions of chlorine with inorganic and organic compounds during water treatment—Kinetics and mechanisms: A critical review. *Water Res.* **42**, 13–51.
- Emmenegger L., King D. W., Sigg L. and Sulzberger B. (1998) Oxidation kinetics of Fe(II) in a eutrophic Swiss lake. *Environ. Sci. Technol.* **32**, 2990–2996.
- Ensing B., Buda F. and Baerends E. J. (2003) Fenton-like chemistry in water: oxidation catalysis by Fe(III) and H₂O₂. *J. Phys. Chem. A* **107**, 5722–5731.
- Farquhar J., Bao T. H. and Thiemens M. H. (2000) Atmospheric influence of earth's earliest sulfur cycle. *Science* **289**, 756–759.
- Farquhar J. and Wing B. A. (2003) Multiple sulfur isotopes and the evolution of the atmosphere. *Earth Planet. Sci. Lett.* **213**, 1–13.

- Folkes L. K., Candeias L. P. and Wardman P. (1995) Kinetics and mechanisms of hypochlorous acid reactions. *Arch. Biochem. Biophys.* **323**, 120–126.
- González A. G., Santana-Casiano J. M., Pérez N. and González-Dávila M. (2010) Oxidation of Fe(II) in natural waters at high nutrient concentrations. *Environ. Sci. Technol.* **44**, 8095–8101.
- González-Dávila M., Santana-Casiano J. M. and Millero F. J. (2006) Competition between O₂ and H₂O₂ in the oxidation of Fe(II) in Natural Waters. *J. Sol. Chem.* **35**, 95–111.
- Hicks M. and Gebicki J. M. (1986) Rate constants for reaction of hydroxyl radicals with Tris, Tricine and Hepes buffers. *FEBS Lett.* **199**, 92–94.
- Holland H. D. (1984) *The Chemical Evolution of the Atmosphere and Oceans*. Princeton University Press, Princeton, NJ.
- Holland H. D. (2006) Oxygenation of atmosphere and oceans. *Philos. Trans. R. Soc. Lond. B Biol. Sci.* **361**, 903–915.
- Holmes P. R. and Crundwell F. K. (2000) The kinetics of the oxidation of pyrite by ferric ions and dissolved oxygen: an electrochemical study. *Geochim. Cosmochim. Acta* **64**, 263–274.
- Kasting J. F. and Ono S. (2006) Paleoclimates: the first two billion years. *Phil. Trans. Royal Soc. Sect. B*, doi:10.1098/rstb.2006.1839.
- Keeling R. F., Körtzinger A. and Gruber N. (2010) Ocean deoxygenation in a warming world. *Annu. Rev. Mar. Sci.* **2**, 199–229.
- King D. W., Lounsbury H. A. and Millero F. J. (1995) Rates and mechanism of Fe(II) oxidation at nanomolar total iron concentration. *Environ. Sci. Technol.* **29**, 818–824.
- King D. W. (1998) Role of carbonate speciation on the oxidation rate of Fe(II) in aquatic systems. *Environ. Sci. Technol.* **32**, 2997–3003.
- King D. W. and Farlow R. (2000) Role of carbonate speciation on the oxidation of Fe(II) by H₂O₂. *Mar. Chem.* **70**, 201–209.
- Koppenol W. H. and Liebman J. F. (1984) The oxidizing nature of the hydroxyl radical. A comparison with ferryl ion (FeO²⁺). *J. Phys. Chem.* **88**, 99–101.
- Koppenol W. H., Sanbury D. M. and Bounds P. L. (2010) Electrode potentials of partially reduced oxygen species, from dioxygen to water. *Free Radic. Biol. Med.* **49**, 317–322.
- Laidler K. J. (1987) *Chemical Kinetics*, 3rd ed., Harper and Row, New York.
- Liang L., McNabb J. A., Paulk J. M., Gu B. and McCarthy J. F. (1993) Kinetics of Fe(II) oxygenation at low partial pressure of oxygen in the presence of natural organic matter. *Environ. Sci. Technol.* **27**, 1864–1870.

- Liss P. S. (1973) Process of gas exchange across an air-water interface. *Deep-Sea Res.* **20**, 221–238.
- Mao Y., Pham A. N., Rose A. L. and Waite T. D. (2011) Influence of phosphate on the oxidation kinetics of nanomolar Fe(II) in aqueous solution at circumneutral pH. *Geochim. Cosmochim. Acta* **75**, 4601–4610.
- Miller D. M., Buettner G. R. and Aust S. D. (1990) Transition metals as catalysts of "Autoxidation" reactions. *Free Radic. Biol. Med.* **8**, 95–108.
- Millero F. J. (1985) The effect of ionic interactions on the oxidation of metals in natural waters. *Geochim. Cosmochim. Acta* **49**, 547–553.
- Millero F. J. (1987) Estimate of the life time of superoxide in seawater. *Geochim. Cosmochim. Acta* **51**, 351–353.
- Millero F. J., Sotolongo S. and Izaguirre M. (1987) The oxidation kinetics of Fe(II) in seawater. *Geochim. Cosmochim. Acta* **51**, 793–801.
- Millero F. J. and Sotolongo S. (1989) The oxidation of Fe(II) with H₂O₂ in seawater. *Geochim. Cosmochim. Acta* **53**, 1867–1873.
- Murakami T., Sreenivas B., Das Sharma S. and Sugimori H. (2011) Quantification of atmospheric oxygen levels during the Paleoproterozoic using paleosol compositions and iron oxidation kinetics. *Geochim. Cosmochim. Acta* **75**, 3982–4004.
- Ohmoto H., Watanabe Y. and Kumazawa K. (2004) Evidence from massive siderite beds for a CO₂-rich atmosphere before ~1.8 billion years ago, *Nature* **429**, 395–399.
- O'Sullivan D. W., Hanson A. K. and Kester D. R. (1995) Stopped flow luminol chemiluminescence determination of Fe(II) and reducible iron in seawater at subnanomolar levels. *Mar. Chem.* **49**, 65–77.
- Pavlov A. A. and Kasting J. F. (2002) Mass-independent fractionation of sulfur isotopes in Archean sediments: Strong evidence for an anoxic Archean atmosphere. *Astrobiology* **2**, 27–41.
- Paulmier A. and Ruiz-Pino D. (2009) Oxygen minimum zones (OMZs) in the modern ocean. *Prog. Oceanogr.* **80**, 113–128.
- Pham A. N. and Waite T. D. (2008) Oxygenation of Fe(II) in natural waters revisited: Kinetic modeling approaches, rate constant estimation and the importance of various reaction pathways. *Geochim. Cosmochim. Acta* **72**, 3616–3630.
- Rimstidt J. D. and Vaughan D. J. (2003) Pyrite oxidation: a state-of-the-art assessment of the reaction mechanism. *Geochim. Cosmochim. Acta* **67**, 873–880.
- Rose A. L. and Waite T. D. (2001) Chemiluminescence of luminol in the presence of iron(II) and oxygen: Oxidation mechanism and implications for its analytical use. *Anal. Chem.* **73**, 5909–5920.

- Rose A. L. and Waite T. D. (2002) Kinetic model for Fe(II) Oxidation in seawater in the absence and presence of natural organic matter. *Environ. Sci. Technol.* **36**, 433–444.
- Rush J. D. and Bielski B. H. J. (1985) Pulse radiolytic studies of the reactions of HO_2/O_2^- with Fe(II)/Fe(III) ions. The reactivity of HO_2/O_2^- with ferric ions and its implication on the occurrence of the Haber-Weiss reaction. *J. Phys. Chem.* **89**, 5062–5066.
- Rye R. and Holland H. D. (1998) Paleosols and the evolution of atmospheric oxygen: A critical review. *Am. J. Sci.* **298**, 621–672.
- Santana-Casiano J. M., González-Dávila M., Rodríguez M. J. and Millero F. J. (2000) The effect of organic compounds in the oxidation kinetics of Fe(II). *Mar. Chem.* **70**, 211–222.
- Santana-Casiano J. M., González-Dávila M. and Millero F. J. (2004) The oxidation of Fe(II) in NaCl- HCO_3^- and seawater solutions in the presence of phthalate and salicylate ions: a kinetic model. *Mar. Chem.* **85**, 27–40.
- Santana-Casiano J. M., González-Dávila M. and Millero F. J. (2005) Oxidation of nanomolar levels of Fe(II) with oxygen in natural waters. *Environ. Sci. Technol.* **39**, 2073–2079.
- Schaich K. M. (1992) Metals and lipid oxidation. Contemporary issues. *Lipid* **27**, 209–218.
- Singer P. C. and Stumm W. (1970) Acidic mine drainage: The rate-determining step. *Science* **167**, 1121–1123.
- Sreenivas B. and Murakami T. (2005) Emerging views on the atmospheric oxygen evolution during the Precambrian. *J. Mineral. Petrol. Sci.* **100**, 184–201.
- Stuglik Z. and Zagórski Z. P. (1981) Pulse radiolysis of neutral iron(II) solutions: oxidation of ferrous ions by OH radicals. *Radiat. Phys. Chem.* **17**, 229–233.
- Stumm W. and Lee G. F. (1961) Oxygenation of ferrous iron. *Ind. Eng. Chem.* **53**, 143–146.
- Stumm W. and Morgan J. J. (1996) *Aquatic Chemistry*, 3rd Ed. John Wiley & Sons, New York.
- Sugimori H., Yokoyama T. and Murakami T. (2009) Kinetics of biotite dissolution and Fe behavior under low O_2 conditions and their implications for Precambrian weathering. *Geochim. Cosmochim. Acta* **73**, 3767–3781.
- Sugimori H., Kanzaki Y., Yokota K. and Murakami T. (2011) Nonlinear dependence of the oxidation rate of Fe(II) on dissolved oxygen under low- O_2 conditions in aqueous solutions. *J. Mineral. Petrol. Sci.* **106**, 142–152.
- Sugimori H., Kanzaki Y. and Murakami T. (2012) Relationships between Fe

- redistribution and PO_2 during mineral dissolution under low O_2 conditions. *Geochim. Cosmochim. Acta*, **84**, 29–46.
- Tamura H., Goto K. and Nagayama M. (1976a) Effect of anions on the oxygenation of ferrous ion in neutral solutions. *J. Inorg. Nucl. Chem.* **38**, 113–117.
- Tamura H., Goto K. and Nagayama M. (1976b) The effect of ferric hydroxide on the oxygenation of ferrous ions in neutral solutions. *Corros. Sci.* **16**, 197–207.
- Teutsch N., von Gunten U., Porcell D., Cirpka O. A. and Halliday A. N. (2005) Adsorption as a cause for iron isotope fractionation in reduced groundwater. *Geochim. Cosmochim. Acta* **69**, 4175–4185.
- Teutsch N., Schmid M., Müller B., Halliday A. N., Bürgmann H. and Wehrli B. (2009) Large iron isotope fractionation at oxic-anoxic boundary in Lake Nyos. *Earth Planet. Sci. Lett.* **285**, 52–60.
- Theis T. L. and Singer P. C. (1974) Complexation of iron(II) by organic matter and its effect on iron(II) oxygenation. *Environ. Sci. Technol.* **8**, 569–573.
- Trapp J. M. and Millero F. J. (2007) The oxidation of iron (II) with oxygen in NaCl brines. *J. Sol. Chem.* **36**, 1479–1493.
- Truong G. L., De Laat J. and Legube B. (2004) Effects of chloride and sulfate on the rate of oxidation of ferrous ion by H_2O_2 . *Water Res.* **38**, 2384–2394.
- Williamson M. A. and Rimstidt J. D. (1994) The kinetics and electrochemical rate-determining step of aqueous pyrite oxidation. *Geochim. Cosmochim. Acta* **58**, 5443–5454.
- Xiao C., Palmer D. A., Wesolowski D. J., Lovitz S. B. and King D. W. (2002) Carbon dioxide effects on luminol and 1,10-phenanthroline chemiluminescence. *Anal. Chem.* **74**, 2210–2216.
- Yang X. and Chasteen N. D. (1999) Ferroxidase activity of ferritin: effects of pH, buffer and Fe(II) and Fe(III) concentrations on Fe(II) autoxidation and ferroxidation. *Biochem. J.* **338**, 615–618.

IV. Estimates of atmospheric O₂ in the Paleoproterozoic from paleosols

1. Introduction

The environments of the Earth's surface greatly changed in the Paleoproterozoic and Neoproterozoic including atmosphere, ocean, life and climate (e.g., see reviews by Holland (2006) and Och and Shields-Zhou (2012) and references therein). The increase in atmospheric oxygen during the Paleoproterozoic, in particular, is a key to understand the co-evolution of life and environment (Anbar and Knoll, 2002; Knoll, 2003). It has been long since suggested and now is widely accepted that there was a great increase of atmospheric oxygen in the Paleoproterozoic, called as "the Great Oxidation Event (GOE)" (Holland, 2002). Many lines of geological evidence are consistent with the GOE in the Paleoproterozoic, including detrital minerals (Rasmussen and Buick, 1999), banded iron formations (Beukes and Klein, 1990), red beds (Chandler, 1980), paleosols, fossil weathering profiles (Rye and Holland, 1998), and carbon (Karhu and Holland, 1996) and sulfur isotopes (Canfield, 1998). The significant transition in oxygen levels in the early Paleoproterozoic have been confirmed by the presence of mass independent fractionation of sulfur (MIF-S where $\Delta^{33}\text{S} \cong \delta^{33}\text{S} - 0.515 \times \delta^{34}\text{S} \neq 0$) in marine sediments prior to the early Paleoproterozoic and the absence of MIF-S in the later ages (Farquhar et al., 2000). Subsequent studies of multiple sulfur isotopes have further constrained the ages and the partial pressures of atmospheric oxygen (P_{O_2}) in the GOE from the sedimentary sulfur records; $\leq \sim 10^{-6}$ atm of P_{O_2} at ≥ 2.45 Ga, $\geq \sim 10^{-6}$ atm at 2.32 Ga, and to $\geq \sim 10^{-3}$ atm at 2.0 Ga (Pavlov and Kasting, 2002; Farquhar and Wing, 2003; Bekker et al., 2004). In addition to sulfur isotopes, other proxies such as C, Cr, Os and U have suggested the timing of the GOE (Karhu and Holland, 1996; Hannah et al., 2004; Bekker et al., 2006; Scott et al., 2008; Partin et al., 2013). On the contrary, it is still uncertain how oxygen increased in the GOE and why in this particular period of time in the Earth's history (e.g., Holland, 2002, 2009; Catling and Claire, 2005; Kasting, 2013).

Quantitative analysis of geological records can help elucidate how oxygen increased in the GOE. Out of the geological records, paleosols can be a powerful tool to estimate P_{O_2} levels because they should reflect the concentrations of atmospheric oxygen at the time of weathering, mineral-water-rock interactions at the Earth's surface. Holland and co-workers have used the Fe contents of paleosols, and proposed an increase model of atmospheric oxygen in the Paleoproterozoic (e.g., Holland, 1984;

Holland, 1994; Rye and Holland, 1998). However, their method was still a semi-quantitative one. Murakami et al. (2011) have introduced Fe(II) oxidation kinetics for quantitative estimation of P_{O_2} levels, applying it to Fe(II) and Fe(III) distributions recorded in paleosols in the Paleoproterozoic, and have suggested that atmospheric oxygen increased gradually in long term in the GOE. Recently, Yokota et al. (2013) have developed a model by which Fe redistributions during weathering can be predicted as a function of P_{O_2} . Yokota et al. (2013) have applied their model to Fe records in paleosols in the Paleoproterozoic and demonstrated that the estimation of P_{O_2} in the era can be made without the constraints from other geological records. However, the kinetic law of Fe(II) oxidation used by Murakami et al. (2011) is an assumed one, and the rate expression for Fe(II) oxidation used by Yokota et al. (2013) is the one experimentally determined at $>10^{-3}$ atm of P_{O_2} . In addition, the model calculation by Yokota et al. (2013) requires the parameters relevant to weathering, namely, pH, partial pressure of atmospheric carbon dioxide (P_{CO_2}), water flow rate, temperature and O_2 diffusion into soil at the time of weathering which affect P_{O_2} estimates and have not been explored yet. The estimates of P_{O_2} given by Yokota et al. (2013) may vary due to the uncertainties in these parameters for paleosols in the Paleoproterozoic. All these ambiguities related to weathering prompt me to more precisely estimate P_{O_2} levels in the Paleoproterozoic.

The aims of this chapter are (1) to develop a new weathering model including advanced kinetic law for Fe(II) oxidation by O_2 obtained in the previous chapter (Chapter III) by considering steady-state weathering, (2) to effectively constrain the above parameters (pH, P_{CO_2} , water flow rate, temperature and O_2 diffusion into soil) for Paleoproterozoic paleosols, (3) to quantify P_{O_2} levels in the Paleoproterozoic by applying the new model to the Paleoproterozoic paleosols, and (4) to finally provide more robust estimates of P_{O_2} than previously estimated.

2. P_{O_2} estimation method

Fe(II)-bearing primary minerals such as biotite and chlorite release Fe(II) in solution by weathering. Depending on weathering conditions such as Fe(II) oxidation kinetics and water flow rate, some portion of the dissolved Fe(II) is oxidized to Fe(III), which will form Fe(III) (oxyhydr)oxides and remain in the weathering profile because of the low solubility of Fe(III), while the remaining (unoxidized) portion flows out of the profile (e.g., Murakami et al., 2011). The ϕ value represents the ratio between the precipitated Fe(III)-(oxyhydr)oxides from dissolved Fe(II) to the total dissolved-Fe(II) over the entire weathering profile during weathering (Yokota et al., 2013). The present

weathering model basically calculates a ϕ value for a given P_{O_2} value. In Section 2, I formulate the model for the calculation of ϕ as a function of P_{O_2} assuming steady state of weathering, with introducing newly-determined kinetic law for Fe(II) oxidation (Chapter III). In Section 3, I constrain the parameters (i.e., pH, P_{CO_2} , water flow rate, temperature and O_2 diffusion into soil) to better estimate the P_{O_2} levels in the Paleoproterozoic.

2.1. Formulation for the calculation of ϕ

Considering the definition of ϕ , I need to formulate the behaviors of both Fe(II) and Fe(III) in a weathering profile. Firstly, I describe the behaviors of Fe(II) in both rock and water phases in the weathering profile. Time-evolution of the Fe(II) concentration in rock phase ([Fe(II)-rock], mol m⁻³) is given by

$$\frac{1}{\theta\sigma} \frac{d[\text{Fe(II)-rock}]}{dt} = -D_{\text{Fe(II)}} + P_{\text{Fe(II)}} \quad (1)$$

where θ and σ are the porosity (m³ m⁻³) and water saturation ratio (L m⁻³) of the weathering profile, respectively, and t denotes time (yr). $D_{\text{Fe(II)}}$ and $P_{\text{Fe(II)}}$ in the right-hand side of Eq. (1) are the rate of Fe(II) dissolution from Fe(II)-bearing minerals (mol L⁻¹ yr⁻¹) and the rate of Fe(II) precipitation as Fe(II)-bearing secondary minerals (mol L⁻¹ yr⁻¹), respectively. Eq. (1) means that the Fe(II) concentration in rock phase is determined by the reactions of Fe(II)-bearing minerals. On the other hand, time-evolution of the Fe(II) concentration in porewater ([Fe(II)], mol L⁻¹) of the weathering profile is given by

$$\frac{d[\text{Fe(II)}]}{dt} = D_{\text{Fe(II)}} - P_{\text{Fe(II)}} - \lambda[\text{Fe(II)}] - k_f[\text{Fe(II)}] \quad (2)$$

where λ is the pseudo-first order rate constant for Fe(II) oxidation by O_2 (yr⁻¹) (e.g., Stumm and Lee, 1961) and k_f is the rate constant for Fe(II) removal by water flow (yr⁻¹) (e.g., Berner, 1978). Eq. (2) describes that Fe(II) in porewater is supplied by dissolution of Fe(II)-bearing minerals ($D_{\text{Fe(II)}}$) and lost by precipitation of Fe(II)-bearing secondary minerals ($P_{\text{Fe(II)}}$), oxidation of Fe(II) to Fe(III) by O_2 ($\lambda[\text{Fe(II)}]$) and water flow ($k_f[\text{Fe(II)}]$). The loss of Fe(II) in porewater out of the weathering profile by diffusion is considered to be negligible compared to that by water flow (Maher, 2010), and thus is omitted from Eq. (2). Similarly to Eqs. (1) and (2), time-evolutions of Fe(III) concentration in rock phase ([Fe(III)-rock], mol m⁻³) and in porewater ([Fe(III)], mol L⁻¹) are described by the following respective equations:

$$\frac{1}{\theta\sigma} \frac{d[\text{Fe(III)}\text{-rock}]}{dt} = -D_{\text{Fe(III)}} + P_{\text{Fe(III)}} \quad (3)$$

$$\frac{d[\text{Fe(III)}]}{dt} = D_{\text{Fe(III)}} - P_{\text{Fe(III)}} + \lambda[\text{Fe(II)}] - k_f[\text{Fe(III)}] \quad (4)$$

where $D_{\text{Fe(III)}}$ and $P_{\text{Fe(III)}}$ are the rate of Fe(III) dissolution from Fe(III)-bearing minerals ($\text{mol L}^{-1} \text{yr}^{-1}$) and the rate of Fe(III) precipitation as Fe(III)-bearing secondary minerals ($\text{mol L}^{-1} \text{yr}^{-1}$), respectively. Eq. (3) means that Fe(III) concentration in rock phase is determined by dissolution and precipitation of Fe(III)-bearing minerals ($D_{\text{Fe(III)}}$ and $P_{\text{Fe(III)}}$, respectively). Eq. (4) describes that Fe(III) in porewater is supplied by dissolution of Fe(III)-bearing minerals ($D_{\text{Fe(III)}}$) and Fe(II) oxidation to Fe(III) in porewater ($\lambda[\text{Fe(II)}]$) and lost by precipitation of Fe(III)-bearing secondary minerals ($P_{\text{Fe(III)}}$) and water flow ($k_f[\text{Fe(III)}]$).

The concentrations in porewater, $[\text{Fe(II)}]$ and $[\text{Fe(III)}]$, are considered to reach those at steady state in a relatively short period of time (Stonestrom et al., 1998; Brantley and White, 2009). Then, from $d[\text{Fe(II)}]/dt = 0$ in Eq. (2),

$$D_{\text{Fe(II)}} - P_{\text{Fe(II)}} = \lambda[\text{Fe(II)}]_{\text{ss}} + k_f[\text{Fe(II)}]_{\text{ss}} \quad (5)$$

where $[\text{Fe(II)}]_{\text{ss}}$ is the steady-state concentration of Fe(II) in porewater (mol L^{-1}). Similarly, from $d[\text{Fe(III)}]/dt = 0$ in Eq. (4),

$$D_{\text{Fe(III)}} - P_{\text{Fe(III)}} = -\lambda[\text{Fe(II)}]_{\text{ss}} + k_f[\text{Fe(III)}]_{\text{ss}} \quad (6)$$

where $[\text{Fe(III)}]_{\text{ss}}$ is the steady-state concentration of Fe(III) in porewater (mol L^{-1}). I can assume $[\text{Fe(III)}]_{\text{ss}} \cong 0$ because of the low solubility of Fe(III)-(oxyhydr)oxides. Then, Eq. (6) reduces to

$$D_{\text{Fe(III)}} - P_{\text{Fe(III)}} = -\lambda[\text{Fe(II)}]_{\text{ss}} \quad (7)$$

Using Eqs. (5) and (7), Eqs. (1) and (3) can be rewritten, respectively, as

$$\frac{1}{\theta\sigma} \frac{d[\text{Fe(II)}\text{-rock}]}{dt} = -(\lambda + k_f)[\text{Fe(II)}]_{\text{ss}} \quad (8)$$

$$\frac{1}{\theta\sigma} \frac{d[\text{Fe(III)}\text{-rock}]}{dt} = \lambda[\text{Fe(II)}]_{\text{ss}} \quad (9)$$

I define here the loss amount of Fe(II) and the gain amount of Fe(III) per unit rock volume during the whole weathering duration time (t_{tot} , yr) as $[\text{Fe(II)}\text{-rock}]_{\text{loss}}$ and $[\text{Fe(III)}\text{-rock}]_{\text{gain}}$ (mol m^{-3}), respectively. Then, using Eqs. (8) and (9), $[\text{Fe(II)}\text{-rock}]_{\text{loss}}$ and $[\text{Fe(III)}\text{-rock}]_{\text{gain}}$ are given by the following respective equations:

$$[\text{Fe(II)-rock}]_{\text{loss}} \equiv - \int_{t=0}^{t=t_{\text{wt}}} \frac{d[\text{Fe(II)-rock}]}{dt} dt = (\lambda + k_f) \int_{t=0}^{t=t_{\text{wt}}} \theta \sigma [\text{Fe(II)}]_{\text{ss}} dt \quad (10)$$

$$[\text{Fe(III)-rock}]_{\text{gain}} \equiv \int_{t=0}^{t=t_{\text{wt}}} \frac{d[\text{Fe(III)-rock}]}{dt} dt = \lambda \int_{t=0}^{t=t_{\text{wt}}} \theta \sigma [\text{Fe(II)}]_{\text{ss}} dt \quad (11)$$

In Eqs. (10) and (11), I assumed that λ and k_f are constant during weathering of a given profile. On the other hand, ϕ is defined as (see the first paragraph of Section 2)

$$\phi \equiv \frac{[\text{Fe(III)-rock}]_{\text{gain}}}{[\text{Fe(II)-rock}]_{\text{loss}}} \quad (12)$$

By substituting Eqs. (10) and (11) into (12),

$$\phi = \frac{\lambda}{\lambda + k_f} \quad (13)$$

Eq. (13) can calculate a ϕ value once λ and k_f are given. Using the concentrations of O_2 and OH^- in porewater ($[\text{O}_2]$ and $[\text{OH}^-]$ (mol L^{-1}), respectively), λ can be represented by (e.g., Yokota et al., 2013)

$$\lambda = k[\text{O}_2]^x [\text{OH}^-]^2 \quad (14)$$

where k is the rate constant ($\text{mol}^{-3} \text{L}^3 \text{yr}^{-1}$) for Fe(II) oxidation by O_2 and x is the parameter describing the dependence of λ on O_2 . $[\text{O}_2]$ in Eq. (14) can be converted to P_{O_2} :

$$[\text{O}_2] = f K_{\text{HO}} P_{\text{O}_2} \quad (15)$$

where K_{HO} is the Henry's constant for gaseous- O_2 dissolution into water ($\text{mol L}^{-1} \text{atm}^{-1}$). In Eq. (15), f is the parameter (≤ 1) which describes the difference between "soil P_{O_2} " (actual P_{O_2} in porewater) and atmospheric P_{O_2} by O_2 diffusion into soil; when O_2 diffuses fast into soil and/or consumption of O_2 in soil is slow, "soil P_{O_2} " = atmospheric P_{O_2} and thus $f = 1$ while when O_2 diffusion into soil is slow and/or consumption of O_2 in soil is fast, "soil P_{O_2} " < atmospheric P_{O_2} and thus f can be < 1. $[\text{OH}^-]$ in Eq. (14) can be written as a function of pH:

$$[\text{OH}^-] = K_w 10^{\text{pH}} \quad (16)$$

where K_w is the water dissociation constant ($\text{mol}^2 \text{L}^{-2}$). Considering Eqs. (13)–(16), pH and P_{O_2} are the determinant factors of λ and thus ϕ . On the other hand, k_f in Eq. (13) is related to volumetric water flow per unit rock volume, q ($\text{L m}^{-3} \text{yr}^{-1}$):

$$q = \theta \sigma k_f \quad (17)$$

By Eq. (17), ϕ is related to volumetric water flow q . Using Eqs. (13)–(17), the relationship between ϕ and P_{O_2} for a given set of parameters (pH, k_f , f and temperature) can be calculated. Namely, Eqs. (13)–(17) based on steady-state weathering clearly reveal which parameters affect the ϕ - P_{O_2} relationship: they are pH (or P_{CO_2}), water flow rate, temperature and O_2 diffusion into soil but not dissolution rate of Fe(II)-bearing primary minerals or total weathering duration time.

To confirm the validity of the present method (Eqs. (13)–(17)), the calculated ϕ - P_{O_2} relationships were compared to those by Yokota et al. (2013) who have already confirmed the validity of their method. Fig. 1 compares the calculated ϕ - P_{O_2} relationships between the present study (curves) and Yokota et al. (2013) (open symbols) with varying O_2 diffusion (Fig. 1a), pH (Fig. 1b), water flow (Fig. 1c) and temperature (Fig. 1d) (see the caption of Fig. 1 for the details). Because I have not yet introduced the new kinetic law of Fe(II) oxidation at this stage (Section 2.2), the same values of k and x in Eq. (14) were used as those by Yokota et al. (2013). Fig. 1 clearly indicates that the calculated ϕ - P_{O_2} relationships are essentially the same between the present study (curves) and Yokota et al. (2013), and thus, the present method (Eqs. (13)–(17)) can accurately calculate the ϕ - P_{O_2} relationship for a given set of the parameters, pH, k_f , f and temperature. Fig. 1 also indicates that these parameters are only sensitive to determine ϕ (Eq. (13)), and thus, the ϕ - P_{O_2} relationship. By assuming steady-state weathering, which is now confirmed to be valid, the present model can avoid the complicated assumptions (e.g., weathering profile size and primary mineral) and time-consuming calculations (e.g., the Fe(II) concentration calculations for a number of layers in one weathering profile) which are necessary for the model by Yokota et al. (2013).

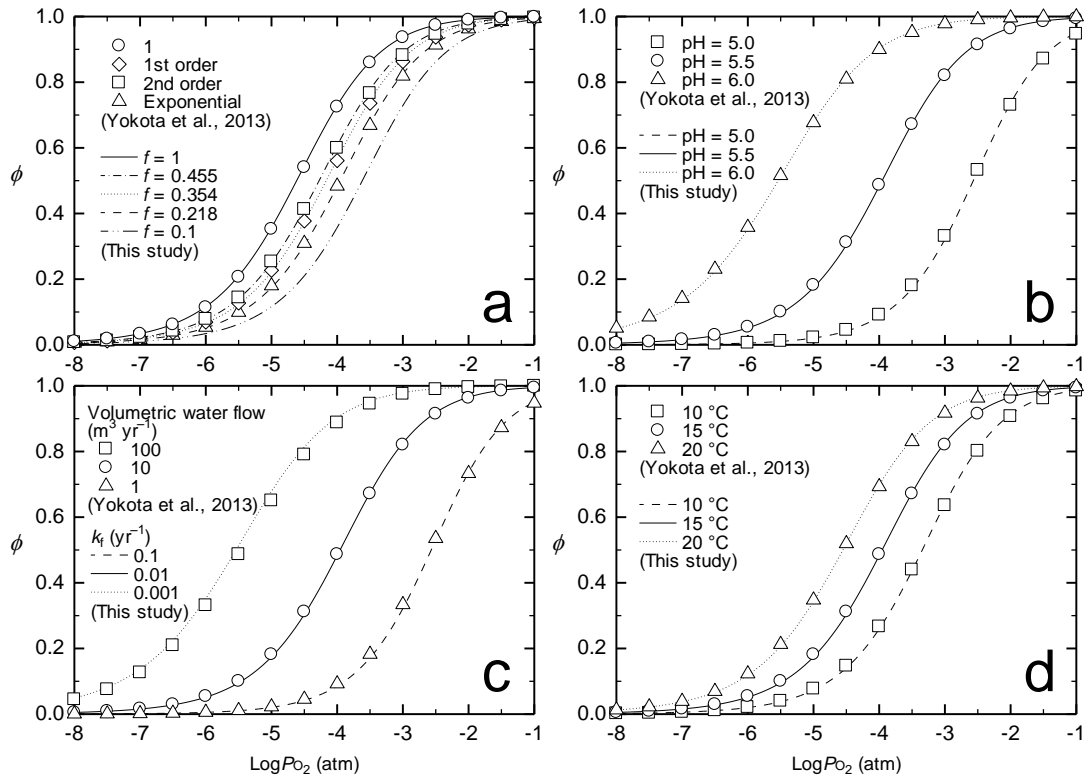


Figure 1. Comparison of calculated ϕ - P_{O_2} relationships between the present study (curves) and Yokota et al. (2013) (open symbols), with the parameters of (a) O_2 diffusion (f), (b) pH, (c) water flow (k_f) and (d) temperature being varied. Open symbols in Figs. 1a–d are from Figs. 7, 4, 5 and 8 of Yokota et al. (2013), respectively. Four types of O_2 diffusion in Yokota et al. (2013) are denoted as "1", "1st order", "2nd order" and "exponential", which correspond to 1, 0.354, 0.455 and 0.218 of f in the present study (Fig. 1a). The ϕ - P_{O_2} relationship with $f = 0.1$ for the present study (double dotted and dashed curve) is also shown for comparison (Section 3.1). The volumetric water flows considered by Yokota et al. (2013) (1 – $100 \text{ m}^3 \text{ yr}^{-1}$) are converted to k_f values in the present study (10^{-3} – 0.1 yr^{-1}) (Fig. 1c). The parameter values fixed for the calculations are 5.5 of pH, $10 \text{ m}^3 \text{ yr}^{-1}$ of volumetric water flow (or 10^{-2} yr^{-1} of k_f), $15 \text{ }^\circ\text{C}$ of temperature and "exponential" approximation of O_2 diffusion (or 0.218 of f); only one of the parameters is changed for the calculations for each figure. The same values for all parameters are used as those by Yokota et al. (2013) for each calculation.

2.2. Introduction of new Fe(II) oxidation kinetics in the model

I modify the kinetic expression for Fe(II) oxidation by O₂, i.e., Eq. (14), by introducing newly-determined kinetic law for Fe(II) oxidation (Chapter III) to the model. The Fe(II) oxidation kinetic law was determined for $P_{O_2} > \sim 10^{-3}$ atm (Sugimori et al., 2011 and references therein). Recently, Sugimori et al. (2012) have calculated the Fe(II) oxidation rates based on olivine dissolution experiments at $\sim 10^{-4}$ –0.2 atm of P_{O_2} , pH ~ 6.3 and 25 °C. In Chapter III, I have examined and determined the rate law based on Fe(II) oxidation experiments at $\sim 10^{-5}$ –0.2 atm of P_{O_2} , pH 7.7–8.3 and 22 °C. Further modification of Eq. (14) is required because Eq. (14) considers the Fe(II) oxidation reaction only by Fe(II)-hydroxyl species with O₂ (i.e., the rate is a function of [OH⁻] and [O₂] in Eq. (14)). In addition to Fe(II)-hydroxyl species, Fe(II)-carbonate species also affect the overall Fe(II) oxidation rate (e.g., Millero and Izaguirre, 1989; King, 1998; Santana-Casiano et al., 2005), and the contribution of Fe(II)-carbonate species to the overall Fe(II) oxidation rate is dependent on P_{CO_2} levels (c.f., King, 1998).

In Chapter III, I have reported that the k and x values in Eq. (14) vary with P_{O_2} ; $k = 10^{15.46} \text{ mol}^{-3} \text{ L}^3 \text{ min}^{-1}$ and $x = 0.98$ at $\sim 10^{-3}$ –0.2 atm of P_{O_2} while $k = 10^{13.41} \text{ mol}^{-3} \text{ L}^3 \text{ min}^{-1}$ and $x = 0.58$ at $\sim 10^{-5}$ – 10^{-3} atm of P_{O_2} (Chapter III); $k = 10^{15.78} \text{ mol}^{-3} \text{ L}^3 \text{ min}^{-1}$ and $x = 1$ at 0.2 atm of P_{O_2} while $k = 10^{14.05} \text{ mol}^{-3} \text{ L}^3 \text{ min}^{-1}$ and $x = 0.51$ at 8.9×10^{-3} – 8.7×10^{-5} atm of P_{O_2} (in Chapter III, data from Sugimori et al. (2012)). These changes in k and x with P_{O_2} suggest that the mechanism of Fe(II) oxidation changes at $\sim 8 \mu\text{mol L}^{-1}$ of [O₂]; Fe(II) is oxidized dominantly by O₂ where $x = 1$ at [O₂] $> \sim 8 \mu\text{mol L}^{-1}$ while H₂O₂, derived from O₂, dominantly oxidizes Fe(II) where $x = 0.5$ at [O₂] $< \sim 8 \mu\text{mol L}^{-1}$ (Chapter III). Based on the mechanisms of Fe(II) oxidation suggested in Chapter III, I rewrite Eq. (14) as

$$\lambda = \begin{cases} k_{\text{high}} [\text{O}_2] [\text{OH}^-]^2 & ([\text{O}_2] > 8 \mu\text{mol L}^{-1}) \\ k_{\text{low}} [\text{O}_2]^{0.5} [\text{OH}^-]^2 & ([\text{O}_2] < 8 \mu\text{mol L}^{-1}) \end{cases} \quad (18)$$

where $k_{\text{high}} = 10^{21.18}$ and $k_{\text{low}} = 10^{18.70} \text{ mol}^{-3} \text{ L}^3 \text{ yr}^{-1}$ at 22 °C, which are consistent with the rates reported in Chapter III under both high and low O₂ conditions. To represent the temperature dependence of k_{high} , I used 29 kJ mol⁻¹ as the activation energy given by Millero et al. (1987). The temperature dependence of k_{low} was assumed to be the same as the temperature dependence of the reaction between Fe(II) and H₂O₂, because H₂O₂, derived from O₂, is suggested to be the dominant oxidant under low O₂ conditions (Chapter III). Because Millero and Sotolongo (1989) have shown that the rate of Fe(II)

oxidation by H_2O_2 is temperature-independent, I assumed that k_{low} is temperature-independent.

To include the CO_2 (Fe(II)-carbonate species) effects on the Fe(II) oxidation rate, I further modify the expression of λ (Eq. (18)) as

$$\lambda = \begin{cases} \alpha_{\text{high}} k_{\text{high}} [\text{O}_2] [\text{OH}^-]^2 & ([\text{O}_2] > 8 \mu\text{mol L}^{-1}) \\ \alpha_{\text{low}} k_{\text{low}} [\text{O}_2]^{0.5} [\text{OH}^-]^2 & ([\text{O}_2] < 8 \mu\text{mol L}^{-1}) \end{cases} \quad (19)$$

where α_{high} and α_{low} are the factors that describe the differences in Fe(II) oxidation rate by including CO_2 effects when O_2 level is high and low, respectively. α_{high} is defined by the following equation:

$$\alpha_{\text{high}} \equiv \frac{k_{\text{CH-high}}}{k_{\text{OH-high}}} \quad (20)$$

where $k_{\text{CH-high}}$ is the apparent rate constant of Fe(II) oxidation by O_2 with the reactions of both Fe(II)-hydroxyl and Fe(II)-carbonate species with O_2 ($\text{mol}^{-1} \text{L min}^{-1}$) (Appendix A) and $k_{\text{OH-high}}$ is the apparent rate constant of Fe(II) oxidation only by Fe(II)-hydroxyl species with O_2 ($\text{mol}^{-1} \text{L min}^{-1}$). The values of $k_{\text{CH-high}}$ were obtained from the kinetic data on the rate constants of Fe(II)-hydroxyl and Fe(II)-carbonate species with O_2 given by King (1998) and Santana-Casiano et al. (2005) (see Appendix A for the details of the calculation of $k_{\text{CH-high}}$). Using the kinetic data on reactions of Fe(II)-hydroxyl species with O_2 given by Santana-Casiano et al. (2005), $k_{\text{OH-high}} = 10^{16.46} [\text{OH}^-]^2$ ($\text{mol}^{-1} \text{L min}^{-1}$) at 25 °C. The temperature dependences of $k_{\text{OH-high}}$ and $k_{\text{CH-high}}$ were assumed to be the same as that of k_{high} (29 kJ mol^{-1} of activation energy, Millero et al. (1987)). Using the values of $k_{\text{CH-high}}$ (Fig. A2a in Appendix A) and $k_{\text{OH-high}}$, the α_{high} values were calculated and are plotted as a function of P_{CO_2} and pH in Fig. 2a. The α_{high} values range from 10^{-2} to 10^2 under the conditions of pH = 4–9 and $P_{\text{CO}_2} = 10^{-4}$ –1 atm, meaning that the inclusion of Fe(II)-carbonate species changes Fe(II) oxidation rate by up to two orders of magnitude, and thus is important to accurately describe the rate of Fe(II) oxidation by O_2 in $\text{H}_2\text{O}-\text{CO}_2$ system.

Similarly to Eq. (20), α_{low} in Eq. (19) is defined as

$$\alpha_{\text{low}} \equiv \frac{k_{\text{CH-low}}}{k_{\text{OH-low}}} \quad (21)$$

where $k_{\text{CH-low}}$ is the apparent rate constant of Fe(II) oxidation by H_2O_2 with the reactions of both Fe(II)-hydroxyl and Fe(II)-carbonate species with H_2O_2 ($\text{mol}^{-1} \text{L min}^{-1}$) (Appendix A) and $k_{\text{OH-low}}$ is the apparent rate constant of Fe(II) oxidation only by Fe(II)-hydroxyl species with H_2O_2 ($\text{mol}^{-1} \text{L min}^{-1}$). The values of $k_{\text{CH-low}}$ were obtained

from the rate constants of Fe(II)-hydroxyl and Fe(II)-carbonate species with H_2O_2 , reported by King and Farlow (2000) (see Appendix A for the details). The values of $k_{\text{OH-low}}$ were calculated to be $10^{13.07}[\text{OH}^-]$ ($\text{mol}^{-1} \text{L min}^{-1}$) from the kinetic data on the reactions of Fe(II)-hydroxyl species with H_2O_2 given by González-Davila et al. (2005). $k_{\text{OH-low}}$ can be assumed to be temperature-independent (Millero and Sotolongo, 1989). $k_{\text{CH-low}}$ is not temperature-independent; its temperature dependence was determined from the data given by Millero and Sotolongo (1989) and González-Davila et al. (2005) (see Table A3 in Appendix A). The values of $k_{\text{CH-low}}$ (Fig. A2b in Appendix A) and $k_{\text{OH-low}}$, and Eq. (21) allowed me to calculate α_{low} values which are plotted as a function of P_{CO_2} and pH in Fig. 2b. The calculated α_{low} values are in the range of 10^{-1} – 10^2 when $\text{pH} = 4$ – 9 and $P_{\text{CO}_2} = 10^{-4}$ – 1 atm. Thus, it is necessary to include Fe(II)-carbonate species in Fe(II) oxidation reaction under low O_2 conditions.

The modification of k (k_{high} and k_{low}) and x and the inclusion of α (α_{high} and α_{low}) in Fe(II) oxidation rate expression (Eq. (19)) will improve the accuracy of P_{O_2} estimates in the present model. The parameters for Fe(II) oxidation kinetics are listed in Table 1, together with the thermodynamic data relevant to Fe(II) oxidation (i.e., K_w and K_{HO} , in Eqs. (15) and (16)). See also Tables A1–A3 in Appendix A, which were used for the calculations of $k_{\text{CH-high}}$ and $k_{\text{CH-low}}$.

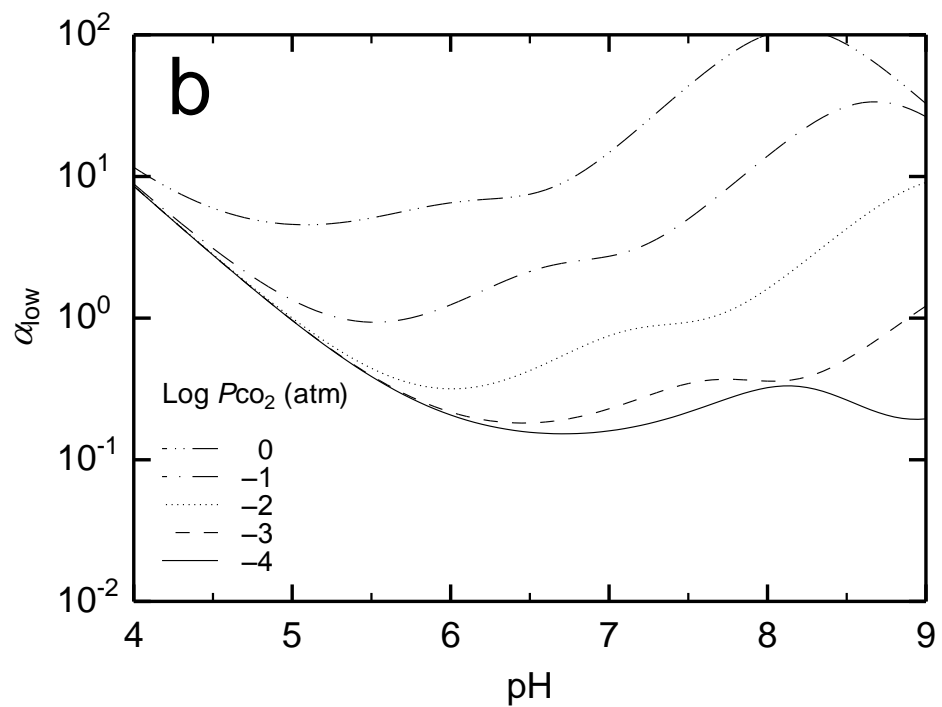
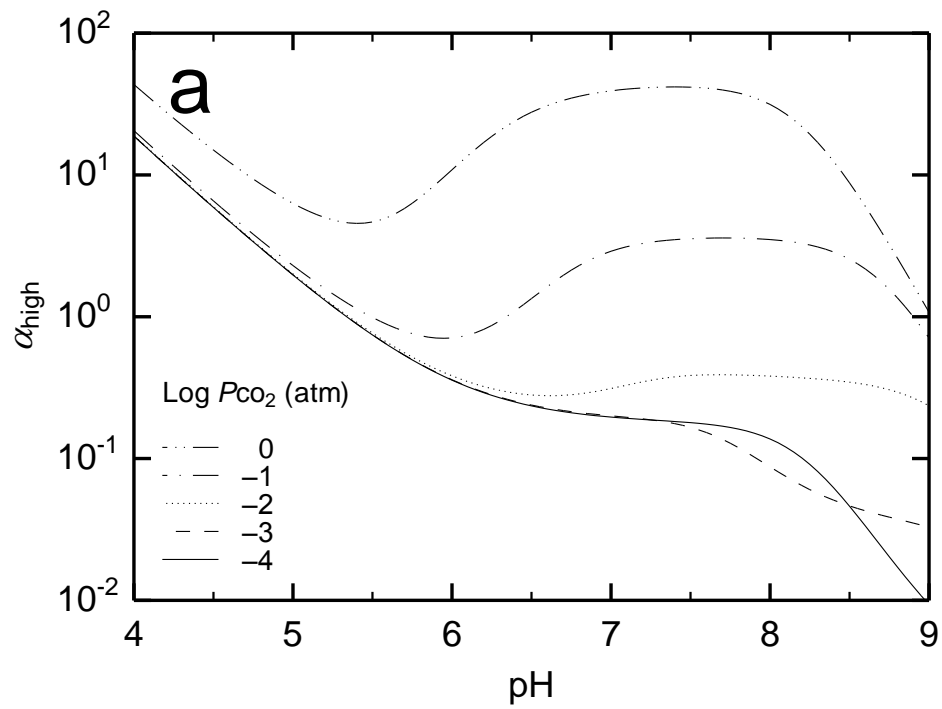


Figure 2. Variations of (a) α_{high} and (b) α_{low} with pH and P_{CO_2} . The values are calculated at 25 °C.

See text for the definitions of α_{high} and α_{low} .

Table 1. The parameters for Fe(II) oxidation.

Parameter	Equation ^a	Reference
k_w	$4 \times 10^{-19} T^3 - 3 \times 10^{-16} T^2 + 8 \times 10^{-14} T - 8 \times 10^{-12}$ ^b	Stumm and Morgan (1996)
k_{HO}	$6 \times 10^{-7} T^2 - 0.0004 T + 0.0607$ ^b	Wilhelm et al. (1977)
k_{high} ^c	$10^{21.18} \exp\{-29(1/T - 1/295.15)/R\}$	Chapter III in this thesis, Millero et al. (1987)
k_{low} ^c	$10^{18.70}$	Chapter III in this thesis, Millero and Sotolongo (1989)
$k_{OH-high}$ ^d	$10^{16.46} \exp\{-29(1/T - 1/298.15)/R\} [OH^-]^2$	Santana-Casiano et al. (2005), Millero et al. (1987)
k_{OH-low} ^d	$10^{13.07} [OH^-]$	González-Davila et al. (2005), Millero and Sotolongo (1989)

^a T is the absolute temperature (K) and R is the gas constant, $8.3 \times 10^{-3} \text{ kJ mol}^{-1} \text{ K}^{-1}$.

^b The equations are fitting functions of the calculated values at 0–30 °C by equations given in references.

^c Unit is $\text{mol}^{-3} \text{ L}^3 \text{ yr}^{-1}$.

^d Unit is $\text{mol}^{-1} \text{ L min}^{-1}$

2.3. P_{O_2} estimation equation for paleosols

Using the modified expression for ϕ (Eq. (13)) and the modified Fe(II) oxidation kinetic expression (Eq. (19)), the estimation of P_{O_2} can be made by the following equation:

$$P_{O_2} = \frac{1}{fK_{HO}} \left(\frac{\phi}{1-\phi} \times \frac{k_f}{\alpha k K_w^2 10^{2pH}} \right)^{1/x} \quad (22)$$

As mentioned in the previous section, k , x and α in Eq. (22) have different values at different O_2 levels (Eq. (19)) and α is also a function of pH and P_{CO_2} (Fig. 2). Eq. (22) shows that once the values of ϕ , pH, P_{CO_2} , k_f , f and temperature are obtained for a given paleosol, I can calculate the P_{O_2} level for the paleosol.

Murakami et al. (2011) have screened the Precambrian paleosols and have picked up five Paleoproterozoic paleosols which can be regarded to retain the ϕ values at the time of weathering. For the calculation of P_{O_2} , I used the five Paleoproterozoic paleosols, namely, the Cooper Lake, Pronto/NAN, Gaborone, Drakenstein and Flin Flon paleosols. The formation ages of the five paleosols are listed in Table 2 together with the observed ϕ values given by Murakami et al. (2011).

3. Constraints on parameter values for the Paleoproterozoic paleosols

I give constraints on the values of pH, P_{CO_2} , k_f , f and temperature during paleoweathering of the Paleoproterozoic paleosols for the estimation of P_{O_2} from Eq. (22) in this section. Murakami et al. (2011) and I, in Chapter II, have given some parameter values which were utilized for the present study. The parameter values not given by Murakami et al. (2011) or in Chapter II were estimated from the literature on the Paleoproterozoic paleosols and weathering.

3.1. Temperature and O_2 diffusion into soil (f)

In Chapter II, I have constrained the temperatures at which eight Neoproterozoic-Paleoproterozoic paleosols formed, including the above five Paleoproterozoic paleosols, mainly based on the temperature-solute composition relationships in the literature. The estimates of temperature for the five Paleoproterozoic paleosols in Chapter II are listed in Table 2. Although different temperature ranges have

been obtained for different paleosols (Table 2), I first considered 0–30 °C as the general temperature range in Section 3. The temperature ranges specific to the paleosols (e.g., 12–29 °C for the Gaborone paleosol) will be used in Section 4 after all parameter values are determined in the range of 0–30 °C of temperature in Section 3.

It is difficult to give constraints on individual f values for the Paleoproterozoic paleosols. The range of 0.1–1 (Fig. 1a) was adopted as likely one for f for the present study although the range could be too large. Nonetheless, the range of 0.1–1 covers the O₂ diffusion conditions in weathering profiles considered by Yokota et al. (2013) (Fig. 1a) and can cover most conditions of weathering profiles (c.f., Holland and Zbinden, 1988; Pinto and Holland, 1988; Sheldon, 2006).

3.2. pH and P_{CO_2}

In Chapter II, I have developed the method by which P_{CO_2} can be estimated from paleosols for given temperatures. Because the method also estimates pH and cation concentrations in porewater in the course of estimation of P_{CO_2} , the consistent sets of pH and P_{CO_2} can be obtained by the method. The pH/ P_{CO_2} -temperature relationships given in Chapter II for the five Paleoproterozoic are illustrated in Figs. 3 and 4, respectively, and the data are listed in Table 3. Although there are large uncertainties in pH and P_{CO_2} (the areas between pairs of thin curves in Figs. 3 and 4, respectively), I have shown that the geometric means of the maximum and minimum pH and P_{CO_2} are the most likely values (bold curves in Figs. 3 and 4, respectively) (see Section 3.1 in Chapter II). Thus, in the present study, only the most likely pH and P_{CO_2} values were considered. Note that for the Cooper Lake paleosol, estimates of pH and P_{CO_2} cannot be made at higher temperatures (> 9 °C) (Figs. 3 and 4, see Section 4.2 in Chapter II). Therefore, the estimation of P_{O_2} for the Cooper Lake paleosol was conducted only at low temperatures (< 9 °C) while the estimation of P_{O_2} for the other paleosols were made in the general temperature range (0–30 °C) (Section 3.1).

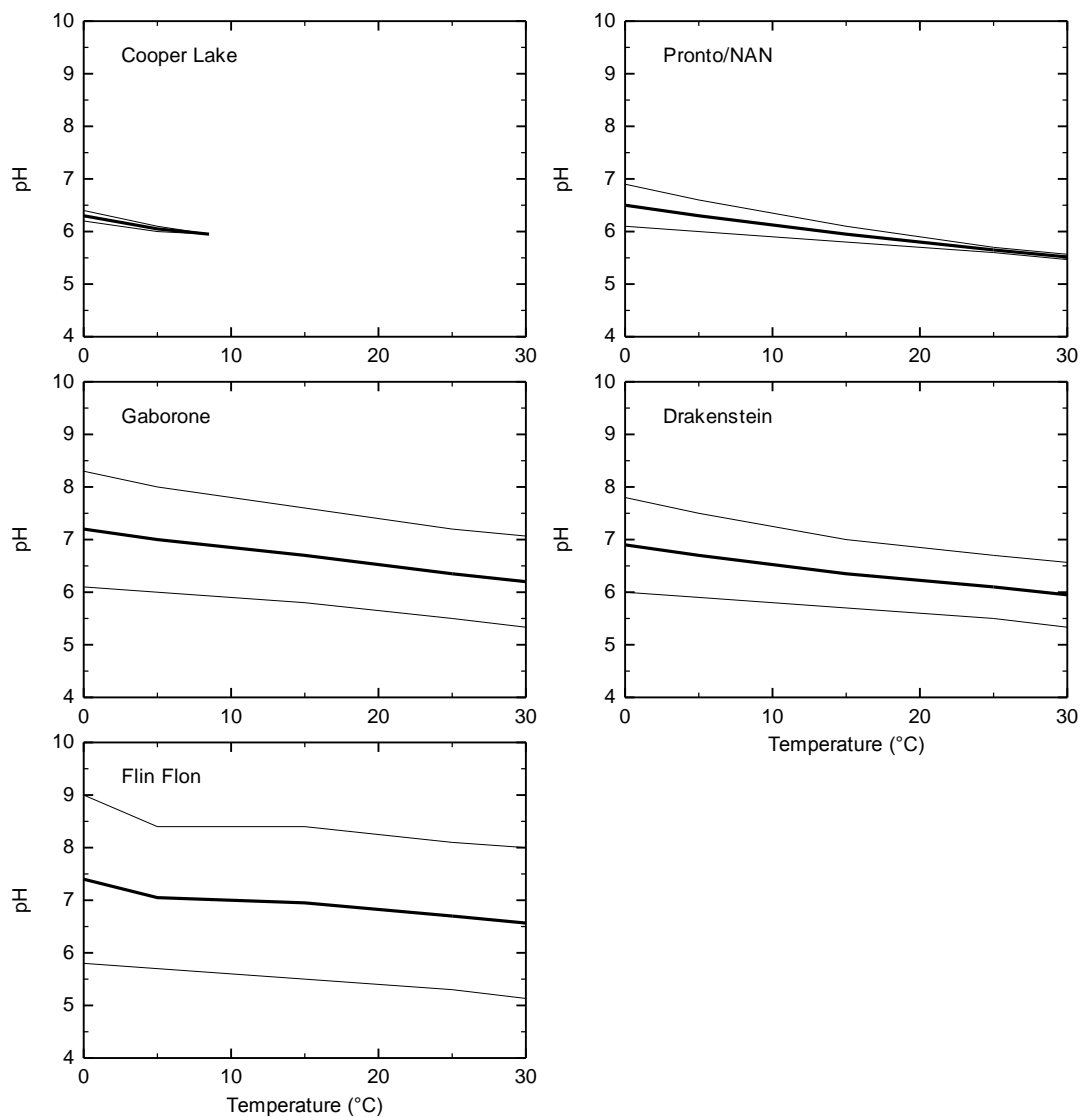


Figure 3. Estimated pH of porewater for the Paleoproterozoic paleosols, plotted against temperature (0–30 °C). The possible range of pH for a given paleosol is represented by the area between pairs of thin curves and the geometric means of the maximum and minimum pH are plotted as bold curves. Note that for the Cooper Lake paleosol, estimation cannot be made at > 9 °C. The data are from Chapter II in this thesis.

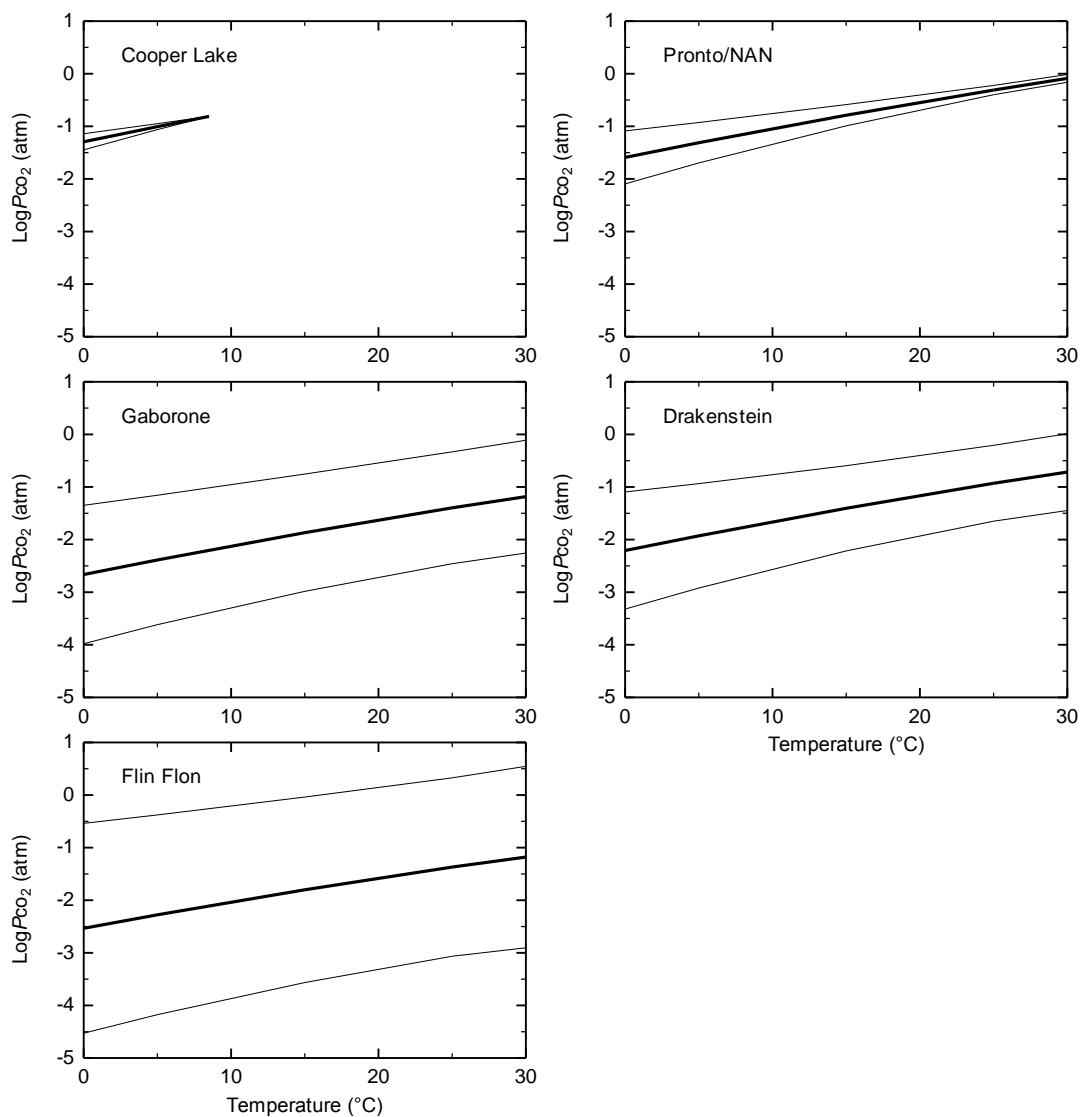


Figure 4. Estimated P_{CO_2} for the Paleoproterozoic paleosols, plotted against temperature (0–30 °C).

The possible range of P_{CO_2} for a given paleosol is represented by the area between pairs of thin curves and the geometric means of the maximum and minimum P_{CO_2} are plotted as bold curves. Note that for the Cooper Lake paleosol, estimation cannot be made at > 9 °C. The data are from Chapter II in this thesis.

Table 2. Physicochemical parameters and formation ages for the Paleoproterozoic paleosols.

Paleosol	Age ^a (Ga)	ϕ ^b	Temperature ^c (°C)	CF ^d	d ^d (km)	θ ^e	[Si-rock] _{loss} ^f (mol m ⁻³)	$\Sigma[X\text{-rock}]_{\text{loss}}$ ^f (eq m ⁻³)	h ^g (m)	k_f ^h (yr ⁻¹)
Cooper Lake	2.475–2.440	0.01	0–9	0.69	7	0.36	7870	14760	7.4	0.16 (0.08–0.32)
Pronto/NAN	2.475–2.440	0.01–0.03	0–30	0.79	7	0.29	5890	10650	2.2	0.15 (0.10–0.22)
Gaborone	2.245–2.059	0.51–0.75	12–29	0.64	9	0.38	11410	12530	23.5	0.22 (0.17–0.28)
Drakenstein	2.222–1.928	0.69–0.95	0–30	0.62	7	0.44	11530	16540	7.7	0.23 (0.11–0.45)
Flin Flon	1.9–1.8	≥ 0.97	8–30	0.89	8	0.26	2260	7040	10.3	0.11 (0.04–0.35)

^a From Rye and Holland (1998).

^b ϕ is the ratio of the precipitated Fe(III)-(oxyhydr)oxides from the dissolved Fe(II) to the total dissolved Fe(II) during weathering. The values are from Murakami et al. (2011).

^c From Chapter II in this thesis.

^d d is the burial depth (km) and CF is the compaction factor of paleosol. The values are from Murakami et al. (2011).

^e θ is the porosity, estimated from d and CF in Table 1 using Eqs. (25) and (26).

^f Calculated from the retention factors (see Chapter II in this thesis).

^g h is the thickness of paleosol corrected for compaction factor. The values are calculated from the uncorrected thickness of paleosols (Utsunomiya et al. (2003), G-Farrow and Mossman (1988), Yang and Holland (2003), Wiggering and Beukes (1990) and Holland et al. (1989) for the Cooper Lake, Pronto/NAN, Gaborone, Drakenstein and Flin Flon paleosols, respectively) and the CF values in Table 2.

^h Estimated in this study (Section 3.3). The most likely values are listed with possible ranges in parentheses.

Table 3. Estimated $[\text{Si}]_{\text{ss}}$, pH and P_{CO_2} at various temperatures for the Paleoproterozoic paleosols ^a.

Paleosol	Age ^b (Ga)	Parameter	0 (°C)	5 (°C)	15 (°C)	25 (°C)	40 (°C)
Cooper Lake	2.475–2.440	$\log [\text{Si}]_{\text{ss}}$ (mol L ⁻¹)	-(2.95–3.00)	-(2.90–2.92)	n.c. ^c	n.c.	n.c.
		pH	6.2–6.4	6.0–6.1	n.c.	n.c.	n.c.
		$\log P_{\text{CO}_2}$ (atm)	-(1.14–1.45)	-(0.95–1.06)	n.c.	n.c.	n.c.
Pronto/NAN	2.475–2.440	$\log [\text{Si}]_{\text{ss}}$ (mol L ⁻¹)	-(2.95–3.13)	-(2.90–3.04)	-(2.80–2.87)	-(2.71–2.75)	-(2.59–2.61)
		pH	6.1–6.9	6.0–6.6	5.8–6.1	5.6–5.7	5.2–5.3
		$\log P_{\text{CO}_2}$ (atm)	-(1.09–2.10)	-(0.93–1.70)	-(0.59–0.99)	-(0.22–0.40)	0.31–0.40
Gaborone	2.245–2.059	$\log [\text{Si}]_{\text{ss}}$ (mol L ⁻¹)	-(2.95–3.42)	-(2.90–3.34)	-(2.80–3.20)	-(2.71–3.10)	-(2.59–2.98)
		pH	6.1–8.3	6.0–8.0	5.8–7.6	5.5–7.2	5.0–6.8
		$\log P_{\text{CO}_2}$ (atm)	-(1.35–3.98)	-(1.16–3.62)	-(0.75–2.98)	-(0.33–2.46)	-1.84–0.33
Drakenstein	2.222–1.928	$\log [\text{Si}]_{\text{ss}}$ (mol L ⁻¹)	-(2.95–3.35)	-(2.90–3.25)	-(2.80–3.09)	-(2.71–2.97)	-(2.59–2.86)
		pH	6.0–7.8	5.9–7.5	5.7–7.0	5.5–6.7	5.0–6.3
		$\log P_{\text{CO}_2}$ (atm)	-(1.10–3.32)	-(0.94–2.92)	-(0.60–2.22)	-(0.20–1.65)	-1.04–0.45
Flin Flon	1.9–1.8	$\log [\text{Si}]_{\text{ss}}$ (mol L ⁻¹)	-(2.95–3.66)	-(2.90–3.58)	-(2.80–3.44)	-(2.71–3.32)	-(2.59–3.23)
		pH	5.8–9.0	5.7–8.4	5.5–8.4	5.3–8.1	4.8–7.8
		$\log P_{\text{CO}_2}$ (atm)	-(0.54–4.53)	-(0.39–4.18)	-(0.04–3.56)	-3.06–0.33	-2.58–0.99

^a After Chapter II in this thesis.

^b From Rye and Holland (1998).

^c Not calculated (see Chapter II in this thesis for details).

3.3. Water flow (k_f)

There have been no reports on the estimates of the water flow (k_f in the present study) for the five Paleoproterozoic paleosols. Furthermore, the estimation method of k_f from paleosols has not been reported, either. I estimated k_f for the Paleoproterozoic paleosols using the parameters below, recorded in the paleosols. Three relationships can be utilized to constrain k_f from the paleosols: (i) the mass balance of Si between rock and water phases, (ii) the relationship between weathering flux and runoff and (iii) the relationship between k_f and hydraulic conductivity, which are described in Section 3.3.1, 2 and 3, respectively. By combining the constraints on k_f from the three relationships, the k_f values for the Paleoproterozoic paleosols are estimated (Section 3.3.4).

3.3.1. Constraints from mass balance of Si

Applying the equation, describing the mass balance of elements between rock and water phases during weathering, given in Chapter II, to Si,

$$[\text{Si - rock}]_{\text{loss}} = \theta \sigma k_f [\text{Si}]_{\text{ss}} t_{\text{tot}} \quad (23)$$

where $[\text{Si-rock}]_{\text{loss}}$ is the loss amount of Si from rock phase per unit rock volume (mol m^{-3}) and $[\text{Si}]_{\text{ss}}$ is the steady-state concentration of Si in porewater in a weathering profile (mol L^{-1}). Eq. (23) (or the mass balance of Si) means that the loss amount of Si from rock phase per unit rock volume ($[\text{Si-rock}]_{\text{loss}}$) must be equal to the amount of Si transported out of weathering profile by water flow ($\sigma \theta k_f [\text{Si}]_{\text{ss}} t_{\text{tot}}$). For the derivation of Eq. (23), it was assumed that θ , σ , k_f and $[\text{Si}]_{\text{ss}}$ are constant during weathering of a given profile (Chapter II). Solving Eq. (23) for k_f ,

$$k_f = \frac{[\text{Si - rock}]_{\text{loss}}}{\theta \sigma [\text{Si}]_{\text{ss}} t_{\text{tot}}} \quad (24)$$

Eq. (24) shows that I can estimate k_f by giving $[\text{Si-rock}]_{\text{loss}}$, $[\text{Si}]_{\text{ss}}$, θ , σ and t_{tot} . Si was chosen out of the possible elements because $[\text{Si}]_{\text{ss}}$ can be constrained to a relatively small range (Holland, 1978; Rye et al., 1995; Ohmoto et al., 2004), and thus, k_f . Indeed, $[\text{Si}]_{\text{ss}}$ has been constrained in Chapter II as a function of temperature and is given for the five Paleoproterozoic paleosols in Table 3. The values of $[\text{Si-rock}]_{\text{loss}}$ for the Paleoproterozoic paleosols are also given in Chapter II (Table 2). Total weathering duration time t_{tot} was assumed to be between 5×10^4 and 10^6 yr (Price et al., 2005). The porosity θ of a paleosol can be estimated from the relationship between compaction

factor, CF , burial depth of paleosols, d (km), and porosity θ , which has been given by Sheldon and Retallack (2001):

$$CF = \frac{1 - \theta}{1 - \theta \exp(-\kappa d)} \quad (25)$$

where κ is the empirically-determined parameter (Sheldon and Retallack, 2001):

$$\kappa = 0.03 \exp(4.52\theta) \quad (26)$$

Using the values of d and CF for the Paleoproterozoic paleosols estimated by Murakami et al. (2011) (Table 2), the values of θ were calculated for the Paleoproterozoic paleosols and are listed in Table 2. The water saturation ratio σ is hard to constrain. I assume that σ is in the range of $1-10^3 \text{ L m}^{-3}$. Note that σ cannot exceed 10^3 L m^{-3} , because the value of 10^3 L m^{-3} corresponds to the water-saturated condition.

Out of the parameters, $[\text{Si-rock}]_{\text{loss}}$, $[\text{Si}]_{\text{ss}}$, θ , σ and t_{tot} (Tables 2 and 3), $[\text{Si}]_{\text{ss}}$ is temperature dependent (Table 3), and thus, k_f is also temperature dependent (Eq. (24)). In Figs. 5a–c, the estimated ranges of k_f are plotted as a function of temperature when $\sigma = 10^3$, 10^2 and 10 L m^{-3} , respectively, for the Pronto/NAN paleosol as an example. The estimation of k_f at $30 \text{ }^\circ\text{C}$ was conducted by obtaining the value of $[\text{Si}]_{\text{ss}}$ at $30 \text{ }^\circ\text{C}$, which is interpolated from those at different temperatures listed in Table 3. Compared with the large change in k_f caused by the change in σ (see the difference in scale of the vertical axis between Figs. 5a–c), the difference in k_f caused by temperature difference is minor (Figs. 5a–c). Therefore, σ , but not temperature, affects k_f dominantly; the k_f values consistent at $0-30 \text{ }^\circ\text{C}$ for a given σ value are taken as the estimates of k_f for the σ value (shaded areas in Figs. 5a–c). The ranges of k_f shown as shaded areas in Figs. 5a–c are plotted as a function of σ in Fig. 5d, indicating the large effects of σ on the estimates of k_f clearly. As expected from Eq. (24), there is an inverse relationship between σ and k_f . Fig. 5d shows that k_f can be changed by orders of magnitude when the σ value is changed by the same orders.

3.3.2. Constraints from empirical relationship between weathering flux and runoff

Bluth and Kump (1994) have reported the empirical relationships between Si-flux/bicarbonate-flux by weathering (F_{Si} and F_{CO_2} , $\text{mol m}^{-2} \text{ yr}^{-1}$, respectively) and runoff (r , m yr^{-1}) for different lithologies, which are respectively described by

$$\log F_{\text{Si}} = a \log r + b \quad (27) \quad \text{and}$$

$$\log F_{\text{CO}_2} = c \log r + d \quad (28)$$

where a , b , c and d represent the empirical constants which vary with lithology. For example, $a = 0.8023$, $b = -0.7172$, $c = 0.691$ and $d = -0.436$ for basalt while $a = 0.8489$,

$b = -0.8702$, $c = 0.749$ and $d = -0.58$ for granite. Note that r in Eqs. (27) and (28) is related to k_f by the following equation:

$$r = 10^{-3} \times h \theta \sigma k_f \quad (29)$$

where 10^{-3} is the unit conversion number ($\text{m}^3 \text{L}^{-1}$) and h is the thickness (m) of a paleosol corrected for the compaction factor, CF . Eq. (29) shows that the estimation of r leads to the estimation of k_f for paleosols, given the values of h , θ and σ . The values of h and θ are available for the Paleoproterozoic paleosols (Table 2) and the σ values are in the range of $1-10^3 \text{ L m}^{-3}$ (Section 3.3.1). The estimation of r for the Paleoproterozoic paleosols can be made by Eqs. (27) and (28), once the values of F_{Si} and F_{CO_2} are obtained for the Paleoproterozoic paleosols. F_{Si} can be calculated from

$$F_{\text{Si}} = \frac{h[\text{Si} - \text{rock}]_{\text{loss}}}{t_{\text{tot}}} \quad (30)$$

Similarly, the flux of bicarbonate by weathering is calculated from

$$F_{\text{CO}_2} = \frac{h \sum_X Z_X [\text{X} - \text{rock}]_{\text{loss}}}{t_{\text{tot}}} \quad (31)$$

where $X = \text{Na}, \text{K}, \text{Mg}, \text{Ca}$ and Fe , Z_X is the valence number of X and $[\text{X-rock}]_{\text{loss}}$ is the loss amount of X from rock phase per unit rock volume (mol m^{-3}). The right hand side of Eq. (31) is equal to the total cation flux ($\text{eq m}^{-2} \text{yr}^{-1}$) (Chapter II). The values of $\sum Z_X [\text{X-rock}]_{\text{loss}}$ were calculated following the method in Chapter II and are tabulated in Table 2 for the Paleoproterozoic paleosols, together with the values of $[\text{Si-rock}]_{\text{loss}}$. I calculated F_{Si} and F_{CO_2} values for the Paleoproterozoic paleosols from Eqs. (30) and (31), respectively, using the values of $[\text{Si-rock}]_{\text{loss}}$, $\sum Z_X [\text{X-rock}]_{\text{loss}}$ and h in Table 2 with $t_{\text{tot}} = 5 \times 10^4 - 10^6 \text{ yr}$.

The two different sets of the equations, i.e., Eqs. (27) and (30), and Eqs. (28) and (31) can give two sets of r for each paleosol. Note that the five Paleoproterozoic paleosols were developed on basalts except that the Pronto/NAN on granite (Murakami et al., 2011) and the corresponding values of a , b , c and d for Eqs. (27) and (28) are given above. Then, I calculated r values for each paleosol from Eqs. (27) and (28). The calculated ranges of r can be converted to the ranges of k_f for a given σ value (Eq. (29)). The estimates of k_f from the relationships between F_{Si} and r (Eqs. (27), (29) and (30)) and those between F_{CO_2} and r (Eqs. (28), (29) and (31)) are plotted as the areas between pairs of dashed lines and between those of dotted lines, respectively, as a function of σ for the Paleoproterozoic paleosols (Fig. 6). Also plotted in Fig. 6 are the estimates from the mass balance of Si obtained in the Section 3.3.1, represented by the areas between pairs of solid lines. Fig. 6 demonstrates that k_f is proportional to reciprocal σ for a given

r (Eq. (29)) for the $F_{\text{Si}}-r$ and $F_{\text{CO}_2}-r$ relationships as is seen for the k_f estimates from the mass balance of Si (Eq. (24)). I can obtain the k_f - σ regions consistent between the three types of the estimates, which are represented by shaded areas in Fig. 6. The obtained k_f values still have large uncertainties and are in the range of 0.01 – 1000 yr^{-1} . The large uncertainties of k_f are due to those of σ .

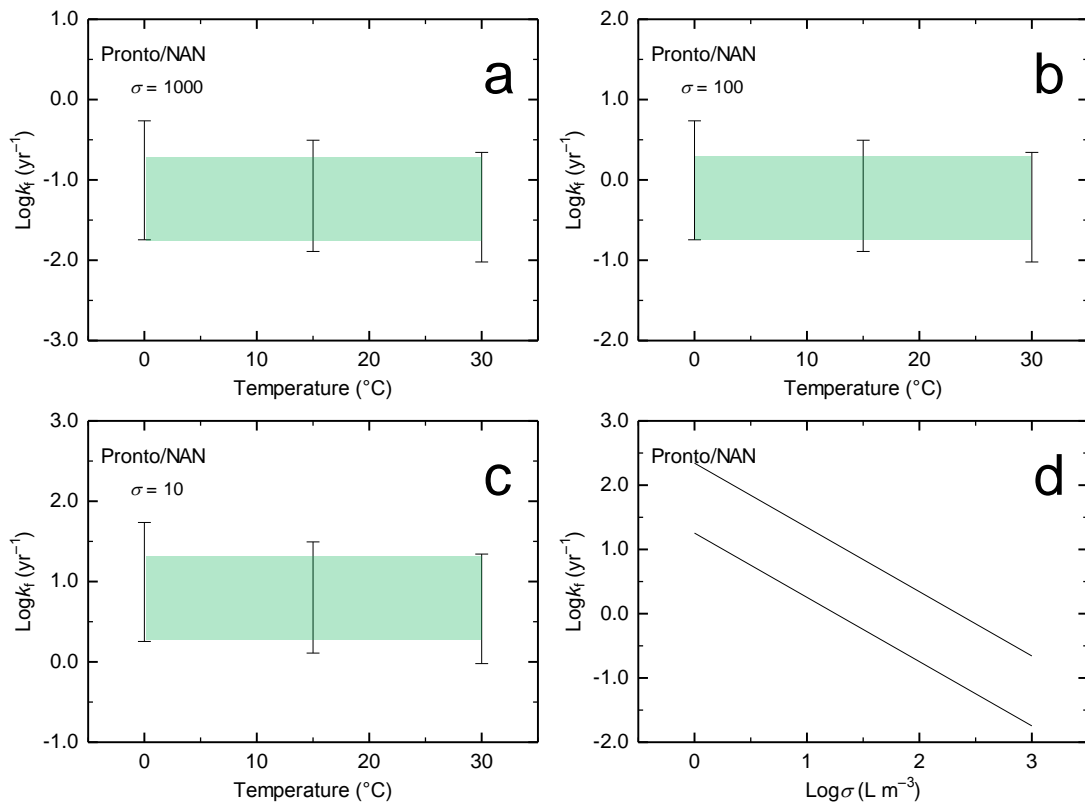


Figure 5. Estimation of k_f based on the mass balance of Si for the Pronto NAN paleosol for (a) $\sigma = 1000 \text{ L m}^{-3}$, (b) $\sigma = 100 \text{ L m}^{-3}$ and (c) $\sigma = 10 \text{ L m}^{-3}$ plotted against temperature (0–30 $^{\circ}\text{C}$), and (d) the k_f range consistent between 0–30 $^{\circ}\text{C}$ plotted against σ (1 – 10^3 L m^{-3}). The Pronto/NAN paleosol is taken as an example. The k_f values consistent between 0–30 $^{\circ}\text{C}$ are represented by shaded areas in Figs. 5a–c.

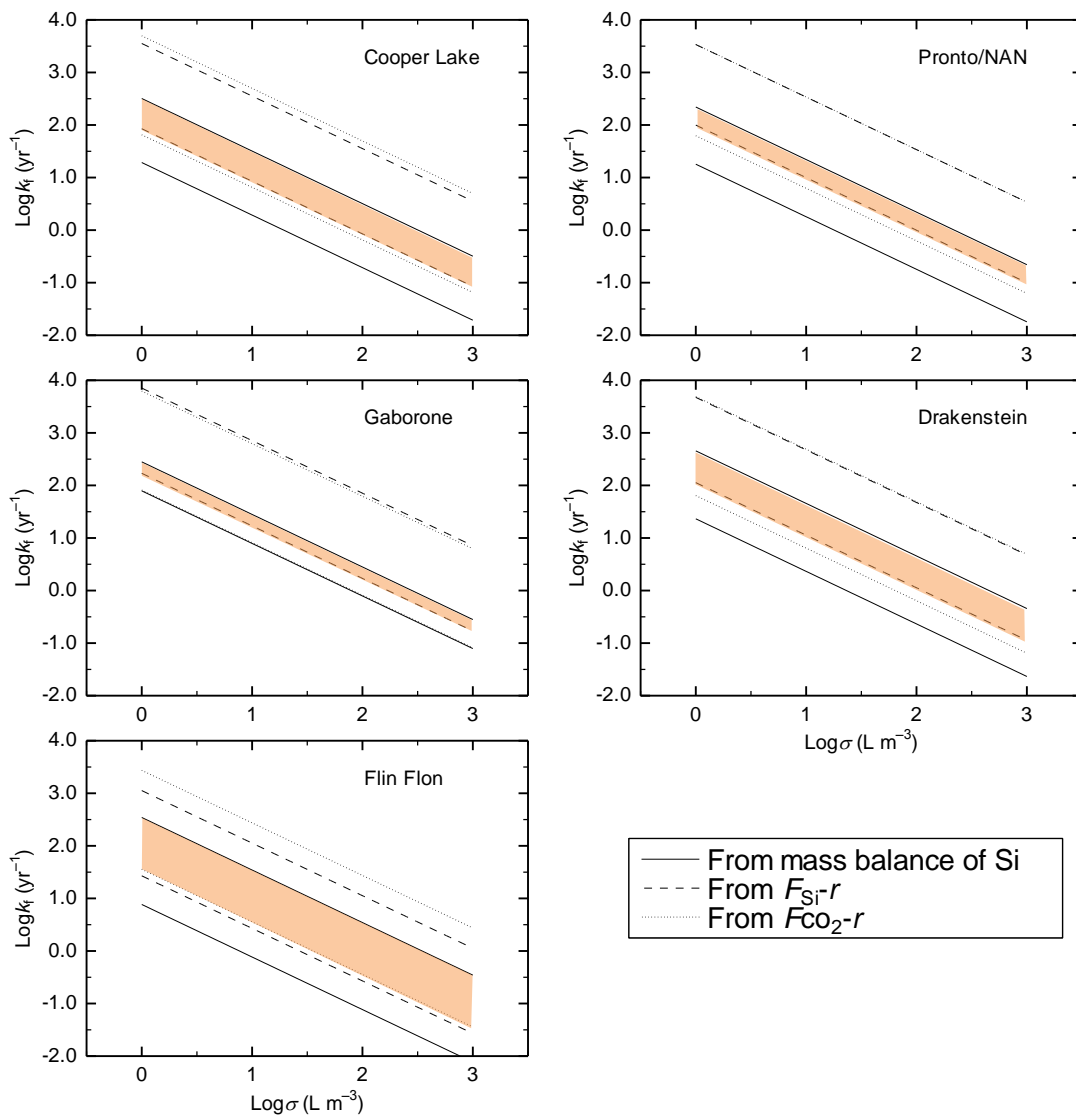


Figure 6. Estimated k_f values for the Paleoproterozoic paleosols based on the mass balance of Si (the areas between pairs of solid lines), the relationships between Si flux and runoff (the areas between pairs of dashed lines) and the relationships between bicarbonate flux and runoff (the areas between pairs of dotted lines), plotted against σ ($1\text{--}10^3 \text{ L m}^{-3}$). The k_f - σ regions consistent between the three types of the estimates are represented as shaded areas.

3.3.3. Constraints from hydraulic conductivity

The volumetric water flow per unit rock volume, q , is related to the hydraulic conductivity of a weathering profile (K_h , m yr^{-1}). According to Darcy's law (c.f., Hillel, 1980),

$$qh \times 10^{-3} = K_h \Delta H / h \quad (32)$$

where ΔH is the hydraulic head difference (m) and 10^{-3} is the unit conversion number ($\text{m}^3 \text{L}^{-1}$). The volumetric water flow per unit rock volume (q , $\text{L m}^{-3} \text{yr}^{-1}$) is converted to the volumetric water flux per unit rock area ($qh \times 10^{-3}$, m yr^{-1}), which is proportional to hydraulic gradient ($\Delta H/h$) with the proportionality represented by K_h (Hillel, 1980). I can assume $\Delta H = h$ for the weathering profile in steady state (c.f., Stonestrom et al., 1998), and then, using Eq. (17), Eq. (32) can be rewritten as

$$k_f = 10^3 K_h / \theta \sigma h \quad (33)$$

from which I can constrain k_f by evaluating K_h . The value of K_h depends on various factors, including σ (Hillel, 1980). Empirically, the following relationship between K_h and σ is known (Hillel, 1980):

$$K_h \propto \sigma^m \quad (34)$$

where $m > 1$ (c.f., Hillel, 1980; Toledo et al., 1990). Thus, Eqs. (33) and (34) indicate that the value of k_f increases with σ (c.f., Stonestrom et al., 1998; Yokoyama, 2013). Then, when the weathering profile is water-saturated, i.e., $\sigma = 1000 \text{ L m}^{-3}$, k_f must be the maximum, and be equal to $K_{h\text{-sat}}/\theta h$ (yr^{-1}) where $K_{h\text{-sat}}$ is the hydraulic conductivity when the profile is water-saturated (m yr^{-1}). For a clayey soil, $K_{h\text{-sat}}$ is in the range of $0.01\text{--}10 \text{ m yr}^{-1}$ (Hillel, 1980) and therefore, the maximum k_f must be in the range of $0.0002\text{--}100 \text{ yr}^{-1}$ assuming $h = 1\text{--}10 \text{ m}$ and $\theta = 0.1\text{--}0.5$. The estimates of k_f for the Paleoproterozoic paleosols with $\sigma = 1000 \text{ L m}^{-3}$ (Fig. 6) are within the range of $0.0002\text{--}100 \text{ yr}^{-1}$, and thus, can be regarded to represent the k_f values derived from $K_{h\text{-sat}}$. Therefore, the k_f values for the Paleoproterozoic paleosols with $\sigma = 1000 \text{ L m}^{-3}$ (Fig. 6) should be the maximum k_f values, i.e., the upper constraints on k_f .

3.3.4. k_f values for the Paleoproterozoic paleosols

Combining the constraints on k_f given in Sections 3.3.1–3.3.3, I can estimate most likely values of k_f for the Paleoproterozoic paleosols. In Fig. 7, the k_f - σ regions estimated from the mass balance of Si and the weathering flux-runoff relationships (shaded areas in Fig. 6) are represented by the areas between pairs of solid lines, and the

upper constraints on k_f from hydraulic conductivity are represented by the dashed horizontal bold lines. These constraints give the most likely k_f - σ regions as shown by the shaded areas in Fig. 7 where the k_f values are significantly constrained. I take the geometric means of the maximum and minimum k_f values in the shaded areas in Fig. 7 as the most likely values of k_f : 0.16, 0.15, 0.22, 0.23 and 0.11 yr^{-1} for the Cooper Lake, Pronto/NAN, Gaborone, Drakenstein and Flin Flon paleosols, respectively (Table 2). These values of k_f are similar to those observed in modern weathering profiles (0.07–0.18 yr^{-1} , White et al., 1998, 2002, 2005, 2009). The errors of k_f are ± 0.28 , ± 0.17 , ± 0.11 , ± 0.30 and ± 0.49 in log unit for the Cooper Lake, Pronto/NAN, Gaborone, Drakenstein and Flin Flon paleosols, respectively, and thus not so significant. I assume that k_f is temperature-independent parameter in the present study (c.f., Section 3.3.1), and thus use the most likely values of k_f for all temperatures (0–30 °C).

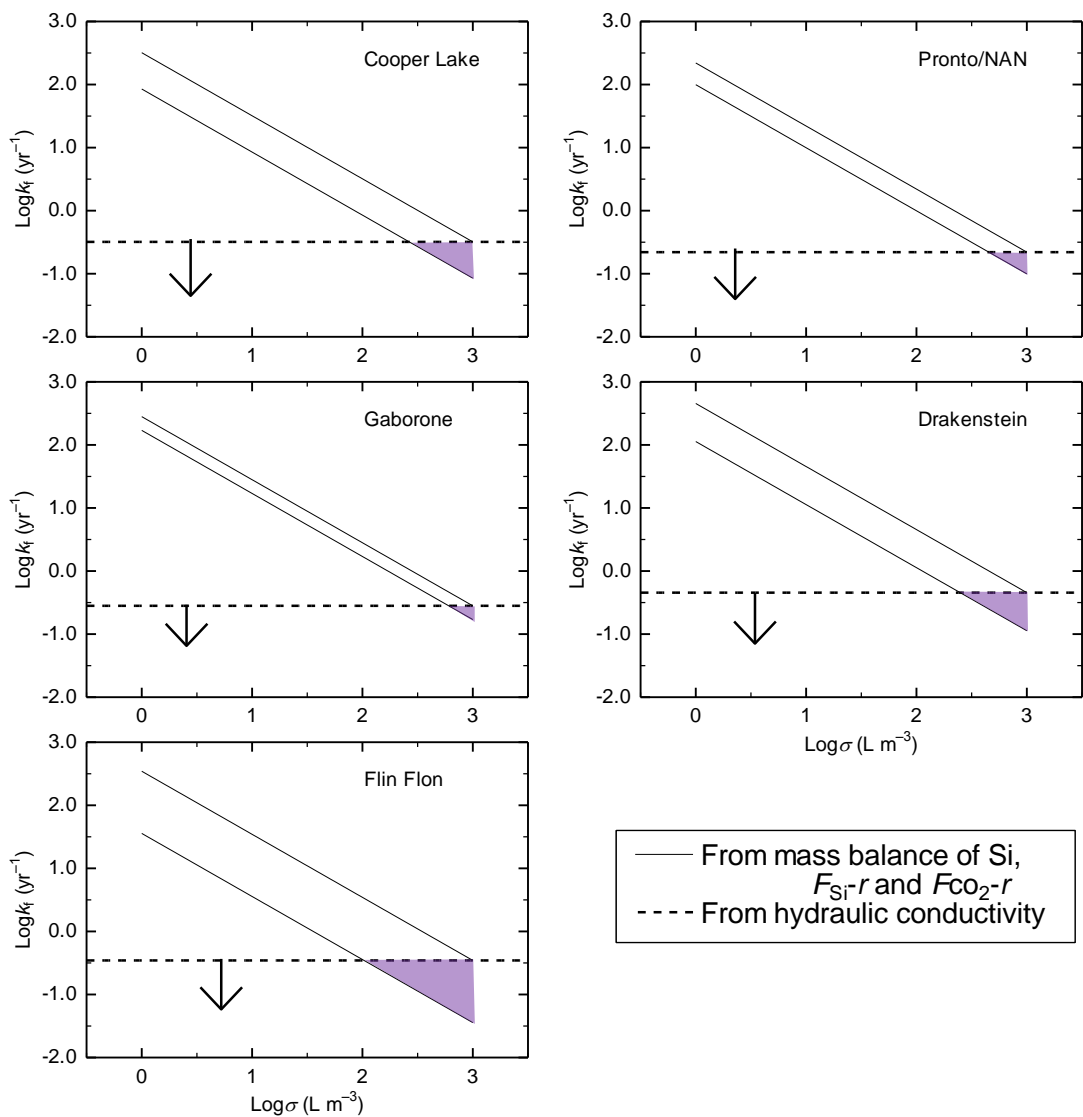


Figure 7. Constraints on k_f for the Paleoproterozoic paleosols from the mass-balance of Si and the relationships between weathering fluxes and runoff (the areas between pairs of solid lines, the same as the shaded areas in Fig. 6) and from the relationship between k_f and hydraulic conductivity (dashed lines), plotted against σ . The constraints from the relationship between k_f and hydraulic conductivity set the upper limits on k_f (see arrows). The k_f - σ regions consistent between the constraints from all the relationships are represented by shaded areas.

4. Atmospheric O₂ evolution in the Paleoproterozoic

Using the parameters constrained for the Paleoproterozoic paleosols in Section 3 (Tables 2 and 3 and Figs. 3, 4 and 7), I can calculate P_{O_2} levels for the Paleoproterozoic paleosols from Eq. (22) in Section 2. In Fig. 8, P_{O_2} levels calculated for the Paleoproterozoic paleosols are plotted against temperature (0–30 °C, spaced by 1 °C), with $f = 0.1$ and 1, the minimum and maximum values (open and solid squares, respectively) corresponding to the maximum and minimum P_{O_2} estimates, respectively. Error bars in Fig. 8 represent the errors of observed ϕ for the paleosols (Table 2). The most likely values of pH, P_{CO_2} and k_f were used for the calculations (bold curves in Figs. 3 and 4, and Table 2). Note that the P_{O_2} levels calculated for the Flin Flon paleosol are only lower limits (see arrows in Fig. 8) because of the available ϕ value (Table 2). The P_{O_2} levels for the Cooper Lake paleosol are those at < 9 °C because of the available CO₂ and pH estimates at < 9 °C (Figs. 3 and 4). Fig. 8 shows that the estimated P_{O_2} value generally decreases as temperature increases, because at higher temperatures, the Fe(II) oxidation rate constant is larger and thus less oxygen is required for a given ϕ value. Strictly, the temperature dependences of estimated P_{O_2} are different between the paleosols; the P_{O_2} values estimated for the Pronto/NAN and Flin Flon paleosols are more temperature-dependent than those for the Gaborone and Drakenstein paleosols; for the Cooper Lake paleosol, the temperature dependence of the estimated P_{O_2} values at lower temperatures (< 6 °C) is even opposite to those exhibited by the other paleosols. The present model reveals that the complicated temperature dependence of P_{O_2} (Fig. 8) results from the temperature dependence of P_{CO_2} (Fig. 4) and the effects of P_{CO_2} on Fe(II) oxidation (Section 2.2 and Appendix A), which is not expected by Yokota et al. (2013) (c.f., Fig. 1d). On the other hand, the effects of f on P_{O_2} are straightforward; the range of 0.1–1 of f causes the difference in estimated P_{O_2} levels by one order of magnitude as expected from Eq. (22).

I plot P_{O_2} levels against age in the Paleoproterozoic by adding the temperature range and formation age specific to each paleosol (Table 2) to the calculated results (Fig. 8) in Fig. 9. The vertical and horizontal lengths of boxes in Fig. 9 represent the possible ranges of P_{O_2} (with uncertainties discussed in Section 3) and age (with uncertainties in Table 2), respectively. Note that the estimated P_{O_2} levels at ~1.85 Ga (the Flin Flon paleosol) only show the lower limits of P_{O_2} (arrow attached to the box at ~1.85 Ga in Fig. 9). The P_{O_2} range at ~2.46 Ga in Fig. 9 is the range consistent between the Cooper Lake and Pronto/NAN paleosols. Fig. 9 reveals that P_{O_2} increased from $10^{-6.7}$ – $10^{-5.4}$

atm at ~2.46 Ga (the Cooper Lake and Pronto/NAN paleosols) to $10^{-5.2}$ – $10^{-3.2}$ atm at ~2.15 Ga (the Gaborone paleosol), $10^{-3.9}$ – $10^{-1.2}$ atm at ~2.08 Ga (the Drakenstein paleosol) and to more than $10^{-4.6}$ – $10^{-2.5}$ atm at ~1.85 Ga (the Flin Flon paleosol). These estimated levels of P_{O_2} are consistent with the constraints indicated by the presence and absence of MIF-S in sedimentary records (arrows with dashed base lines in Fig. 9), supporting that the estimation of P_{O_2} for the present study is reasonable. Furthermore, Kurzweil et al. (2013) have recently suggested that $P_{O_2} = \sim 10^{-7.7}$ – $10^{-5.7}$ atm at 2.5–2.4 Ga based on the analyses of multiple sulfur isotopes, which is also well consistent with my estimate at ~2.46 Ga (the Cooper Lake and Pronto/NAN paleosols).

The uncertainties in P_{O_2} are relatively small, considering the large uncertainties in temperature and f . The P_{O_2} ranges shown in Fig. 9 do not consider the uncertainties in k_f . With the uncertainties in k_f , the maximum and minimum P_{O_2} increases and decreases, respectively, by 0.56, 0.22, 0.60 and 0.98 in log unit, at ~2.46, ~2.15, ~2.08 and ~1.85 Ga, respectively, which does not change the general conclusion given in this chapter. Note that the present estimates of P_{O_2} depend on the estimates of the most likely pH and P_{CO_2} reported in Chapter II (bold lines in Figs. 3 and 4, Section 3.2).

I compare my estimates of P_{O_2} in Fig. 9 with the quantitative patterns of oxygen rise at 2.5–2.0 Ga proposed by Claire et al. (2006), Goldblatt et al. (2006) and Beal et al. (2011) (Figs. 10a, b and c, respectively) who have used box modeling. Beal et al. (2011) have modified the model by Claire et al. (2006) by introducing the faster anaerobic oxidation of methane. A slightly rapid rise of oxygen at ~2.4 Ga is proposed by Claire et al. (2006) (Fig. 10a) while Goldblatt et al. (2006) and Beal et al. (2011) propose an almost sudden rise of oxygen by ~5 orders of magnitude at ~2.4 Ga (Figs. 10b and c). The increase model by Claire et al. (2006) is consistent with the present estimates of P_{O_2} while the models by Goldblatt et al. (2006) and Beal et al. (2011) are inconsistent. Recently, on the other hand, Murakami et al. (2011) have suggested that the oxygen rise in the GOE might have been gradual in long term, based on the Fe(II) kinetics and behaviors of Fe and Mn in the Paleoproterozoic paleosols (Fig. 10d). Fig. 10 suggests that a drastic rise of oxygen would not have occurred at ~2.4 Ga, supporting a slightly rapid rise of oxygen at ~2.4 Ga and a gradual rise of oxygen in the Paleoproterozoic in long term.

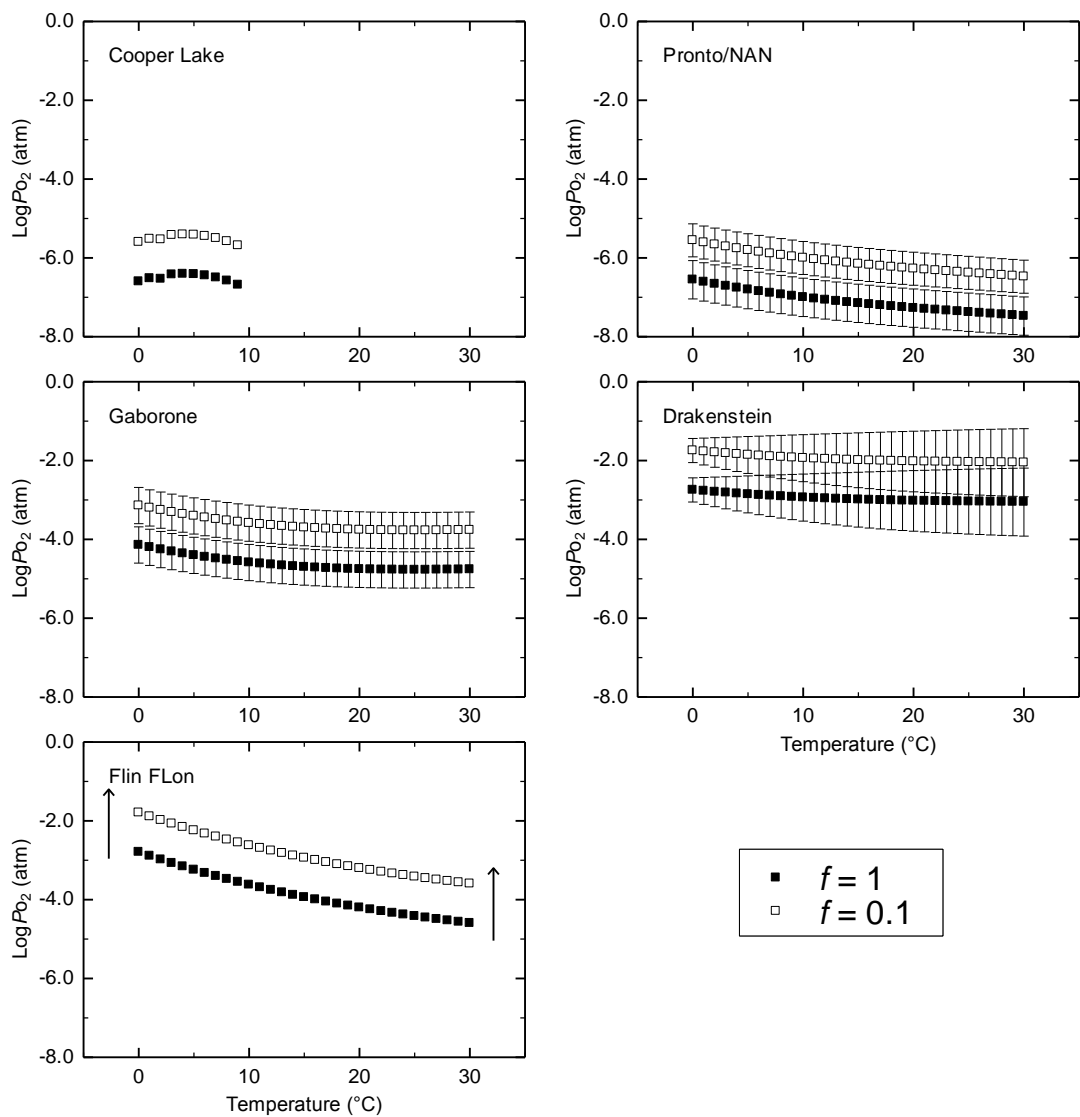


Figure 8. Estimates of P_{O_2} at different temperatures for the Paleoproterozoic paleosols with $f=1$ (solid squares) and 0.1 (open squares). The vertical bars represent the errors of observed ϕ reported for the paleosols (Table 2). Note that the estimates of P_{O_2} for the Flin Flon paleosol denote only lower limits (see arrows).

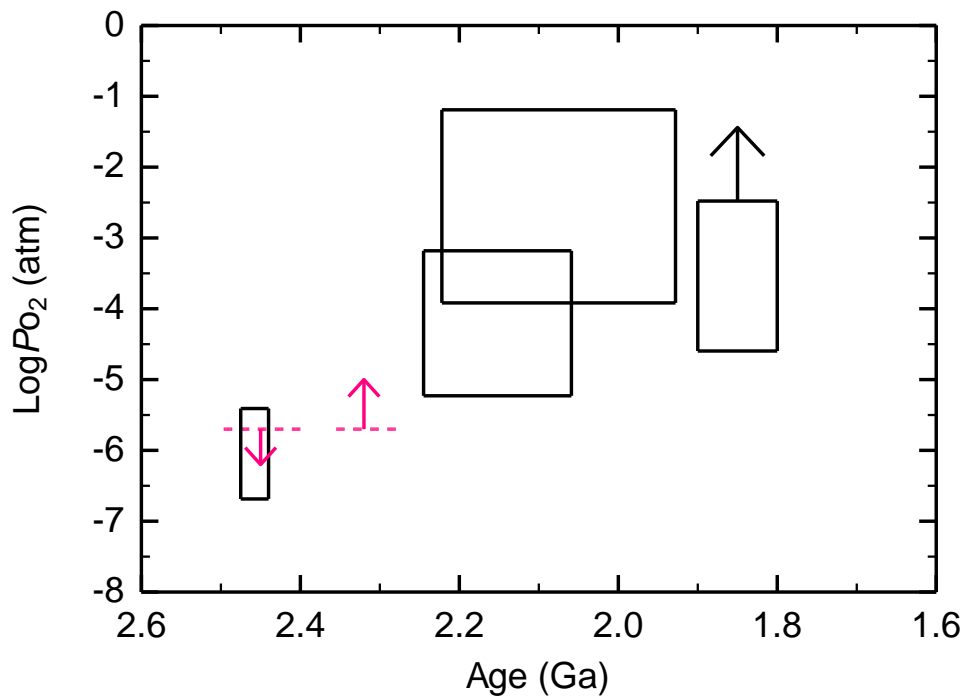


Figure 9. Variation of P_{O_2} with age in the Paleoproterozoic. Boxes represent the possible ranges of P_{O_2} and formation age of the Paleoproterozoic paleosols. The box at ~2.45 Ga shows the P_{O_2} range consistent between the Cooper Lake and Pronto/NAN paleosols. The box at ~1.85 Ga (the Flin Flon paleosol) only gives the lower limit (see an arrow attached to the box). The arrows with dashed base lines represent the P_{O_2} constraints from the absence and presence of MIF-S.

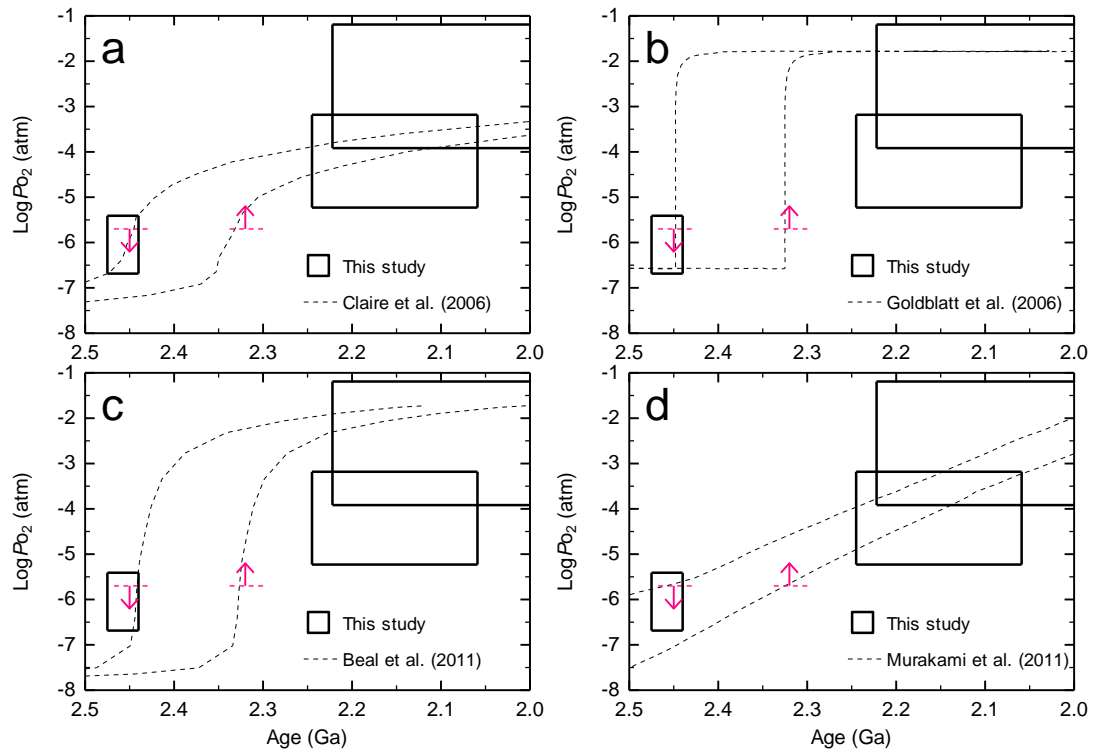


Figure 10. Comparison of the estimated P_{O_2} levels (boxes) with the quantitative patterns of oxygen rise at 2.0–2.5 Ga (dashed curves) proposed by (a) Claire et al (2006), (b) Goldblatt et al. (2006), (c) Beal et al. (2011) and (d) Murakami et al. (2011). The arrows with dashed base lines represent the constraints on P_{O_2} from the presence and absence of MIF-S.

5. Conclusions

The Paleoproterozoic paleosols were utilized to more precisely estimate atmospheric oxygen levels in the GOE or in the Paleoproterozoic than previously estimated. To estimate P_{O_2} levels from the paleosols, I developed a new weathering model that considers steady-state weathering and essentially calculates the ratio of the precipitated Fe(III)-(oxyhydr)oxides from dissolved Fe(II) to the total dissolved Fe(II) during weathering (ϕ), as a function of P_{O_2} . The input parameters, pH of porewater, P_{CO_2} , water flow rate, temperature and O_2 diffusion into soil at the time of weathering, which significantly affect the P_{O_2} estimates, were scrutinized so that the model can give robust estimates of P_{O_2} . I adopted the parameter values of P_{CO_2} and pH specific to the paleosols given in Chapter II. The water flow parameter, k_f , was estimated from the mass balance of Si, the relationships between weathering fluxes and runoff, and the relationships between hydraulic conductivity and k_f , for each Paleoproterozoic paleosol. The temperatures specific to the paleosols at the time of weathering were adopted from Chapter II while the effects of diffusion of O_2 into soil were assumed in a reasonable range. To further improve the accuracy of estimation of P_{O_2} by the model, the Fe(II) oxidation kinetic law in the model was modified so that the effects of P_{O_2} , pH and P_{CO_2} were accurately reflected in the Fe(II) oxidation kinetic expression. Using the constrained values of the above parameters for the Paleoproterozoic paleosols, the present model calculated P_{O_2} levels for each paleosol: $10^{-6.7}$ – $10^{-5.4}$ atm at ~2.46 Ga, $10^{-5.2}$ – $10^{-3.2}$ atm at ~2.15 Ga, $10^{-3.9}$ – $10^{-1.2}$ atm at ~2.08 Ga and more than $10^{-4.6}$ – $10^{-2.5}$ atm at ~1.85 Ga. These constraints on P_{O_2} indicate that the gradual rise of oxygen in the Paleoproterozoic is likely in long term, as suggested by Murakami et al. (2011). Comparison of the calculated P_{O_2} levels to the estimates of P_{O_2} in the literature suggests that a drastic rise of oxygen would not have occurred at ~2.4 Ga, supporting a slightly rapid rise of oxygen at ~2.4 Ga and a gradual rise of oxygen in the Paleoproterozoic in long term.

The present model with the scrutinized parameter values can provide more robust P_{O_2} estimates than previously reported. However, I still have large uncertainties for the parameters, which will be improved in the future.

Appendix A

In H₂O-CO₂ system, Fe(II) oxidation by O₂ and H₂O₂ occurs in the forms of Fe(II)-hydroxyl and Fe(II)-carbonate species, namely, Fe(II)OH⁺, Fe(II)(OH)₂⁰, Fe(II)HCO₃⁺, Fe(II)CO₃⁰, Fe(II)(CO₃)₂²⁻ and Fe(II)(CO₃)(OH)⁻, in addition to the form of free Fe(II) (King, 1998; Santana-Casiano et al., 2005). The concentrations of these species are determined by the association/dissociation reactions and the thermodynamic constants for the reactions listed in Table A1. The contribution of concentration of species *i* ([*i*], mol L⁻¹) to the total Fe(II) concentration ($\beta_i \equiv [i]/[\text{Fe(II)}]$) can be calculated using the thermodynamic constants in Table A1. Fig. A1 shows the β values for Fe(II)-hydroxyl and Fe(II)-carbonate species at $P_{\text{CO}_2} = 10^{-4}$ and 1 atm (Figs. A1a and b, respectively).

The overall oxidation rate of Fe(II) by O₂ is determined by the reactions of all Fe(II) species (free Fe(II), Fe(II)-hydroxyl and Fe(II)-carbonate species) with O₂ and their rate constants, which are listed in Table A2. Defining $k_{i\text{-high}}$ as the rate constant for the reaction of species *i* with O₂ (mol⁻¹ L min⁻¹), the overall oxidation rate by O₂ is described by

$$\frac{d[\text{Fe(II)}]}{dt} = -4 \sum_i k_{i\text{-high}} [i][\text{O}_2] = -4[\text{Fe(II)}][\text{O}_2] \sum_i \beta_i k_{i\text{-high}} \quad (\text{A1})$$

where 4 is the stoichiometric number of Fe(II) oxidation by O₂ and the unit of *t* is min only in this appendix. I defined $k_{\text{CH-high}}$ as the apparent rate constant of Fe(II) oxidation by O₂ in which the reactions of both Fe(II)-hydroxyl and Fe(II)-carbonate species are taken into account. Thus, by excluding the effects of [Fe(II)] and [O₂] from Eq. (A1), $k_{\text{CH-high}}$ is obtained:

$$k_{\text{CH-high}} = 4 \sum_i \beta_i k_{i\text{-high}} \quad (\text{A2})$$

The value of $k_{\text{CH-high}}$ was obtained based on Eq. (A2) and the thermodynamic and kinetic data in Tables A1 and A2, and is plotted as a function of pH and P_{CO_2} in Fig. A2a.

Similarly, the overall oxidation rate of Fe(II) by H₂O₂ is represented by the sum of the rates of the reactions of all Fe(II) species (free Fe(II), Fe(II)-hydroxyl and Fe(II)-carbonate species) with H₂O₂. The rate constants for the reactions are listed in Table A3. Defining $k_{i\text{-low}}$ as the rate constant of species *i* with H₂O₂ (mol⁻¹ L min⁻¹), the overall oxidation rate by H₂O₂ is described by

$$\frac{d[\text{Fe(II)}]}{dt} = -2 \sum_i k_{i\text{-low}} [i][\text{H}_2\text{O}_2] = -2[\text{Fe(II)}][\text{H}_2\text{O}_2] \sum_i \beta_i k_{i\text{-low}} \quad (\text{A3})$$

where 2 is the stoichiometric number of Fe(II) oxidation by H₂O₂. I defined $k_{\text{CH-low}}$ as the apparent rate constant of Fe(II) oxidation by H₂O₂ which takes into account the

reactions of Fe(II)-hydroxyl and Fe(II)-carbonate species. Thus, by excluding the effects of [Fe(II)] and [H₂O₂] from Eq. (A3), $k_{\text{CH-low}}$ is obtained:

$$k_{\text{CH-low}} = 2 \sum_i \beta_i k_{i-\text{low}} \quad (\text{A4})$$

The value of $k_{\text{CH-low}}$ was obtained based on Eq. (A4) and the thermodynamic and kinetic data in Tables A1 and A3, and is plotted as a function of pH and P_{CO_2} in Fig. A2b.

Table A1. Thermodynamic constants for Fe(II) speciation.

Reaction	Equilibrium constant at 25°C in log unit	Standard change in enthalpy (kJ mol ⁻¹)
H ₂ O = H ⁺ + OH ⁻	-14.00 ^a	-58.7 ^a
CO ₂ + H ₂ O = H ₂ CO ₃	-1.47 ^a	-21.3 ^a
H ₂ CO ₃ = H ⁺ + HCO ₃ ⁻	-6.35 ^a	11.9 ^a
HCO ₃ ⁻ = H ⁺ + CO ₃ ²⁻	-10.33 ^a	17.0 ^a
Fe(II) + H ₂ O = Fe(II)OH ⁺ + H ⁺	-9.51 ^b	40.3 ^c
Fe(II) + 2H ₂ O = Fe(II)(OH) ₂ ⁰ + 2H ⁺	-20.61 ^b	120.8 ^c
Fe(II) + HCO ₃ ⁻ = Fe(II)HCO ₃ ⁺	1.47 ^b	-18.0 ^c
Fe(II) + CO ₃ ²⁻ = Fe(II)CO ₃ ⁰	5.69 ^b	-45.6 ^c
Fe(II) + 2CO ₃ ²⁻ = Fe(II)(CO ₃) ₂ ²⁻	7.45 ^b	-15.5 ^{c,d}
Fe(II) + CO ₃ ²⁻ + OH ⁻ = Fe(II)(CO ₃)(OH) ⁻	9.97 ^b	-184.0 ^{c,d}

^a From Stumm and Morgan (1996).

^b From King (1998).

^c From Delany and Lundeen (1990).

^d Extrapolated from the relationships between the equilibrium constants and the standard enthalpy changes for the other Fe(II) species.

Table A2. Rate constants of oxidation of Fe(II) species by O₂ at 25 °C.

Reaction ^a	Rate constant at 25°C in log unit (mol ⁻¹ L min ⁻¹)	Reference
Fe(II) + O ₂ ⇒ Fe(III) + O ₂ ⁻	-4.26	King (1998)
Fe(II)OH ⁺ + O ₂ ⇒ Fe(III)OH ²⁺ + O ₂ ⁻	2.62	King (1998)
Fe(II)(OH) ₂ ⁰ + O ₂ ⇒ Fe(III)(OH) ₂ ⁺ + O ₂ ⁻	7.72	King (1998)
Fe(II)HCO ₃ ⁺ + O ₂ ⇒ Fe(III)HCO ₃ ²⁺ + O ₂ ⁻	-0.60	Santana-Casiano et al. (2005)
Fe(II)CO ₃ ⁰ + O ₂ ⇒ Fe(III)CO ₃ ⁺ + O ₂ ⁻	-0.55	Santana-Casiano et al. (2005)
Fe(II)(CO ₃) ₂ ²⁻ + O ₂ ⇒ Fe(III)(CO ₃) ₂ ⁻ + O ₂ ⁻	5.82	King (1998)
Fe(II)(CO ₃)(OH) ⁻ + O ₂ ⇒ Fe(III)(CO ₃)(OH) ⁰ + O ₂ ⁻	4.0	King (1998)

^a Activation energies of all the reactions are assumed to be 29 kJ mol⁻¹.

Table A3. Rate constants and activation energies of oxidation of Fe(II) species by H₂O₂.

Reaction	Rate constant at 25°C in log unit ^a (mol ⁻¹ L min ⁻¹)	Activation energy (kJ mol ⁻¹)
Fe(II) + H ₂ O ₂ ⇒ Fe(III) + OH ⁻ + OH [•]	3.70	35.6 ^b
Fe(II)OH ⁺ + H ₂ O ₂ ⇒ Fe(III)OH ²⁺ + OH ⁻ + OH [•]	7.36	46.0 ^b
Fe(II)(OH) ₂ ⁰ + H ₂ O ₂ ⇒ Fe(III)(OH) ₂ ⁺ + OH ⁻ + OH [•]	10.8	55.4 ^c
Fe(II)HCO ₃ ⁺ + H ₂ O ₂ ⇒ Fe(III)HCO ₃ ²⁺ + OH ⁻ + OH [•]	5.57	56.2 ^d
Fe(II)CO ₃ ⁰ + H ₂ O ₂ ⇒ Fe(III)CO ₃ ⁺ + OH ⁻ + OH [•]	6.12	56.2 ^c
Fe(II)(CO ₃)(OH) ⁻ + H ₂ O ₂ ⇒ Fe(III)(CO ₃)(OH) ⁰ + OH ⁻ + OH [•]	9.30	120.2 ^c

^a From King and Farlow (2000).

^b From Millero and Sotolongo (1989).

^c From González-Davila et al. (2005).

^d Assumed to be the same as the activation energy of Fe(II)CO₃⁰ + H₂O₂.

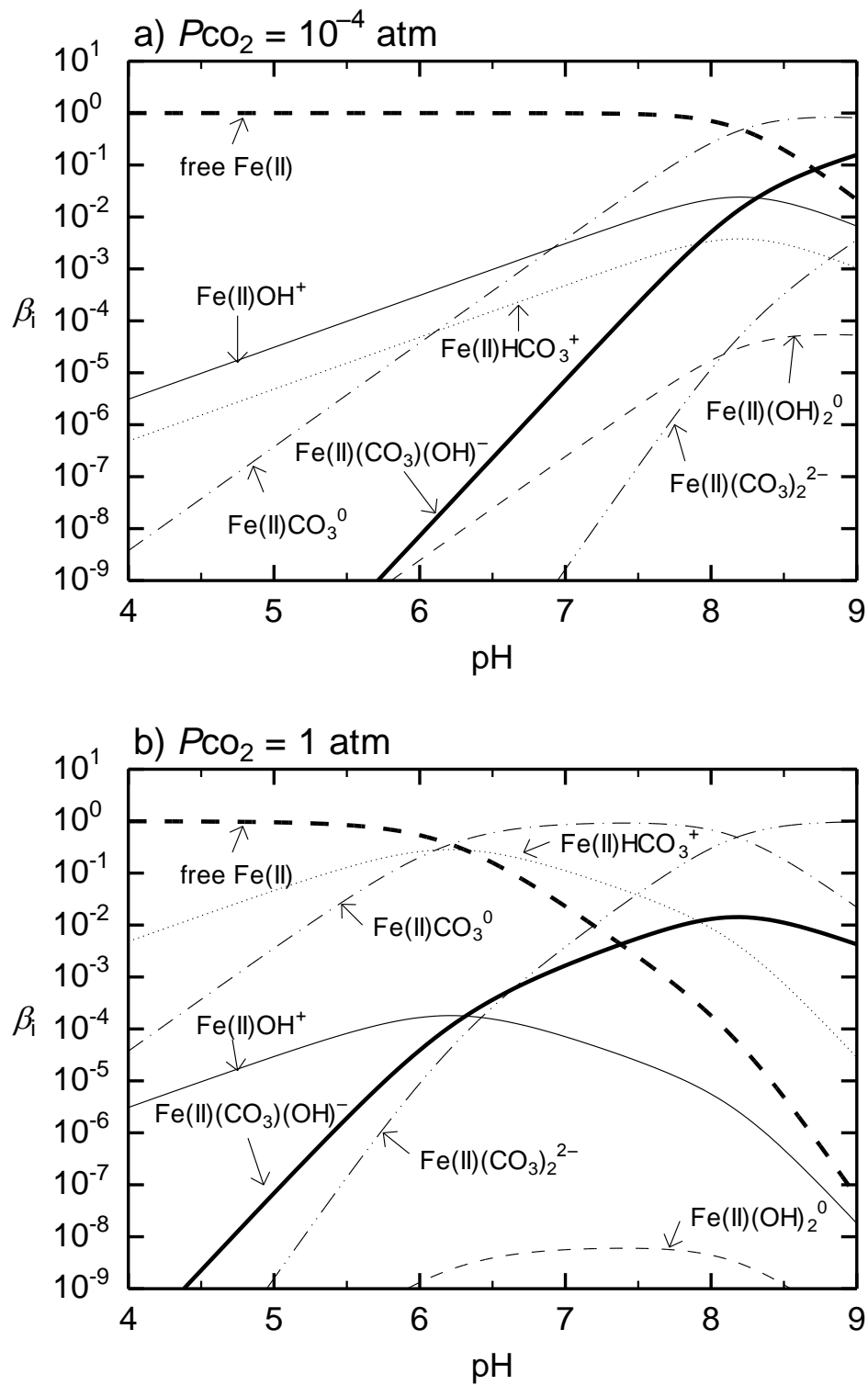


Figure A1. Concentration-contributions of various Fe(II) species (β_i) as a function of pH when P_{CO_2} = (a) 10^{-4} atm and (b) 1 atm. The values at 25 °C are calculated. The definition of β_i is given in Appendix A.

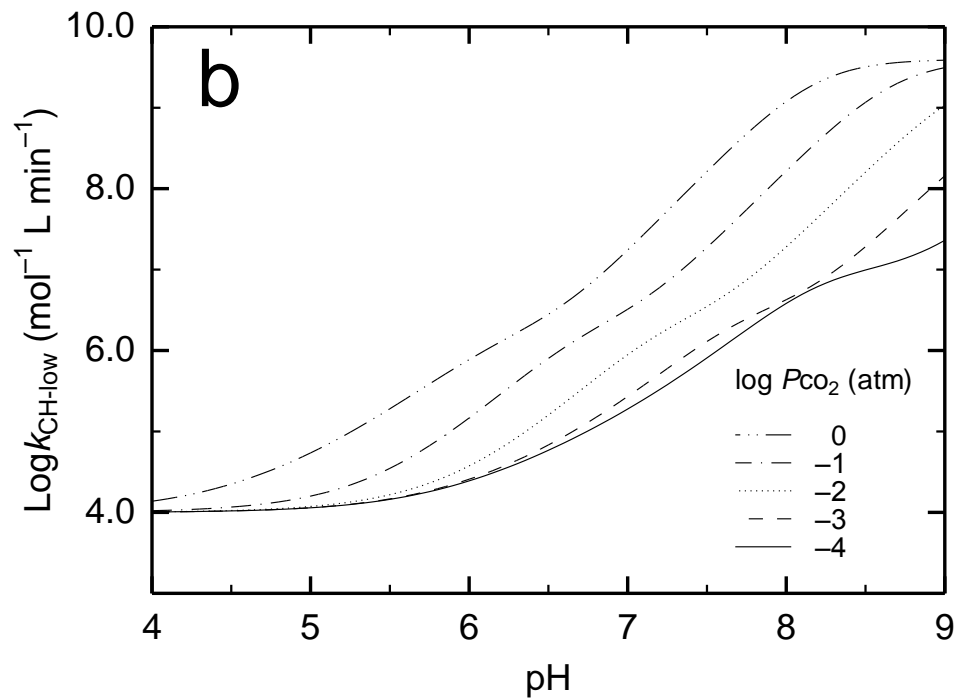
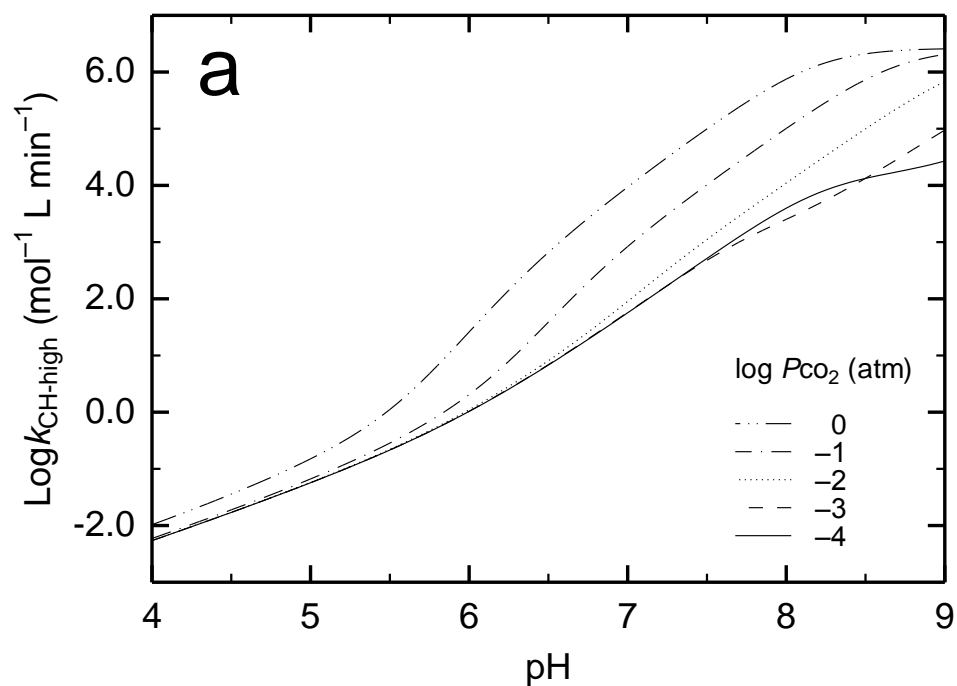


Figure A2. The apparent rate constants of Fe(II) with (a) O_2 and (b) H_2O_2 as a function of pH and P_{CO_2} . The values at 25 °C are calculated. The definitions of $k_{\text{CH-high}}$ and $k_{\text{CH-low}}$ are given in Appendix A.

References

- Anbar A. D. and Knoll A. H. (2002) Proterozoic ocean chemistry and evolution: A bioinorganic bridge? *Science* **297**, 1137–1142.
- Beal E. J., Claire M. W. and House C. H. (2011) High rates of anaerobic methanotrophy at low sulfate concentrations with implications for past and present methane levels. *Geobiology* **9**, 131–139.
- Bekker A., Holland H. D., Wang P. -L., Rumble III D., Stein H. J., Hannah J. L., Coetzee L. L. and Beukes N. J. (2004) Dating the rise of atmospheric oxygen. *Nature* **427**, 117–120.
- Bekker A., Karhu J. A. and Kaufman A. J. (2006) Carbon isotope record for the onset of the Lomagundi carbon isotope excursion in the Great Lakes area, North America. *Precambrian Res.* **148**, 145–180.
- Berner R. A. (1978) Rate control of mineral dissolution under Earth surface conditions. *Am. J. Sci.* **278**, 1235–1252.
- Beukes N. J. and Klein C. (1990) Geochemistry and sedimentology of a facies transition — from microbanded to granular iron-formation — in the early Proterozoic Transvaal Supergroup, South Africa. *Precambrian Res.* **47**, 99–139.
- Brantley S. L. and White A. F. (2009) Approaches to modeling weathered regolith. *Rev. Mineral. Geochem.* **70**, 435–484.
- Canfield D. E. (1998) A new model for Proterozoic ocean chemistry. *Nature* **396**, 450–453.
- Catling D. C. and Claire M. W. (2005) How Earth's atmosphere evolved to an oxic state: A status report. *Earth Planet. Sci. Lett.* **237**, 1–20.
- Claire M. W., Catling D. C. and Zahnle K. J. (2006) Biogeochemical modelling of the rise in atmospheric oxygen. *Geobiol.* **4**, 239–269.
- Farquhar J., Bao T. H. and Thiemens M. H. (2000) Atmospheric influence of earth's earliest sulfur cycle. *Science* **289**, 756–759.
- Farquhar J. and Wing B. A. (2003) Multiple sulfur isotopes and the evolution of the atmosphere. *Earth Planet. Sci. Lett.* **213**, 1–13.
- G-Farrow C. E. and Mossman D. J. (1988) Geology of Precambrian paleosols at the base of the Huronian supergroup, Elliot Lake, Ontario, Canada. *Precambrian Res.* **42**, 107–139.
- Goldblatt C., Lenton T. M. and Watson A. J. (2006) Bistability of atmospheric oxygen and the Great Oxidation. *Nature* **443**, 683–686.

- González-Davila M., Santana-Casiano J. M. and Millero F. J. (2005) Oxidation of iron (II) nanomolar with H₂O₂ in seawater. *Geochim. Cosmochim. Acta* **69**, 83–93.
- Hannah J. L., Bekker A., Stein H. J., Markey R. J. and Holland H. D. (2004) Primitive Os and 2316 Ma age for marine shale: implications for Paleoproterozoic glacial events and the rise of atmospheric oxygen. *Earth Planet. Sci. Lett.* **225**, 43–52.
- Hillel D. (1980) *Fundamentals of Soil Physics*. Academic Press.
- Holland H. D. (1984) *The Chemical Evolution of the Atmosphere and Oceans*. Princeton University Press, Princeton, NJ.
- Holland H. D., Feakes C. R. and Zbinden E. A. (1989) The Flin Flon paleosol and the composition of the atmosphere 1.8 bybp. *Am. J. Sci.* **289**, 362–389.
- Holland H. D. (1994) Early Proterozoic atmospheric change. In *Early Life on Earth: Nobel Symposium 84* (ed. S. Bengtson). Columbia University Press, New York, pp. 237–244.
- Holland H. D. and Zbinden E. A. (1988) Paleosols and the evolution of atmosphere: Part I. In *Physical and Chemical weathering in Geochemical cycles* (eds. A. Larman and M. Meybeck). Reidel Dordrecht, pp. 61–82.
- Holland H. D. (2002) Volcanic gases, black smokers, and the Great Oxidation Event. *Geochim. Cosmochim. Acta* **66**, 3811–3826.
- Holland H. D. (2009) Why the atmosphere became oxygenated: A proposal. *Geochim. Cosmochim. Acta* **73**, 5241–5255.
- Holland H. D. (2006) The oxygenation of the atmosphere and oceans. *Philos. Trans. R. Soc. B* **361**, 903–915.
- Karhu J. A. and Holland H. D. (1996) Carbon isotopes and the rise of atmospheric oxygen. *Geology* **24**, 867–870.
- Kasting J. F. (2013) What caused the rise of atmospheric O₂? *Chem. Geol.* <http://dx.doi.org/10.1016/j.chemgeo.2013.05.039>
- King D. W. (1998) Role of carbonate speciation on the oxidation rate of Fe(II) in aquatic systems. *Environ. Sci. Technol.* **32**, 2997–3003.
- King D. W. and Farlow R. (2000) Role of carbonate speciation on the oxidation of Fe(II) by H₂O₂. *Mar. Chem.* **70**, 201–209.
- Knoll A. H. (2003) The geological consequences of evolution. *Geobiol.* **1**, 3–14.
- Kurzweil F., Claire M., Thomazo C., Peters M., Hannington M. and Strauss H. (2013) Atmospheric sulfur rearrangement 2.7 billion years ago: Evidence for oxygenic photosynthesis. *Earth Planet. Sci. Lett.* **366**, 17–26.
- Maher K. (2010) The dependence of chemical weathering rates on fluid residence time. *Earth Planet Sci. Lett.* **294**, 101–110.

- Mao Y., Pham A. N., Rose A. L. and Waite T. D. (2011) Influence of phosphate on the oxidation kinetics of nanomolar Fe(II) in aqueous solution at circumneutral pH. *Geochim. Cosmochim. Acta* **75**, 4601–4610.
- Millero F. J., Sotolongo S. and Izaguirre M. (1987) The oxidation kinetics of Fe(II) in seawater. *Geochim. Cosmochim. Acta* **51**, 793–801.
- Millero F. J. and Izaguirre M. (1989) Effect of ionic strength and ionic interactions on the oxidation of Fe(II). *J. Solution Chem.* **18**, 585–599.
- Millero F. J. and Sotolongo S. (1989) The oxidation of Fe(II) with H₂O₂ in seawater. *Geochim. Cosmochim. Acta* **53**, 1867–1873.
- Murakami T., Sreenivas B., Das Sharma S. and Sugimori H. (2011a) Quantification of atmospheric oxygen levels during the Paleoproterozoic using paleosol compositions and iron oxide kinetics. *Geochim. Cosmochim. Acta* **75**, 3982–4004.
- Och L. M. and Shields-Zhou G. A. (2012) The Neoproterozoic oxygenation event: Environmental perturbations and biogeochemical cycling. *Earth-Sci. Rev.* **110**, 26–57.
- Ohmoto H., Watanabe Y. and Kumazawa K. (2004) Evidence from massive siderite beds for a CO₂-rich atmosphere before ~1.8 billion years ago, *Nature* **429**, 395–399.
- Partin C. A., Bekker A., Planavsky N. J., Scott C. T., Gill B. C., Li C., Podkovyrov V., Maslov A., Konhauser K. O., Lalonde S. V., Love G. D., Poulton S. W. and Lyons T. W. (2013) Large-scale fluctuations in Precambrian atmospheric and oceanic oxygen levels from the record of U in shales. *Earth Planet. Sci. Lett.* **369/370**, 284–293.
- Pavlov A. A. and Kasting J. F. (2002) Mass-independent fractionation of sulfur isotopes in Archean sediments: Strong evidence for an anoxic Archean atmosphere. *Astrobiology* **2**, 27–41.
- Pham A. N. and Waite T. D. (2008) Oxygenation of Fe(II) in natural waters revisited: Kinetic modeling approaches, rate constant estimation and the importance of various reaction pathways. *Geochim. Cosmochim. Acta* **72**, 3616–3630.
- Pinto J. P. and Holland H. D. (1988) Paleosols and the evolution of the atmosphere; part II. In *Paleosols and Weathering through Geologic Time* (eds. J. Reinhardt and W. Silgeo). Spec. Pap. Geol. Soc., America, pp. 21–34.
- Price J. R., Velbel M. A. and Patino L. C. (2005) Rates and time scales of clay-mineral formation by weathering in saprolitic regoliths of the southern Appalachians from geochemical mass balance. *Geol. Soc. Am. Bull.* **117**, 783–794.
- Rasmussen B. and Buick R. (1999) Redox state of the Archean atmosphere: Evidence from detrital heavy minerals in ca. 3250–2750 Ma sandstones from Pilbara Craton, Australia. *Geology* **27**, 115–118.

- Rye R., Kuo P. H. and Holland H. D. (1995) Atmospheric carbon dioxide concentrations before 2.2 billion years ago. *Nature* **378**, 603–605.
- Rye R. and Holland H. D. (1998) Paleosols and the evolution of atmospheric oxygen: A critical review. *Am. J. Sci.* **298**, 621–672.
- Santana-Casiano J. M., González-Dávila M. and Millero F. J. (2005) Oxidation of nanomolar levels of Fe(II) with oxygen in natural waters. *Environ. Sci. Technol.* **39**, 2073–2079.
- Scott C., Lyons T. W., Bekker A., Shen Y., Poulton S. W., Chu X. and Anbar A. D. (2008) Tracing the stepwise oxygenation of the Proterozoic ocean. *Nature* **452**, 456–459.
- Sheldon N. D. and Retallack G. J. (2001) Equation for compaction of paleosols due to burial. *Geology* **29**, 247–250.
- Sheldon N. D. (2006) Precambrian paleosols and atmospheric CO₂ levels. *Precambrian Res.* **147**, 148–155.
- Singer P. C. and Stumm W. (1970) Acidic mine drainage: The rate-determining step. *Science* **167**, 1121–1123.
- Sreenivas B. and Murakami T. (2005) Emerging views on the atmospheric oxygen evolution during the Precambrian. *J. Mineral. Petrol. Sci.* **100**, 184–201.
- Stonestrom D. A., White A. F. and Akstin K. (1998) Determining rates of chemical weathering in soils — Solute transport versus profile evolution. *J. Hydrol.* **209**, 331–345.
- Stumm W. and Lee G. F. (1961) Oxygenation of ferrous iron. *Ind. Eng. Chem.* **53**, 143–146.
- Stumm W. and Morgan J. J. (1996) *Aquatic Chemistry*, 3rd Ed. John Wiley & Sons, New York.
- Sugimori H., Kanzaki Y., Yokota K. and Murakami T. (2011) Nonlinear dependence of the oxidation rate of Fe(II) on dissolved oxygen under low-O₂ conditions in aqueous solutions. *J. Mineral. Petrol. Sci.* **106**, 142–152.
- Sugimori H., Kanzaki Y. and Murakami T. (2012) Relationships between Fe redistribution and Po₂ during mineral dissolution under low O₂ conditions. *Geochim. Cosmochim. Acta*, **84**, 29–46.
- Toledo P. G., Novy R. A., Davis H. T. and Scriven L. E. (1990) Hydraulic conductivity of porous media at low water content. *Soil Sci. Soc. Am. J.* **54**, 673–679.
- Utsunomiya S., Murakami T., Nakada M. and Kasama T. (2003) Iron oxidation state of a 2.45-Byr-old paleosol developed on mafic volcanics. *Geochim. Cosmochim. Acta* **67**, 213–221.

- White A. F., Blum A. E., Schulz M. S., Vivit D. V., Stonestrom D. A., Larsen M., Murphy S. F. and Eberl D. (1998) Chemical weathering in a tropical watershed, Luquillo Mountains, Puerto Rico: I. Long-term versus short-term weathering fluxes. *Geochim. Cosmochim. Acta* **62**, 209–226.
- White A. F., Blum A. E., Schulz M. S., Huntington T. G., Peters N. E. and Stonestrom D. A. (2002) Chemical weathering of the Panola Granite: Solute and regolith elemental fluxes and the weathering rate of biotite. In *Water-Rock Interaction, Ore Deposits and Environmental Geochemistry: A Tribute to David A. Crerar* (eds. R. Hellmann and S. A. Wood), pp. 37–59, Special Publication 7. Geochemical Society.
- White A. F., Schulz M. S., Vivit D. A., Blum A. E., Stonestrom D. A. and Harden J. W. (2005) Chemical weathering rates of a soil chronosequence on granitic alluvium: III. Hydrochemical evolution and contemporary solute fluxes and rates. *Geochim. Cosmochim. Acta* **69**, 1975–1996.
- White A. F., Schulz M. S., Stonestrom D. A., Vivit D. V., Fitzpatrick J., Bullen T. D., Maher K. and Blum A. E. (2009) Chemical weathering of a marine terrace chronosequence, Santa Cruz, California. Part II: Solute profiles, gradients and the comparisons of contemporary and long-term weathering rates. *Geochim. Cosmochim. Acta* **73**, 2769–2803.
- Wiggering H. and Beukes N. J. (1990) Petrography and geochemistry of a 2000–2200-Ma-old hematitic paleo-alteration profile on Ongeluk basalt of the Transvaal Supergroup, Griqualand West, South Africa. *Precambrian Res.* **46**, 241–258.
- Wilhelm E., Battino R. and Wilcock R. (1977) Low-pressure solubility of gases in liquid water. *Chem. Rev.* **77**, 219–262.
- Yang W. and Holland H. D. (2003) The Hekpoort paleosol profile in strata 1 at Gaborone, Botswana: Soil formation during the Great Oxidation Event. *J. Am. Sci.* **303**, 187–220.
- Yokota K., Kanzaki Y. and Murakami T. (2013) Weathering model for the quantification of atmospheric oxygen evolution during the Paleoproterozoic. *Geochim. Cosmochim. Acta* **117**, 332–347.
- Yokoyama T. (2013) Characterization of the reaction and transport properties of porous rhyolite and its application to the quantitative understanding of the chemical weathering rate. *Geochim. Cosmochim. Acta* **118**, 295–311.

V. Effects of atmospheric composition on apparent activation energy of silicate weathering: Implications for evolution of atmospheric CO₂ in the Precambrian

1. Introduction

Silicate weathering is considered to be the net sink of atmospheric CO₂ (e.g., Berner et al., 1983; Amiotte Suchet et al., 2003). Understanding of silicate weathering is thus indispensable to comprehend the regulation of the surface temperature of the Earth because CO₂ is a greenhouse-effect gas. The silicate weathering rate, temperature and partial pressure of atmospheric CO₂ (P_{CO_2}) are related to one another by the “apparent” activation energy of weathering which describes the temperature dependence of weathering (Brady, 1991; Brady and Carroll, 1994). In contrast to the activation energy of elementary reaction, weathering includes more than one elementary reaction step and thus the activation energy of weathering is apparent (Lasaga, 1981, 1984). Due to the importance of the apparent activation energy of weathering, the temperature dependence of silicate mineral dissolution has been investigated intensively both in the laboratory and field (e.g., Gislason and Eugster, 1987; Velbel, 1993; Dorn and Brady, 1993; Casey and Ludwig, 1995; Brantley and Chen, 1995; Nagy, 1995; Blum and Stillings, 1995; White and Blum, 1995; Brady and Gislason, 1997; White et al., 1999; Dessert et al., 2001; 2003; Dalai et al., 2002; Gislason and Oelkers, 2003; Oliva et al., 2003; Riebe et al., 2004; Sak et al., 2004; West et al., 2005; Navarre-Sitchler and Brantley, 2007; Gislason et al., 2009; Clow and Mast, 2010; Norton and von Blackenburg, 2010; Turner et al., 2010; Williams et al., 2010; Rasmussen et al., 2011; Dere et al., 2013). Despite such intensive efforts to determine the apparent activation energy of weathering, different values of the temperature dependence have been reported. Even for dissolution of a single mineral in laboratory experiments, no unique value has been obtained for the apparent activation energy (e.g., Rimstidt et al., 2012). The variation in apparent activation energy in laboratory experiments has been attributed to the difference in solution composition (Casey and Sposito, 1992; Brantley and Chen, 1995; Cama et al., 1999). In natural weathering systems, solution compositions are more condensed than those in laboratory experiments and therefore the effects of solution composition should be more significant than in the laboratory (Lasaga, 1995; Cama et al., 1999; Williams et al., 2010; Rasmussen et al., 2011). The relationship between apparent activation energy and solution composition is not yet fully understood and therefore the uncertainty in

apparent activation energy of natural weathering of silicates still remains. Such uncertainty in the temperature dependence of silicate weathering can undermine the P_{CO_2} and temperature estimation through the Earth's history by chemical weathering models (Brady, 1991).

Many chemical weathering models have been constructed to reveal past and possibly predict future P_{CO_2} levels and temperatures (e.g., Caldeira and Kasting, 1992; Lovelock and Kump, 1994; Le Hir et al., 2009; Godd ris et al., 2013) (see, however, important caution on the construction and utilization of weathering model by Hochella and Banfield (1995)). The model for estimating P_{CO_2} levels in the Phanerozoic has been constructed by Berner and his coworkers (Berner et al., 1983; Lasaga et al., 1985; Berner, 1991, 1994, 2006; Berner and Kothavala, 2001). The estimated P_{CO_2} levels by the model of Berner and those derived from geological records (e.g., Yapp and Poths, 1996; Mora et al., 1996; Ekart et al., 1999) are consistent with one another, which has resulted in deeper understanding of transitions of P_{CO_2} and temperature in the Phanerozoic. On the other hand, due to the paucity of geological records, P_{CO_2} levels in the Precambrian are less understood than those in the Phanerozoic. The Precambrian Earth was less illuminated and thus cooler than today if the Earth had the same atmospheric composition as that in today, because the Sun was younger and thus fainter (Sagan and Mullen, 1972; Feulner, 2012). Therefore, P_{CO_2} estimation becomes a more serious issue when I consider the climates in the older ages (Walker, 1982). Despite the fainter Sun in the Precambrian, evidence for the existence of liquid water can go back to as far as 4.4 Ga (e.g., Valley et al., 2002; Nutman, 2006) and the geological records for the possibility of global glaciations have been reported only in the late Neoproterozoic (e.g., Hoffman et al., 1998), in the early Paleoproterozoic (e.g., Bekker et al., 2005) and in the late Mesoarchean (e.g., Young et al., 1998), indicating that most of the Precambrian were warm enough to allow the existence of liquid water. Even hot climate has been suggested for most of the Archean from mainly isotopic records (e.g., Knauth and Epstein, 1976; Karhu and Epstein, 1986; Lowe and Tice, 2004, 2007; Gaucher et al., 2008). Moderate to warm climate in the most Precambrian must be assessed for consistency from the view point of the relationships between P_{CO_2} , temperature and silicate weathering where the apparent activation energy of silicate weathering is the key parameter.

This chapter is undertaken to investigate the determinant factor(s) of the apparent activation energy of natural silicate weathering in a theoretical framework, addressing solution composition effects. Formulations of the chemical rate expressions for silicate weathering and the apparent activation energy of silicate weathering reveal that the

atmospheric composition can affect the apparent activation energy of silicate weathering, and thus silicate weathering flux. The relationships between the atmospheric composition, the apparent activation energy and the silicate weathering flux are then established, which enables me to elucidate the effects of CO₂ as well as CH₄ and O₂ on silicate weathering. Finally, as implications of the findings of the present study, the evolution of atmospheric CO₂ and temperature and triggers of the global glaciations in the Precambrian are discussed.

2. Formulation of rate and apparent activation energy of silicate weathering

I investigate the apparent activation energy of silicate weathering in a natural weathering system by formulating the apparent activation of silicate weathering in three different scales, namely, (i) dissolution/precipitation of each mineral, (ii) elemental loss as the net reactions of the minerals and (iii) weathering flux from the weathering profile. First, I introduce the rate expressions in scales (i)–(iii) (Section 2.1), and then the apparent activation energies of weathering in all scales are presented based on the rate expressions (Section 2.2). Note that the term "apparent activation energy" is used for the temperature dependences of the rates in all scales, i.e., the apparent activation energies of each mineral-reaction, elemental loss and weathering flux are differently formulated from one another and represent the temperature dependences of each mineral-reaction rate, elemental loss rate by weathering and weathering flux, respectively. I focus on the formulation of the apparent activation energies in different scales in Section 2; the relationships in apparent activation energy between the three scales are discussed in Section 3, based on the equations in Section 2. The relationships in apparent activation energy between the three scales are useful for the estimation of the apparent activation energy of silicate weathering consistent between the scales, which is also attempted in Section 3. The concept described above is schematically shown in Fig. 1.

2.1. Rate formulation

The rate expressions for chemical weathering of silicates in the scales of dissolution/precipitation of each mineral, elemental loss per unit rock volume and weathering flux per unit rock area are described in Sections 2.1.1, 2.1.2 and 2.1.3, respectively. The rate expressions are used to formulate apparent activation energies in the three scales later in Section 2.2. The parameters used for the present study are listed in Table 1.

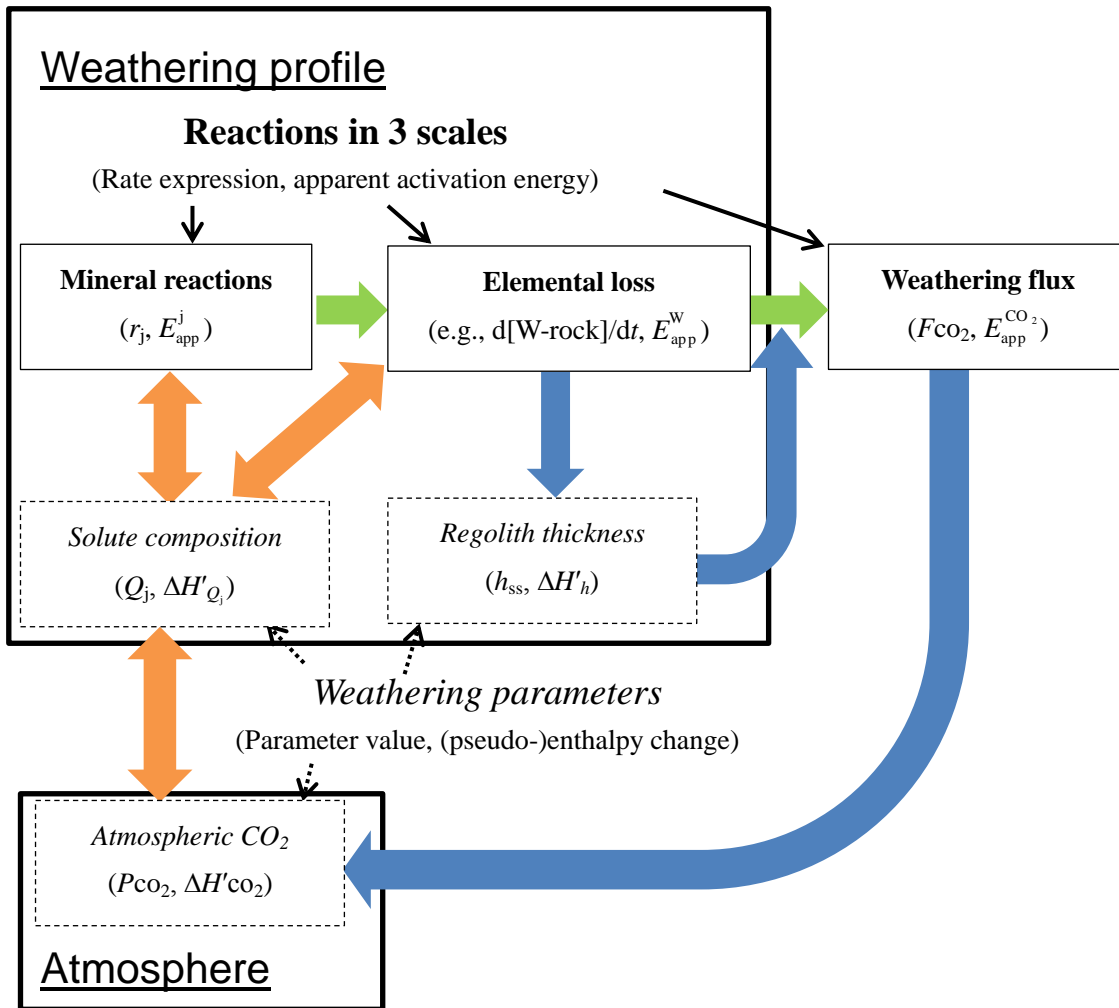


Figure 1. Schematics of 3-scale reactions in a weathering profile considered in the present study and their relations with atmospheric composition. Two bold boxes represent the weathering profile and atmosphere. The 3-scale reactions are denoted in bold letters in three thin solid boxes within or outside the box of the weathering profile (see three thin solid arrows). In parentheses in the box for a given reaction scale, the symbols for the rate expression and the apparent activation energy for the reaction in the scale are given. In parentheses in the box for a given parameter, the symbols for the parameters and the (pseudo-)enthalpy changes for the parameters are denoted. The (pseudo-)enthalpy change for a given parameter represents the temperature dependence of the parameter (see Section 2.2 for the details). Bold arrows denote the interactions between the parameters.

Table 1. List of symbols used with their explanations.

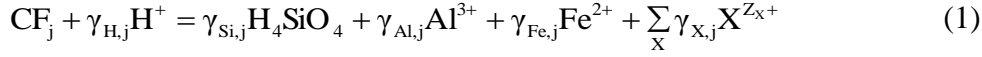
Symbol	Explanation
a_j	Parameter to describe the dependency of saturation degree on reaction rate of mineral j (dimensionless)
A_{sil}	Silicate rock area in continents (m^2)
$\alpha_{\text{w},j}$	Rate contribution of mineral j to loss rate of element W ($W = X, \text{Si}, \text{Al}$ and Fe) by silicate weathering (dimensionless)
b_j	Parameter to describe the dependency of saturation degree on reaction rate of mineral j (dimensionless)
$\beta_{\text{X},j}$	Contribution of element Y ($Y = X, \text{Al}$ and Fe) to total concentration of cations (dimensionless)
c	Molar volume of total dissolved solid ($\text{m}^3 \text{mol}^{-1}$)
CDF	Ratio of chemical denudation rate to total denudation rate (dimensionless)
d	Empirical constant to describe the relationship between E_{app} and $\ln A$ (dimensionless)
D	Total denudation rate (m yr^{-1})
D_0	Mineral supply rate at zero regolith thickness (m yr^{-1})
δ	Dependence of D on regolith thickness (m^{-1})
e	Empirical constant to describe the relationship between E_{app} and $\ln A$ (dimensionless)
E_{app}^j	Apparent activation energy of reaction of mineral j (kJ mol^{-1})
E_j	Apparent activation energy of dissolution of mineral j at far-from-equilibrium (kJ mol^{-1})
$E_{\text{app}}^{\text{W}}$	Apparent activation energy of W loss ($W = X, \text{Si}, \text{Al}$ and Fe) by silicate weathering (kJ mol^{-1})
$E_{\text{app}}^{\text{Rock}}$	Apparent activation energy of loss of total cations by silicate weathering (kJ mol^{-1})
$E_{\text{app}}^{\text{Rock-2}}$	Apparent activation energy of loss of total dissolved solid by silicate weathering (kJ mol^{-1})
$E_{\text{app}}^{\text{CO}_2}$	Apparent activation energy of flux of total cations by silicate weathering (kJ mol^{-1})
ΔE_{app}^j	Change in E_{app}^j as the effects of saturation degree (kJ mol^{-1})
ΔE_{ox}	Change in $E_{\text{app}}^{\text{CO}_2}$ by increase in O_2 (kJ mol^{-1})
f_{Al}	Ratio of Al^{3+} to total dissolved Al (dimensionless)
F_{CO_2}	Flux of total cations by silicate weathering ($\text{mol m}^{-2} \text{yr}^{-1}$)
F_0	Constant weathering flux at $T = T_{\text{univ}}$ ($\text{mol m}^{-2} \text{yr}^{-1}$)
F_{in}	In-flux of CO_2 , assumed to be degassing rate of CO_2 (mol yr^{-1})
F_{out}	Out-flux of CO_2 , assumed to be weathering flux of CO_2 (mol yr^{-1})
$\gamma_{i,j}$	Stoichiometric number of species i on dissolution of mineral j (dimensionless)
$\gamma_{\text{tot},j}$	Total mole number of elements which 1 mole of mineral j contains (dimensionless)
h	Regolith thickness (m)
h_{ss}	h at steady state (m)
ΔH_j°	Standard enthalpy change by dissolution of mineral j (kJ mol^{-1})
$\Delta H'_{Q_j}$	Temperature dependence of Q_j (kJ mol^{-1})
$\Delta H'_f$	Temperature dependence of k_f (kJ mol^{-1})
$\Delta H'_\lambda$	Temperature dependence of λ (kJ mol^{-1})
$\Delta H'_q$	Temperature dependence of q (kJ mol^{-1})
ΔH_1°	Standard enthalpy change by dissociation of carbonic acid (kJ mol^{-1})
$\Delta H_{\text{HC}}^\circ$	Standard enthalpy change by CO_2 dissolution into water (kJ mol^{-1})
$\Delta H'_{\text{CO}_2}$	Temperature dependence of P_{CO_2} (kJ mol^{-1})

Table 1. (continued)

Symbol	Explanation
$\Delta H'_{H^+}$	Temperature dependence of $[H^+]_{ss}$ (kJ mol^{-1})
ΔH°_{Al}	Average standard enthalpy change by Al hydrolysis (kJ mol^{-1})
$\Delta H'_h$	Temperature dependence of h_{ss} (kJ mol^{-1})
η_{Wj}	Contribution of element W to total concentration of dissolved solid (dimensionless)
[i]	Concentration of species i in porewater (mol L^{-1})
[i] _{ss}	[i] at steady state (mol L^{-1})
k_j	Rate constant of dissolution of mineral j ($\text{mol m}^{-2} \text{yr}^{-1}$)
k_f	Rate constant for removal of elements by water flow (yr^{-1})
k_{ox}	Rate constant of Fe^{2+} oxidation ($\text{mol}^{-3} \text{L}^3 \text{yr}^{-1}$)
K_j	Equilibrium constant of mineral j (mineral-dependent dimension)
K_1	Equilibrium constant for dissociation of carbonic acid (mol L^{-1})
K_{HC}	Henry's constant for CO_2 dissolution into water ($\text{mol L}^{-1} \text{atm}^{-1}$)
κ	Unit conversion number from atm to mol (mol atm^{-1})
$L(t)$	Change rate in reciprocal temperature by change in luminosity ($\text{K}^{-1} \text{yr}^{-1}$)
λ	Pseudo-first order rate constant for Fe^{2+} oxidation (yr^{-1})
n_{CO_2}	Indicator of weathering feedback on P_{CO_2} (dimensionless)
n_{Al}	Average hydrolysis number of dissolved Al (dimensionless)
PhE	Physical denudation rate (m yr^{-1})
ϕ	Ratio of Fe^{3+} precipitated in weathering profile to total dissolved Fe^{2+} (dimensionless)
ψ	Ratio of Fe^{2+} flown out of weathering profile to total dissolved Fe^{2+} (dimensionless)
q	Volumetric water flow per unit rock volume ($\text{L m}^{-3} \text{yr}^{-1}$)
Q_j	Reaction activity quotient of mineral j (mineral-dependent dimension)
r_j	Reaction rate of mineral j ($\text{mol m}^{-3} \text{yr}^{-1}$)
R_g	Gas constant ($\text{kJ mol}^{-1} \text{K}^{-1}$)
[Rock]	Concentration of total cations in rock phase (eq m^{-3})
[Rock-2]	Concentration of total weatherable elements in rock phase (mol m^{-3})
S_j	Accessible surface area of mineral j per unit rock volume ($\text{m}^2 \text{m}^{-3}$)
σ	Water saturation ratio of weathering profile (L m^{-3})
t	Time (yr)
T	Absolute temperature (K)
T_{univ}	Universal temperature at which silicate weathering flux becomes constant (K)
T_{thr}	Threshold temperature at which $n_{\text{CO}_2} = 0$ (K)
θ	Porosity of weathering profile ($\text{m}^3 \text{m}^{-3}$)
[W-rock]	Concentration of element W (W = X, Si, Al and Fe) in rock phase (mol m^{-3})
Z_X	Valence number of cation X (dimensionless)
Z_{Al}	Average valence number of Al (dimensionless)

2.1.1. Silicate dissolution/precipitation

The reaction rate of each silicate is described here. Dissolution/precipitation of a certain silicate j is described as



where CF_j is the chemical formula of silicate j , $\gamma_{i,j}$ represents the stoichiometric number of species i on dissolution of silicate j , X refers to major cations, Na, K, Mg and Ca, and Z_X is the valence number of cation X . In Reaction (1), the reaction from the left to right represents dissolution of silicate j and the reaction in the inverse direction expresses precipitation of silicate j . Note that Reaction (1) can be used for the reactions of (hydr)oxides by setting appropriate γ values. In addition to silicates, amorphous silica (SiO_2) and gibbsite ($Al(OH)_3$) are included in the present study due to the common existence of these minerals in weathering profiles of silicate rocks (e.g., White, 1995). Fe^{3+} -bearing minerals are excluded from the present study, because I assume that Fe^{3+} is immobile due to low solubility of Fe^{3+} -hydroxides (e.g., Yokota et al., 2013). The minerals considered for dissolution/precipitation are listed in Table 2, together with the values of $\gamma_{i,j}$ and standard enthalpy change (the standard enthalpy change is dealt with in Section 2.2). Charge conservation of Reaction (1) is represented by

$$\gamma_{H,j} = 3\gamma_{Al,j} + 2\gamma_{Fe,j} + \sum_X Z_X \gamma_{X,j} \quad (2)$$

The total mole number of elements that silicate j contains is defined as $\gamma_{tot,j}$:

$$\gamma_{tot,j} \equiv \sum_X \gamma_{X,j} + \gamma_{Si,j} + \gamma_{Al,j} + \gamma_{Fe,j} \quad (3)$$

The values of $\gamma_{tot,j}$ are also listed in Table 2.

The reaction rate of silicate j per unit rock volume, r_j ($\text{mol m}^{-3} \text{yr}^{-1}$), is represented as

$$r_j = S_j k_j \left\{ 1 - \left(\frac{Q_j}{K_j} \right)^{a_j} \right\}^{b_j} \quad (4)$$

where S_j is the surface area of silicate j accessible to solution per unit rock volume ($\text{m}^2 \text{m}^{-3}$) and k_j is the forward reaction rate constant of silicate j ($\text{mol m}^{-2} \text{yr}^{-1}$). Q_j and K_j are the reaction activity quotient and the equilibrium constant for silicate j , respectively. a_j and b_j are the constants describing the effects of saturation degree (Q_j/K_j) on the reaction rate of silicate j . The term representing the effect of saturation degree (Q_j/K_j) (i.e., $\{1 -$

$(Q_j/K_j)^{a_j} b_j$ in Eq. (4)) can be more complex, depending on the property of each mineral (e.g., Lasaga and Luttge, 2001), mineral's history (Beig and Lüttge, 2006; Yang and Steefel, 2008), stoichiometry of activation complex (e.g., Schott et al., 2009), production of secondary minerals (Murakami et al., 1998), formation of leached layer (Daval et al., 2011) and size of mineral (Emmanuel and Ague, 2011). In the present study, the possible variation in the term representing the effect of (Q_j/K_j) is regarded as the variation in a_j and b_j in Eq. (4). The value of Q_j is defined as

$$Q_j = \frac{[\text{H}_4\text{SiO}_4]^{\gamma_{\text{Si},j}} [\text{Al}^{3+}]^{\gamma_{\text{Al},j}} [\text{Fe}^{2+}]^{\gamma_{\text{Fe},j}}}{[\text{H}^+]^{\gamma_{\text{H},j}}} \prod_{\text{X}} [\text{X}^{\text{Z}_{\text{X}^+}}]^{\gamma_{\text{X},j}} \quad (5)$$

where [species i] denotes the concentration of species i in porewater (mol L^{-1}). Depending on the value of Q_j in Eq. (5), Eq. (4) represents the dissolution or precipitation rate: when $Q_j < K_j$, r_j is positive and represents the dissolution rate of silicate j; when $Q_j > K_j$, r_j is negative and represents the precipitation rate of silicate j. By using Eq. (4), the solution composition effects on apparent activation energy can be addressed (Lasaga, 1995). Integration of Eq. (4) for all the minerals in silicate rock leads to the rate expressions in the larger scale (see next section).

2.1.2. Elemental loss by silicate weathering

The loss rate of a certain element per unit rock volume is described as the sum of all reaction rates of the minerals that contain the element. For cation X, the loss rate is expressed as the time-derivative of X concentration in rock phase ($[\text{X-rock}]$, mol m^{-3}):

$$\frac{d[\text{X-rock}]}{dt} = -\sum_j \gamma_{\text{X},j} r_j \quad (6)$$

where t denotes the time (yr). To address the solution composition effects on apparent activation energy (Lasaga, 1995), water phase is also considered in the present study. The time evolution of concentration of cation X in porewater, $[\text{X}]$ (mol L^{-1}), is represented by

$$\frac{d[\text{X}]}{dt} = \frac{1}{\theta\sigma} \sum_j \gamma_{\text{X},j} r_j - k_f [\text{X}] \quad (7)$$

where θ and σ represent the porosity ($\text{m}^3 \text{m}^{-3}$) and the water saturation ratio (L m^{-3}) of the weathering profile, respectively. In Eq. (7), $k_f[\text{X}]$ is the rate of X removed by water flow where k_f is the rate constant (yr^{-1}) (Berner, 1978). The contribution of rainwater to porewater is not considered in Eq. (7) for simplicity, which will not change the main conclusions given in this chapter (c.f., Appendix C in Chapter II). The cation

concentrations in porewater are reported to reach to those at steady state, i.e., $d[X]/dt = 0$, in a relatively short period of time (Stonestrom et al., 1998; Brantley and White, 2009). From $d[X]/dt = 0$, the steady-state concentration of X in porewater, $[X]_{ss}$ (mol L^{-1}), is obtained:

$$[X]_{ss} = \frac{\sum_j \gamma_{X,j} r_j}{\sigma \theta k_f} \quad (8)$$

In the right hand side of Eq. (8), the denominator $\sigma \theta k_f$ is equal to the volumetric water flow per unit rock volume, q ($L m^{-3} yr^{-1}$):

$$q = \sigma \theta k_f \quad (9)$$

From Eqs. (6), (8) and (9),

$$\frac{d[X - \text{rock}]}{dt} = -q[X]_{ss} \quad (10)$$

Eq. (10) represents the relationship between the steady-state concentration of X in porewater and the loss rate of X by weathering.

Similarly to the equations for X, the steady-state concentration of Si in porewater ($[Si]_{ss}$, mol L^{-1}) and Si loss rate by weathering are represented by the following respective equations:

$$[Si]_{ss} = \frac{\sum_j \gamma_{Si,j} r_j}{q} \quad (11)$$

$$\frac{d[Si - \text{rock}]}{dt} = -\sum_j \gamma_{Si,j} r_j = -q[Si]_{ss} \quad (12)$$

where $[Si - \text{rock}]$ (mol m^{-3}) (Eq. (12)) is the Si concentration in rock phase (mol m^{-3}).

Similarly, for Al,

$$[Al]_{ss} = \frac{\sum_j \gamma_{Al,j} r_j}{q} \quad (13)$$

$$\frac{d[Al - \text{rock}]}{dt} = -\sum_j \gamma_{Al,j} r_j = -q[Al]_{ss} \quad (14)$$

where $[Al]_{ss}$ (Eq. (13)) is the steady-state concentration of Al in porewater (mol L^{-1}) and $[Al - \text{rock}]$ (Eq. (14)) is the Al concentration in rock phase (mol m^{-3}). Note that the average valence number of dissolved alumina, Z_{Al} , is not constant, but determined by the average hydrolyzed number, n_{Al} :

$$Z_{Al} = 3 - n_{Al} \quad (15)$$

The average hydrolyzed number is dependent on pH. For example, at pH = 5.0, $n_{Al} = 1$,

meaning that all the dissolved Al species can be approximated by $\text{Al}(\text{OH})^{2+}$ (mono-hydrolyzed Al), and thus $Z_{\text{Al}} = +2$ according to Eq. (15). I list the values of Z_{Al} and n_{Al} at various pH in Table 3, together with the average standard enthalpy changes for Al-hydrolysis, $\Delta H^\circ_{\text{Al}}$ (kJ mol^{-1}) ($\Delta H^\circ_{\text{Al}}$ is dealt with in Section 3). See Appendix A for the details of Z_{Al} , n_{Al} and $\Delta H^\circ_{\text{Al}}$.

Formulation of the loss rate of Fe by silicate weathering is more complicated than that of X, Si and Al. For the loss of Fe by weathering, I need to understand Fe^{2+} oxidation reaction in weathering. When Fe^{2+} -bearing mineral dissolves, the dissolved Fe^{2+} is oxidized to Fe^{3+} under the presence of oxygen and Fe^{3+} precipitates immediately as Fe^{3+} -hydroxides due to the low solubilities of Fe^{3+} -hydroxides. The precipitation reaction of Fe^{3+} -hydroxides is fast and oxidation of Fe^{2+} to Fe^{3+} is usually rate-limiting in the formation of Fe^{3+} -hydroxides (Sugimori et al., 2012). Therefore I need not to consider the fast precipitation of Fe^{3+} -hydroxides, but must take into account the relatively slow Fe^{2+} oxidation for the Fe loss by weathering. Due to the low solubilities of Fe^{3+} -hydroxides, it can be assumed that the total concentration of dissolved Fe, $[\text{Fe}]$ (mol L^{-1}), is that of Fe^{2+} . Including the oxidation rate of Fe^{2+} , the time evolution of $[\text{Fe}]$ is given by

$$\frac{d[\text{Fe}]}{dt} = \frac{1}{\theta\sigma} \sum_j \gamma_{\text{Fe},j} r_j - k_f [\text{Fe}] - \lambda [\text{Fe}] \quad (16)$$

where λ is the pseudo-first-order rate constant for Fe^{2+} oxidation (yr^{-1}). The λ value is usually given by (Stumm and Lee, 1961; Yokota et al., 2013)

$$\lambda = k_{\text{ox}} [\text{O}_2]_{\text{ss}} [\text{OH}^-]_{\text{ss}}^2 \quad (17)$$

where k_{ox} is the rate constant ($\text{mol}^{-3} \text{L}^3 \text{yr}^{-1}$), and $[\text{O}_2]_{\text{ss}}$ and $[\text{OH}^-]_{\text{ss}}$ are the steady-state concentrations of dissolved oxygen and hydroxyl ion, respectively, in porewater (mol L^{-1}). At steady state, $[\text{Fe}]$ becomes $[\text{Fe}]_{\text{ss}}$ (mol L^{-1}), which is given by

$$[\text{Fe}]_{\text{ss}} = \frac{\sum_j \gamma_{\text{Fe},j} r_j}{\theta\sigma(k_f + \lambda)} \quad (18)$$

The time evolution of Fe concentration in rock phase, $[\text{Fe-rock}]$ (mol m^{-3}), is given by

$$\frac{d[\text{Fe-rock}]}{dt} = - \left(\sum_j \gamma_{\text{Fe},j} r_j - \theta\sigma\lambda [\text{Fe}]_{\text{ss}} \right) \quad (19)$$

Using Eqs. (9) and (18), Eq. (19) can be rewritten:

$$\frac{d[\text{Fe-rock}]}{dt} = -q[\text{Fe}]_{\text{ss}} \quad (20)$$

Murakami et al. (2011) and Yokota et al. (2013) have introduced a useful parameter ψ to

describe weathering of Fe. I introduce here simpler definition for ψ than that given by Murakami et al. (2011) and Yokota et al. (2013):

$$\psi = \frac{k_f}{\lambda + k_f} \quad (21)$$

The complementary parameter of ψ is defined as ϕ :

$$\phi \equiv 1 - \psi = \frac{\lambda}{\lambda + k_f} \quad (22)$$

Both ψ and ϕ are the indicators of oxygen level because λ is a function of $[\text{O}_2]_{\text{ss}}$ or partial pressure of atmospheric oxygen (P_{O_2}) (Eq. (17), see also Chapter IV). Using Eqs. (9), (18) and (21), Eq. (20) can be rewritten;

$$\frac{d[\text{Fe-rock}]}{dt} = -\psi \sum_j \gamma_{\text{Fe},j} r_j \quad (23)$$

Eq. (23) describes that when the oxygen level is extremely high (i.e., $\psi \cong 0$, Eq. (21)), Fe-loss becomes zero, while when the oxygen level is extremely low (i.e., $\psi \cong 1$, Eq. (21)), Fe-loss can become significant, consistent with the weathering model of Yokota et al. (2013).

Using the equations for the above elemental loss rates, I consider the loss rate of total cations by weathering. Time evolution of the equivalent concentration of total cations in rock phase, $[\text{Rock}] (\equiv \sum Z_X [\text{X-rock}] + Z_{\text{Al}} [\text{Al-rock}] + 2[\text{Fe-rock}], \text{ eq m}^{-3})$, is represented by

$$\frac{d[\text{Rock}]}{dt} = -q \left(\sum_X Z_X [\text{X}]_{\text{ss}} + Z_{\text{Al}} [\text{Al}]_{\text{ss}} + 2[\text{Fe}]_{\text{ss}} \right) \quad (24)$$

Using Eqs. (2), (8), (9), (11), (13), (15), (18), (22) and (23), Eq. (24) can be alternatively expressed as

$$\frac{d[\text{Rock}]}{dt} = -\sum_j (\gamma_{\text{H},j} - n_{\text{Al}} \gamma_{\text{Al},j} - 2\phi \gamma_{\text{Fe},j}) r_j \quad (25)$$

Under most weathering conditions, the charge balance equation in porewater is given by (Chapter II)

$$\sum_X Z_X [\text{X}]_{\text{ss}} + Z_{\text{Al}} [\text{Al}]_{\text{ss}} + 2[\text{Fe}]_{\text{ss}} \cong [\text{HCO}_3^-]_{\text{ss}} \quad (26)$$

where $[\text{HCO}_3^-]_{\text{ss}}$ is the steady-state concentration of atmosphere-derived bicarbonate ion in porewater (mol L^{-1}). From Eqs. (24) and (26), I obtain

$$\frac{d[\text{Rock}]}{dt} = -q [\text{HCO}_3^-]_{\text{ss}} \quad (27)$$

Eqs. (26) and (27) are justified at $4 < \text{pH} < 9$ and $P_{\text{CO}_2} > 10^{-4.5}$ atm. Therefore, Eq. (27) represents the CO_2 consumption rate per unit rock volume at $4 < \text{pH} < 9$ and $P_{\text{CO}_2} >$

$10^{-4.5}$ atm. As the CO_2 consumption rate, the unit of Eq. (27) is $\text{mol m}^{-3} \text{yr}^{-1}$.

In a similar way to the formulation of the loss rate of total cations, I can formulate the loss rate of total dissolved solid (TDS). Defining the total concentration of weatherable elements in rock phase as [Rock-2] ($\equiv \sum[\text{X-rock}] + [\text{Si-rock}] + [\text{Al-rock}] + [\text{Fe-rock}]$, mol m^{-3}), the loss rate of TDS is written as

$$\frac{d[\text{Rock} - 2]}{dt} = -q \left(\sum_{\text{X}} [\text{X}]_{\text{ss}} + [\text{Si}]_{\text{ss}} + [\text{Al}]_{\text{ss}} + [\text{Fe}]_{\text{ss}} \right) \quad (28)$$

From Eqs. (3), (6), (12), (14), (21), (22) and (23), Eq. (28) can be rewritten:

$$\frac{d[\text{Rock} - 2]}{dt} = -\sum_j (\gamma_{\text{tot},j} - \phi \gamma_{\text{Fe},j}) r_j \quad (29)$$

The loss rate of TDS (Eq. (28) or (29)) is necessary to determine the regolith thickness and thus weathering flux (see next section).

2.1.3. Weathering flux of silicates

In Section 2.1.2, I formulated the loss rates of each element, total cations and TDS with their units being $\text{mol m}^{-3} \text{yr}^{-1}$. Weathering flux, which has a unit of $\text{mol m}^{-2} \text{yr}^{-1}$, is more complicated to obtain, although weathering flux can be obtained by simply multiplying the elemental loss rate ($\text{mol m}^{-3} \text{yr}^{-1}$) by regolith thickness, h (m). However, it is difficult to estimate the steady-state regolith thickness, h_{ss} (m) (e.g., Gabet and Mudd, 2009; Hilley et al., 2010; Lebedeva et al., 2010; Brantley and Lebedeva, 2011). Regolith thickness (h) varies with time, dependent on mineral supply rate, D (m yr^{-1}), physical erosion rate, PhE (m yr^{-1}), and also chemical weathering rate. Time evolution of the regolith thickness is represented by (c.f., Riebe et al., 2004)

$$\frac{dh}{dt} = D - PhE - ch \left| \frac{d[\text{Rock} - 2]}{dt} \right| \quad (30)$$

where c is the molar volume of TDS ($\text{m}^3 \text{mol}^{-1}$). Note that D can be the same as the weathering advance rate (e.g., White et al., 2008) or the soil production rate (e.g., Heimsath et al., 1997) at steady state. D is a function of h and can be expressed by (Heimsath et al., 1997)

$$D = D_0 \exp(-\delta h) \quad (31)$$

where D_0 is the mineral supply rate at zero regolith thickness (m yr^{-1}) and δ denotes the dependence of D on regolith thickness (m^{-1}). At steady state, $dh/dt = 0$, and

$$D_0 \exp(-\delta h_{\text{ss}}) = PhE + ch_{\text{ss}} \left| \frac{d[\text{Rock} - 2]}{dt} \right| \quad (32)$$

Solving Eq. (32), I can obtain h_{ss} for a given set of D_0 , δ , PhE , c and $d[\text{Rock-2}]/dt$. In

the present study, I do not attempt to solve Eq. (32) for h_{ss} because my focus is on the temperature dependence of h_{ss} and for such a purpose, Eq. (32) itself is enough (Section 2.2.3). The weathering flux of total cations, F_{CO_2} ($\text{mol m}^{-2} \text{yr}^{-1}$), is obtained by multiplying the loss rate of total cations (Eqs. (26) and (27)) by h_{ss} as mentioned above:

$$F_{CO_2} = h_{ss} \left| \frac{d[\text{Rock}]}{dt} \right| \quad (33)$$

The weathering flux of a given element can be obtained similarly to Eq. (33). For example, Si-flux is represented by $h_{ss}|d[\text{Si-rock}]/dt|$ ($\text{mol m}^{-2} \text{yr}^{-1}$). In the present study, however, I discuss the CO_2 regulation at the Earth and therefore the formulation of the weathering flux and apparent activation energy is conducted only for F_{CO_2} .

Table 2. Stoichiometry and standard enthalpy change for various minerals^a.

Mineral	Y _{Na,j}	Y _{K,j}	Y _{Mg,j}	Y _{Ca,j}	Y _{Fe,j}	Y _{Al,j}	Y _{Si,j}	Y _{H,j}	Y _{tot,j}	ΔH_j° (kJ mol ⁻¹) ^b
Albite	1	0	0	0	0	1	3	4	5	-54.15
Anorthite	0	0	0	1	0	2	2	8	5	-292.9
K-feldspar	0	1	0	0	0	1	3	4	5	-26.31
Diopside	0	0	1	1	0	0	2	4	4	-138.6
Enstatite	0	0	1	0	0	0	1	2	2	-85.82
Ferrosillite	0	0	0	0	1	0	1	2	2	-60.09
Wollastonite	0	0	0	1	0	0	1	2	2	-78.17
Tremolite	0	0	5	2	0	0	8	14	15	-429.0
Hedenbergite	0	0	0	1	1	0	2	4	4	-128.5
Jadeite	1	0	0	0	0	1	2	4	4	-83.54
Fayalite	0	0	0	0	2	0	1	4	3	-153.8
Forsterite	0	2	0	0	0	0	1	4	3	-208.6
Muscovite	0	1	0	0	0	3	3	10	7	-230.8
Phlogopite	0	1	3	0	0	1	3	10	8	-312.8
Annite	0	1	0	0	3	1	3	10	8	-259.9
Anthrophyllite	0	0	7	0	0	0	8	14	15	-508.7
Illite	0	0.6	0.25	0	0	2.3	3.5	8	6.65	-166.4
Beidellite-Mg	0	0	0.165	0	0	2.33	3.67	7.32	6.17	-160.2
Beidellite-Ca	0	0	0	0.165	0	2.33	3.67	7.32	6.17	-157.0
Kaolinite	0	0	0	0	0	2	2	6	4	-143.7
Amorphous silica	0	0	0	0	0	0	1	0	1	16.52
Gibbsite	0	0	0	0	0	1	0	3	1	-95.66

^a Data are from the Lawrence Livermore National Laboratory thermodynamic dataset, thermo.com.v8r6+.dat (Delany and Lundeen, 1990).

^b ΔH_j° is the standard enthalpy change, defined by Eq. (38) (Section 2.2.1).

Table 3. The values of Z_{Al} , n_{Al} and $\Delta H^\circ_{\text{Al}}$ at different pH.

pH	Z_{Al}^{a}	n_{Al}^{a}	$\Delta H^\circ_{\text{Al}}$ (kJ mol ⁻¹) ^a
3.0	3	0	0
5.0	2	1	50
5.8	1	2	109
6.3	0	3	145
7.9	-1	4	177

^a Z_{Al} , n_{Al} and $\Delta H^\circ_{\text{Al}}$ are the average valence number of dissolved Al, the average hydrolyzed number of dissolved Al and the average standard enthalpy change for hydrolysis of Al, respectively, and they are defined by Eqs. (A7), (A8) and (A9), respectively. Z_{Al} , n_{Al} and $\Delta H^\circ_{\text{Al}}$ are calculated based on the data by Stumm and Morgan (1996) (Table A1, see Appendix A for details). Z_{Al} and n_{Al} are those at 25 °C and 1 atm.

2.2. Apparent activation energy

I here consider the apparent activation energy of silicate weathering based on the equations presented in Section 2.1. I first introduce the general equation by which the apparent activation energy is defined. In general, a chemical reaction rate can be written in the Arrhenius expression (e.g., White and Blum, 1995):

$$r_{\text{I}} = A_{\text{I}} \exp\left(-\frac{E_{\text{app}}^{\text{I}}}{R_{\text{g}}T}\right) \quad (34)$$

where r_{I} , A_{I} and $E_{\text{app}}^{\text{I}}$ are the rate, the pre-exponential factor and the apparent activation energy (kJ mol⁻¹), respectively, of a certain chemical reaction I. R_{g} and T denote the gas constant (8.3×10^{-3} kJ K⁻¹ mol⁻¹) and the absolute temperature (K), respectively. From Eq. (34),

$$E_{\text{app}}^{\text{I}} = -R_{\text{g}} \frac{d \ln |r_{\text{I}}|}{d(1/T)} \quad (35)$$

By applying Eq. (35) to the equations presented in Section 2.1, the apparent activation energies for dissolution/precipitation of silicates, elemental loss by silicate weathering, and weathering flux of silicates are obtained separately (Sections 2.2.1, 2.2.1 and 2.2.3, respectively). The relationships in apparent activation energy between the three scales

are considered later in Section 3.

2.2.1. Apparent activation energy of silicate dissolution/precipitation

The apparent activation energy of dissolution/precipitation of silicate j , E_{app}^j (kJ mol^{-1}), is obtained by applying Eq. (35) to Eq. (4),

$$E_{\text{app}}^j = -R_g \frac{d \ln |r_j|}{d(1/T)} = -R_g \frac{d \ln k_j}{d(1/T)} - b_j R_g \frac{d \ln \{1 - (Q_j / K_j)^{a_j}\}}{d(1/T)} \quad (36)$$

Note that S_j in Eq. (4) is assumed to be temperature-independent in the present study. I define the temperature dependences of k_j , K_j and Q_j as follows:

$$\frac{d \ln k_j}{d(1/T)} \equiv -\frac{E_j}{R_g} \quad (37)$$

$$\frac{d \ln K_j}{d(1/T)} \equiv -\frac{\Delta H_j^\circ}{R_g} \quad (38)$$

$$\frac{d \ln Q_j}{d(1/T)} \equiv -\frac{\Delta H'_{Q_j}}{R_g} \quad (39)$$

The temperature dependence of the forward reaction constant k_j is described as E_j (kJ mol^{-1}) in Eq. (37). Eq. (38) describes the temperature dependence of thermodynamic constant as the standard enthalpy change, ΔH_j° (kJ mol^{-1}). The values of ΔH_j° for various minerals are listed in Table 2. In Eq. (39), $\Delta H'_{Q_j}$ (kJ mol^{-1}) represents the temperature dependence of Q_j as a pseudo-enthalpy change. In the present study, the pseudo-enthalpy change ($\Delta H'$) is defined for non-thermodynamic constants as the parameter that is analogous to the standard enthalpy change for thermodynamic constants. Thus, the temperature dependences of non-thermodynamic constants (e.g., Q_j) are represented by the pseudo-enthalpy changes (e.g., $\Delta H'_{Q_j}$ in Eq. (39)), in a similar way to that the temperature dependences of thermodynamic constants (e.g., K_j) are represented by the standard enthalpy changes (e.g., ΔH_j° in Eq. (38)). Using Eqs. (37)–(39), I can express Eq. (36) as

$$E_{\text{app}}^j = E_j - a_j b_j \left\{ \frac{(Q_j / K_j)^{a_j}}{1 - (Q_j / K_j)^{a_j}} \right\} (\Delta H'_{Q_j} - \Delta H_j^\circ) \quad (40)$$

In Eq. (40), the value within curly braces approaches negative or positive infinity as Q_j

→ K_j . Therefore, the apparent activation energy of a mineral reaction can change significantly near equilibrium, depending on the value of $(\Delta H'_{Q_j} - \Delta H^\circ_j)$. Although ΔH°_j is uniquely determined by thermodynamics (Table 2), $\Delta H'_{Q_j}$ is dependent on Q_j which is determined by solute concentrations (Eq. (5)). Because the solute concentrations are in turn determined by the loss rates of elements (e.g., Eq. (8)), the values of Q_j and thus $\Delta H'_{Q_j}$ are influenced by the apparent activation energies of elemental losses by silicate weathering. Such relationships in the apparent activation energies between the three scales are discussed in Section 3, after all the apparent activation energies in the three scales are formulated.

2.2.2. Apparent activation energy of elemental loss by silicate weathering

The apparent activation energies of X, Si and Al loss by silicate weathering (E_{app}^X , E_{app}^{Si} and E_{app}^{Al} (kJ mol^{-1}), respectively) are obtained by applying Eq. (35) to Eqs. (6), (12) and (14), respectively, and using Eq. (36),

$$E_{app}^X = -R_g \frac{d}{d(1/T)} \ln \left| \frac{d[X - \text{rock}]}{dt} \right| = \sum_j \frac{\gamma_{X,j} r_j E_{app}^j}{\sum_j \gamma_{X,j} r_j} \quad (41)$$

$$E_{app}^{Si} = -R_g \frac{d}{d(1/T)} \ln \left| \frac{d[Si - \text{rock}]}{dt} \right| = \sum_j \frac{\gamma_{Si,j} r_j E_{app}^j}{\sum_j \gamma_{Si,j} r_j} \quad (42)$$

$$E_{app}^{Al} = -R_g \frac{d}{d(1/T)} \ln \left| \frac{d[Al - \text{rock}]}{dt} \right| = \sum_j \frac{\gamma_{Al,j} r_j E_{app}^j}{\sum_j \gamma_{Al,j} r_j} \quad (43)$$

Eqs. (41)–(43) indicate that the apparent activation energies of X, Si and Al loss by silicate weathering depend on the apparent activation energies of the minerals which supply the elements. Contribution of a certain mineral to the apparent activation energy of loss of an element is equivalent to the rate-contribution of the mineral to the loss rate of the element. For example, the rate-contribution of mineral j to the X loss rate, $\alpha_{X,j}$, is defined by

$$\alpha_{X,j} \equiv \frac{\gamma_{X,j} r_j}{\sum_j \gamma_{X,j} r_j} \quad (44)$$

$\alpha_{X,j}$ is positive or negative when mineral j is dissolving or precipitating, respectively.

Using Eq. (44), Eq. (41) can be simplified as

$$E_{\text{app}}^{\text{X}} = \sum_j \alpha_{\text{X},j} E_{\text{app}}^j \quad (45)$$

Similarly, I can rewrite Eqs. (42) and (43) as

$$E_{\text{app}}^{\text{Si}} = \sum_j \alpha_{\text{Si},j} E_{\text{app}}^j \quad (46)$$

$$E_{\text{app}}^{\text{Al}} = \sum_j \alpha_{\text{Al},j} E_{\text{app}}^j \quad (47)$$

where

$$\alpha_{\text{Si},j} \equiv \frac{\gamma_{\text{Si},j} r_j}{\sum_j \gamma_{\text{Si},j} r_j} \quad (48)$$

$$\alpha_{\text{Al},j} \equiv \frac{\gamma_{\text{Al},j} r_j}{\sum_j \gamma_{\text{Al},j} r_j} \quad (49)$$

According to Eqs. (45)–(47), it is expected that $E_{\text{app}}^{\text{X}}$, $E_{\text{app}}^{\text{Si}}$ and $E_{\text{app}}^{\text{Al}}$ vary significantly when the rate-contribution of one mineral changes and/or one mineral has very different apparent activation energy from the others. On the other hand, when one mineral dominates the loss rate of a certain element, then the apparent activation energy of the loss of the element should be same as that for dissolution of the mineral (e.g., White et al., 1999).

The apparent activation energy of Fe loss by silicate weathering, $E_{\text{app}}^{\text{Fe}}$ (kJ mol^{-1}), can be obtained by applying Eq. (35) to (23), and using Eq. (36),

$$E_{\text{app}}^{\text{Fe}} = -R_g \frac{d}{d(1/T)} \ln \left| \frac{d[\text{Fe-rock}]}{dt} \right| = \sum_j \alpha_{\text{Fe},j} E_{\text{app}}^j - R_g \frac{d \ln \psi}{d(1/T)} \quad (50)$$

where

$$\alpha_{\text{Fe},j} \equiv \frac{\gamma_{\text{Fe},j} r_j}{\sum_j \gamma_{\text{Fe},j} r_j} \quad (51)$$

In the right hand side of Eq. (50), the first term represents the contributions of various Fe^{2+} -bearing silicate minerals. The second term represents the temperature dependence of ψ , which is a function of k_f and λ (Eq. (21)). I define the temperature dependences of k_f and λ as the pseudo-enthalpy changes (kJ mol^{-1}):

$$\Delta H'_f \equiv -R_g \frac{d \ln k_f}{d(1/T)} \quad (52)$$

$$\Delta H'_\lambda \equiv -R_g \frac{d \ln \lambda}{d(1/T)} \quad (53)$$

Then, using Eqs. (21), (22), (52) and (53), Eq. (50) can be extended:

$$E_{\text{app}}^{\text{Fe}} = \sum_j \alpha_{\text{Fe},j} E_{\text{app}}^j + \phi(\Delta H'_f - \Delta H'_\lambda) \quad (54)$$

Eq. (54) indicates that the value of $E_{\text{app}}^{\text{Fe}}$ changes with P_{O_2} because ϕ is determined by P_{O_2} (Eqs. (17) and (22)). The effects of oxygen on $E_{\text{app}}^{\text{Fe}}$ are discussed in Section 5.3.

The apparent activation energy of total-cation loss by silicate weathering, $E_{\text{app}}^{\text{Rock}}$ (kJ mol^{-1}), can be obtained by applying Eq. (35) to (25) and using Eqs. (36), (52) and (53):

$$\begin{aligned} E_{\text{app}}^{\text{Rock}} &= -R_g \frac{d}{d(1/T)} \ln \left| \frac{d[\text{Rock}]}{dt} \right| \\ &= \frac{\sum_j (\gamma_{\text{H},j} - n_{\text{Al}} \gamma_{\text{Al},j} - 2\phi \gamma_{\text{Fe},j}) r_j E_{\text{app}}^j}{\sum_j (\gamma_{\text{H},j} - n_{\text{Al}} \gamma_{\text{Al},j} - 2\phi \gamma_{\text{Fe},j}) r_j} \\ &\quad + 2\psi \phi (\Delta H'_f - \Delta H'_\lambda) \frac{\sum_j \gamma_{\text{Fe},j} r_j}{\sum_j (\gamma_{\text{H},j} - n_{\text{Al}} \gamma_{\text{Al},j} - 2\phi \gamma_{\text{Fe},j}) r_j} \\ &\quad - R_g \frac{d \ln Z_{\text{Al}}}{d(1/T)} \frac{Z_{\text{Al}} \sum_j \gamma_{\text{Al},j} r_j}{\sum_j (\gamma_{\text{H},j} - n_{\text{Al}} \gamma_{\text{Al},j} - 2\phi \gamma_{\text{Fe},j}) r_j} \end{aligned} \quad (55)$$

I define here the contribution of equivalent concentration of element Y ($Z_Y[Y]_{\text{ss}}$) to the total equivalent concentration of cations ($\cong [\text{HCO}_3^-]_{\text{ss}}$, Eq. (26)) as β_Y :

$$\beta_Y \equiv \frac{Z_Y[Y]_{\text{ss}}}{[\text{HCO}_3^-]_{\text{ss}}} \quad (56)$$

where $Y = X, \text{Al}$ and Fe . Using Eqs. (8), (9) (11), (13), (18), (21), (22) and (27), $\beta_X, \beta_{\text{Al}}$ and β_{Fe} can be represented by the following respective equations:

$$\beta_X = \frac{Z_X \sum_j \gamma_{X,j} r_j}{\sum_j (\gamma_{\text{H},j} - n_{\text{Al}} \gamma_{\text{Al},j} - 2\phi \gamma_{\text{Fe},j}) r_j} \quad (57)$$

$$\beta_{\text{Al}} = \frac{Z_{\text{Al}} \sum_j \gamma_{\text{Al},j} r_j}{\sum_j (\gamma_{\text{H},j} - n_{\text{Al}} \gamma_{\text{Al},j} - 2\phi \gamma_{\text{Fe},j}) r_j} \quad (58)$$

$$\beta_{\text{Fe}} = \frac{2\psi \sum_j \gamma_{\text{Fe},j} r_j}{\sum_j (\gamma_{\text{H},j} - n_{\text{Al}} \gamma_{\text{Al},j} - 2\phi \gamma_{\text{Fe},j}) r_j} \quad (59)$$

Then, from Eqs. (57)–(59), Eq. (55) can be simplified as

$$E_{\text{app}}^{\text{Rock}} = \sum_Y \beta_Y E_{\text{app}}^Y - \beta_{\text{Al}} R_g \frac{d \ln Z_{\text{Al}}}{d(1/T)} \quad (60)$$

Usually I can assume $\beta_{\text{Al}} \cong 0$ (Garrels and Mackenzie, 1971). Then Eq. (60) can be further simplified:

$$E_{\text{app}}^{\text{Rock}} = \sum_Y \beta_Y E_{\text{app}}^Y \quad (61)$$

Eq. (61) indicates that, by determining E_{app}^Y and β_Y values, I can estimate $E_{\text{app}}^{\text{Rock}}$.

In a similar way to the formulation of $E_{\text{app}}^{\text{Rock}}$, the apparent activation energy of loss of TDS by silicate weathering, $E_{\text{app}}^{\text{Rock-2}}$ (kJ mol^{-1}), can be obtained. The contribution of the steady-state concentration of element W to that of TDS is defined as η_W :

$$\eta_W = \frac{[\text{W}]_{\text{ss}}}{\sum_{\text{W}} [\text{W}]_{\text{ss}}} \quad (62)$$

where $W = X, \text{Si}, \text{Al}$ and Fe . Using Eqs. (8), (9), (28) and (29), η_X is represented as

$$\eta_X = \frac{\sum_j \gamma_{X,j} r_j}{\sum_j (\gamma_{\text{tot},j} - \phi \gamma_{\text{Fe},j}) r_j} \quad (63)$$

η_{Si} and η_{Al} can be obtained by substituting X in Eq. (63) with Si and Al, respectively.

From Eqs. (18), (21), (22), (28) and (29), η_{Fe} is given by

$$\eta_{\text{Fe}} = \frac{\psi \sum_j \gamma_{\text{Fe},j} r_j}{\sum_j (\gamma_{\text{tot},j} - \phi \gamma_{\text{Fe},j}) r_j} \quad (64)$$

Then, applying Eq. (35) to (29), and using Eqs. (41)–(43), (50), (54), (63) and (64),

$$E_{\text{app}}^{\text{Rock-2}} = -R_g \frac{d}{d(1/T)} \ln \left| \frac{d[\text{Rock-2}]}{dt} \right| = \sum_{\text{W}} \eta_{\text{W}} E_{\text{app}}^{\text{W}} \quad (65)$$

Eq. (65) indicates that $E_{\text{app}}^{\text{Rock-2}}$ can be estimated by determining η_{W} and $E_{\text{app}}^{\text{W}}$.

2.2.3. Apparent activation energy of weathering flux

To obtain the apparent activation energy of weathering flux of total cations, $E_{\text{app}}^{\text{CO}_2}$ (kJ mol^{-1}), the temperature dependence of h_{ss} is required (Eq. (33)). I define the temperature dependence of h_{ss} as $\Delta H'_h$:

$$\Delta H'_h \equiv -R_g \frac{d \ln h_{\text{ss}}}{d(1/T)} \quad (66)$$

From Eqs. (32), (65) and (66),

$$\Delta H'_h = -\frac{c|d[\text{Rock} - 2]/dt|}{\delta D + c|d[\text{Rock} - 2]/dt|} E_{\text{app}}^{\text{Rock-2}} \quad (67)$$

where I assume that D_0 , δ , PhE and c are temperature-independent in Eq. (32). In Eq. (67), δD has the unit of yr^{-1} and represents the first-order rate constant for a total denudation rate. Also, $c|d[\text{Rock}-2]/dt|$ has the unit of yr^{-1} , which represents the first-order rate constant for a chemical denudation rate. I here define the chemical depletion fraction (CDF) as (c.f., Riebe et al. (2001))

$$CDF = \frac{c|d[\text{Rock} - 2]/dt|}{\delta D} \quad (68)$$

Using Eq. (68), Eq. (67) can be expressed alternatively:

$$\Delta H'_h = -\frac{CDF}{1 + CDF} E_{\text{app}}^{\text{Rock-2}} \quad (69)$$

Then, I can obtain the apparent activation energy of weathering flux, $E_{\text{app}}^{\text{CO}_2}$, by applying Eq. (35) to Eq. (33) and using Eqs. (55), (66) and (69):

$$\begin{aligned} E_{\text{app}}^{\text{CO}_2} &\equiv -R_g \frac{d \ln F_{\text{CO}_2}}{d(1/T)} \\ &= E_{\text{app}}^{\text{Rock}} + \Delta H'_h \\ &= E_{\text{app}}^{\text{Rock}} - \frac{CDF}{1 + CDF} E_{\text{app}}^{\text{Rock-2}} \end{aligned} \quad (70)$$

Eq. (70) indicates that once CDF , $E_{\text{app}}^{\text{Rock}}$ and $E_{\text{app}}^{\text{Rock-2}}$ are determined, I can estimate $E_{\text{app}}^{\text{CO}_2}$. Note that when one considers apparent activation energy of weathering flux, $\Delta H'_h$ must be added to that of elemental loss by weathering (e.g., apparent activation energy of Si flux = $E_{\text{app}}^{\text{Si}} + \Delta H'_h$).

3. Estimation of apparent activation energy of silicate weathering

I have introduced the apparent activation energies of silicate dissolution/precipitation (Section 2.2.1), elemental loss by silicate weathering (Section 2.2.2) and weathering flux of silicates (Section 2.2.3), separately. As mentioned in each section, these energies are correlated with one another, and therefore, should be considered together to obtain consistent apparent-activation energies. In the following, I first examine the relationship in apparent activation energy between the mineral reaction and elemental loss by weathering using the equations in Sections 2.2.1 and 2.2.2, through which consistent apparent-activation energies of elemental losses are estimated

(Section 3.1). Then, from the relationship of apparent activation energy between the elemental loss and flux by weathering, the apparent activation energy of weathering flux is estimated, using the equations in Sections 2.2.2 and 2.2.3 (Section 3.2).

3.1. Estimation of apparent activation energy of elemental loss by silicate weathering

To consider the apparent activation energy of reaction of each silicate (Section 2.2.1), I must take into account the temperature dependence of Q_j , $\Delta H'_j$ (Eq. (39)). Using Eq. (5), Q_j at steady state can be represented as

$$Q_j = \frac{[\text{Si}]_{\text{ss}}^{\gamma_{\text{Si},j}} [\text{Al}^{3+}]_{\text{ss}}^{\gamma_{\text{Al},j}} [\text{Fe}]_{\text{ss}}^{\gamma_{\text{Fe},j}}}{[\text{H}^+]_{\text{ss}}^{\gamma_{\text{H},j}}} \prod_{\text{X}} [\text{X}]_{\text{ss}}^{\gamma_{\text{X},j}} \quad (71)$$

where $[\text{Al}^{3+}]_{\text{ss}}$ and $[\text{H}^+]_{\text{ss}}$ are the steady-state concentrations of Al^{3+} and H^+ in porewater (mol L^{-1}), respectively. The steady-state concentrations of elements were obtained from the equations for elemental loss by weathering in Section 2.1.2. For example, from Eq. (10),

$$[\text{X}]_{\text{ss}} = q^{-1} \left| \frac{d[\text{X} - \text{rock}]}{dt} \right| \quad (72)$$

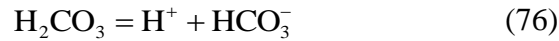
$[\text{Si}]_{\text{ss}}$ and $[\text{Fe}]_{\text{ss}}$ can be similarly formulated by using Eqs. (12) and (20), respectively. However, $[\text{Al}^{3+}]_{\text{ss}}$ in Eq. (71) is not the same as $[\text{Al}]_{\text{ss}}$ defined in Eq. (13). The ratio of Al^{3+} to the total dissolved Al is defined here as f_{Al} :

$$f_{\text{Al}} \equiv \frac{[\text{Al}^{3+}]_{\text{ss}}}{[\text{Al}]_{\text{ss}}} \quad (73)$$

Then, from Eqs. (73) and (14),

$$[\text{Al}^{3+}]_{\text{ss}} = f_{\text{Al}} q^{-1} \left| \frac{d[\text{Al} - \text{rock}]}{dt} \right| \quad (74)$$

$[\text{H}^+]_{\text{ss}}$ in Eq. (71) is related to the following reactions:



Using the Henry's constant K_{HC} ($\text{mol L}^{-1} \text{atm}^{-1}$) and the equilibrium constant K_1 (mol L^{-1}) for Reactions (75) and (76), respectively, $[\text{H}^+]_{\text{ss}}$ can be represented as

$$[\text{H}^+]_{\text{ss}} = \frac{K_1 K_{\text{HC}} P_{\text{CO}_2}}{[\text{HCO}_3^-]_{\text{ss}}} \quad (77)$$

The steady-state bicarbonate concentration in Eq. (77) is related to the loss rate of total

cations (Eq. (27)). From Eqs. (27) and (77),

$$[H^+]_{ss} = qK_1K_{HC}P_{CO_2} \left| \frac{d[Rock]}{dt} \right|^{-1} \quad (78)$$

From Eqs. (72), (74), and (78), Q_j is rewritten as

$$Q_j = \left| \frac{d[Rock]}{dt} \right|^{\gamma_{H,j}} \prod_W \left| \frac{d[W - rock]}{dt} \right|^{\gamma_{W,j}} f_{Al}^{\gamma_{Al,j}} q^{-(\gamma_{W,j} + \gamma_{H,j})} (K_1K_{HC}P_{CO_2})^{-\gamma_{H,j}} \quad (79)$$

where $W = X, Si, Al$ and Fe . To obtain $\Delta H'_{Q_j}$ by using Eq. (79), the temperature dependences of q , K_1 , K_{HC} and P_{CO_2} are required and those are defined by the following respective equations:

$$\frac{d \ln q}{d(1/T)} \equiv -\frac{\Delta H'_q}{R_g} \quad (80)$$

$$\frac{d \ln K_1}{d(1/T)} \equiv -\frac{\Delta H'_1}{R_g} \quad (81)$$

$$\frac{d \ln K_{HC}}{d(1/T)} \equiv -\frac{\Delta H'_{HC}}{R_g} \quad (82)$$

$$\frac{d \ln P_{CO_2}}{d(1/T)} \equiv -\frac{\Delta H'_{CO_2}}{R_g} \quad (83)$$

The temperature dependence of f_{Al} is also required for the calculation of $\Delta H'_{Q_j}$ according to Eq. (79). Because f_{Al} is pH-dependent (Appendix A), I need to first define the temperature dependence of $[H^+]_{ss}$, $\Delta H'_{H^+}$ as

$$\Delta H'_{H^+} \equiv -R_g \frac{d \ln [H^+]_{ss}}{d(1/T)} \quad (84)$$

Using Eq. (84), the temperature dependence of f_{Al} is defined by

$$\frac{d \ln f_{Al}}{d(1/T)} \equiv \frac{\Delta H^\circ_{Al} - n_{Al} \Delta H'_{H^+}}{R_g} \quad (85)$$

ΔH°_{Al} in Eq. (85) is the average standard enthalpy change for Al-hydrolysis, which is pH-dependent as well as n_{Al} (Table 3 and Fig. A1). See Appendix A for the details of ΔH°_{Al} and n_{Al} and of the formulation of Eq. (85). Then, from the definition of $\Delta H'_{Q_j}$ (Eq. (39)), equations in Section 2.2.2 and Eqs. (79)–(85),

$$\Delta H'_{Q_j} = \sum_W \gamma_{W,j} E_{app}^W + \gamma_{H,j} E_{app}^{Rock} - (\gamma_{tot,j} + \gamma_{H,j}) \Delta H'_q - \gamma_{H,j} (\Delta H'_{CO_2} + \Delta H_1^\circ + \Delta H_H^\circ) - \gamma_{Al,j} \Delta H_{Al}^\circ + n_{Al} \gamma_{Al,j} \Delta H'_{H^+} \quad (86)$$

I can extend $\Delta H'_{H^+}$ in Eq. (86) by using Eqs. (78) and (84):

$$\Delta H'_{H^+} = \Delta H'_q + \Delta H_1^\circ + \Delta H_{HC}^\circ + \Delta H'_{CO_2} - E_{app}^{Rock} \quad (87)$$

Substituting Eq. (87) into Eq. (86), I finally obtain

$$\Delta H'_{Q_j} = \sum_W \gamma_{W,j} E_{app}^W + (\gamma_{H,j} - n_{Al} \gamma_{Al,j}) E_{app}^{Rock} - (\gamma_{tot,j} + \gamma_{H,j} - n_{Al} \gamma_{Al,j}) \Delta H'_q - (\gamma_{H,j} - n_{Al} \gamma_{Al,j}) (\Delta H'_{CO_2} + \Delta H_1^\circ + \Delta H_{HC}^\circ) - \gamma_{Al,j} \Delta H_{Al}^\circ \quad (88)$$

In Eq. (88), ΔH_1° and ΔH_{HC}° are thermodynamically determined and $\Delta H'_q$ can be assumed (Table 4). ΔH_{Al}° and n_{Al} are thermodynamically determined once pH is assumed (Table 3). As for $\Delta H'_{CO_2}$, I discuss the relationships between $\Delta H'_{CO_2}$ and P_{CO_2} later in Section 5.1. Here $\Delta H'_{CO_2}$ is taken as a variable. The values of γ for the minerals are given in Table 2. Once the values of E_{app}^W are determined, E_{app}^{Rock} is also determined if the contribution ratios (β_Y values) are known (Eq. (61)). Therefore, by assuming the values of $\Delta H'_{CO_2}$, β_Y and E_{app}^W , $\Delta H'_{Q_j}$ can be calculated from Eqs. (61) and (88) and the data in Tables 2–4.

Once $\Delta H'_{Q_j}$ is determined, it affects the apparent activation energy of the reaction of mineral j (E_{app}^j) according to Eq. (40). Defining ΔE_{app}^j (kJ mol⁻¹) as the difference between E_{app}^j and E_j as the effects of $(\Delta H'_{Q_j} - \Delta H_j^\circ)$ in Eq. (40), ΔE_{app}^j is given by

$$\Delta E_{app}^j \equiv E_{app}^j - E_j = -a_j b_j \left\{ \frac{(Q_j / K_j)^{a_j}}{1 - (Q_j / K_j)^{a_j}} \right\} (\Delta H'_{Q_j} - \Delta H_j^\circ) \quad (89)$$

ΔE_{app}^j is plotted against Q_j/K_j for different $(\Delta H'_{Q_j} - \Delta H_j^\circ)$ values with $a_j = b_j = 1$ in Fig. 2a, showing that ΔE_{app}^j approaches negative or positive infinity with approaching equilibrium, depending on the $(\Delta H'_{Q_j} - \Delta H_j^\circ)$ values. Such large effects of saturation degree (Q_j/K_j) on apparent activation energy are consistent with the proposition by Lasaga (1995) and the experimental results of Cama et al. (1999). Because $\Delta H'_{Q_j}$ is a function of $\Delta H'_{CO_2}$ (Eq. (88)), ΔE_{app}^j (and thus E_{app}^j) is expected to be dependent on $\Delta H'_{CO_2}$. The effects of various a_j and b_j are depicted in Figs. 2b and c where I used the complex combinations of a_j and b_j reported for dissolution of albite (Hellmann and Tisserand, 2006, Fig. 2b) and diopside (Daval et al., 2010, Fig. 2c), respectively. Figs. 2b and c show that ΔE_{app}^j can be significant even at very low value of Q_j/K_j , depending

on the values of a_j and b_j (e.g., as low as 10^{-10} of Q_j/K_j for diopside, Fig. 2c). Nonetheless, the smaller the $|\Delta H'_{Q_j} - \Delta H^\circ_j|$ value becomes, the smaller the ΔE_{app}^j value is.

The change in E_{app}^j depicted as ΔE_{app}^j in Fig. 2a in turn affects E_{app}^W (e.g., Eq. (45)), and finally E_{app}^{Rock} (Eq. (61)), which again affects $\Delta H'_{Q_j}$, ΔE_{app}^j and E_{app}^j . Therefore, with a large value of $|\Delta E_{app}^j|$, the values of E_{app}^j , E_{app}^W and E_{app}^{Rock} never converge, which is in contrast with the apparent activation energies observed for modern weathering profiles (e.g., White and Blum, 1995; Dessert et al., 2001). Accordingly, for a set of E_{app}^j , E_{app}^W and E_{app}^{Rock} to be determined for given weathering conditions (i.e., for a given $\Delta H'_{CO_2}$ value), ΔE_{app}^j for the minerals should be minimum. Such conditions are satisfied only when the value of $|\Delta H'_{Q_j} - \Delta H^\circ_j|$ is at minimum or in a relatively small range (Fig. 2), which allows me to obtain a unique set of E_{app}^W and E_{app}^{Rock} for a given $\Delta H'_{CO_2}$.

Caution must be paid to the fact that different minerals have different values of Q_j/K_j in porewater. Then the effect of $|\Delta H'_{Q_j} - \Delta H^\circ_j|$ on ΔE_{app}^j is smaller for minerals with larger $|\Delta H^\circ_j|$ than those with smaller $|\Delta H^\circ_j|$; Figs. 2b and c demonstrate that the ΔE_{app}^j value of diopside with larger $|\Delta H^\circ_j|$ ($138.6 \text{ kJ mol}^{-1}$) is less affected by the $|\Delta H'_{Q_j} - \Delta H^\circ_j|$ value than that of albite with smaller $|\Delta H^\circ_j|$ ($54.15 \text{ kJ mol}^{-1}$). Therefore, considering the difference in $|\Delta H^\circ_j|$ between minerals (Table 2), I take $|(\Delta H'_{Q_j} - \Delta H^\circ_j)/\Delta H^\circ_j|$ instead of $|\Delta H'_{Q_j} - \Delta H^\circ_j|$ for the estimation of E_{app}^W and E_{app}^{Rock} . By minimizing the value of $|(\Delta H'_{Q_j} - \Delta H^\circ_j)/\Delta H^\circ_j|$ for mineral j involved in silicate weathering, I estimate a set of E_{app}^W and E_{app}^{Rock} for a given $\Delta H'_{CO_2}$ value, using Eq. (88) and Tables 2–4. It must be clarified that the estimation is based on the assumption that the effect of saturation degree on the reaction rate of mineral j is significant (e.g., Sak et al., 2004; Ganor et al., 2007; Maher et al., 2009; Emmanuel and Ague, 2011; Yokoyama, 2013).

For the calculation, the β_Y values are assumed and listed in Table 5. I consider only low- O_2 conditions here (the effect of increasing oxygen level is discussed in Section 5.3) and I can assume $\beta_{Fe} = \beta_{Mg}$ (Sugimori et al., 2012). The other β_Y values are chosen so that the ratios of β values (e.g., β_{Na}/β_{Ca}) are similar to those reported for modern weathering (Holland, 1978; Meybeck, 1987) (Table 5). The steps for the calculation of E_{app}^W and E_{app}^{Rock} are the following: (1) the E_{app}^W values ($W = X, Si, Al$ and Fe) are chosen arbitrarily between -300 – 300 kJ mol^{-1} with a resolution of 10 kJ mol^{-1} , and the E_{app}^{Rock} value is calculated according to Eq. (61) using the β_Y values in Table 5, (2) the $|(\Delta H'_{Q_j} - \Delta H^\circ_j)/\Delta H^\circ_j|^2$ value is calculated for mineral j using Eq. (88) and Tables 2–4, and summed up for all the minerals listed in Table 2, and (3) the values of E_{app}^W are adopted when the minimum value of $\sum_j |(\Delta H'_{Q_j} - \Delta H^\circ_j)/\Delta H^\circ_j|^2$ is obtained. The value of $\Delta H'_{CO_2}$ varies as 50, 100, 150, 200 and 250 kJ mol^{-1} . Because ΔH°_{Al} and n_{Al} are pH-dependent

(Table 3) in Eq. (88), I also consider the effects of pH that is assumed to be 3.0, 5.0, 5.8, 6.3 and 7.9 (Table 3). Once I have estimated E_{app}^W and E_{app}^{Rock} in the steps above, I can calculate E_{app}^{Rock-2} by assuming η_W and using the estimated E_{app}^W (Eq. (65)). The assumed values for η_W are listed in Table 5, and they are consistent with the assumed values of β_Y . The value of η_{Si} is chosen so that the η_{Si}/η_{Mg} ratio becomes the same as that of Holland (1978) (Table 5).

The calculated values of E_{app}^W , E_{app}^{Rock} and E_{app}^{Rock-2} are plotted against $\Delta H'CO_2$ values in Figs. 3a–d. Because the pH effects on E_{app}^W are significant only for the relationships between E_{app}^{Al} and $\Delta H'CO_2$, the calculated values of E_{app}^W at different pHs are plotted only for E_{app}^{Al} (Fig. 3c). The effects of $\Delta H'CO_2$ on E_{app}^W are significant except for E_{app}^{Si} , which is constant at 50 kJ mol^{-1} (Fig. 3a). Figs. 3a, b and d indicate that there are positive correlations between $\Delta H'CO_2$ and E_{app}^W , E_{app}^{Rock} and E_{app}^{Rock-2} in general. The positive relationships are explained as follows: when $\Delta H'CO_2$ decreases, the value of $\Delta H'Q_j$ is increased (Eq. (88)) and thus the value of ΔE_{app}^j decreases for dissolution and increases for precipitation (Eq. (89), Fig. 2a). When mineral j is dissolving, the decrease in ΔE_{app}^j decreases E_{app}^j , leading to decreases in E_{app}^W (e.g., Eqs. (44) and (45)). When mineral j is precipitating, the increase in ΔE_{app}^j increases E_{app}^j , which decreases E_{app}^W because the precipitating phase has a negative value for contribution ratio $\alpha_{W,j}$ in Eqs. (44), (48), (49) and (51). Therefore, whether mineral j is dissolving or precipitating, decreasing $\Delta H'CO_2$ results in decreases in E_{app}^W , leading to decreases in E_{app}^{Rock} and E_{app}^{Rock-2} (Eqs. (61) and (65)). Such effects will continue until $\Delta E_{app}^j \cong 0$. Similarly, when $\Delta H'CO_2$ is increased, the values of E_{app}^W , E_{app}^{Rock} and E_{app}^{Rock-2} are increased. Because, together with E_{app}^W , the value of E_{app}^j changes even if I assume some value for E_j in Eq. (40) or (89), the changes in both E_{app}^j and E_{app}^W (e.g., Eq. (45)) occur in the same direction as that in $\Delta H'CO_2$. Therefore, the positive correlation between $\Delta H'CO_2$ on E_{app}^W , E_{app}^{Rock} and E_{app}^{Rock-2} (i.e., positive slopes in $\Delta H'CO_2$ - E_{app}^W , $\Delta H'CO_2$ - E_{app}^{Rock} and $\Delta H'CO_2$ - E_{app}^{Rock-2} diagrams shown in Figs. 3a–d) is reasonable.

The extents of dependences of E_{app}^W on $\Delta H'CO_2$ are different between monovalent and divalent cations (Figs. 3a and b, respectively). For Na and K, $dE_{app}^W/d\Delta H'CO_2$ (i.e., the slope of $\Delta H'CO_2$ - E_{app}^W diagram) is ~ 0.35 (Fig. 3a) while for Mg, Ca and Fe, $dE_{app}^W/d\Delta H'CO_2$ is ~ 0.71 – 0.74 (Fig. 3b). Therefore, weathering of divalent cations is more affected by $\Delta H'CO_2$ than that of monovalent cations. Valence effects on the relationship between E_{app}^W and $\Delta H'CO_2$ calculated for the major cations and Fe can explain the prominent effects of pH on E_{app}^{Al} shown in Fig. 3c. Depending on pH, the average valence of dissolved Al (Z_{Al}) changes from +3 to -1 (Table 3 and Fig. 3c). The dependences of E_{app}^{Al} on $\Delta H'CO_2$ are different at different Z_{Al} and the values of dE_{app}^{Al}

$/d\Delta H'_{CO_2}$ are 1.06, 0.72, 0.36, 0 and -0.34 at $Z_{Al} = 3, 2, 1, 0$ and -1 , respectively. The relationships between Z_{Al} and $dE_{app}^{Al}/d\Delta H'_{CO_2}$ at $Z_{Al} = 1$ and 2 are consistent with the Z_W - $dE_{app}^W/d\Delta H'_{CO_2}$ relationship with $W = X$ and Fe . Then, I can expect the general relationship:

$$dE_{app}^W/d\Delta H'_{CO_2} = 0.35(\pm 0.02) \times Z_W \quad (90)$$

Eq. (90) explains $dE_{app}^{Al}/d\Delta H'_{CO_2} = 1.06, 0$ and -0.34 at $Z_{Al} = 3, 0$ and -1 , respectively.

In addition, Eq. (90) explains the independence of E_{app}^{Si} on $\Delta H'_{CO_2}$ (i.e., $dE_{app}^{Si}/d\Delta H'_{CO_2} = 0$, Fig. 3b), because $Z_{Si} = 0$ at the pH range considered in the present study (Section 2.1.2). The general relationship in Eq. (90) may be due to the temperature dependence of $[H^+]_{ss}$ ($\Delta H'_{H^+}$, Eq. (84)), because $d\Delta H'_{H^+}/d\Delta H'_{CO_2}$ is obtained to be 0.36 from Eq. (87) and Fig. 3d at the assumed pHs. Then, the general relationship in Eq. (90) means

$$dE_{app}^W/d\Delta H'_{H^+} = Z_W \quad (91)$$

Eq. (91) is qualitatively consistent with the perception that the temperature dependence of proton concentration must be reflected in that of weathering loss of cations (e.g., Casey and Sposito, 1992; Lasaga, 1995). Eqs. (90) and (91) expect me that the value of $dE_{app}^{Rock}/d\Delta H'_{CO_2}$ is between 0.35 and 0.7 from Eq. (61). Because divalent cations usually contribute to the total cations more than monovalent cations (Table 5), $dE_{app}^{Rock}/d\Delta H'_{CO_2}$ should be rather near to 0.7. Actually, Fig. 3d shows that $dE_{app}^{Rock}/d\Delta H'_{CO_2} = 0.64$. Because of inclusion of E_{app}^{Si} in E_{app}^{Rock-2} (Eq. (65)), $dE_{app}^{Rock-2}/d\Delta H'_{CO_2}$ is less than $dE_{app}^{Rock}/d\Delta H'_{CO_2}$. In the present study, $dE_{app}^{Rock-2}/d\Delta H'_{CO_2}$ is calculated to be 0.42 (Fig. 3d).

Table 4. Temperature dependences of q , K_1 and K_{HC} .

Explanation	Value	Reference
$\Delta H'_q$ Temperature dependence of volumetric water flow per unit rock volume, q (L m ⁻³) (Eq. (80))	30	Berner et al. (1983); Le Hir et al. (2009) ^a
$\Delta H'_1$ Temperature dependence of thermodynamic constant for carbonic acid dissociation, K_1 (mol L ⁻¹) (Eq. (81))	11.9	Stumm and Morgan (1996)
$\Delta H'_{\text{HC}}$ Temperature dependence of Henry's constant for dissolution of CO ₂ into water, K_{HC} (mol L ⁻¹ atm ⁻¹) (Eq. (82))	-21.3	Stumm and Morgan (1996)

^a From the temperature dependence of continental runoff. Although $\Delta H'_q$ can be temperature-dependent (Berner et al., 1983; Le Hir et al., 2009), I assume the value as constant in the present study. This assumption does not change the main conclusion in the present study.

Table 5. Assumed contributions of elements to concentrations of total cations and TDS.

	Contribution to total cations (β) ^a					Contribution to TDS (η) ^b					
	β_{Na}	β_{K}	β_{Mg}	β_{Ca}	β_{Fe}	η_{Na}	η_{K}	η_{Mg}	η_{Ca}	η_{Fe}	η_{Si}
This study	0.145	0.072	0.232	0.319	0.232	0.170	0.085	0.136	0.187	0.136	0.285
Meybeck (1987) ^c	0.17	0.07	0.31	0.44	-	0.17	0.07	0.16	0.22	-	0.37
Holland (1978)	0.204	0.102	0.408	0.286	-	0.189	0.094	0.189	0.132	-	0.396

^a β is defined in Eq. (56).

^b η is defined in Eq. (62).

^c η is calculated assuming that $[\text{Si}]_{\text{ss}}/[\text{Ca}]_{\text{ss}}$ is 0.167, based on Tables 5 and 7 of Meybeck (1987).

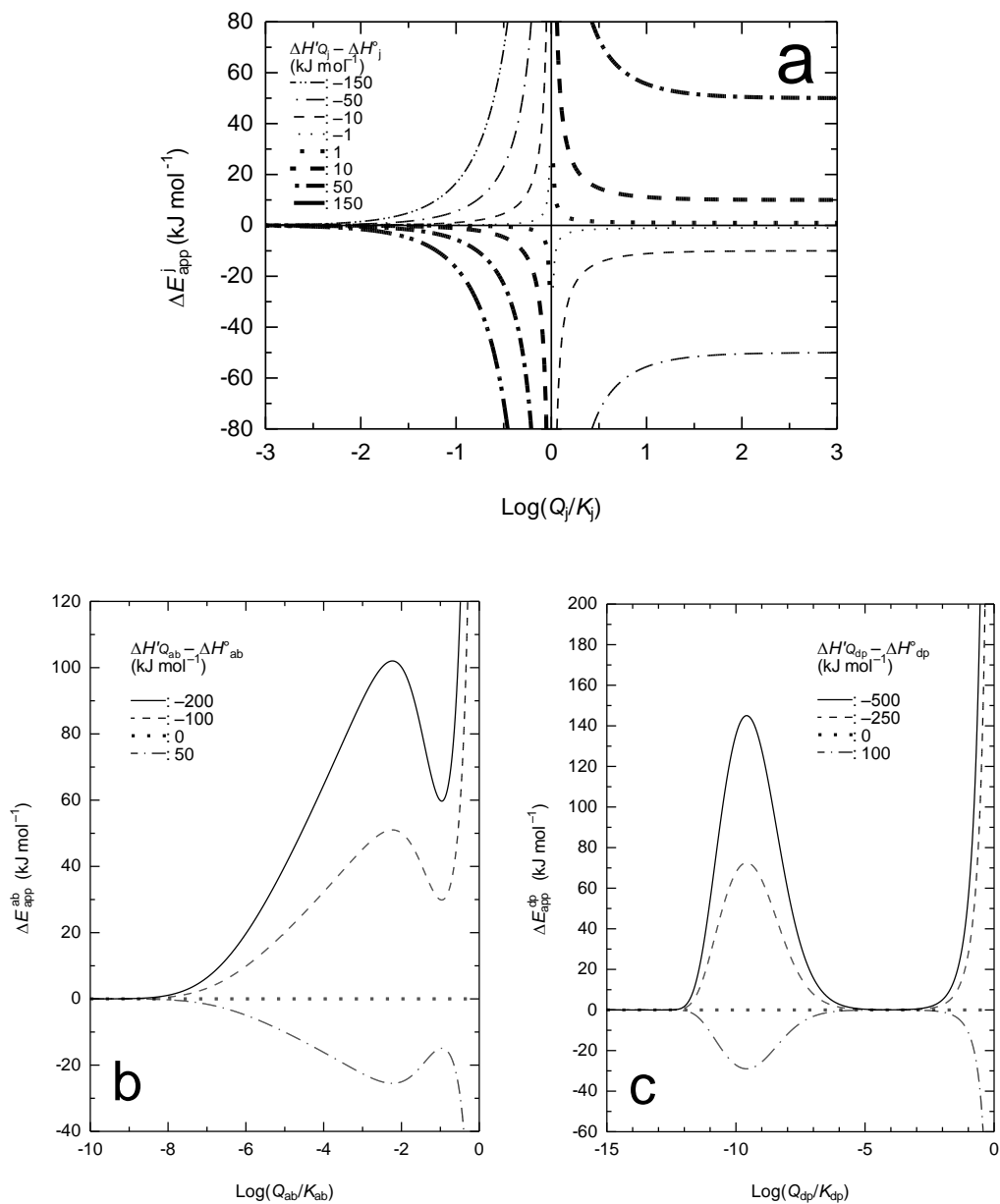


Figure 2. Deviation of apparent activation energy for reaction of mineral j from E_j^j (ΔE_{app}^j) plotted against Q_j/K_j at different $(\Delta H^j_{Q_j} - \Delta H^j)$ values with (a) $a_j = b_j = 1$, (b) a_j and b_j from the rate law of albite dissolution by Hellmann and Tisserand (2006) ($j = \text{albite}$, abbreviated as “ab”) and (c) a_j and b_j from the rate law of diopside dissolution by Daval et al. (2010) ($j = \text{diopside}$, abbreviated as “dp”). Negative $\text{log}(Q_j/K_j)$ indicates that silicate j is dissolving while positive $\text{log}(Q_j/K_j)$ means that silicate j is precipitating.

3.2. Estimation of apparent activation energy of silicate-weathering flux

Estimated values of E_{app}^{Rock-2} in Fig. 3d are useful to deduce the apparent activation energy of weathering flux, because the calculation of the apparent activation energy of weathering flux requires $\Delta H'_h$, which is a function of E_{app}^{Rock-2} (Eq. (70), Section 2.2.3). According to Eq. (70), I can calculate $E_{app}^{CO_2}$ from the estimated E_{app}^{Rock} and E_{app}^{Rock-2} values once a value of CDF is assumed; when $CDF = 0$, $E_{app}^{CO_2} = E_{app}^{Rock}$ while when $CDF = 1$, $E_{app}^{CO_2} = E_{app}^{Rock} - (1/2) \times E_{app}^{Rock-2}$. In Fig. 3e, $E_{app}^{CO_2}$ with $CDF = 0$ and 1 are plotted against $\Delta H'_{CO_2}$, using E_{app}^{Rock-2} and E_{app}^{Rock} in Fig. 3d. The value of CDF is determined by the relative significance of physical erosion for a given chemical erosion rate (Eq. (68)); when physical erosion is large relative to chemical erosion, the ratio of chemical erosion to the total denudation rate (CDF , Eq. (68)) is small and vice versa. Thus, the CDF value reflects weathering regime; $CDF = 0$ reflects the reaction-controlled weathering regime and $CDF = 1$ reflects the transport-controlled weathering regime (e.g., Stallard, 1995; Norton and von Blanckenburg, 2010). Lower values of the apparent activation energy in the transport-controlled regime (Fig. 3e) are consistent with modern weathering observation (Riebe et al., 2004; Rasmussen et al., 2011; Dere et al., 2013).

Because the weathering flux of silicates regulates atmospheric CO_2 levels, the relationship between $\Delta H'_{CO_2}$ and $E_{app}^{CO_2}$ is especially important. I will use the relationship between $\Delta H'_{CO_2}$ and $E_{app}^{CO_2}$ at $CDF = 0.2$ as the standard relationship in the following discussions (Sections 4–6), which is given by

$$E_{app}^{CO_2} = 0.57 \Delta H'_{CO_2} - 5.77 \quad (92)$$

from Eq. (70) and Fig. 3d. The choice of the standard relationship is based on the present-day ratio of the physical to chemical erosion rate where $CDF \cong 0.2$ (Garrels and Mackenzie, 1971). Because perfectly transport-controlled weathering regime (i.e., $CDF = 1$) does not occur (e.g., Riebe et al., 2004) and the physical erosion rate can be assumed to be larger than the chemical erosion rate in the global scale (e.g., Garrels and Mackenzie, 1971; Willenbring and von Blanckenburg, 2010), the low value of CDF is appropriate as the standard in global-scale weathering.

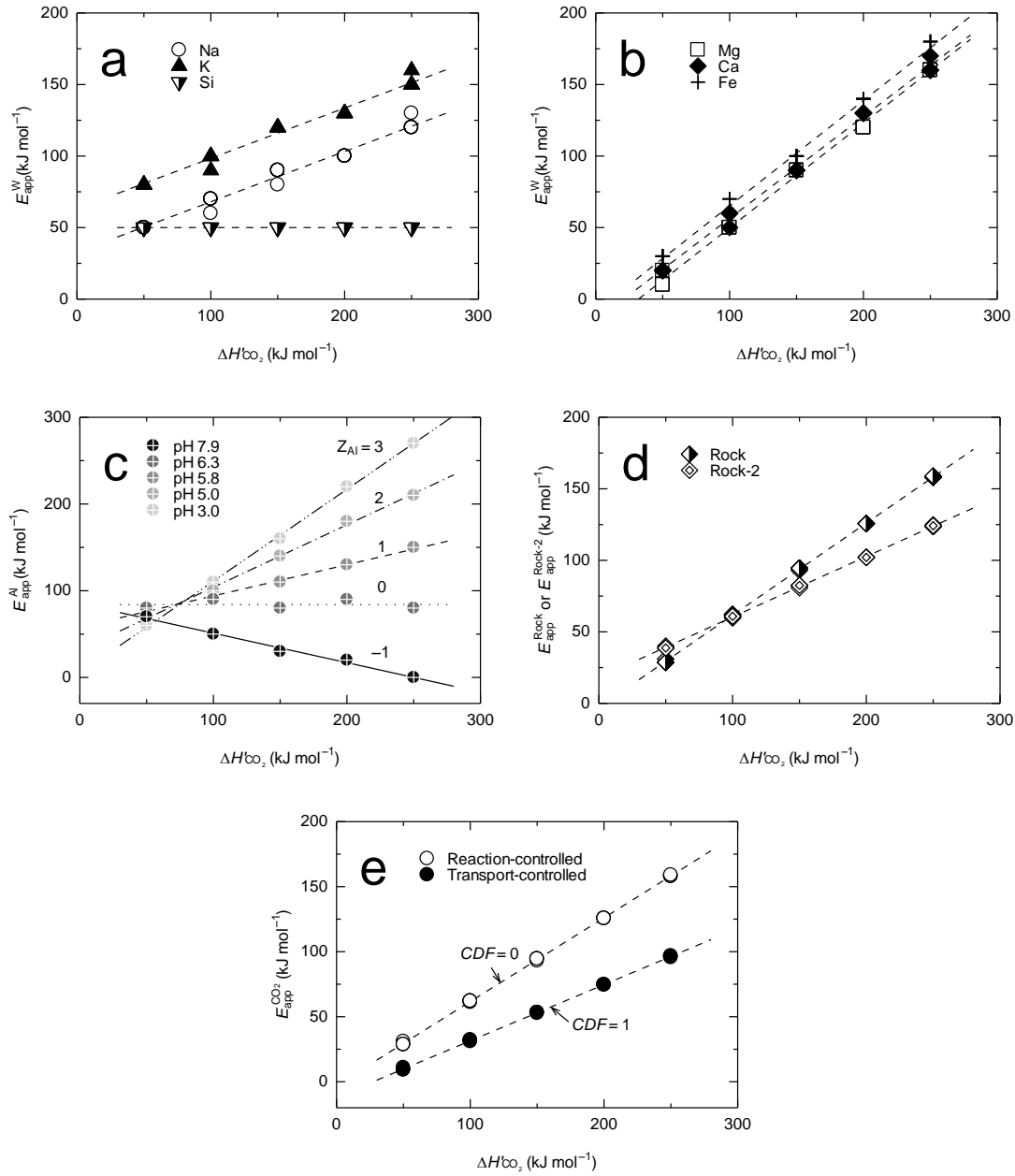


Figure 3. Estimated apparent activation energies plotted against $\Delta H'_{\text{CO}_2}$. The values of (a) $E_{\text{app}}^{\text{Si}}$, $E_{\text{app}}^{\text{Na}}$, $E_{\text{app}}^{\text{K}}$, (b) $E_{\text{app}}^{\text{Mg}}$, $E_{\text{app}}^{\text{Ca}}$, $E_{\text{app}}^{\text{Fe}}$, (c) $E_{\text{app}}^{\text{Al}}$, (d) $E_{\text{app}}^{\text{Rock}}$, $E_{\text{app}}^{\text{Rock-2}}$ and (e) $E_{\text{app}}^{\text{CO}_2}$ are plotted against $\Delta H'_{\text{CO}_2}$. All estimated values at different pH (3.0, 5.0, 5.8, 6.3 and 7.9) are plotted, but the pH effects are negligible except for $E_{\text{app}}^{\text{Al}}$ that varies significantly with pH (Fig. 3c). Lines indicate the linear regressions. $E_{\text{app}}^{\text{CO}_2}$ in reaction-controlled (open circles) and transport-controlled (closed circles) regimes are plotted in Fig. 3e. The CDF values corresponding to the two regimes are also denoted (see the main text).

4. Estimation of silicate-weathering flux

The apparent activation energies estimated in the previous section will allow me to obtain the weathering flux of total cations through compensation law (Lasaga, 1981, 1998; Lasaga et al., 1994). The compensation law describes the relationship between the apparent activation energy and pre-exponential factor by the form of

$$\ln A_L = d_L E_{\text{app}}^L + e_L \quad (93)$$

where A_L and E_{app}^L are the pre-exponential factor and the apparent activation energy, respectively, for any reactions of chemical reaction type L (L refers to, e.g., diffusion, oxide dissolution). When L is mineral dissolution, for instance, the reactions mean dissolution of quartz, albite and so on (e.g., Lasaga et al., 1994). d_L and e_L are the constants empirically obtained by plotting $\ln A$ against E_{app} for various reactions of chemical reaction type L. Once a unique set of d_L and e_L is obtained, the universal temperature, T_{univ}^L (K), is determined by (Lasaga, 1981, 1998; Lasaga et al., 1994)

$$T_{\text{univ}}^L = \frac{1}{d_L R_g} \quad (94)$$

At $T = T_{\text{univ}}^L$, all the reaction rates of chemical reaction type L become the same as (Lasaga, 1981, 1998; Lasaga et al., 1994)

$$r_0^L = \exp(e_L) \quad (95)$$

Then any reaction rate of chemical reaction type L can be represented by

$$r_L = r_0^L \exp \left\{ -\frac{E_{\text{app}}^L}{R_g} \left(\frac{1}{T} - \frac{1}{T_{\text{univ}}^L} \right) \right\} \quad (96)$$

Empirical compensation laws have been reported for diffusion (Lasaga, 1981, 1998) and mineral dissolution (Walther and Wood, 1986; Lasaga et al., 1994; Lasaga, 1998). From the empirical compensation law for dissolution of various minerals, 698, 509 and 318 K have been suggested for the universal temperature of mineral dissolution by Lasaga et al. (1994). The variation in the suggested universal temperatures (698, 509 and 318 K) indicates that the universal temperature of mineral dissolution has a large error and therefore it cannot be applied directly to natural weathering system. Instead, I here attempt to give an empirical compensation law for natural weathering flux using the reported values of the apparent activation energy and pre-exponential factor from the literature on modern weathering. Because the apparent activation energies in the

literature are obtained as those for weathering fluxes with the same dimension (i.e., $\text{mol m}^{-2} \text{ yr}^{-1}$), they must include $\Delta H'_h$ and must be equal to $E_{\text{app}}^{\text{W}} + \Delta H'_h$, $E_{\text{app}}^{\text{Rock}} + \Delta H'_h$ ($\equiv E_{\text{app}}^{\text{CO}_2}$) or $E_{\text{app}}^{\text{Rock-2}} + \Delta H'_h$ (Section 2.2.3). For example, the apparent activation energy of Si flux (e.g., White and Blum, 1995) must be $E_{\text{app}}^{\text{Si}} + \Delta H'_h$ by the definition of the present study while the apparent activation energy of bicarbonate flux (e.g., Dessert et al., 2001) is the same as $E_{\text{app}}^{\text{Rock}} + \Delta H'_h$. Because there is not abundant data on apparent activation energy for modern weathering flux of bicarbonate, I used all the values of $\ln A$ and $E_{\text{app}}^{\text{W}} + \Delta H'_h$, $E_{\text{app}}^{\text{Rock}} + \Delta H'_h$ ($\equiv E_{\text{app}}^{\text{CO}_2}$) and $E_{\text{app}}^{\text{Rock-2}} + \Delta H'_h$ in the existent datasets, and plotted them altogether in Fig. 4. Note that I also included the data of White et al. (1999) in the dataset, which have been obtained from whole-rock weathering experiments in the laboratory (White et al., 1999). Fig. 4 unambiguously shows that there must be a compensation law for modern weathering flux. Because the dataset in Fig. 4 includes the experimental data of White et al. (1999) and the results from various weathering conditions (vegetation, elevations, temperatures etc.), I consider that the compensation law in Fig. 4 should represent the general nature of silicate rock weathering, not only of modern silicate weathering. From the linear regression with $R^2 = 0.98$ (solid line in Fig. 4), the universal temperature of weathering flux, T_{univ} (K), is calculated to be 283 K (10 °C). The errors in T_{univ} are ± 10 K from 2 times the standard deviation in d in Eq. (94). The low T_{univ} may be due to the constraint on weathering flux; at $T = \sim 273$ K, the weathering flux must converge toward zero because of the absence of liquid water. The constant flux, F_0 ($\text{mol m}^{-2} \text{ yr}^{-1}$) at $T = T_{\text{univ}}$, is calculated to be $0.081 \text{ mol m}^{-2} \text{ yr}^{-1}$ with errors being ± 0.04 (from 2 times the standard deviation in e in Eq. (95)). Using T_{univ} and F_0 , F_{CO_2} can be represented by the following equation:

$$F_{\text{CO}_2} = F_0 \exp \left\{ - \frac{E_{\text{app}}^{\text{CO}_2}}{R_g} \left(\frac{1}{T} - \frac{1}{T_{\text{univ}}} \right) \right\} \quad (97)$$

Eq. (97), a general rate law of weathering flux, can roughly predict weathering flux of bicarbonate at any temperature once apparent activation energies are estimated.

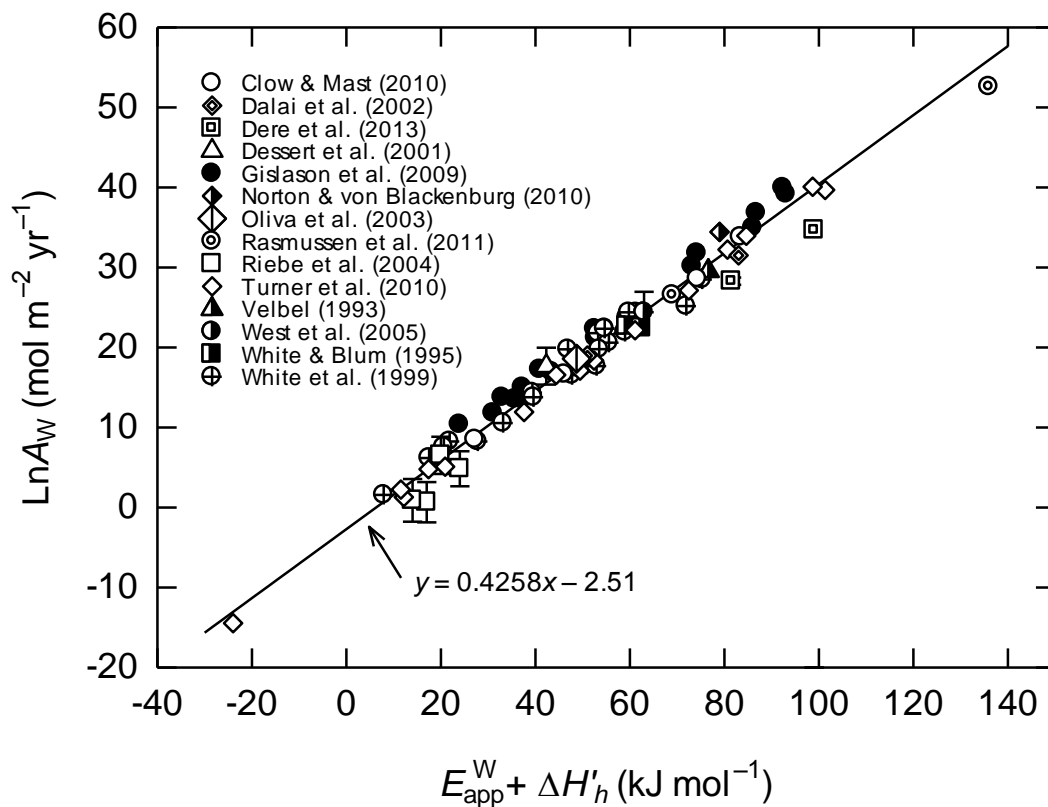


Figure 4. Empirical compensation law for modern weathering flux. Using all data on modern weathering flux available (fluxes of each element, TDS, total cations and bicarbonate), natural logarithms of pre-exponential factor ($\text{Ln}A$) are plotted against apparent activation energy. Error bars are from the ranges of precipitation and physical erosion rate (e.g., West et al., 2005; Riebe et al., 2004). Solid line is the linear regression, representing the compensation law.

5. Effects of atmospheric compositions on silicate weathering

In Sections 3 and 4, I have established the relationships between $\Delta H'_{\text{CO}_2}$ and $E_{\text{app}}^{\text{CO}_2}$ (Eq. (92), Section 3), and the relationships between $E_{\text{app}}^{\text{CO}_2}$, T and F_{CO_2} (Eq. (97)). In this section, I discuss the effects of atmospheric composition on silicate weathering, because $\Delta H'_{\text{CO}_2}$ and/or $E_{\text{app}}^{\text{CO}_2}$ can be affected by atmospheric composition. CO_2 , CH_4 and O_2 are possible constituents of atmosphere that can affect $\Delta H'_{\text{CO}_2}$ and/or $E_{\text{app}}^{\text{CO}_2}$. The effects of CO_2 , CH_4 and O_2 on silicate weathering are discussed in Sections 5.1, 5.2, and 5.2, respectively.

5.1. Effects of CO_2

5.1.1. Silicate weathering flux as a function of P_{CO_2}

I have deduced that the temperature dependence of P_{CO_2} ($\Delta H'_{\text{CO}_2}$, Eq. (83)) can change and determine the apparent activation energy of silicate weathering flux ($E_{\text{app}}^{\text{CO}_2}$) (Eq. (92)) in Section 3. Because F_{CO_2} is strongly affected by $E_{\text{app}}^{\text{CO}_2}$ (Eq. (97), Section 4), it is important to consider what determines $\Delta H'_{\text{CO}_2}$. In the global scale, $\Delta H'_{\text{CO}_2}$ should refer to the greenhouse effect of CO_2 (Eq. (83)). Although the greenhouse effect of CO_2 can be affected by various physical and chemical factors, I consider here only the global average greenhouse effect of CO_2 (e.g., Kasting and Ackerman, 1986), and do not take into account, for example, ice-albedo feedback (e.g., Pierrehumbert et al., 2011). The greenhouse effects of CO_2 on the surface temperature have been investigated by climate models (Kasting and Ackerman, 1986; Kasting, 1987, 1988; Haqq-Misra et al., 2008; von Paris et al., 2008). The surface temperatures are plotted as a function of P_{CO_2} at various luminosities (70, 75, 80, 85, 90, 95 and 100% of today's luminosity) in Fig. 5a. Although the literature cited here adopt different assumptions and calculation methods (Kasting, 1988; von Paris et al., 2008), the general picture of the relationship between P_{CO_2} and temperature can be obtained from Fig. 5a. Dotted curves in Fig. 5a are extrapolated ones from the literature data at 80, 85, 90 and 95 % of today's luminosity (squares, diamonds, circles and triangles, respectively), showing that the temperature increases monotonically as P_{CO_2} increases in general. On the other hand, the dashed curve with 100% of today's luminosity shows an abrupt increase in temperature at around $P_{\text{CO}_2} = 10^{-1.5}$ atm. The abrupt increase for the dashed curve is due to the relative humidity parameterization and has little physical significance (Kasting and Ackerman,

1986). Therefore, in the present study, the abrupt temperature increase is not considered. Based on solid and dotted curves in Fig. 5a, the values of $\Delta H'_{\text{CO}_2}$ are calculated according to Eq. (83) and plotted as a function of P_{CO_2} at 70, 80, 85, 90 and 95 % of today's luminosity in Fig. 5b; the general trend is similar between different luminosities: $\Delta H'_{\text{CO}_2}$ is rather constant at higher P_{CO_2} levels while decreasing P_{CO_2} increases $\Delta H'_{\text{CO}_2}$ at lower P_{CO_2} levels. The general relationships between P_{CO_2} and $\Delta H'_{\text{CO}_2}$ can be approximated by (at 70 % luminosity; Kasting and Ackerman, 1986)

$$\Delta H'_{\text{CO}_2} \cong \begin{cases} -88.7 \log P_{\text{CO}_2} - 10.6 & (P_{\text{CO}_2} \leq 10^{-0.5} \text{ atm}) \\ 34 & (P_{\text{CO}_2} > 10^{-0.5} \text{ atm}) \end{cases} \quad (98)$$

The differences of $\Delta H'_{\text{CO}_2}$ from Eq. (98) at different luminosities shown in Fig. 5b are not so significant and thus do not change the main conclusions given in this chapter.

The general relationships between P_{CO_2} and $\Delta H'_{\text{CO}_2}$ (Eq. (98)) will be violated by the presence of biota in weathering systems, like in the modern (Schwartzman and Volk, 1989; Berner, 1992, 1995, 1997; Keller and Wood, 1993; Lovelock and Kump, 1994; Moulton et al., 2000). Plant respiration and decomposition of organic matters (e.g., Garrels and Mackenzie, 1971; Holland, 1978; Sposito, 1989; Maher et al., 2009) make "soil P_{CO_2} " as high as $\sim 10^{-2}$ atm, which is higher than the present-day atmospheric level ($10^{-3.5}$ atm) and affects modern silicate weathering. Additionally and more importantly, biological activity reduces the fluctuation of soil P_{CO_2} with temperature. For example, based on a year-round soil P_{CO_2} and soil temperature reported by Breecker et al. (2009), small values of $\Delta H'_{\text{CO}_2}$ (23–27 kJ mol⁻¹) are calculated for modern soils (Fig. 5c). These values are much smaller than the expected values from abiotic greenhouse effect for corresponding soil P_{CO_2} levels (~ 170 – 260 kJ mol⁻¹, Eq. (98)). Although the greenhouse effect and the biological activity effect (e.g., plant respiration) should not be compared directly to one another because of the significant difference in the spatial and temporal scales (i.e., global P_{CO_2} and surface average temperature in the geological time scale vs. local soil P_{CO_2} and temperature in the year-round time scale), it is argued that biota makes $\Delta H'_{\text{CO}_2}$ of a weathering system fixed at a low value which does not correspond to atmospheric P_{CO_2} and its greenhouse effect (c.f., Johnson et al., 1994; Lloyd and Taylor, 1994; Kirschbaum, 1995; Piñol et al., 1995; Bouma et al., 1997; Davidson et al., 1998). Therefore, the use of Eq. (98) should be limited to the Precambrian assuming little effect of biota on soil P_{CO_2} .

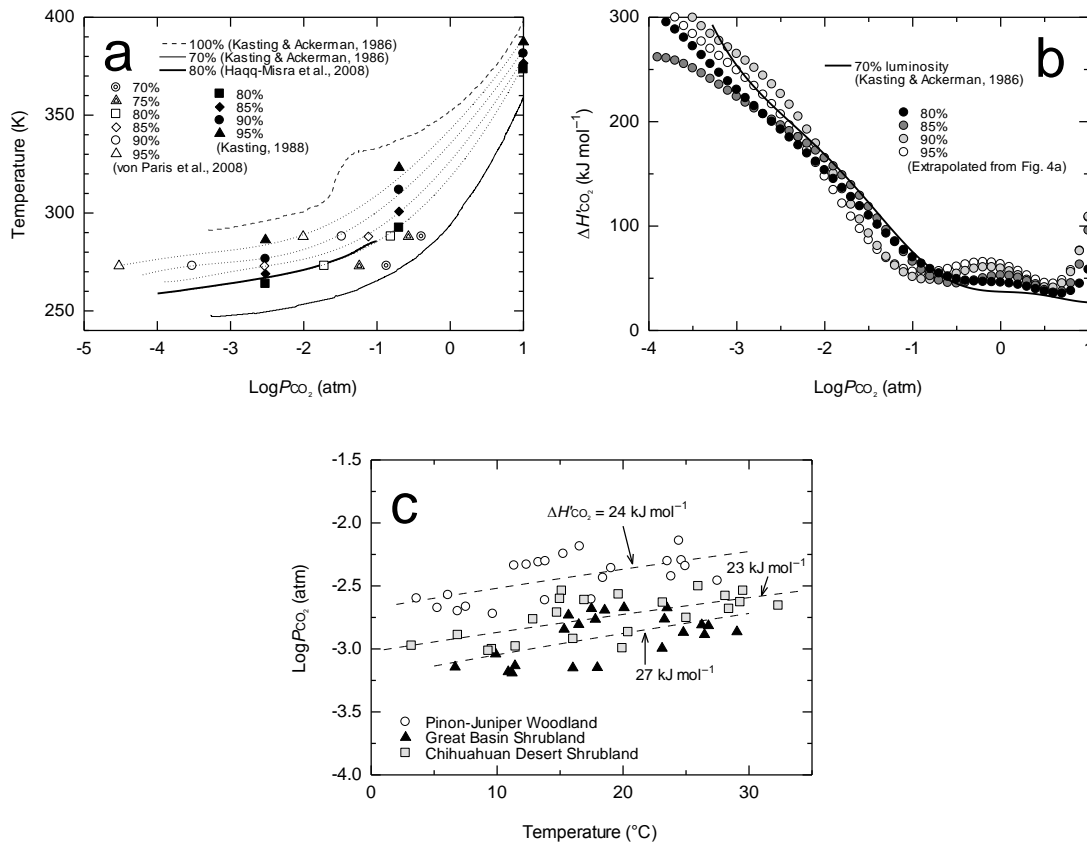


Figure 5. Relationships between P_{CO_2} and average global surface temperature at different luminosities from various climate models (a), relationships between P_{CO_2} and $\Delta H'_{CO_2}$ (b), and effects of biota on soil P_{CO_2} and $\Delta H'_{CO_2}$ (c). The luminosity is represented by percentage (%) of today's luminosity. Four dotted curves in Fig. 5a are extrapolated for 80, 85, 90 and 95 % luminosities from the results of Kasting (1988) and von Paris et al. (2008). Solid curve in Fig. 5b is obtained for 70 % luminosity using a fitting function to solid curve in Fig. 5a and Eq. (83). Circles in Fig. 5b are obtained for 80, 85, 90 and 95 % luminosities from fitting functions of extrapolated dotted curves in Fig. 5a. The data for Fig. 5c are from Breecker et al. (2009); different symbols denote different types of biome (see Breecker et al. (2009) for the details). Dashed lines in Fig. 5c are fitting functions by the forms of Eq. (83) (i.e., $\ln P_{CO_2} = a_1 - (\Delta H'_{CO_2}/R_g)(1/T)$ where a_1 is the fitting parameter). Calculated $\Delta H'_{CO_2}$ values are denoted for different biomes.

Using the relationships between $\Delta H'_{\text{CO}_2}$ and P_{CO_2} (Eq. (98)), between $\Delta H'_{\text{CO}_2}$ and $E_{\text{app}}^{\text{CO}_2}$ (Eq. (92)) and between F_{CO_2} , T and $E_{\text{app}}^{\text{CO}_2}$ (Eq. (97)), I can describe the relationship between F_{CO_2} and P_{CO_2} at different temperatures. F_{CO_2} as a function of P_{CO_2} is plotted at 0, 15 and 30 °C in Fig. 6. When $P_{\text{CO}_2} > 10^{-0.5}$ atm, F_{CO_2} is affected only by temperature though slightly (Fig. 6); at this range of P_{CO_2} , change in P_{CO_2} does not affect $\Delta H'_{\text{CO}_2}$ (Eq. (98)) and thus $E_{\text{app}}^{\text{CO}_2}$ (Eq. (92)). At $P_{\text{CO}_2} < 10^{-0.5}$ atm, the weathering flux, F_{CO_2} , is higher at lower P_{CO_2} when $T > T_{\text{univ}}$ (solid and dashed lines in Fig. 6) while F_{CO_2} becomes lower when $T < T_{\text{univ}}$ (dotted line in Fig. 6). These non-straightforward effects of P_{CO_2} on F_{CO_2} are attributed to the general rate law (Eq. (97)) (Section 4). The effects of $E_{\text{app}}^{\text{CO}_2}$ on F_{CO_2} are changed at $T = T_{\text{univ}}$ due to the compensation law: higher $E_{\text{app}}^{\text{CO}_2}$ means larger and smaller F_{CO_2} at $T > T_{\text{univ}}$ and $< T_{\text{univ}}$, respectively, from Eq. (97). Because $\log P_{\text{CO}_2}$ and $E_{\text{app}}^{\text{CO}_2}$ are linearly related at $P_{\text{CO}_2} < 10^{-0.5}$ atm (Eqs. (92) and (98)), the effects of $\log P_{\text{CO}_2}$ on F_{CO_2} are also changed at $T = T_{\text{univ}}$ when $P_{\text{CO}_2} < 10^{-0.5}$ atm (Fig. 6). Then, it is expected that the feedback of weathering on P_{CO_2} can be more complex than previously thought, which will be discussed in the next section.

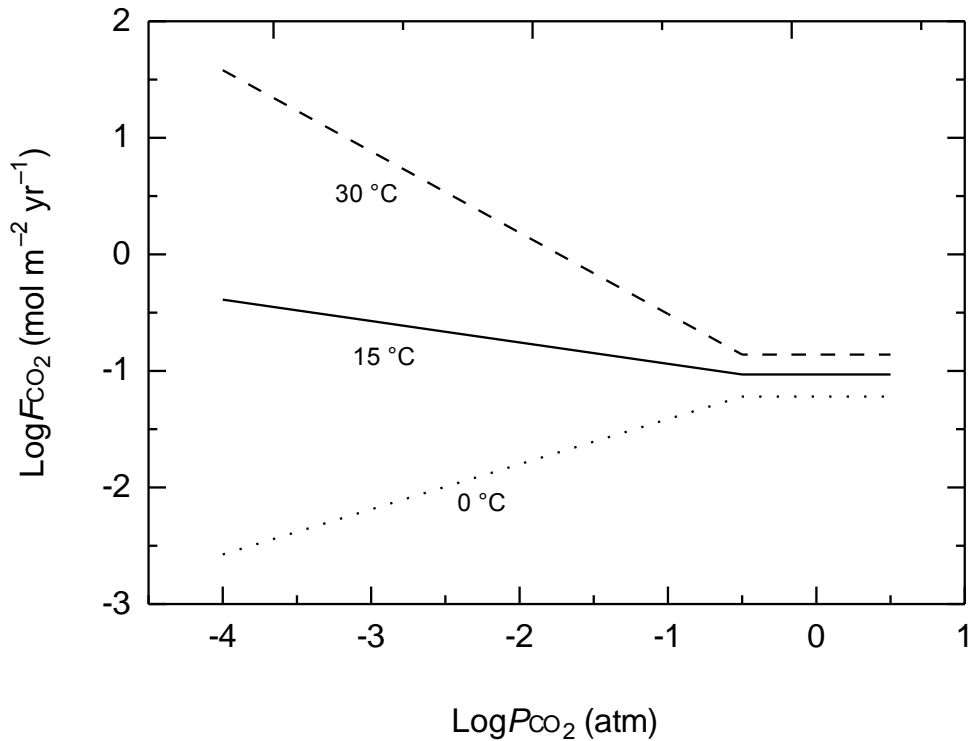


Figure 6. Effects of P_{CO_2} on F_{CO_2} at 0, 15 and 30 °C. Calculations are based on Eqs. (92), (97) and (98).

5.1.2. Feedback of silicate weathering flux on P_{CO_2}

Based on the relationships between F_{CO_2} , P_{CO_2} and temperature (Eqs. (92), (97) and (98)), I discuss the effects of change in P_{CO_2} on F_{CO_2} , that is, the weathering feedback on P_{CO_2} . I consider the change between states A and B; at state A, $P_{CO_2} = P_{CO_2}(A)$, $T = T(A)$, $E_{app}^{CO_2} = E_{app}^{CO_2}(A)$ and $F_{CO_2} = F_{CO_2}(A)$ while at state B, $P_{CO_2} = P_{CO_2}(B)$, $T = T(B)$, $E_{app}^{CO_2} = E_{app}^{CO_2}(B)$ and $F_{CO_2} = F_{CO_2}(B)$. The changes in temperature and P_{CO_2} between the two states are related by Eq. (83):

$$\ln P_{CO_2}(B) - \ln P_{CO_2}(A) = -\frac{\Delta H'_{CO_2}}{R_g} \left\{ \frac{1}{T(B)} - \frac{1}{T(A)} \right\} \quad (99)$$

Weathering fluxes at states A and B are obtained from Eq. (97):

$$F_{CO_2}(A) = F_0 \exp \left[-\frac{E_{app}^{CO_2}(A)}{R_g} \left\{ \frac{1}{T(A)} - \frac{1}{T_{univ}} \right\} \right] \quad (100)$$

$$F_{CO_2}(B) = F_0 \exp \left[-\frac{E_{app}^{CO_2}(B)}{R_g} \left\{ \frac{1}{T(B)} - \frac{1}{T_{univ}} \right\} \right] \quad (101)$$

From Eqs. (100) and (101), and using Eq. (99), the change in weathering flux is given by

$$\begin{aligned} & \ln F_{CO_2}(B) - \ln F_{CO_2}(A) \\ &= \frac{E_{app}^{CO_2}(B) - E_{app}^{CO_2}(A)}{R_g} \left\{ \frac{1}{T_{univ}} - \frac{1}{T(B)} \right\} + \frac{E_{app}^{CO_2}(A)}{\Delta H'_{CO_2}} \{ \ln P_{CO_2}(B) - \ln P_{CO_2}(A) \} \end{aligned} \quad (102)$$

In Eq. (102), the first term in the right hand side represents the effects of the change in apparent activation energy by P_{CO_2} change (Eqs. (92) and (98)), and the second term represents the effects of temperature change (Eq. (97)). By comparing the change in P_{CO_2} (Eq. (99)) to that in F_{CO_2} (Eq. (102)), the feedback between F_{CO_2} and P_{CO_2} is determined as positive or negative. I define the indicator of the feedback of weathering as n_{CO_2} :

$$n_{CO_2} \equiv \frac{d \ln F_{CO_2}}{d \ln P_{CO_2}} \cong \frac{\ln F_{CO_2}(B) - \ln F_{CO_2}(A)}{\ln P_{CO_2}(B) - \ln P_{CO_2}(A)} \quad (103)$$

When $n_{CO_2} > 0$, the feedback is negative because an increase in P_{CO_2} is mitigated by the

concomitant increase in F_{CO_2} . On the contrary, $n_{CO_2} < 0$ indicates positive feedback in which an increase in P_{CO_2} is further enhanced by the decrease in F_{CO_2} .

Using Eqs. (99), (102) and (103), the feedback indicator is represented by

$$n_{CO_2} = \frac{E_{app}^{CO_2}(B) - E_{app}^{CO_2}(A)}{\ln P_{CO_2}(B) - \ln P_{CO_2}(A)} \times \frac{T(B) - T_{univ}}{R_g T_{univ} T(B)} + \frac{E_{app}^{CO_2}(A)}{\Delta H'_{CO_2}} \quad (104)$$

In Eq. (104), the term $\{E_{app}^{CO_2}(B) - E_{app}^{CO_2}(A)\}/\{\ln P_{CO_2}(B) - \ln P_{CO_2}(A)\}$ can be alternatively represented by

$$\frac{E_{app}^{CO_2}(B) - E_{app}^{CO_2}(A)}{\ln P_{CO_2}(B) - \ln P_{CO_2}(A)} = \frac{dE_{app}^{CO_2}}{d \ln P_{CO_2}} = \frac{dE_{app}^{CO_2}}{d\Delta H'_{CO_2}} \times \frac{d\Delta H'_{CO_2}}{d \log P_{CO_2}} \times \frac{1}{\ln 10} \quad (105)$$

Then, from Eqs. (104) and (105),

$$n_{CO_2} = \frac{dE_{app}^{CO_2}}{d\Delta H'_{CO_2}} \times \frac{d\Delta H'_{CO_2}}{d \log P_{CO_2}} \times \frac{T(B) - T_{univ}}{R_g T_{univ} T(B) \ln 10} + \frac{E_{app}^{CO_2}(A)}{\Delta H'_{CO_2}} \quad (106)$$

Eq. (106) indicates that n_{CO_2} is determined by the three parameters, $dE_{app}^{CO_2}/d\Delta H'_{CO_2}$, $d\Delta H'_{CO_2}/d \log P_{CO_2}$ and $E_{app}^{CO_2}/\Delta H'_{CO_2}$. In the present study, I have deduced that $dE_{app}^{CO_2}/d\Delta H'_{CO_2}$ is non-zero (0.57, Eq. (92)). Then, depending on the value of $d\Delta H'_{CO_2}/d \log P_{CO_2}$, n_{CO_2} can be a function of temperature according to Eq. (106). In Fig. 7, n_{CO_2} is plotted as a function of temperature at various P_{CO_2} levels, using Eqs. (92), (98) and (106). When $P_{CO_2} > 10^{-0.5}$ atm, n_{CO_2} is 0.40 and independent of temperature (horizontal dashed line in Fig. 7). This is because $d\Delta H'_{CO_2}/d \log P_{CO_2} = 0$ and $E_{app}^{CO_2}/\Delta H'_{CO_2} = 0.40$ at $P_{CO_2} > 10^{-0.5}$ atm (Eqs. (92) and (98)). At lower P_{CO_2} ($< 10^{-0.5}$ atm), n_{CO_2} decrease as T increases (solid, dotted, dotted and dashed and double-dotted and dashed curves in Fig. 7). The temperature dependence at $P_{CO_2} < 10^{-0.5}$ atm is due to negative $d\Delta H'_{CO_2}/d \log P_{CO_2}$ (-88.7 , Eq. (98)) at this P_{CO_2} range. Fig. 7 also reveals that there are almost little effects of P_{CO_2} on n_{CO_2} at $< 10^{-0.5}$ atm of P_{CO_2} . The little difference in n_{CO_2} between different P_{CO_2} levels are induced by slight differences in the value of $E_{app}^{CO_2}/\Delta H'_{CO_2}$ (the second term in Eq. (106)) between different P_{CO_2} ($E_{app}^{CO_2}/\Delta H'_{CO_2} = 0.50, 0.54, 0.55$ and 0.56 at $P_{CO_2} = 10^{-1}, 10^{-2}, 10^{-3}$ and 10^{-4} atm, respectively, from Eqs. (92) and (98)). Note that at $T = T_{univ}$, n_{CO_2} always equals $E_{app}^{CO_2}/\Delta H'_{CO_2}$ (Eq. (106); see arrows in Fig. 7).

Importantly, at $< 10^{-0.5}$ atm of P_{CO_2} , n_{CO_2} changes from positive to negative at some threshold temperature (Fig. 7). I define this threshold temperature as T_{thr} (K), which is determined from $n_{CO_2} = 0$ in Eq. (106):

$$T_{\text{thr}} = \left\{ \frac{1}{T_{\text{univ}}} + R_g \frac{E_{\text{app}}^{\text{CO}_2} (\text{A})}{\Delta H'_{\text{CO}_2}} \left(\frac{dE_{\text{app}}^{\text{CO}_2}}{d\Delta H'_{\text{CO}_2}} \times \frac{d\Delta H'_{\text{CO}_2}}{d\log P_{\text{CO}_2}} \right)^{-1} \ln 10 \right\}^{-1} \quad (107)$$

Eq. (107) indicates that T_{thr} is determined by the values of $E_{\text{app}}^{\text{CO}_2}/\Delta H'_{\text{CO}_2}$, $dE_{\text{app}}^{\text{CO}_2}/d\Delta H'_{\text{CO}_2}$ and $d\Delta H'_{\text{CO}_2}/d\log P_{\text{CO}_2}$ as n_{CO_2} is determined by the three parameters. The value of $dE_{\text{app}}^{\text{CO}_2}/d\Delta H'_{\text{CO}_2}$ is 0.57 in the present study (Eq. (92)). Because $d\Delta H'_{\text{CO}_2}/d\log P_{\text{CO}_2} = 0$ at $P_{\text{CO}_2} > 10^{-0.5}$ atm, I cannot calculate T_{thr} from Eq. (107) at this P_{CO_2} range (horizontal dashed line in Fig. 7). When $P_{\text{CO}_2} < 10^{-0.5}$ atm, $d\Delta H'_{\text{CO}_2}/d\log P_{\text{CO}_2} = -88.7$ (Eq. (98)); thus $T_{\text{thr}} = 299, 300, 301$ and 301 K (26, 27, 28 and 28 °C) are obtained from Eq. (107) (Fig. 7) at $P_{\text{CO}_2} = 10^{-1}, 10^{-2}, 10^{-3}$ and 10^{-4} atm, respectively. The slight differences in T_{thr} at different P_{CO_2} are due to those in $E_{\text{app}}^{\text{CO}_2}/\Delta H'_{\text{CO}_2}$ ($E_{\text{app}}^{\text{CO}_2}/\Delta H'_{\text{CO}_2} = 0.50, 0.54, 0.55$ and 0.56 at $P_{\text{CO}_2} = 10^{-1}, 10^{-2}, 10^{-3}$ and 10^{-4} atm, respectively, from Eqs. (92) and (98)).

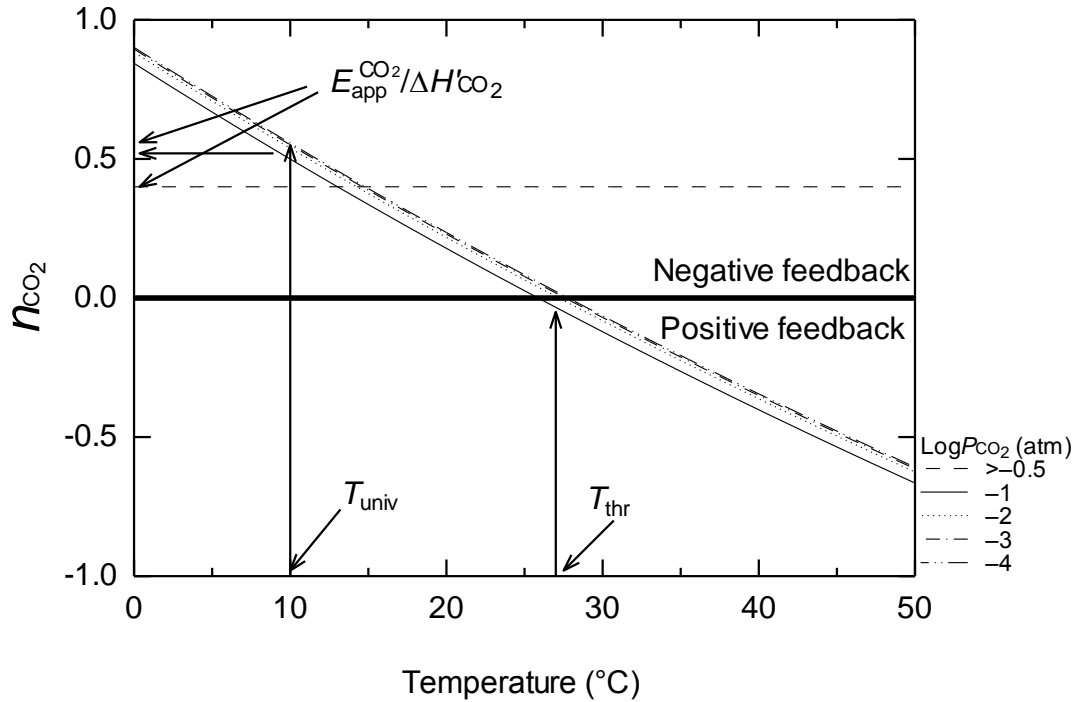


Figure 7. Indicator of feedback (n_{CO_2}) plotted against temperature at $10^{-4}, 10^{-3}, 10^{-2}, 10^{-1}$ and $>10^{-0.5}$ atm of P_{CO_2} , based on Eq. (106). Horizontal bold line indicates $n_{\text{CO}_2} = 0$. T_{thr} is the temperature at which n_{CO_2} becomes 0. At $T = T_{\text{univ}}$, n_{CO_2} always becomes $E_{\text{app}}^{\text{CO}_2}/\Delta H'_{\text{CO}_2}$ (see arrows).

The above discussion on n_{CO_2} is useful to deduce the stability of CO_2 and temperature with respect to silicate weathering. When $P_{\text{CO}_2} < 10^{-0.5}$ atm and $T > T_{\text{thr}}$, a slight CO_2 change will make P_{CO_2} decrease or increase immediately due to positive feedback, until $T < T_{\text{thr}}$ or $P_{\text{CO}_2} > 10^{-0.5}$ atm, both of which are stable due to negative feedback (Fig. 7). Under the stable, high CO_2 conditions ($P_{\text{CO}_2} > 10^{-0.5}$ atm), the constant degree of negative feedback operates at any temperatures and P_{CO_2} levels due to the temperature- and P_{CO_2} -independent n_{CO_2} value (0.40). Because of the high P_{CO_2} values ($> 10^{-0.5}$ atm) and the negative feedback, the conditions are stable against glaciations. Under the stable, low CO_2 conditions ($P_{\text{CO}_2} < 10^{-0.5}$ atm and $T < T_{\text{thr}}$), because the value of n_{CO_2} becomes higher as temperature decreases at any P_{CO_2} (Fig. 7), the feedback becomes more negative at lower temperatures. Thus, glaciations hardly occur under these conditions. The stability against glaciations in the low CO_2 stable conditions ($P_{\text{CO}_2} < 10^{-0.5}$ atm and $T < T_{\text{thr}}$) may explain the stable climates in the most Precambrian, especially that in the Mesoproterozoic, where P_{CO_2} were $< 10^{-0.5}$ atm (Kasting, 1987; Tajika and Matsui, 1992) and free from glaciations (e.g., Walker, 1982; Pierrehumbert et al., 2011).

As demonstrated above, n_{CO_2} and T_{thr} depend on mainly $dE_{\text{app}}^{\text{CO}_2}/d\Delta H'\text{CO}_2$ and $d\Delta H'\text{CO}_2/d\log P_{\text{CO}_2}$ (Eqs. (92) and (98)). I used the standard relationship between $E_{\text{app}}^{\text{CO}_2}$ and $\Delta H'\text{CO}_2$ (Eq. (92)) and the general trend of $d\Delta H'\text{CO}_2/d\log P_{\text{CO}_2}$ (Eq. (98)) in the calculations above. As indicated in Fig. 3e, the relationships between $E_{\text{app}}^{\text{CO}_2}$ and $\Delta H'\text{CO}_2$ can be affected by an assumed *CDF* value. For example, if I use the relationship between $E_{\text{app}}^{\text{CO}_2}$ and $\Delta H'\text{CO}_2$ in transport-controlled regime (*CDF* = 1, Fig. 3e), the value of $dE_{\text{app}}^{\text{CO}_2}/d\Delta H'\text{CO}_2$ becomes 0.43. If I assume reaction-controlled regime (*CDF* = 0, Fig. 3e), the value of $dE_{\text{app}}^{\text{CO}_2}/d\Delta H'\text{CO}_2$ is 0.64. Therefore, by a shift between reaction- and transport-controlled regimes, the value of $dE_{\text{app}}^{\text{CO}_2}/d\Delta H'\text{CO}_2$ can change and thus n_{CO_2} and T_{thr} are also affected. Nevertheless, because I can assume $dE_{\text{app}}^{\text{CO}_2}/d\Delta H'\text{CO}_2 > 0$, the trends seen in Fig. 7 will be the same; n_{CO_2} is larger at lower temperatures and $T_{\text{thr}} > T_{\text{univ}}$ when $P_{\text{CO}_2} < 10^{-0.5}$ atm, and n_{CO_2} is temperature-independent and positive at $P_{\text{CO}_2} > 10^{-0.5}$ atm.

5.2. Effects of CH₄

Methane has been considered to have played a significant role as a greenhouse-effect gas until the surface of the Earth was fully oxidized (e.g., Pavlov et al., 2000; Kharecha et al., 2005). However, with a high ratio of CH₄/CO₂ (>~0.1), organic haze is formed which works as an anti-greenhouse-effect gas (Trainer et al., 2006; Haqq-Misra et al., 2008). Moderate amount of CH₄, compared to CO₂ (i.e., CH₄/CO₂ < ~0.1), can provide an efficient warming effect on the Earth (Haqq-Misra et al., 2008). Although CH₄ does not have direct influences on silicate weathering, it can affect silicate weathering by interfering the greenhouse effect of CO₂, i.e., the relationships between $\Delta H'_{\text{CO}_2}$ and P_{CO_2} (Eq. (98)). Here, I consider only the global average greenhouse effect of CH₄, and do not take into account ice-albedo feedback (e.g., Pierrehumbert et al., 2011) or formation of fractal organic haze (Wolf and Toon, 2010). Haqq-Misra et al. (2008) have provided detailed model results on the relationships between temperature, P_{CO_2} and P_{CH_4} at 2.8 Ga (at 80% of today's luminosity). Using their results, I calculated $\Delta H'_{\text{CO}_2}$ from Eq. (83) as done for Fig. 5b, and plot $\Delta H'_{\text{CO}_2}$ as a function of $\log P_{\text{CO}_2}$ at different P_{CH_4} levels in Fig. 8a; the presence of CH₄ significantly affects the relationships between P_{CO_2} and $\Delta H'_{\text{CO}_2}$. It is obvious that there is no monotonically decreasing tendency of $\Delta H'_{\text{CO}_2}$ with increase in P_{CO_2} for a given P_{CH_4} level as seen in Fig. 5b where CO₂ alone is considered. For example, at $P_{\text{CH}_4} = 10^{-4}$ atm (dashed curve in Fig. 8a), the P_{CO_2} - $\Delta H'_{\text{CO}_2}$ relationships at high P_{CO_2} levels (>~ $10^{-2.5}$ atm) seems to be similar to those when no methane exists (thin solid curve in Fig. 8a), but at lower P_{CO_2} levels (<~ $10^{-2.5}$ atm), the trend between P_{CO_2} and $\Delta H'_{\text{CO}_2}$ is inversed and at still lower P_{CO_2} levels (<~ $10^{-3.5}$ atm), $\Delta H'_{\text{CO}_2}$ becomes low and constant. Similar P_{CO_2} - $\Delta H'_{\text{CO}_2}$ relationship can be recognized at $P_{\text{CH}_4} = 10^{-3}$ atm (dotted and dashed curve in Fig. 8a). From the relationships between P_{CO_2} and $\Delta H'_{\text{CO}_2}$ at $P_{\text{CH}_4} = 10^{-4}$ and 10^{-3} atm, it is speculated that the slope of $\log P_{\text{CO}_2}$ - $\Delta H'_{\text{CO}_2}$ diagram (i.e., $d\Delta H'_{\text{CO}_2}/d\log P_{\text{CO}_2}$) depends on CH₄/CO₂ ratios; at low CH₄/CO₂ ratio (<~0.03), $d\Delta H'_{\text{CO}_2}/d\log P_{\text{CO}_2}$ is negative, at mediate CH₄/CO₂ ratio (>~0.03, <~0.15), $d\Delta H'_{\text{CO}_2}/d\log P_{\text{CO}_2}$ is positive and at high CH₄/CO₂ ratio (>~0.15), $d\Delta H'_{\text{CO}_2}/d\log P_{\text{CO}_2}$ is 0. Such dependences of $d\Delta H'_{\text{CO}_2}/d\log P_{\text{CO}_2}$ on CH₄/CO₂ ratios are roughly consistent with the relationships between P_{CO_2} and $\Delta H'_{\text{CO}_2}$ at $P_{\text{CH}_4} = 10^{-2.5}$ and 10^{-2} atm (dotted curve and solid bold curve, respectively, in Fig. 8a).

Based on the dependence of $d\Delta H'_{\text{CO}_2}/d\log P_{\text{CO}_2}$ on CH₄/CO₂ ratios, I here consider the feedback between F_{CO_2} and P_{CO_2} (n_{CO_2}) at different CH₄/CO₂ ratios. According to

Eqs. (106) and (107), the trend of n_{CO_2} and the deviation of T_{thr} from T_{univ} are determined mainly by the values of $dE_{\text{app}}^{\text{CO}_2}/d\Delta H'\text{CO}_2$ and $d\Delta H'\text{CO}_2/d\log P_{\text{CO}_2}$. Once $dE_{\text{app}}^{\text{CO}_2}/d\Delta H'\text{CO}_2$ is determined (0.57, Eq. (90)), the value of $d\Delta H'\text{CO}_2/d\log P_{\text{CO}_2}$ determines n_{CO_2} and T_{thr} (Eqs. (106) and (107)). Table 6 summarizes the expected trends of T_{thr} and n_{CO_2} based on the values of $d\Delta H'\text{CO}_2/d\log P_{\text{CO}_2}$ at different CH_4/CO_2 ratios. I also give the trends of T_{thr} and n_{CO_2} without CH_4 for comparison. Table 6 shows that the feedbacks of weathering at high and low CH_4/CO_2 ratios ($< \sim 0.03$ (fourth column in Table 6) and $> \sim 0.15$ (second column), respectively) are similar to those under high CO_2 ($> 10^{-0.5}$ atm, fifth column) and lower CO_2 conditions ($< 10^{-0.5}$ atm, sixth column) without methane, respectively. Under these conditions, it is difficult to bring the Earth to glaciation due to negative feedback at low temperatures ($T < T_{\text{thr}}$) (Section 5.1.2). On the other hand, when the CH_4/CO_2 ratio is medium ($> \sim 0.03$ and $< \sim 0.15$) (third column in Table 6), the feedback is negative at high temperatures ($T > T_{\text{thr}}$) and positive at low temperatures ($T < T_{\text{thr}}$), a contrary trend to that when the CH_4/CO_2 ratio is low (fourth column in Table 6). The calculated values of n_{CO_2} are plotted as a function of temperature at different P_{CO_2} when $P_{\text{CH}_4} = 10^{-3}$ atm in Fig. 8b. Consistent with Table 6, n_{CO_2} is positive and temperature-independent when the CH_4/CO_2 ratio is high (dashed line), n_{CO_2} is lower at lower temperatures when the CH_4/CO_2 ratio is medium (solid curve) and n_{CO_2} is higher at lower temperatures when the CH_4/CO_2 ratio is low (dotted curve). Both Table 6 and Fig. 8b indicate that it is possible to cause global glaciation when the CH_4/CO_2 ratio is mediate ($> \sim 0.03$ and $< \sim 0.15$), because positive feedback ($n_{\text{CO}_2} < 0$) operates at $T < T_{\text{thr}}$.

The discussion on n_{CO_2} at different CH_4/CO_2 ratios not only indicates the complexity of $\text{CH}_4\text{-CO}_2$ interactions but also suggests that the presence of CH_4 at significant concentrations can destabilize the atmosphere at low temperatures. While it is difficult to bring the Earth to global glaciation without methane in the general $P_{\text{CO}_2}\text{-}\Delta H'\text{CO}_2$ trend (Table 6 and Fig. 7), it is possible with interference of CH_4 (Table 6 and Fig. 8b). Therefore, the emergence of CH_4 with $\sim 0.03 < \text{CH}_4/\text{CO}_2 < \sim 0.15$ can be one of the possible triggers of global glaciations. These conditions of CH_4 are especially significant in the Neoproterozoic and Paleoproterozoic when the P_{O_2} levels were very low (Young et al., 1998; Farquhar and Wing, 2003; Papineau et al., 2007). The glaciation at ~ 2.9 Ga is considered to have occurred under anoxic conditions based on significant MIF-S signals (Domagal-Goldman et al., 2008). Under anoxic conditions, CH_4 can rise to significant concentrations (Pavlov et al., 2003; Kharecha et al., 2005). When CH_4 is supplied into atmosphere sufficiently to make the CH_4/CO_2 ratios of ~ 0.03 to $< \sim 0.15$, at low temperatures ($< \sim 5$ °C), P_{CO_2} either increases or decreases immediately, with a slight

CO₂ change, due to positive feedbacks of weathering (Table 6 and Fig. 8b). In the former case, P_{CO_2} increases until the CH₄/CO₂ ratio changes to $< \sim 0.03$ and thus CO₂ becomes the dominant greenhouse-effect gas after all, avoiding glaciations (Section 5.1). On the other hand, in the latter case, P_{CO_2} decreases until CH₄/CO₂ $> \sim 0.15$, and then organic haze (CH₄/CO₂ $> \sim 0.1$) forms, causing glaciations due to the decreased P_{CO_2} and the organic haze. The latter case may be the sequence of events that caused the glaciation at ~ 2.9 Ga.

Table 6. Effects of CH₄/CO₂ ratio on feedback of weathering.

	CH ₄ /CO ₂			Without CH ₄	
	High ($> \sim 0.15$)	Medium ($> \sim 0.03, < \sim 0.15$)	Low ($< \sim 0.03$)	P_{CO_2} $> 10^{-0.5}$ atm	P_{CO_2} $< 10^{-0.5}$ atm
$d\Delta H_{\text{CO}_2}/d\log P_{\text{CO}_2}$	0	+ ^b	- ^c	0	-
T_{thr}	nc ^a	$< T_{\text{univ}}$	$> T_{\text{univ}}$	nc ^a	$> T_{\text{univ}}$
n_{CO_2} at $T > T_{\text{thr}}$	+	+	-	+	-
n_{CO_2} at $T < T_{\text{thr}}$	+	-	+	+	+

^a Not calculated (Eq. (106)).

^b “+” denotes that the value is > 0 .

^c “-” denotes that the value is < 0 .

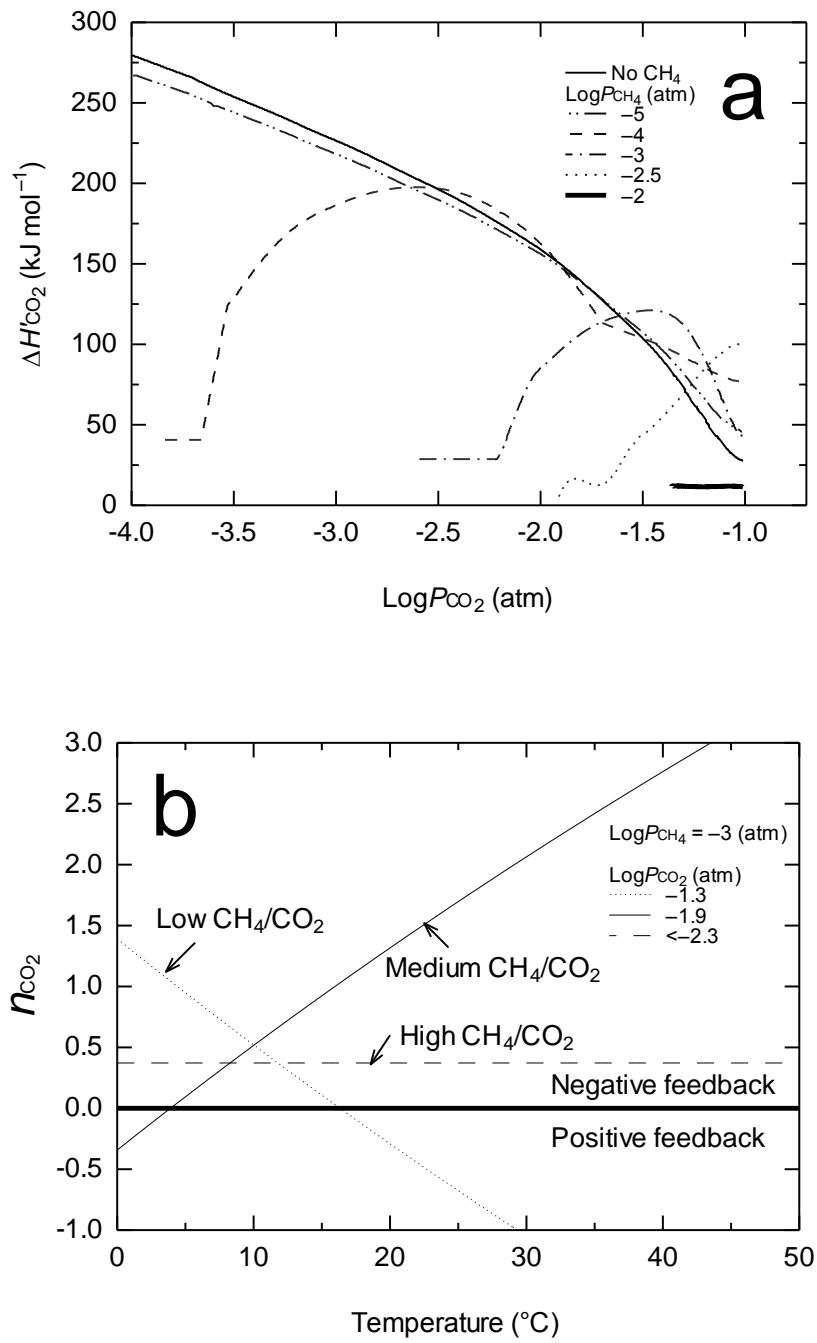


Figure 8. Relationships between $\Delta H'_{\text{CO}_2}$ and P_{CO_2} at 10^{-5} , 10^{-4} , 10^{-3} , $10^{-2.5}$ and 10^{-2} atm of P_{CH_4} and without CH₄ (a), and indicator of feedback (n_{CO_2}) plotted against temperature at $<10^{-2.3}$, $10^{-1.9}$ and $10^{-1.3}$ atm of P_{CO_2} with $P_{\text{CH}_4} = 10^{-3}$ atm (b). The calculations are based on Fig. 10 of Haqq-Misra et al. (2008) for Fig. 8a and on Eq. (106) and Fig. 8a for Fig. 8b.

5.3. Effects of O₂

Although oxygen is not a greenhouse-effect gas and thus does not affect $\Delta H'_{\text{CO}_2}$, oxygen can directly affect the apparent activation energy of silicate weathering by changing the contribution of Fe loss to the losses of total cations and TDS (β_{Fe} and η_{Fe} , respectively) and by involving Fe²⁺ oxidation reaction in weathering processes (e.g., Eq. (16)). In the above discussion and calculations, I have assumed anoxic conditions and used $\beta_{\text{Fe}} = 0.232$ and $\eta_{\text{Fe}} = 0.136$ (Table 5). As P_{O_2} level is increased from anoxic conditions, Fe loss by weathering should approach 0 (Eq. (23)), and thus β_{Fe} and η_{Fe} also approach 0 (Eqs. (59) and (64)). The contribution of $E_{\text{app}}^{\text{Fe}}$ to $E_{\text{app}}^{\text{CO}_2}$ is represented by $\beta_{\text{Fe}} - \eta_{\text{Fe}}CDF/(1 + CDF)$ according to Eq. (70), which also approaches 0 together with β_{Fe} and η_{Fe} as P_{O_2} level increases. To reflect P_{O_2} level in the contribution ratios (β_{Fe} , η_{Fe} and $\beta_{\text{Fe}} - \eta_{\text{Fe}}CDF/(1 + CDF)$), I rewrite β_{Fe} and η_{Fe} as $\beta_{\text{Fe}} = 0.232\psi$ and $\eta_{\text{Fe}} = 0.136\psi$, respectively, because ψ reflects P_{O_2} level ($\psi \cong 0$ and 1 at anoxic and oxic conditions, respectively (Eq. (21))). On the other hand, as Eq. (54) indicates, the temperature dependence of Fe²⁺ oxidation rate (the term of $\phi(\Delta H'_f - \Delta H'_\lambda)$ in Eq. (54)) becomes more significant as P_{O_2} level increases because the ϕ value increases with P_{O_2} level (Eq. (22)). Combining the effects of β_{Fe} , η_{Fe} and $\phi(\Delta H'_f - \Delta H'_\lambda)$, the expected change in $E_{\text{app}}^{\text{CO}_2}$ by oxygen increase (defined as ΔE_{ox} (kJ mol⁻¹)) is represented by

$$\begin{aligned}\Delta E_{\text{ox}} &= \left(\beta_{\text{Fe}} - \frac{CDF}{1 + CDF} \eta_{\text{Fe}} \right) \phi(\Delta H'_f - \Delta H'_\lambda) \\ &= \frac{0.232 - 0.136CDF}{1 + CDF} \psi \phi(\Delta H'_f - \Delta H'_\lambda) \\ &= 0.171 \times \psi \phi(\Delta H'_f - \Delta H'_\lambda)\end{aligned}\quad (108)$$

where I assume $CDF = 0.2$. The value of $(\Delta H'_f - \Delta H'_\lambda)$ depends on P_{CO_2} level and $E_{\text{app}}^{\text{Rock}}$ at the time (Appendix B); if I assume $\Delta H'_f = 0$, the value of $(\Delta H'_f - \Delta H'_\lambda)$ ($= -\Delta H'_\lambda$) can be in the range between -134 and 165 kJ mol⁻¹ (corresponding to $10^{-0.5}$ and 10^{-4} atm of P_{CO_2} , respectively; see Appendix B for the details). Eq. (108) indicates that $|\Delta E_{\text{ox}}|$ yields the highest value at $\phi = \psi = 0.5$ ($\Delta E_{\text{ox}} = -5.7$ – 7.1 kJ mol⁻¹). Then, oxygen has maximum effects on the apparent activation energy of silicate weathering in the midway from anoxic to oxic conditions (i.e., at $\phi = \psi = 0.5$).

I can estimate the maximum change in weathering flux caused by oxygen increase using Eq. (102), by redefining states A and B in Section 5.1.2 as the conditions at $\phi = 0$ (very low P_{O_2} level) and at $\phi = \psi = 0.5$ (intermediate P_{O_2} level), respectively. I assume that states A and B have the same P_{CO_2} and thus the same temperature. Using Eq. (102)

with $T(B) = T(A)$ and $E_{\text{app}}^{\text{CO}_2}(B) = E_{\text{app}}^{\text{CO}_2}(A) + \Delta E_{\text{ox}}$, the change in weathering flux is represented by

$$\ln F_{\text{CO}_2}(B) - \ln F_{\text{CO}_2}(A) = \frac{\Delta E_{\text{ox}}}{R_g} \left\{ \frac{1}{T_{\text{univ}}} - \frac{1}{T(A)} \right\} \quad (109)$$

where $\Delta E_{\text{ox}} = -5.7 - 7.1 \text{ kJ mol}^{-1}$. Eq. (109) shows that when $\Delta E_{\text{ox}} > 0$, weathering flux increases or decreases at $T(A) > T_{\text{univ}}$ or $< T_{\text{univ}}$, respectively. When $\Delta E_{\text{ox}} < 0$, weathering flux increases or decreases at $T(A) < T_{\text{univ}}$ or $> T_{\text{univ}}$, respectively. The change in F_{CO_2} is calculated to be insignificant ($< \sim 10\%$ change; Eq. (109)) due to the small $|\Delta E_{\text{ox}}|$ values. Despite the small change in F_{CO_2} , the increase in F_{CO_2} at $T(A) < T_{\text{univ}}$ with negative ΔE_{ox} is important to consider the possible causes of global glaciations. Although the increase in F_{CO_2} by ΔE_{ox} is small ($< \sim 10\%$), the increase in F_{CO_2} will increase CDF in Eq. (68) and further decrease $E_{\text{app}}^{\text{CO}_2}$ (Eq. (70)), leading to further increase in F_{CO_2} at $T < T_{\text{univ}}$ (Eq. (97)) and thus again increase in CDF . The maximum change in $E_{\text{app}}^{\text{CO}_2}$ by the change in CDF is as large as $\sim 60 \text{ kJ mol}^{-1}$ (Fig. 3e). The change in $E_{\text{app}}^{\text{CO}_2}$ caused by oxygen increase and subsequent CDF increase may be less mitigated by the weathering feedback than when the change in $E_{\text{app}}^{\text{CO}_2}$ is caused by change in P_{CO_2} . Therefore, although ΔE_{ox} itself has only small effects on $E_{\text{app}}^{\text{CO}_2}$ and F_{CO_2} , the repetitive effects by the change in CDF caused by oxygen increase can possibly cause a significant change in F_{CO_2} . It can be concluded that O_2 increase may help triggering global glaciations.

The multiple glaciations in the Paleoproterozoic ($\sim 2.4\text{--}2.2 \text{ Ga}$, Bekker et al., 2005) are considered to have occurred around the same timing as that of the Great Oxidation Event (GOE) where a great increase in P_{O_2} level occurred ($P_{\text{O}_2} < \sim 10^{-6} \text{ atm}$ at $> 2.5 \text{ Ga}$ and $P_{\text{O}_2} > \sim 10^{-6} \text{ atm}$ at $< 2.32 \text{ Ga}$; Farquhar et al., 2000; Pavlov and Kasting, 2002; Farquhar and Wing, 2003, Bekker et al., 2004). The O_2 effect on weathering flux discussed above indicates the possibility that the GOE is one of the possible triggers for the multiple glaciations in the early Paleoproterozoic. Then, it is further expected that during the glaciations ($\sim 2.4\text{--}2.2 \text{ Ga}$, Bekker et al., 2005), P_{O_2} levels are characterized by intermediate ϕ values (around 0.5), i.e., intermediate P_{O_2} levels. $\phi = \psi = 0.5$ is likely to be satisfied when $P_{\text{O}_2} = \sim 10^{-6}\text{--}10^{-3} \text{ atm}$ (Yokota et al., 2013). The P_{O_2} levels of $\sim 10^{-6}\text{--}10^{-3} \text{ atm}$ are thus expected at $\sim 2.4\text{--}2.2 \text{ Ga}$ and the values are consistent with MIF-S records (Papineau et al., 2007), P_{O_2} estimation from paleosols (Murakami et al., 2011; Yokota et al., 2013; Chapter IV in this thesis) and ocean sediments (Sekine et al., 2011).

Oxygen increase is also accompanied by increase in O_3 and formation of the

ozone layer (e.g., Kasting et al., 1985; Segura et al., 2003). Because O₃ is a greenhouse-effect gas (Mitchell, 1989), there might be some effects on silicate weathering by change in O₃ concentration, as CH₄ can affect silicate weathering by interfering the relationship between $\Delta H'_{\text{CO}_2}$ and P_{CO_2} . Although I cannot assess the effects of O₃ concentration on weathering from the literature available, the ozone layer formation and the change in O₃ concentration accompanied by O₂ change might be another possible cause for global glaciations. In addition to the multiple glaciations in the Paleoproterozoic (~2.4–2.2 Ga), there were the global glaciation events in the Neoproterozoic (~0.7–0.6 Ga, e.g., Hoffman and Schrag, 2002; Pierrehumbert et al., 2011), which were associated with a great increase in P_{O_2} (the Neoproterozoic Oxygenation Event (NOE), e.g., Och and Shields-Zhou, 2012). O₃ may have had some role as a greenhouse-effect gas in the Neoproterozoic glaciations (Yang et al., 2012) and thus may have influenced silicate weathering. Then, despite the uncertainties about the role of O₃, the possibility cannot be excluded that the O₂ increase was one of the triggers of the global glaciations in the Neoproterozoic.

6. Implication for evolution of atmospheric CO₂ and temperature

I have discussed the effects of CO₂, CH₄ and O₂ on silicate weathering in Section 5. It has been suggested that the presence of CH₄ with limited ratios of CH₄/CO₂ and the increase in O₂ can be possible causes of global glaciations while with CO₂ alone, global glaciations hardly occur. It is also argued that CO₂ was the dominant greenhouse-effect gas in the Precambrian. To assess the plausibility of this argument, the P_{CO_2} and temperature transitions in the Precambrian are calculated in this section. Comparison of the calculated results with the required P_{CO_2} levels to maintain the Earth warm (i.e., the results from climate models) and with the P_{CO_2} levels derived from geological records helps me confirm CO₂ as the dominant greenhouse-effect gas in the Precambrian. For simplicity, I only consider the general trend of P_{CO_2} - $\Delta H'_{\text{CO}_2}$ (Eq. (98)), assuming the standard $\Delta H'_{\text{CO}_2}$ - $E_{\text{app}}^{\text{CO}_2}$ relationship (Eq. (92)) and ignoring the effects of shift in weathering regime (i.e., CDF variation). Differential equation for the reciprocal of average global surface temperature is given by

$$\frac{d(1/T)}{dt} = L(t) - \frac{R_g}{\Delta H'_{\text{CO}_2}} \frac{d \ln P_{\text{CO}_2}}{dt} \quad (110)$$

where $L(t)$ represents the rate of change in reciprocal temperature ($\text{K}^{-1} \text{yr}^{-1}$) due to the change in luminosity through age (Gough, 1981; Kasting, 1989). Note that I consider

the reciprocal temperature $1/T$, instead of temperature T , for the calculation's sake.

Equation for the P_{CO_2} -age relationship is given by

$$\kappa \frac{dP_{\text{CO}_2}}{dt} = F_{\text{in}} - F_{\text{out}} \quad (111)$$

where F_{in} and F_{out} are in- and out-fluxes of CO_2 (mol yr^{-1}), respectively, and κ is the unit conversion factor from atm to mol. Although the value of κ depends on the water vapor pressure and the pressure of background air and thus κ can vary through age (e.g., Pierrehumbert et al., 2011), κ is assumed here to be $1.74 \times 10^{20} \text{ mol atm}^{-1}$ at all ages (c.f., Berner et al., 1983). Sensitivity analysis (data not shown) indicates that the variation of κ does not change the general conclusion given in this section. F_{in} can be assumed to be the degassing flux of CO_2 (e.g., Godd ris and Veizer, 2000; Lasaga and Ohmoto, 2002). F_{out} can be taken as CO_2 flux by silicate weathering (e.g., Godd ris and Veizer, 2000; Lasaga and Ohmoto, 2002), given by

$$F_{\text{out}} = A_{\text{sil}} F_{\text{CO}_2} \quad (112)$$

where A_{sil} is the silicate rock area in the continents (m^2). Then, from Eqs. (97), (111) and (112),

$$\kappa \frac{dP_{\text{CO}_2}}{dt} = F_{\text{in}} - A_{\text{sil}} F_0 \exp \left\{ - \frac{E_{\text{app}}^{\text{CO}_2}}{R_g} \left(\frac{1}{T} - \frac{1}{T_{\text{univ}}} \right) \right\} \quad (113)$$

Solving Eqs. (110) and (113), with Eqs. (92) and (98), I can obtain the relations of age- P_{CO_2} and age- T , for a given set of age- F_{in} and age- A_{sil} relationships and for given initial conditions of P_{CO_2} and T . The initial conditions are arbitrarily chosen here as $P_{\text{CO}_2} = 10^{-0.5} \text{ atm}$ and $T = 288 \text{ K}$ ($15 \text{ }^\circ\text{C}$) at 4.4 Ga; time, t (yr), is 0 at 4.4 Ga and is forced to proceed towards today until 0.6 Ga ($t = 3.8 \times 10^9 \text{ yr}$) with a time step of 4×10^4 or $4 \times 10^3 \text{ yr}$. For the relationships of age- F_{in} and age- A_{sil} , I consider three cases; (1) both F_{in} and A_{sil} are constant (i. e., the degassing flux and silicate rock area in the continents were constant through age), (2) F_{in} is constant while A_{sil} increases with age (i. e., the degassing flux was constant while the silicate rock area in the continents increased with age) and (3) F_{in} decreases with age while A_{sil} increases with age (i. e., the degassing flux decreased while the silicate rock area in the continents increased with age) (Table 7). In any case, F_{in} and A_{sil} are formulated to be consistent with today's values, $6 \times 10^{12} \text{ mol yr}^{-1}$ and $1.12 \times 10^{14} \text{ m}^2$, respectively, at 0 Ga ($t = 4.4 \times 10^9 \text{ yr}$). Actual age- F_{in} and age- A_{sil} relationships for the calculation of the three cases are listed in Table 7, together with the other parameters ($L(t)$, F_0 and T_{univ}). See Fig. C1 in Appendix C for the illustrations of $L(t)$, F_{in} and A_{sil} plotted against age.

Table 7. Parameters for calculation of transitions of P_{CO_2} and temperature in the Precambrian.

Parameter	Case (1)	Case (2) ^a	Case (3) ^a	Reference ^b
$L(t)$ [$K^{-1} yr^{-1}$]			$-4.527 \times 10^{-15}t - 6.412 \times 10^{-5}$	1
F_0 [$mol yr^{-1} yr^{-1}$]			0.081	This study
T_{univ} [K]			283	This study
F_{in} [$mol yr^{-1}$]	6.0×10^{12}	6.0×10^{12}	$6.0 \times 10^{12} \times \max\{(-9.1483 \times 10^{-41}t^6 + 7.9795 \times 10^{-32}t^4 - 2.7054 \times 10^{-23}t^3 + 4.6787 \times 10^{-15}t^2 - 4.837 \times 10^{-7}t + 35.409), (1.89 \times 10^{-55}t^6 - 3.096 \times 10^{-46}t^5 + 2.0391 \times 10^{-36}t^4 - 6.9108 \times 10^{-27}t^3 + 1.2803 \times 10^{-17}t^2 - 1.2976 \times 10^{-8}t + 8.0013)\}$	2,3
A_{sil} [m^2]	1.12×10^{14}	$1.12 \times 10^{14} \times (9.3 \times 10^{-30} \times t^3 - 1.159 \times 10^{-19} \times t^2 + 5.482 \times 10^{-10} \times t + 0.0334)$	$1.12 \times 10^{14} \times (9.3 \times 10^{-30} \times t^3 - 1.159 \times 10^{-19} \times t^2 + 5.482 \times 10^{-10} \times t + 0.0334)$	4,5

^a Unit of t is yr.

^b 1—Kasting (1989); 2—Marty and Tolstikhin (1998); 3—Zhang and Zinder (1993); 4— Amiotte Suchet et al. (2003); 5— Dhuime et al. (2012).

Figs. 9a and b show the P_{CO_2} and temperature transitions, respectively. The bold solid, dotted and dashed curves in Figs. 9a and b corresponds to cases (1), (2) and (3), respectively. As references, I also plot two thin solid curves in Fig. 9a which represent the P_{CO_2} levels required to maintain the surface temperature at 0 (lower curve) and 15 °C (upper curve) from von Paris et al. (2008), and plot thin solid horizontal line which denotes 1 atm of P_{CO_2} as another reference. The calculated results in Fig. 9 show that the transitions strongly depend on the F_{in} - and A_{sil} -age relationships (Walker et al., 1981). For example, in cases (2) and (3), low A_{sil} at the early time of the Earth makes much CO_2 remain in atmosphere (bold dotted and dashed curves), very different results from that in case (1) where A_{sil} is constantly high from $t = 0$ (bold curve). In case (3), P_{CO_2} increases as high as 100 atm where temperature is 230 °C at 4.0 Ga; after reaching steady state at high temperature, P_{CO_2} gradually decreases by the effect of increasing luminosity ($L(t)$). Sudden changes in P_{CO_2} and temperature can be seen at around 2.1 Ga. This is what is expected from the discussion on the feedback in Section 5.1.2 where it has been found that the conditions of $P_{CO_2} < 10^{-0.5}$ atm and $T > T_{thr}$ are unstable. After the temperature drops to well less than T_{thr} , P_{CO_2} decreases gradually because the negative feedback strongly works again. In case (2), similar patterns of temperature and P_{CO_2} transitions to those in case (3) are depicted (dotted curves in Figs. 9a and b). In case (2), the early increases in P_{CO_2} and temperature are milder than those in case (3) due to time-constant F_{in} . The highest P_{CO_2} level (5.1 atm) corresponds to the highest temperature (89 °C) at 4.1 Ga. Due to lower F_{in} in case (2) than that in case (3), transition from stable high CO_2 condition ($> 10^{-0.5}$ atm) to another stable condition ($P_{CO_2} < 10^{-0.5}$ atm and $T < T_{thr}$) occurs earlier (~3.2 Ga) and more smoothly than in case (3). In case (1), on the other hand, P_{CO_2} decreases at first because high A_{sil} makes F_{out} large and dP_{CO_2}/dt becomes negative (Eq. (113)). Then, the temperature decrease caused by the P_{CO_2} decrease makes F_{CO_2} smaller until a balance in CO_2 flux is reached (i.e., $dP_{CO_2}/dt = 0$). After reaching the steady state, luminosity increase ($L(t)$) makes F_{CO_2} larger and thus gradually decreases P_{CO_2} with the steady state condition being kept. Due to the negative feedback at low temperatures ($T < T_{thr}$) at $P_{CO_2} < 10^{-0.5}$ atm, the condition of $T < 273$ K (0 °C) is not achieved and no abrupt changes in P_{CO_2} and temperature occur. In cases (1)–(3), P_{CO_2} results in 18–21 PAL at 0.6 Ga.

It is very likely that P_{CO_2} in the Precambrian was high enough to warm the Earth above freezing point of water for all cases (Fig. 9a). To confirm this conclusion, I arbitrarily increase F_0 to the extent where T is minimized in the range of > 273 K (0 °C). Increasing F_0 has the same effect as those of increasing A_{sil} and/or decreasing F_{in} without changing F_0 (Eq. (113)), and therefore, the range of F_0 which allows $T > 273$ K

(0 °C) indicates the combined uncertainties of F_0 , A_{sil} and F_{in} within which $T > 273$ K (0 °C) is maintained. In Figs. 10a and b, the P_{CO_2} and temperature are plotted, respectively, with $F_0 = 0.10, 0.25$ and $0.49 \text{ mol m}^{-2} \text{ yr}^{-1}$ for cases (1), (2) and (3), respectively. Because the change of F_0 from 0.081 to 0.10, 0.25 and $0.49 \text{ mol m}^{-2} \text{ yr}^{-1}$ does not make temperature < 0 °C for cases (1), (2) and (3), respectively, it can be argued that the surface temperature is maintained at > 0 °C in the Precambrian by CO_2 alone when the combined uncertainties of F_0 , A_{sil} and F_{in} are within 23%, 210% and 500% of the standards in Table 7 in cases (1), (2) and (3), respectively. Within such combined uncertainties of F_0 , A_{sil} and F_{in} , the P_{CO_2} levels plotted by the curves in Fig. 10a can be regarded as minimum in the Precambrian for the respective assumed cases when CO_2 alone regulates the surface temperature together with silicate weathering. Although the uncertainties in A_{sil} and F_{in} cannot be determined (e.g., Veizer and Jansen, 1979, 1985; Armstrong, 1981; Allègre and Rousseau, 1984; Goldstein and Jacobsen, 1988; Tajika and Matsui, 1993; Zhang and Zindler, 1993; Marty and Tolstikhin, 1998; Tolstikhin and Marty, 1998; Godd ris and Veizer, 2000; Holland, 2009; Belousova et al., 2010; Dhuime et al., 2012), the uncertainty of F_0 is expected to be within 50% from Fig. 4 (Section 4). Then, within large uncertainties of A_{sil} and F_{in} , P_{CO_2} can be high enough to allow $T > 273$ K (0 °C). Both Figs. 9 and 10 have revealed that the scenario of CO_2 as the dominant greenhouse-effect gas is well explained by silicate weathering even with large uncertainties of A_{sil} and F_{in} .

I compare the variations of P_{CO_2} and temperature with age calculated for the present study with those estimated from geological records in Figs. 11a and b. For the comparison of P_{CO_2} levels, I confined the geological records to paleosols in spite of a number of other records (e.g., Grotzinger and Kasting, 1993; Krupp et al., 1994; Kaufman and Xiao, 2003; Hessler et al., 2004; Ohmoto et al., 2004; Kah and Riding, 2007; Rosing et al., 2010; Som et al., 2012) (see also Lichtenegger et al. (2010) for the aeronomical constraint on P_{CO_2}). This is because the present formulation stems from silicate weathering and it is possible to directly compare the present estimates of P_{CO_2} to those by the paleosol records. The P_{CO_2} estimation which utilizes paleosols has been conducted by three different methods, (i) simple thermodynamics (Rye et al., 1995), (ii) the mass balance calculation of paleosol compositions and P_{CO_2} (Holland and Zbinden, 1988; Sheldon, 2006), and (iii) the mass balance between rock and water phases, charge balance in porewater and thermodynamics of the weathering secondary minerals (Chapter II in this thesis). Sheldon (2006) has criticized the method by Rye et al. (1995) because of the wrong application, and I exclude their data from Fig. 11a (square symbols by the method of Sheldon (2006) and circles with X marks by the method

introduced in Chapter II in this thesis). Fig. 11a reveals that the present estimates of P_{CO_2} (the area between two bold curves) are generally larger than those by Sheldon's method (square symbols). I have demonstrated that the method proposed by Sheldon (2006) does not reproduce the soil P_{CO_2} of modern weathering profiles and that Sheldon's method (2006) tends to underestimate P_{CO_2} when applied to both modern weathering profiles and paleosols (Sections 3.1 and 4.1, respectively, in Chapter II). In contrast, the ranges calculated for the present study (the area between two bold curves) are in good agreement with the P_{CO_2} levels estimated from the Neoproterozoic-Paleoproterozoic paleosols in Chapter II (circles with X marks). The agreement of the present estimates with paleosol records supports the argument that atmospheric CO_2 was high enough to warm the Earth above freezing point of water through the Precambrian.

Fig. 11b shows the ranges of temperature calculated for the present study (the area between bold curves), compared to the paleo-temperatures estimated from geological records including oxygen and silicon isotopes (e.g., Knauth and Epstein, 1976; Knauth and Lowe, 2003; Robert and Chaussidon, 2006). It has long been argued whether these geological records, especially oxygen and silicon isotopes, reflect the paleo-temperatures (Walker, 1982; Kasting et al., 2006; Jaffrés et al., 2007; Shields and Kasting, 2007). The results of the present study suggest the possibility that the surface temperature of the Earth might have been high ($> \sim 40$ °C) until around the end of Archean. In contrast, the surface temperature was low and moderate ($0 \sim 15$ °C) in the Proterozoic, which should be compared to higher estimates by geological records.

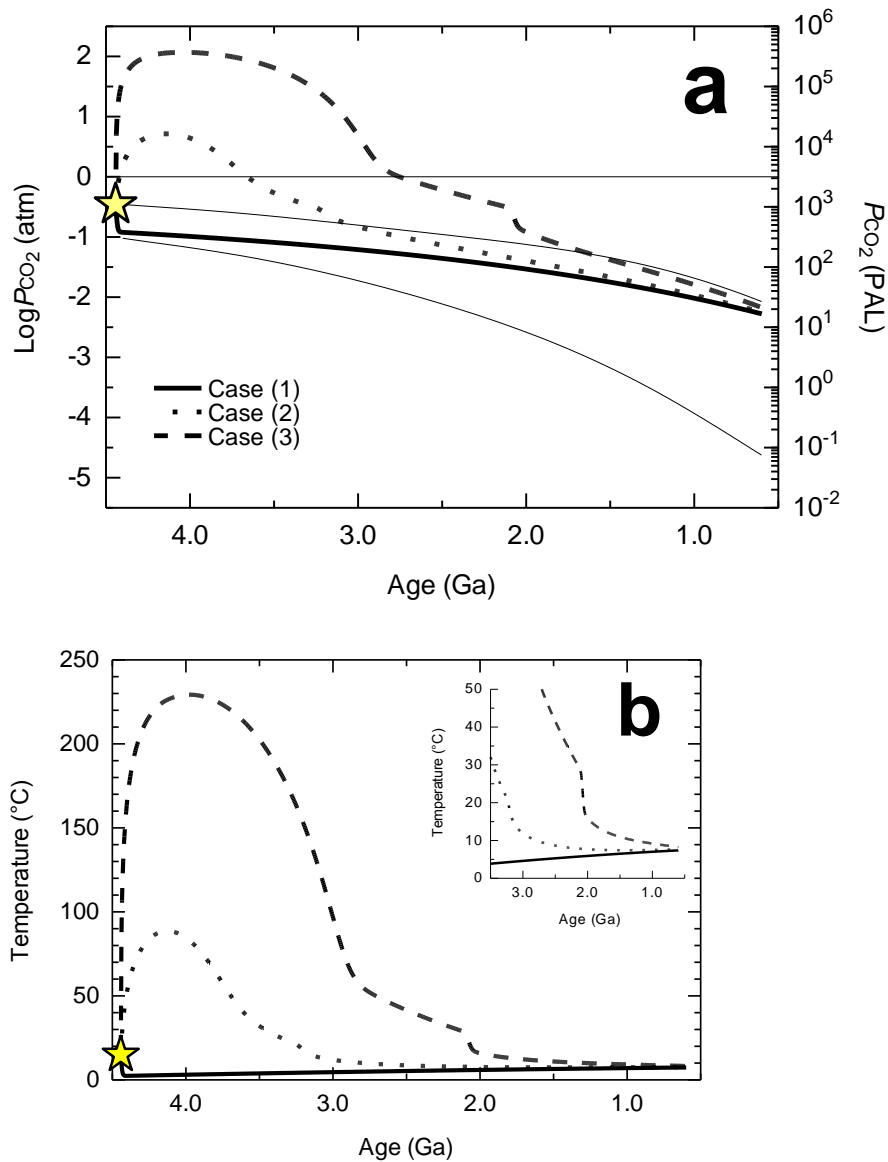


Figure 9. Transitions of (a) P_{CO_2} and (b) temperature in the Precambrian. Bold solid, dotted and dashed curves correspond to cases (1), (2) and (3), respectively. Stars denotes the initial conditions of P_{CO_2} and temperature ($P_{\text{CO}_2} = 10^{-0.5}$ atm and $T = 288$ K at 4.4 Ga). For the detailed conditions of cases (1)–(3), see Table 7. Thin two curves in Fig. 9a represent the required P_{CO_2} levels to keep the average surface temperature of the Earth at 273 K (lower curve) and 288 K (upper curve) from von Paris et al. (2008), and thin horizontal line is a reference, representing 1 atm of P_{CO_2} . Note the difference in scale between the left and right vertical axes in Fig. 9a; the right vertical axis represents P_{CO_2} by the ratio to the present-day atmospheric level (PAL, $10^{-3.5}$ atm). Right upper inset in Fig. 9b is the magnified plot in 0–50 °C of temperature range at 0.5–3.5 Ga.

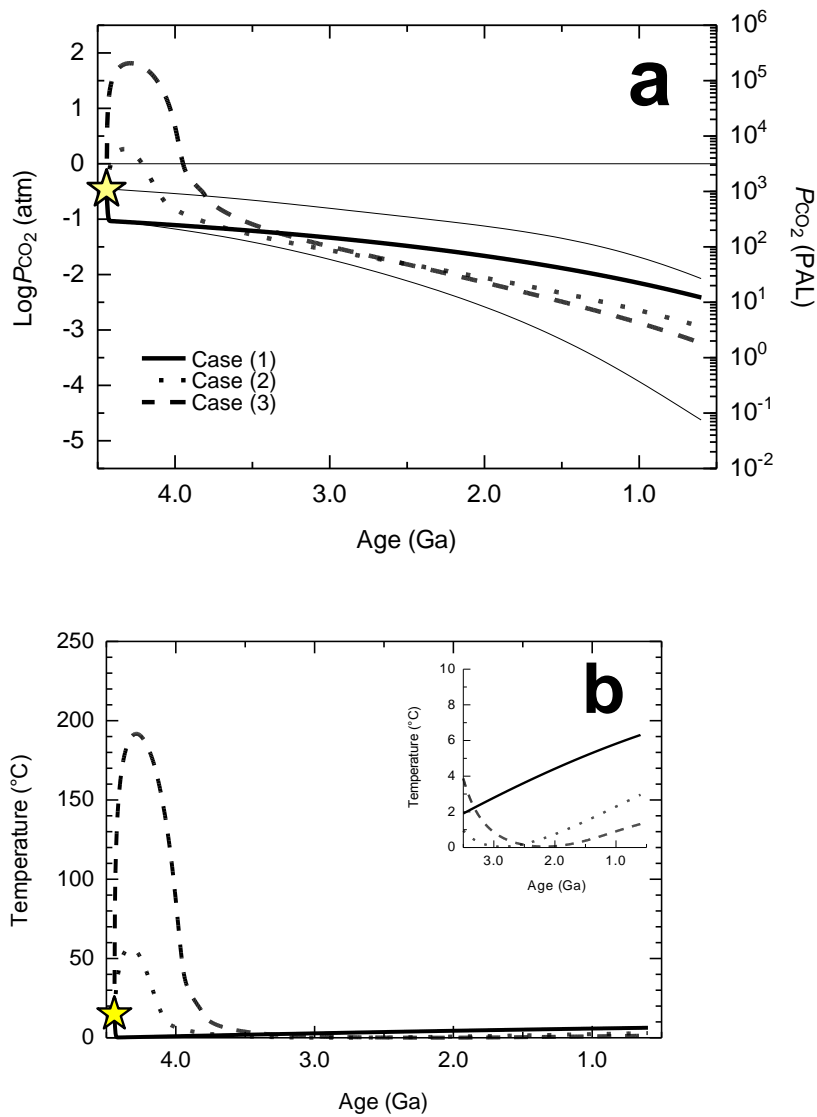


Figure 10. Transitions of (a) P_{CO_2} and (b) temperature in the Precambrian, obtained with F_0 in Eq. (113) increased to 0.10, 0.25 and 0.49 mol m⁻² yr⁻¹ for cases (1), (2) and (3), respectively. Right upper inset in Fig. 10b is the magnified plot in 0–10 °C of temperature range at 0.5–3.5 Ga. For the explanation of symbols, lines and curves, see the caption of Fig. 9.

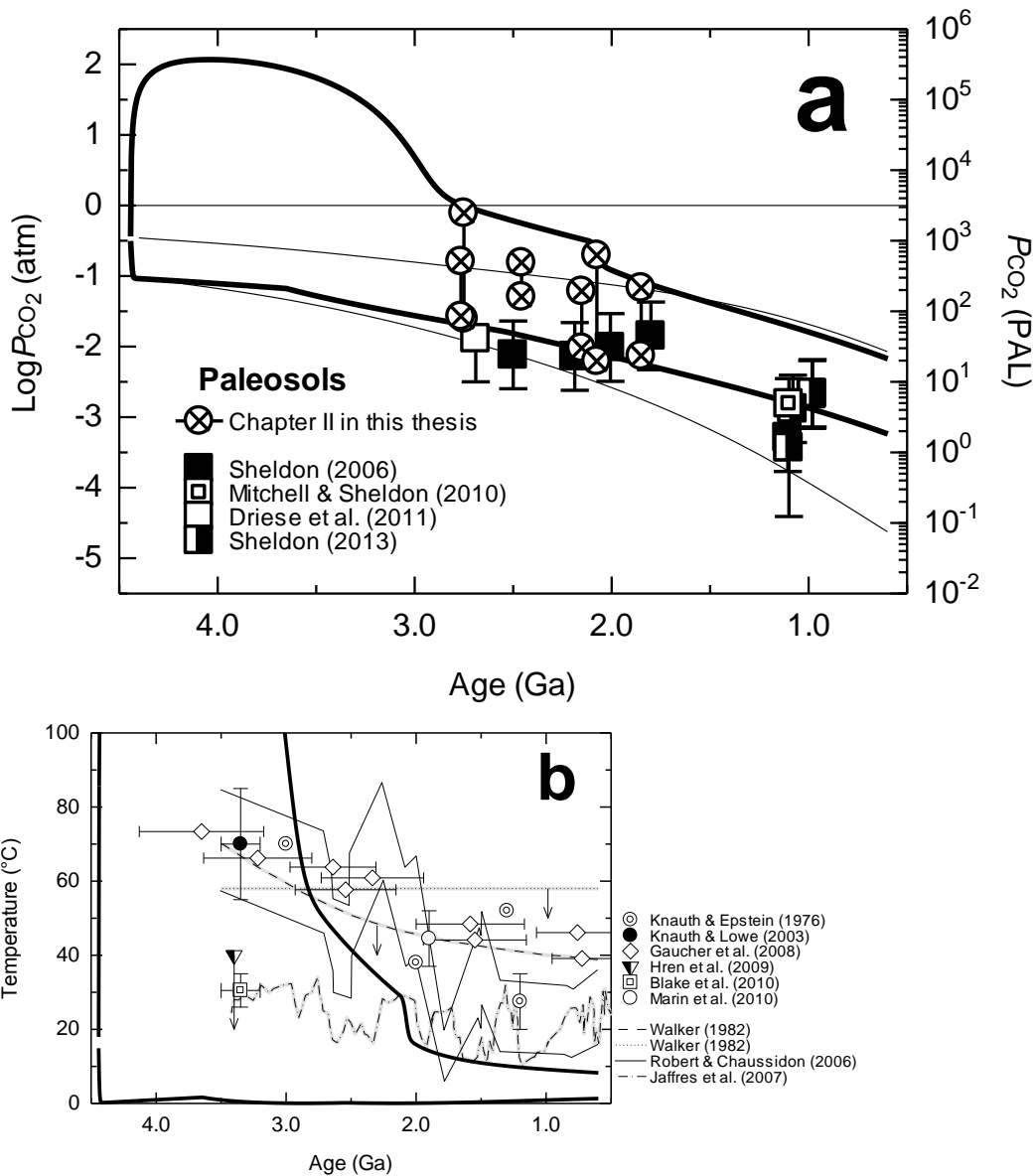


Figure 11. Comparison of (a) estimated P_{CO_2} levels and (b) temperatures in the Precambrian with those from geological records. Only maximum and minimum levels of estimated P_{CO_2} and temperatures for the present study are plotted, represented by bold curves. In Fig. 11a, only the estimates from paleosols are shown as those from geological records. Thin line and curves are the same as those in Fig. 9a. Dashed curve and dotted horizontal line from Walker (1982) in Fig. 11b represent the limits from evidence of life and from gypsum, respectively. Briefly, Knauth and Epstein (1976), Knauth and Lowe (2003), Jaffés et al. (2007), Hren et al. (2009), Blake et al. (2010) and Marin et al. (2010) have used isotope of oxygen (and hydrogen), Robert and Chaussidon (2006) isotope of silicon, and Gaucher et al. (2008) resurrected proteins as indicators of temperature.

7. Conclusions

The effects of atmospheric composition on the apparent activation energy of weathering were investigated. From the relationships in the apparent activation energy between different scales (mineral reaction to total elemental-loss and weathering flux), the apparent activation energy of weathering flux of silicates was estimated as a function of the temperature dependence of P_{CO_2} ($\Delta H'_{\text{CO}_2}$). The estimated apparent activation energies were related to the flux of total cations by silicate weathering (F_{CO_2}) by introducing the compensation law and the general rate law for silicate weathering flux, leading to the establishment of the relationships between $\Delta H'_{\text{CO}_2}$, temperature (T) and F_{CO_2} . Based on the relationships between $\Delta H'_{\text{CO}_2}$, T and F_{CO_2} , I discussed the effects of atmospheric CO_2 , as well as those of CH_4 and O_2 , on the silicate weathering, and their implications for the atmospheric compositions and surface temperatures in the Precambrian.

The effects of CO_2 on silicate weathering were discussed based on the relationships between $\Delta H'_{\text{CO}_2}$, T and F_{CO_2} and the greenhouse effect of CO_2 . In the global-scale weathering, the greenhouse effect of CO_2 represents $\Delta H'_{\text{CO}_2}$. I calculated the ratio of the change in F_{CO_2} to the corresponding change in P_{CO_2} as an indicator of the feedback of silicate weathering on CO_2 using the greenhouse effects of CO_2 in the literature. The calculation revealed that when $P_{\text{CO}_2} > 10^{-0.5}$ atm, the feedback is negative and independent of both temperature and P_{CO_2} . On the other hand, when $P_{\text{CO}_2} < 10^{-0.5}$ atm, the feedback is almost P_{CO_2} -independent but temperature-dependent; at high ($> \sim 30$ °C) and low ($< \sim 30$ °C) temperatures, the feedback is positive and negative, respectively. Thus the conditions of $P_{\text{CO}_2} < 10^{-0.5}$ atm and $> \sim 30$ °C are unstable; with a slight change in CO_2 , the conditions change immediately into either the conditions of $P_{\text{CO}_2} > 10^{-0.5}$ atm or those of $P_{\text{CO}_2} < 10^{-0.5}$ atm and $< \sim 30$ °C. Under the conditions of $P_{\text{CO}_2} < 10^{-0.5}$ atm and $< \sim 30$ °C, the feedback is not only negative but also becomes more negative as temperature decreases. Thus, global glaciations hardly occur under the conditions of $P_{\text{CO}_2} < 10^{-0.5}$ atm and $< \sim 30$ °C. The stable conditions at low temperatures with $P_{\text{CO}_2} < 10^{-0.5}$ atm against glaciations may explain the stable climates in the Precambrian excluding the periods of the glaciations, especially the stable climate in the Mesoproterozoic.

I considered the effects of CH_4 on weathering by calculating the feedback indicator with the relationships between $\Delta H'_{\text{CO}_2}$, T and F_{CO_2} and the greenhouse effects of CH_4 in the literature. With limited ratios of CH_4/CO_2 (~ 0.03 — ~ 0.15), positive

feedback operates at low temperatures ($< \sim 5$ °C). Therefore, when the conditions of ~ 0.03 – ~ 0.15 of CH_4/CO_2 and $< \sim 5$ °C of temperature are satisfied, global glaciations can occur. The emergence of CH_4 with the limited ratios of CH_4/CO_2 may explain the glaciation in the Mesoarchean.

The change in P_{O_2} affects the apparent activation energy of weathering flux of silicates directly by involving oxidation reactions in weathering. When P_{O_2} increases from extremely low levels to $\sim 10^{-6}$ – 10^{-3} atm, F_{CO_2} can increase at low temperatures due to the change in the apparent activation energy. Thus, I concluded that oxygen increase is one of the possible triggers of global glaciations, which may explain the glaciations in the Paleoproterozoic.

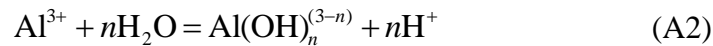
I finally calculated the P_{CO_2} and temperature transitions in the Precambrian, confirming that CO_2 was the dominant greenhouse-effect gas through the eon. The calculated P_{CO_2} and temperature suggest that the Precambrian Earth can have been at > 0 °C only with CO_2 and that the Hadean-Archean might have been hot. The estimates of P_{CO_2} are consistent with those calculated by the other weathering model based on paleosol data, further supporting the argument.

Appendix A

When Al dissolves into water, it forms various species: Al^{3+} , $\text{Al}(\text{OH})^{2+}$, $\text{Al}(\text{OH})_2^+$, $\text{Al}(\text{OH})_3^0$, and $\text{Al}(\text{OH})_4^-$. Therefore, the concentration of total dissolved Al ($[\text{Al}]_{\text{ss}}$) is the sum of these species:

$$[\text{Al}]_{\text{ss}} = \sum_{n=0}^4 [\text{Al}(\text{OH})_n^{(3-n)}]_{\text{ss}} \quad (\text{A1})$$

where $[\text{Al}(\text{OH})_n^{(3-n)}]_{\text{ss}}$ is the steady-state concentration of the aluminum species $\text{Al}(\text{OH})_n^{(3-n)}$ with $n = 0$ – 4 . The species with $n = 1$ – 4 are produced by hydrolysis of Al^{3+} :



I define the hydrolysis constant for Reaction (A2) as K_{Al_n} ($\text{mol}^n \text{L}^{-n}$). Using K_{Al_n} , the steady-state concentration of each species can be represented by

$$[\text{Al}(\text{OH})_n^{(3-n)}]_{\text{ss}} = \frac{K_{\text{Al}_n} [\text{Al}^{3+}]_{\text{ss}}}{[\text{H}^+]_{\text{ss}}^n} \quad (\text{A3})$$

The temperature dependence of K_{Al_n} is described by the standard enthalpy change,

$\Delta H^\circ_{\text{Al}_n}$ (kJ mol⁻¹):

$$\frac{d \ln K_{\text{Al}_n}}{d(1/T)} \equiv - \frac{\Delta H^\circ_{\text{Al}_n}}{R_g} \quad (\text{A4})$$

The values of K_{Al_n} and $\Delta H^\circ_{\text{Al}_n}$ are listed in Table A1. From Eqs. (A1) and (A3),

$$[\text{Al}^{3+}]_{\text{ss}} = [\text{Al}]_{\text{ss}} \left(\sum_{n=0}^4 \frac{K_{\text{Al}_n}}{[\text{H}^+]_{\text{ss}}^n} \right)^{-1} \quad (\text{A5})$$

I defined f_{Al} in Eq. (73) as the ratio of Al^{3+} to total dissolved Al ($f_{\text{Al}} \equiv [\text{Al}^{3+}]_{\text{ss}}/[\text{Al}]_{\text{ss}}$).

Using Eq. (A5), f_{Al} in Eq. (73) can be rewritten as

$$f_{\text{Al}} = \left(\sum_{n=0}^4 \frac{K_{\text{Al}_n}}{[\text{H}^+]_{\text{ss}}^n} \right)^{-1} \quad (\text{A6})$$

Using K_{Al_n} values in Table A1, f_{Al} can be calculated as a function of pH and are plotted as solid curve in Fig. A1a; when pH is increased, f_{Al} decreases, because dissolved Al^{3+} becomes more hydrolyzed (Reaction (A2)). Accordingly, the average valence number, Z_{Al} , the average hydrolyzed number, n_{Al} , and the average standard enthalpy change by hydrolysis, $\Delta H^\circ_{\text{Al}}$ (kJ mol⁻¹), change with pH. The three parameters are defined, using Eq. (A6), by the following equations:

$$Z_{\text{Al}} \equiv \sum_{n=0}^4 (3-n) \frac{[\text{Al}(\text{OH})^{(3-n)}]_{\text{ss}}}{[\text{Al}]_{\text{ss}}} = 3 - \sum_{n=0}^4 n f_{\text{Al}} \frac{K_{\text{Al}_n}}{[\text{H}^+]_{\text{ss}}^n} \quad (\text{A7})$$

$$n_{\text{Al}} \equiv \sum_{n=0}^4 n \frac{[\text{Al}(\text{OH})^{(3-n)}]_{\text{ss}}}{[\text{Al}]_{\text{ss}}} = \sum_{n=0}^4 n f_{\text{Al}} \frac{K_{\text{Al}_n}}{[\text{H}^+]_{\text{ss}}^n} \quad (\text{A8})$$

$$\Delta H^\circ_{\text{Al}} \equiv \sum_{n=0}^4 \Delta H^\circ_{\text{Al}_n} \frac{[\text{Al}(\text{OH})^{(3-n)}]_{\text{ss}}}{[\text{Al}]_{\text{ss}}} = \sum_{n=1}^4 \Delta H^\circ_{\text{Al}_n} f_{\text{Al}} \frac{K_{\text{Al}_n}}{[\text{H}^+]_{\text{ss}}^n} \quad (\text{A9})$$

The three parameters calculated from Eqs. (A7)–(A9) are plotted against pH in Fig. A1. Note that from Eqs. (A7) and (A8), $Z_{\text{Al}} + n_{\text{Al}} = 3$, which is the same as Eq. (15) in the main text. The values of Z_{Al} , n_{Al} and $\Delta H^\circ_{\text{Al}}$ listed in Table 3 are based on Fig. A1.

In the main text, I represented the temperature dependence of f_{Al} by Eq. (85):

$d \ln f_{\text{Al}} / d(1/T) = (\Delta H^\circ_{\text{Al}} - n_{\text{Al}} \Delta H^\circ_{\text{H}^+}) / R_g$. I here explain how Eq. (85) is formulated. Using Eqs. (A4) and (A5),

$$\begin{aligned} \frac{d \ln f_{\text{Al}}}{d(1/T)} &= \frac{d}{d(1/T)} \ln \left(\sum_{n=0}^4 \frac{K_{\text{Al}_n}}{[\text{H}^+]_{\text{ss}}^n} \right)^{-1} \\ &= \frac{1}{R_g} \sum_{n=1}^4 \Delta H^\circ_{\text{Al}_n} f_{\text{Al}} \frac{K_{\text{Al}_n}}{[\text{H}^+]_{\text{ss}}^n} + \frac{d \ln [\text{H}^+]_{\text{ss}}}{d(1/T)} \sum_{n=1}^4 n f_{\text{Al}} \frac{K_{\text{Al}_n}}{[\text{H}^+]_{\text{ss}}^n} \end{aligned} \quad (\text{A10})$$

Using Eqs. (A8) and (A9), Eq. (A10) can be rewritten as

$$\frac{d \ln f_{\text{Al}}}{d(1/T)} = \frac{\Delta H_{\text{Al}}^{\circ}}{R_{\text{g}}} + n_{\text{Al}} \frac{d \ln [\text{H}^+]_{\text{ss}}}{d(1/T)} \quad (\text{A11})$$

The temperature dependence of $[\text{H}^+]_{\text{ss}}$ is defined as $\Delta H'_{\text{H}^+}$ in Eq. (84). From Eqs. (A11) and (84),

$$\frac{d \ln f_{\text{Al}}}{d(1/T)} = \frac{\Delta H_{\text{Al}}^{\circ} - n_{\text{Al}} \Delta H'_{\text{H}^+}}{R_{\text{g}}} \quad (\text{A12})$$

Eq. (A12) is the same as Eq. (85).

Table A1. Thermodynamic parameters of Al^{3+} hydrolysis.

Al species	$\log K_{\text{Al},n} (\text{mol}^n \text{L}^{-n})^{\text{a}}$	$\Delta H'_{\text{Al},n} (\text{kJ mol}^{-1})^{\text{a}}$
Al^{3+}	0	0
$\text{Al}(\text{OH})^{2+}$	-5.0	48.07
$\text{Al}(\text{OH})_2^+$	-10.1	112.5
$\text{Al}(\text{OH})_3^0$	-16.9	167
$\text{Al}(\text{OH})_4^-$	-22.7	177

^a Data are from Stumm and Morgan (1996). $K_{\text{Al},n}$ are those at 25 °C and 1 atm.

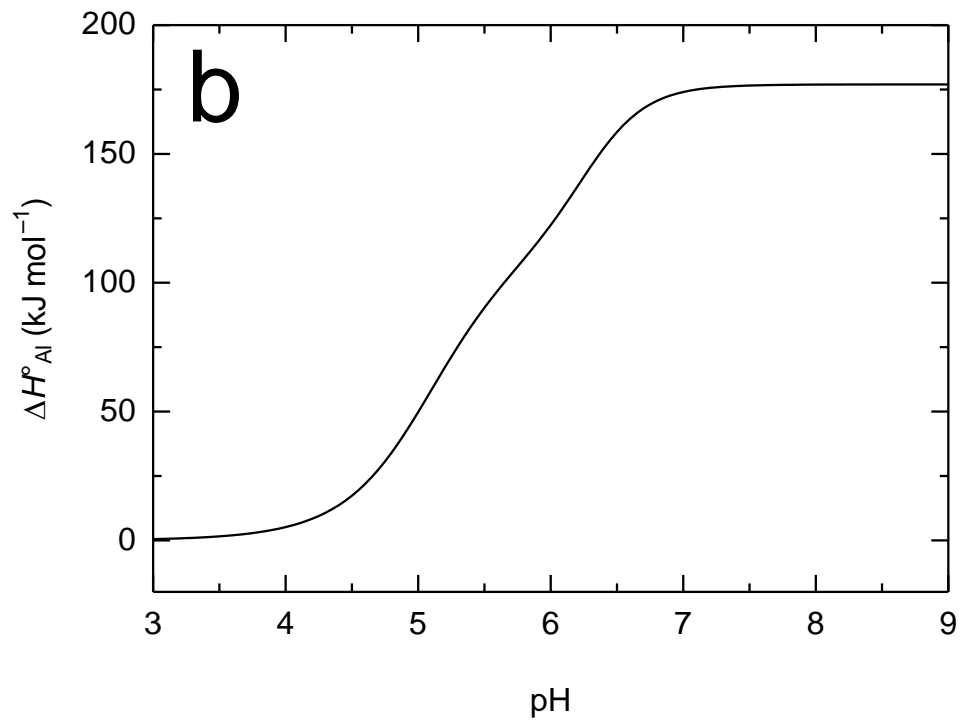
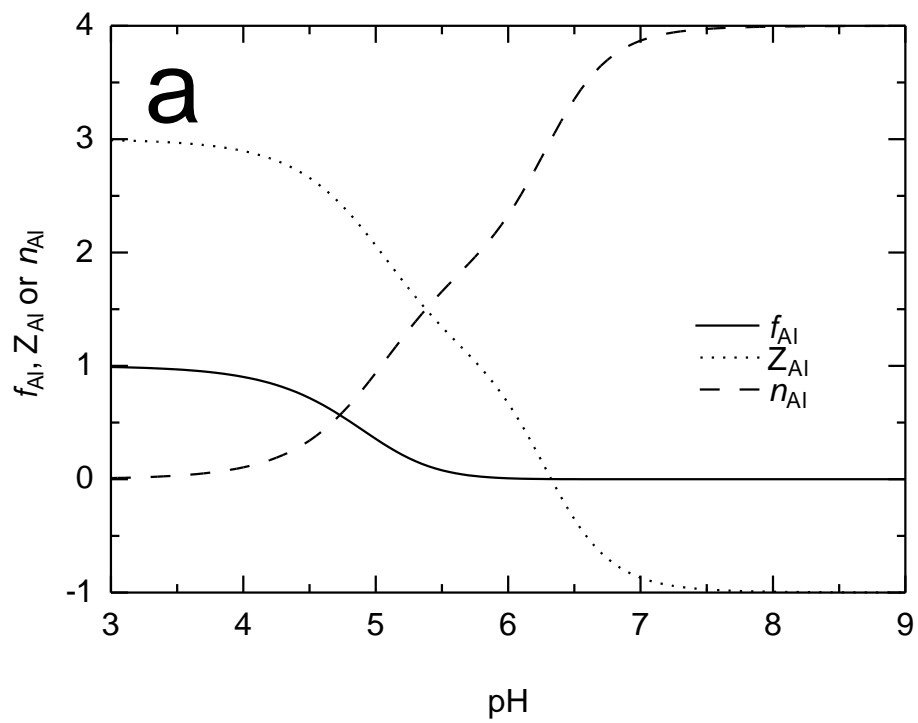


Figure A1. (a) f_{Al} , Z_{Al} , n_{Al} and (b) ΔH°_{Al} plotted against pH.

Appendix B

To consider the effect of oxygen increase on the apparent activation energy of weathering, it is necessary to evaluate the temperature dependence of Fe²⁺ oxidation rate, λ . The λ value is defined in Eq. (17) as $\lambda = k_{\text{ox}}[\text{O}_2]_{\text{ss}}[\text{OH}^-]_{\text{ss}}^2$. In Eq. (17), $[\text{O}_2]_{\text{ss}}$ can be converted to P_{O_2} by the Henry's constant, K_{HO} (mol L⁻¹ atm⁻¹), and $[\text{OH}^-]_{\text{ss}}$ can be converted to $[\text{H}^+]_{\text{ss}}$ by the water dissociation constant, K_{W} (mol² L⁻²);

$$\lambda = k_{\text{ox}} \frac{K_{\text{W}}^2}{[\text{H}^+]_{\text{ss}}^2} K_{\text{HO}} P_{\text{O}_2} \quad (\text{B1})$$

I define the temperature dependences of k_{ox} , K_{HO} , P_{O_2} and K_{W} as $E_{\text{app}}^{\text{ox}}$, $\Delta H_{\text{HO}}^{\circ}$, $\Delta H'_{\text{O}_2}$ and $\Delta H_{\text{W}}^{\circ}$ (kJ mol⁻¹), respectively:

$$E_{\text{app}}^{\text{ox}} \equiv -R_{\text{g}} \frac{d \ln k_{\text{ox}}}{d(1/T)} \quad (\text{B2})$$

$$\Delta H_{\text{HO}}^{\circ} \equiv -R_{\text{g}} \frac{d \ln K_{\text{HO}}}{d(1/T)} \quad (\text{B3})$$

$$\Delta H'_{\text{O}_2} \equiv -R_{\text{g}} \frac{d \ln P_{\text{O}_2}}{d(1/T)} \quad (\text{B4})$$

$$\Delta H_{\text{W}}^{\circ} \equiv -R_{\text{g}} \frac{d \ln K_{\text{W}}}{d(1/T)} \quad (\text{B5})$$

Then, the temperature dependence of λ , $\Delta H'_{\lambda}$ (Eq. (53)), is represented by

$$\Delta H'_{\lambda} = E_{\text{app}}^{\text{ox}} + 2\Delta H_{\text{W}}^{\circ} + \Delta H_{\text{HO}}^{\circ} + \Delta H'_{\text{O}_2} - 2\Delta H'_{\text{H}^+} \quad (\text{B6})$$

The value of $E_{\text{app}}^{\text{ox}}$ is the apparent activation energy of Fe²⁺ oxidation and can be in the range of 25–96 kJ mol⁻¹ (Lowson, 1982; Millero et al., 1987). Because oxygen is not a greenhouse-effect gas, I can assume that $\Delta H'_{\text{O}_2} \cong 0$. The values of $\Delta H_{\text{HO}}^{\circ}$ and $\Delta H_{\text{W}}^{\circ}$ are the standard enthalpy changes of oxygen dissolution into water (–10 kJ mol⁻¹, c.f., Wilhelm et al. (1977)) and of water dissociation (57 kJ mol⁻¹, Stumm and Morgan (1996)), respectively. The value of $\Delta H'_{\text{H}^+}$ depends on P_{CO_2} (Eqs. (87) and (98), and Fig. 3d). When P_{CO_2} is between 10^{-0.5}–10⁻⁴ atm, $\Delta H'_{\text{H}^+}$ is calculated to be 35–146 kJ mol⁻¹ according to Eqs. (87) and (98), and Fig. 3d. The highest and lowest values of $\Delta H'_{\text{H}^+}$ correspond to 10⁻⁴ and 10^{-0.5} atm of P_{CO_2} , respectively. Then, the value of $\Delta H'_{\lambda}$ is calculated to be from 134 to –165 kJ mol⁻¹ with the highest and lowest values of $\Delta H'_{\lambda}$ corresponding to 10^{-0.5} and 10⁻⁴ atm of P_{CO_2} , respectively.

Appendix C

Fig. C1 illustrates $L(t)$, F_{in} and A_{sil} as a function of age. Calculations are based on equations in Table 7.

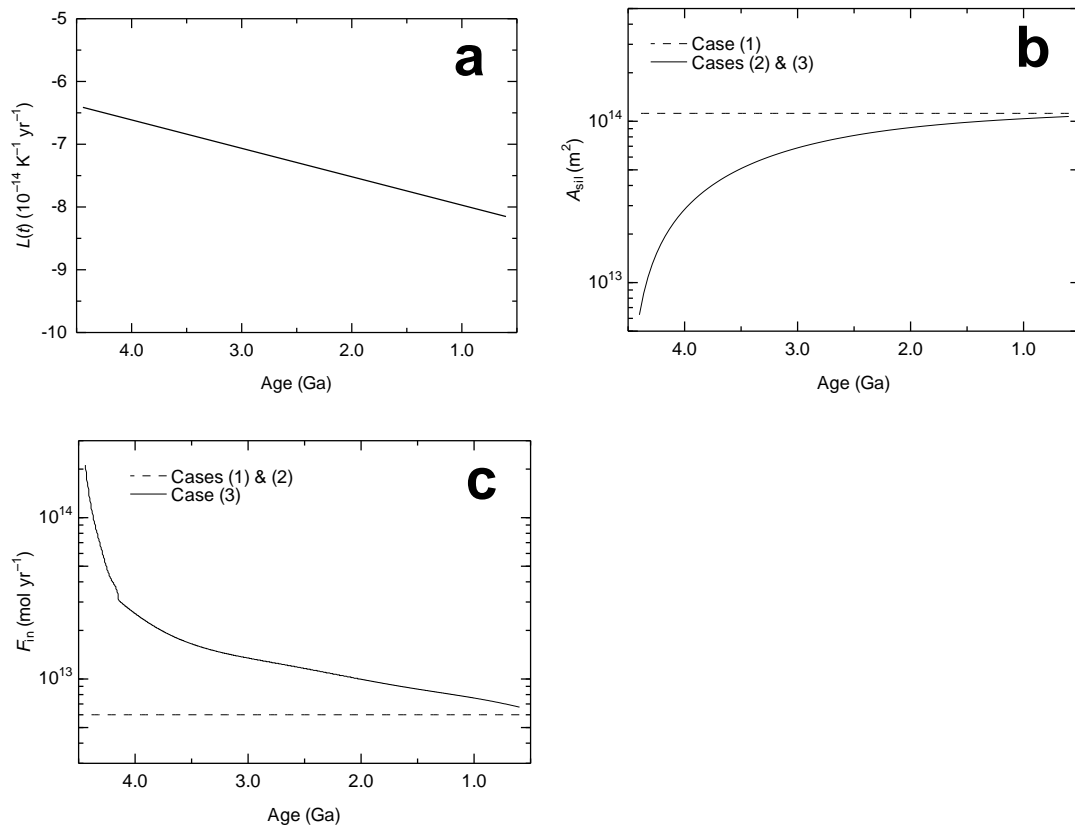


Figure C1. (a) $L(t)$ (b) A_{sil} and (c) F_{in} plotted against age. Calculations are based on Table 7.

References

- Allègre C. J. and Rousseau D. (1984) The growth of the continent through geological time studied by Nd isotope analysis of shales. *Earth Planet. Sci. Lett.* **67**, 19–34.
- Amiotte Suchet P., Probst J-L. and Ludwig W. (2003) Worldwide distribution of continental rock lithology: Implications for the atmospheric/soil CO₂ uptake by continental weathering and alkalinity river transport to the oceans. *Global Biogeochem. Cycles* **17**, 1891–1903.
- Armstrong R. L. (1981) Radiogenic isotopes: the case for crustal recycling on a near-steady-state no-continental-growth Earth. *Philos. Trans. R. Soc. Lond. A* **301**, 443–472.
- Beig M. S. and Lüttge A. (2006) Albite dissolution kinetics as a function of distance from equilibrium: Implications for natural feldspar weathering. *Geochim. Cosmochim. Acta* **70**, 1402–1420.
- Bekker A., Holland H. D., Wang P. -L., Rumble III D., Stein H. J., Hannah J. L., Coetzee L. L. and Beukes N. J. (2004) Dating the rise of atmospheric oxygen. *Nature* **427**, 117–120.
- Bekker A., Kaufman A. J., Karhu J. A. and Eriksson K. A. (2005) Evidence for Paleoproterozoic cap carbonates in North America. *Precambrian Res.* **137**, 167–206.
- Belousova E. A., Kostitsyn Y. A., Griffin W. L., Begg G. C., O'Reilly S. Y. and Pearson N. J. (2010) The growth of the continental crust: Constraints from zircon Hf-isotope data. *Lithos* **119**, 457–466.
- Berner R. A. (1978) Rate control of mineral dissolution under Earth surface conditions. *Am. J. Sci.* **278**, 1235–1252.
- Berner R. A., Lasaga A. C. and Garrels R. M. (1983) The carbonate-silicate geochemical cycle and its effect on atmospheric carbon dioxide over the past 100 million years. *Am. J. Sci.* **283**, 641–683.
- Berner R. A. (1991) A model for atmospheric CO₂ over Phanerozoic time. *Am. J. Sci.* **291**, 339–376.
- Berner R. A. (1992) Weathering, plants, and the long-term carbon cycle. *Geochim. Cosmochim. Acta* **56**, 3225–3231.
- Berner R. A. (1994) GEOCARB II: A revised model of atmospheric CO₂ over Phanerozoic time. *Am. J. Sci.* **294**, 56–91.
- Berner R. A. (1995) Chemical weathering and its effect on atmospheric CO₂ and climate. *Rev. Mineral.* **31**, 565–583.

- Berner R. A. (1997) The rise of plants and their effect on weathering and atmospheric CO₂. *Science* **276**, 544–546.
- Berner R. A. and Kothavala Z. (2001) GEOCARB III: A revised model of atmospheric CO₂ over Phanerozoic time. *Am. J. Sci.* **301**, 182–204.
- Berner R. A. (2006) GEOCARBSULF: A combined model for Phanerozoic atmospheric O₂ and CO₂. *Geochim. Cosmochim. Acta* **70**, 5653–5664.
- Blake R. E., Chang S. J. and Lepland A. (2010) Phosphate oxygen isotope evidence for a temperate biologically active Archean ocean. *Nature* **464**
- Blum A. E. and Stillings L. L. (1995) Feldspar dissolution kinetics. *Rev. Mineral.* **31**, 291–342.
- Bouma T. J., Nielsen K. L., Eissenstat D. M. and Lynch J. P. (1997) Estimating respiration of roots in soil: Interactions with soil CO₂, soil temperature and soil water content. *Plant Soil* **195**, 221–232.
- Brady P. V. (1991) The effect of silicate weathering on global temperature and atmospheric CO₂. *J. Geophys. Res.* **B11**, 18101–18106.
- Brady P. V. and Carroll S. A. (1994) Direct effects of CO₂ and temperature on silicate weathering: Possible implications for climate control. *Geochim. Cosmochim. Acta* **58**, 1853–1856.
- Brady P. V. and Gislason S. R. (1997) Seafloor weathering controls on atmospheric CO₂ and global climate. *Geochim. Cosmochim. Acta* **61**, 965–973.
- Brantley S. L. and Chen Y. (1995) Chemical weathering rates of pyroxene and amphiboles. *Rev. Mineral.* **31**, 119–172.
- Brantley S. L. and White A. F. (2009) Approaches to modeling weathered regolith. *Rev. Mineral. Geochem.* **70**, 435–484.
- Brantley S. L. and Lebedeva M. (2011) Learning to read the chemistry of regolith to understand the critical zone. *Annu. Rev. Earth Planet. Sci.* **39**, 387–416.
- Breecker D. O., Sharp Z. D. and McFadden L. D. (2009) Seasonal bias in the formation of stable isotopic composition of pedogenic carbonate in modern soils from central New Mexico, USA. *Geol. Soc. Am. Bull.* **121**, 630–640.
- Caldeira K. and Kasting J. F. (1992) The life span of the biosphere revisited. *Nature* **360**, 721–723.
- Cama J., Ayora C. and Lasaga A. C. (1999) The derivation-from-equilibrium effect on dissolution rate and on apparent variations in activation energy. *Geochim. Cosmochim. Acta* **17**, 2481–2486.
- Casey W. H. and Sposito G. On the temperature dependence of mineral dissolution rates. *Geochim. Cosmochim. Acta* **56**, 3825–3830.

- Casey W. H. and Ludwig C. (1995) Silicate mineral dissolution as a ligand-exchange reaction. *Rev. Mineral.* **31**, 87–117.
- Clow D. W. and Mast M. A. (2010) Mechanisms for chemostatic behavior in catchments: Implications for CO₂ consumption by mineral weathering. *Chem. Geol.* **269**, 40–51.
- Daval D., Hellmann R., Corvisier J., Tisserand D., Martinez I. and Guyot F. (2010) Dissolution kinetics of diopside as a function of solution saturation state: Macroscopic measurements and implications for modeling of geological storage of CO₂. *Geochim. Cosmochim. Acta* **74**, 2615–2633.
- Daval D., Sissmann O., Menguy N., Saldi G. D., Guyot F., Martinez I., Corvisier J., Garcia B., Machouk I., Knauss K. G. and Hellmann R. (2011) Influence of amorphous silica layer formation on the dissolution rate of olivine at 90 °C and elevated pCO₂. *Chem. Geol.* **284**, 193–209.
- Davidson E. A., Belk E. and Boone R. D. (1998) Soil water content and temperature as independent or confounded factors controlling soil respiration in a temperate mixed hardwood forest. *Glob. Chang. Biol.* **4**, 217–227.
- Dalai T. K., Krishnaswami S. and Sarin M. M. (2002) Major ion chemistry in the headwaters of the Yamuna river system: Chemical weathering, its temperature dependence and CO₂ consumption in the Himalaya. *Geochim. Cosmochim. Acta* **66**, 3397–3416.
- Delany J. M. and Lundeen S. R. (1990) The LLNL thermochemical database. Lawrence Livermore National Laboratory Report UCRL-21658. Lawrence Livermore National Laboratory.
- Dere A. L., White T. S., April R. H., Reynolds B., Miller T. E., Knapp E. P., McKay L. D. and Brantley S. L. (2013) Climate dependence of feldspar weathering in shale soils along a latitudinal gradient. *Geochim. Cosmochim. Acta* **122**, 101–126.
- Dessert C., Dupré B., François L. M., Schott J., Gaillardet J., Chakrapani G. and Bajpai S. (2001) Erosion of Decan Traps determined by river geochemistry: impact on the global climate and the ⁸⁷Sr/⁸⁶Sr ratio of seawater. *Earth Planet. Sci. Lett.* **188**, 459–474.
- Dessert C., Dupré B., Gaillardet J., François L. M. and Allègre C. J. (2003) Basalt weathering laws and the impact of basalt weathering on the global carbon cycle. *Chem. Geol.* **202**, 257–273.
- Dhuime B., Hawkesworth C. J., Cawood P. A. and Storey C. D. (2012) A change in the geodynamics of continental growth 3 billion years ago. *Science* **335**, 1334–1336.
- Dixit S. and Carroll S. A. (2007) Effect of solution saturation state and temperature on

- diopside dissolution. *Geochem. Trans.* **8**.
- Domagal-Goldman S. D., Kasting J. F., Johnston D. T. and Farquhar J. (2008) Organic haze, glaciations and multiple sulfur isotopes in the Mid-Archean Era. *Earth Planet Sci. Lett.* **269**, 29–40.
- Dorn R. I. and Brady P. V. (1995) Rock-based measurement of temperature-dependent plagioclase weathering. *Geochim. Cosmochim. Acta* **59**, 2847–2852.
- Drever J. I. and Clow D. W. (1995) Weathering rates in catchments. *Rev. Mineral.* **31**, 463–483.
- Driese S. G., Jirsa M. A., Ren M., Brantley S. L., Sheldon N. D., Parker D. and Schmitz M. (2011) Neoproterozoic paleoweathering of tonalite and metabasalt: Implications for reconstructions of 2.69 Ga early terrestrial ecosystems and paleoatmospheric chemistry. *Precambrian Res.* **189**, 1–17.
- Emmanuel S. and Ague J. J. (2011) Impact of nano-size weathering products on the dissolution rates of primary minerals. *Chem. Geol.* **282**, 11–18.
- Eiriksdottir E. S., Gislason S. R. and Oelkers E. H. (2013) Does temperature or runoff control the feedback between chemical denudation and climate? Insights from NE Iceland. *Geochim. Cosmochim. Acta* **107**, 65–81.
- Ekart D. D., Cerling T. E., Montañez I. P. and Tabor N. J. (1999) A 400 million year carbon isotope record of pedogenic carbonate: Implications for paleoatmospheric carbon dioxide. *Am. J. Sci.* **299**, 805–827.
- Farquhar J., Bao H. and Thieme M. (2000) Atmospheric influence of Earth's earliest sulfur cycle. *Science* **289**, 756–758.
- Farquhar J. and Wing B. A. (2003) Multiple sulfur isotopes and the evolution of the atmosphere. *Earth Planet Sci. Lett.* **213**, 1–13.
- Feulner G. (2012) The faint young Sun problem. *Rev. Geophys.* **50**, RG2006.
- Fritz B. and Noguera C. (2009) Mineral precipitation kinetics. *Rev. Mineral. Geochem.* **70**, 371–410.
- Gabet E. J. and Mudd S. M. (2009) A theoretical model coupling chemical weathering rates with denudation rates. *Geology* **37**, 151–154.
- Ganor J., Lu P., Zheng Z. and Zhu C. (2007) Bridging the gap between laboratory measurements and field estimations of silicate weathering using simple calculations. *Environ. Geol.* **53**, 599–610.
- Garrels R. M. and Mackenzie F. T. (1971) *Evolution of Sedimentary Rocks*. W. W. Norton & Company, New York, 397 pp.
- Gaucher E. A., Govindarajan S. and Ganesh O. K. (2008) Palaeotemperature trend for Precambrian life inferred from resurrected proteins. *Nature* **451**, 704–707.

- Gislason S. R. and Eugster H. P. (1987) Meteoric water-basalt interactions. I: A laboratory study. *Geochim. Cosmochim. Acta* **51**, 2827–2840.
- Gislason S. R. and Oelkers E. H. (2003) Mechanism, rates, and consequences of basaltic glass dissolution: II. An experimental study of the dissolution rates of basaltic glass as a function of pH and temperature. *Geochim. Cosmochim. Acta* **67**, 3817–3832.
- Gislason S. R., Oelkers E. H., Eiriksdottir E. S., Kardjilov M. I., Gisladottir G., Sigfusson B., Snorrason A., Elefsen S., Hardardottir J., Torssander P. and Oskarsson N. (2009) Direct evidence of the feedback between climate and weathering. *Earth Planet. Sci. Lett.* **277**, 213–222.
- Godderis Y. and Veizer J. (2000) Tectonic control of chemical and isotopic composition of ancient oceans: The impact of continental growth. *Am. J. Sci.* **300**, 434–461.
- Goddéris Y., Roelandt C., Schott J., Pierret M-C. and François L. M. (2009) Towards and integrated model of weathering, climate and biosphere processes. *Rev. Mineral. Geochem.* **70**, 411–434.
- Goddéris Y., Brantley S. L., François L. M., Schott J., Pollard D., Déqué M. and Dury M. (2013) Rates of consumption of atmospheric CO₂ through the weathering of loess during the next 100 yr of climate change. *Biogeosciences* **10**, 135–148.
- Goldstein S. J. and Jacobsen S. B. (1988) Nd and Sr isotopic systematics of river water suspended material: implication for crustal evolution. *Earth Planet. Sci. Lett.* **87**, 249–265.
- Gough D. O. (1981) Solar interior structure and luminosity variations. *Solar Phys.* **74**, 21–34.
- Grotzinger J. P and Kasting J. F. (1993) New constraints on Precambrian ocean composition. *J. Geol.* **101**, 235–243.
- Haqq-Misra J. D., Domagal-Goldman S. D., Kasting P. J. and Kasting J. F. (2008) A revised, hazy methane greenhouse for the Archean Earth. *Astrobiology* **8**, 1127–1137.
- Heimsath A. M., Dietrich W. E., Nishiizumi K. and Finkel R. C. (1997) The soil production function and landscape equilibrium. *Nature* **388**, 358–361.
- Hellmann R. and Tisserand D. (2006) Dissolution kinetics as a function of the Gibbs free energy of reaction: An experimental study based on albite feldspar. *Geochim. Cosmochim. Acta* **70**, 364–383.
- Hessler A. M., Lowe D. R., Jones R. L. and Bird J. D. (2004) A lower limit for atmospheric carbon dioxide levels 3.2 billion years ago. *Nature* **428**, 736–738.
- Hilley G. E., Chamberlain C. P. Moon S., Porder S. and Willett S. D. (2010) Competition between erosion and reaction kinetics in controlling silicate-weathering

- rates. *Earth Planet. Sci. Lett.* **293**, 191–199.
- Hochella M. F. Jr. and Banfield J. F. (1995) Chemical weathering of silicate in nature: A microscopic perspective with theoretical considerations. *Rev. Mineral.* **31**, 353–406.
- Hoffman P. F., Haufman A. J., Halverson G. P. and Schrag D. P. (1998) A Neoproterozoic Snowball Earth. *Science* **281**, 1342–1346.
- Hoffman P. F. and Schrag D. P. (2002) The snowball Earth hypothesis: testing the limits of global change. *Terra Nova* **14**, 129–155.
- Holland H. D. (1978) *The Chemistry of the Atmosphere and Oceans*. John Wiley & Sons, New York, 351pp.
- Holland H. D. (1984) *The Chemical Evolution of the Atmosphere and Oceans*. Princeton University Press, Princeton, NJ, 582 pp.
- Holland H. D. and Zbinden E. A. (1988) Paleosols and the evolution of atmosphere: Part I. In *Physical and Chemical weathering in Geochemical cycles* (eds. A. Larman and M. Meybeck). Reidel Dordrecht, pp. 61–82.
- Holland H. D. (2009) Why the atmosphere became oxygenated: A proposal. *Geochim. Cosmochim. Acta* **73**, 5241–5255.
- Hren M. T., Tice M. M. and Chamberlain C. P. (2009) Oxygen and hydrogen isotope evidence for a temperate climate 3.42 billion years ago. *Nature* **462**, 205–208.
- Jaffrés J. B. D., Shields G. A. and Wallmann K. (2007) The oxygen isotope evolution of seawater: A critical review of a long-standing controversy and an improved geological cycle model for the past 3.4 billion years. *Earth-Sci. Rev.* **83**, 83–122.
- Johnson D., Geisinger D., Walker R., Newman J., Vose J., Elliot K. and Ball T (1994) Soil pCO₂, soil respiration, and root activity in CO₂-fumigated and nitrogen-fertilized ponderosa pine. *Plant Soil* **165**, 129–138.
- Kah L. C. and Riding R. (2007) Mesoproterozoic carbon dioxide levels inferred from calcified cyanobacteria. *Geology* **35**, 799–802.
- Kasting J. F., Holland H. D. and Pinto J. P. (1985) Oxidant abundances in rainwater and the Evolution of atmospheric oxygen. *J. Geophys. Res.* **90**, 10497–10510.
- Kasting J. F. and Ackerman T. P. (1986) Climatic consequences of very high carbon dioxide levels in the Earth's early atmosphere. *Science* **234**, 1383–1385.
- Kasting J. F. (1987) Theoretical constraints on oxygen and carbon dioxide concentrations in the Precambrian atmosphere. *Precambrian Res.* **34**, 205–229.
- Kasting J. F. (1988) Runaway and moist greenhouse atmosphere and the evolution of Earth and Venus. *Icarus* **74**, 472–494.
- Kasting J. F. (1989) Long-term stability of the Earth's climate. *Palaeogeography Palaeoclimatol. Palaeoecol.* **75**, 83–95.

- Kasting J. F. (1993) Earth's early atmosphere. *Science* **259**, 920–926.
- Kaufman A. J. and Xiao S. (2003) High CO₂ levels in the Proterozoic atmosphere estimated from analyses of individual microfossils. *Nature* **425**, 279–282.
- Keller C. K. and Wood B. D. (1993) Possibility of chemical weathering before the advent of vascular land plants. *Nature* **364**, 223–225.
- Kharecha P., Kasting J. F. and Siefert J. (2005) A coupled atmosphere-ecosystem model of the early Archean Earth. *Geobiol.* **3**, 53–76.
- King D. W. (1998) Role of carbonate speciation on the oxidation rate of Fe(II) in aquatic systems. *Environ. Sci. Technol.* **32**, 2997–3003.
- Kirschbaum M. U. F. (1995) The temperature dependence of soil organic matter decomposition, and the effect of global warming on soil organic C storage. *Soil Biol. Biochem.* **27**, 753–760.
- Knauth L. P. and Epstein S. (1976) Hydrogen and oxygen isotope ratios in nodular and bedded cherts. *Geochim. Cosmochim. Acta* **40**, 1095–1108.
- Knauth L. P. and Lowe D. R. (2003) High Archean climatic temperature inferred from oxygen isotope geochemistry of cherts in the 3.5 Ga Swaziland Supergroup, South Africa. *Geol. Soc. Am. Bull.* **115**, 566–580.
- Krupp R., Oberthür T. and Hirdes W. (1994) The early Precambrian atmosphere and hydrosphere: Thermodynamic constraints from mineral deposits. *Econ. Geol.* **89**, 1581–1598.
- Lasaga A. C. (1981b) Rate laws of chemical reactions. *Rev. Mineral.* **8**, 1–68.
- Lasaga A. C. (1981b) The atomic basis of kinetics: Defects in minerals. *Rev. Mineral.* **8**, 261–319.
- Lasaga A. C. (1984) Chemical kinetics of water-rock interactions. *J. Geophys. Res.* **89**, 4009–4025.
- Lasaga A. C., Berner R. A. and Garrels R. M. (1985) An improved geochemical model of atmospheric CO₂ fluctuation over the past 100 million years. In *The Carbon Cycle and Atmospheric CO₂: Natural Variations Archean to Present* (ed. E. T. Sundquist and W. S. Broecker), pp. 397–411. Amer. Geophys. Union.
- Lasaga A. C., Soler J. M., Ganor J., Burch T. E. and Nagy K. (1994) Chemical weathering rate laws and global geochemical cycles. *Geochim. Cosmochim. Acta* **58**, 2361–2386.
- Lasaga A. C. (1995) Fundamental approaches in describing mineral dissolution and precipitation rates. *Rev. Mineral.* **31**, 23–86.
- Lasaga A. C. (1997) *Kinetic Theory in the Earth Sciences*. Princeton University Press.
- Lasaga A. C. and Luttge A. (2001) Variation of crystal dissolution rate based on a

- dissolution stepwave model. *Science* **291**, 2400–2404.
- Lasaga A. C. and Ohmoto H. (2002) The oxygen geochemical cycle: Dynamics and stability. *Geochim. Cosmochim. Acta* **66**, 361–381.
- Le Hir G., Donnadiou Y., Godd ris Y., Pierrehumbert R. T., Halverson G. P., Macouin M., N d lec A. and Ramstein G. (2009) The snowball Earth aftermath: Exploring the limits of continental weathering process. *Earth Planet Sci. Lett.* **277**, 453–463.
- Lichtenegger H. I. M., Lammer H., Grie meier J. -M., Kulikov Yu. N., von Paris P., Hausleitner W., Krauss S. and Rauer H. (2010) Aeronomical evidence for higher CO₂ levels during Earth’s Hadean epoch. *Icarus* **210**, 1–7.
- Lloyd J. and Taylor J. A. (1994) On the temperature dependence of soil respiration. *Funct. Ecol.* **8**, 315–323.
- Lovelock J. E. and Kump L. R. (1994) Failure of climate regulation in a geophysiological model. *Nature* **369**, 732–734.
- Lowe D. R. and Tice M. M. (2004) Geological evidence for Archean atmospheric and climatic evolution: Fluctuating levels of CO₂, CH₄, and O₂ with an overriding tectonic control. *Geology* **32**, 493–496.
- Lowe D. R. and Tice M. M. (2007) Tectonic controls on atmospheric, climatic, and biological evolution 3.5-2.4 Ga. *Precambrian Res.* **158**, 177–197.
- Lowson R. T. (1982) Aqueous oxidation of pyrite by molecular oxygen. *Chem. Rev.* **82**, 461–497.
- Maher K., Steefel C. I., White A. F. and Stonestrom D. A. (2009) The role of reaction affinity and secondary minerals in regulating chemical weathering rates at the Santa Cruz Soil Chronosequence, California. *Geochim. Cosmochim. Acta* **73**, 2804–2831.
- Maher K. (2010) The dependence of chemical weathering rates on fluid residence time. *Earth Planet Sci. Lett.* **294**, 101–110.
- Marin J., Chaussidon M and Robert F. (2010) Microscale oxygen isotope variations in 1.9 Ga Gunflint cherts: Assessments of diagenesis effects and implications for oceanic paleotemperature reconstructions. *Geochim. Cosmochim. Acta* **74**, 116–130.
- Marty B. and Tolstikhin I. N. (1998) CO₂ flux from mid-ocean ridges, arcs and plumes. *Chem. Geol.* **145**, 233–248.
- Meybeck M. (1987) Global chemical weathering of surficial rocks estimated from river dissolved loads. *Am. J. Sci.* **287**, 401–428.
- Millero F. J., Sotolongo S. and Izaguirre M. (1987) The oxidation kinetics of Fe(II) in seawater. *Geochim. Cosmochim. Acta* **51**, 793–801.
- Mitchell J. F. B. (1989) The “greenhouse” effect and climate change. *Rev. Geophys.* **27**, 115–139.

- Mitchell R. L. and Sheldon N. D. (2010) The ~1100 Ma Sturgeon Falls paleosols revisited: Implications for Mesoproterozoic weathering environments and atmospheric CO₂ levels. *Precambrian Res.* **183**, 738–748.
- Mora C. I., Driese S. G. and Colarusso L. A. (1996) Middle to late Paleozoic atmospheric CO₂ levels from soil carbonate and organic matter. *Science* **271**, 1105–1107.
- Moulton K. L., West J. and Berner R. A. (2000) Solute flux and mineral mass balance approaches to the quantification of plant effects on silicate weathering. *Am. J. Sci.* **300**, 539–570.
- Murakami T., Kogure T., Kadohara H. and Ohnuki T. (1998) Formation of secondary minerals and its effect on anorthite dissolution. *Am. Mineral.* **83**, 1209–1219.
- Murakami T., Sreenivas B., Das Sharma S. and Sugimori H. (2011) Quantification of atmospheric oxygen levels during the Paleoproterozoic using paleosol compositions and iron oxide kinetics. *Geochim. Cosmochim. Acta* **75**, 3982–4004.
- Nagy N. L. (1995) Dissolution and precipitation kinetics of sheet silicates. *Rev. Mineral.* **31**, 173–233.
- Navarre-Sitchler A. and Brantley S. L. (2007) Basalt weathering across scales. *Earth Planet. Sci. Lett.* **261**, 321–334.
- Norton K. P. and von Blackenburg F. (2010) Silicate weathering of soil-mantled slopes in an active Alpine landscape. *Geochim. Cosmochim. Acta* **74**, 5243–5258.
- Nutman A. P. (2006) Antiquity of the oceans and continents. *Elements* **2**, 223–227.
- Och L. M. and Shields-Zhou G. A. (2012) The Neoproterozoic oxygenation event: Environmental perturbations and biogeochemical cycling. *Earth-Sci. Rev.* **110**, 26–57.
- Ohmoto H., Watanabe Y. and Kumazawa K. (2004) Evidence from massive siderite beds for a CO₂-rich atmosphere before ~1.8 billion years ago. *Nature* **429**, 395–399.
- Oliva P., Viers J. and Dupré B. (2003) Chemical weathering in granitic environments. *Chem. Geol.* **202**, 225–256.
- Papineau D., Mojzsis S. J. and Schmitt A. K. (2007) Multiple sulfur isotopes from Paleoproterozoic Huronian interglacial sediment and the rise of atmospheric oxygen. *Earth Planet Sci. Lett.* **255**, 188–212.
- Pavlov A. A., Kasting J. F., Brown, L. L., Rages K. A. and Freedman R. (2000) Greenhouse warming by CH₄ in the atmosphere of early Earth. *J. Geophys. Res.* **105**, 11981–11990.
- Pavlov A. A. and Kasting J. F. (2002) Mass-independent fractionation of sulfur isotopes in Archean sediments: Strong evidence for an anoxic Archean atmosphere.

- Astrobiology* **2**, 27–41.
- Pavlov A. A., Hurtgen M. T., Kasting J. F. and Arthur M. A. (2003) Methane-rich Proterozoic atmosphere? *Geology* **31**, 87–90.
- Pierrehumbert R. T., Abbot D. S., Voigt A. and Knoll D. (2011) Climate of the Neoproterozoic. *Annu. Rev. Earth Planet. Sci.* **39**, 417–460.
- Piñol J., Alcañiz J. M. and Rodà F. (1995) Carbon dioxide efflux and pCO₂ in soils of three *Quercus ilex* montane forests. *Biogeochemistry* **30**, 191–215.
- Rasmussen C., Brantley S. L., Richter D. dB., Blum A., Dixon J. and White A. F. (2011) Strong climate and tectonic control on plagioclase weathering in granitic terrain. *Earth Planet. Sci. Lett.* **301**, 521–530.
- Riebe C. S., Kirchner J. W., Granger D. E. and Finkel R. C. (2001) Strong tectonic and weak climatic control of long-term chemical weathering rates. *Geology* **29**, 511–514.
- Riebe C. S., Kirchner J. W. and Finkel R. C. (2004) Erosional and climatic effects on long-term chemical weathering rates in granitic landscapes spanning diverse climate regimes. *Earth Planet. Sci. Lett.* **224**, 547–562.
- Rimstidt J. D., Brantley S. L. and Olse A. A. (2012) Systematic review of forsterite dissolution rate data. *Geochim. Cosmochim. Acta* **99**, 159–178.
- Robert F. and Chaussidon M. (2006) A palaeotemperature curve for the Precambrian oceans based on silicon isotopes in cherts. *Nature* **443**, 469–472.
- Rosing M. T., Bird D. K., Sleep N. H. and Bjerrum C. J. (2010) No climate paradox under the faint early Sun. *Nature* **464**, 744–747.
- Rye R., Kuo P. H. and Holland H. D. (1995) Atmospheric carbon dioxide concentrations before 2.2 billion years ago. *Nature* **378**, 603–605.
- Sagan C. and Mullen G. (1972) Earth and Mars: Evolution of atmospheres and surface temperatures. *Science* **177**, 52–56.
- Sak P. B., Fisher D. M., Gardner T. W., Murphy K. and Brantley S. L. (2004) Rates of weathering rind formation on Costa Rican basalt. *Geochim. Cosmochim. Acta* **68**, 1453–1472.
- Schott J., Pokrovsky O. S. and Oelkers E. H. (2009) The link between mineral dissolution/precipitation kinetics and solution chemistry. *Rev. Mineral. Geochem.* **70**, 207–258.
- Schwartzman D. W. and Volk T. (1989) Biotic enhancement of weathering and the habitability of the Earth. *Nature* **340**, 457–460.
- Schiels G. A. and Kasting J. F. (2007) Evidence for hot early oceans? *Nature* **447**, doi:10.1038/nature05830.

- Segura A., Krelove K., Kasting J. F., Sommerlatt D., Meadows V., Crisp D., Cohen M. and Mlawer E. (2003) Ozone concentrations and ultraviolet fluxes on Earth-like planets around other stars. *Astrobiology* **3**, 689–708.
- Sekine Y., Tajika E., Tada R., Hirai T., Goto K. T., Kuwatani T., Goto K., Yamamoto S., Tachibana S., Isozaki Y. and Kirschvink J. L. (2011) Manganese enrichment in the Gowganda Formation of the Huronian Supergroup: A highly oxidizing shallow-marine environment after the last Huronian glaciation. *Earth Planet Sci. Lett.* **307**, 201–210.
- Sheldon N. D. (2006) Precambrian paleosols and atmospheric CO₂ levels. *Precambrian Res.* **147**, 148–155.
- Sheldon N. D. (2013) Causes and consequences of low atmospheric pCO₂ in the Late Mesoproterozoic. *Chem. Geol.* **362**, 224–231.
- Som S. M., Catling D. C., Harnmeijer J. P., Polivka P. M. and Buick R. (2012) Air density 2.7 billion years ago limited to less than twice modern levels by fossil raindrop imprints. *Nature* **484**, 359–362.
- Sposito G. (1989) *The Chemistry of Soils*. Oxford University Press, New York, 277 pp.
- Stallard R. F. (1995) Relating chemical and physical erosion. *Rev. Mineral.* **31**, 543–564.
- Stonestrom D. A., White A. F. and Akstin K. (1998) Determining rates of chemical weathering in soils — Solute transport versus profile evolution. *J. Hydrol.* **209**, 331–345.
- Stumm W. and Lee G. F. (1961) Oxygenation of ferrous iron. *Ind. Eng. Chem.* **53**, 143–146.
- Stumm W. and Morgan J. J. (1996) *Aquatic Chemistry*, third ed. John Wiley & Sons, New York, 780p.
- Sugimori H., Kanzaki Y. and Murakami T. (2012) Relationship between Fe redistribution and P_{O₂} during mineral dissolution under low O₂ conditions. *Geochim. Cosmochim. Acta* **84**, 29–46.
- Sverdrup H. and Warfvinge P. (1995) Estimating field weathering rates using laboratory kinetics. *Rev. Mineral.* **31**, 485–541.
- Tajika E. and Matsui T. (1992) Evolution of terrestrial proto-CO₂ atmosphere coupled with thermal history of the earth. *Earth Planet. Sci. Lett.* **113**, 251–266.
- Tajika E. and Matsui T. (1993) Evolution of seafloor spreading rate based on ⁴⁰Ar degassing history. *Geophys. Res. Lett.* **20**, 851–854.
- Tolstikhin I. N. and Marty B. (1998) The evolution of terrestrial volatiles: a view from helium, neon, argon and nitrogen isotope modelling. *Chem. Geol.* **147**, 27–52.

- Trainer M. G., Pavlov A. A., Dewitt H. L., Jimenez J. L., McKay C. P., Toon O. B. and Tolbert M. A. (2006) Organic haze on Titan and the early Earth. *Proc. Natl. Acad. Sci.* **103**, 18035–18042.
- Turner B. F., White A. F. and Brantley S. L. (2010) Effects of temperature on silicate weathering: Solute fluxes and chemical weathering in a temperate rain forest watershed, Jamieson Creek, British Columbia. *Chem. Geol.* **269**, 62–78.
- Valley J. W., Peck W. H., King E. M. and Wilde S. A. (2002) A cool early Earth. *Geology* **30**, 351–354.
- Veizer J. and Jansen S. L. (1979) Basement and sedimentary recycling and continental evolution. *J. Geol.* **87**, 341–370.
- Veizer J. and Jansen S. L. (1985) Basement and sedimentary recycling—2: Time dimension to global tectonics. *J. Geol.* **93**, 625–643.
- Velbel M. A. (1993) Temperature dependence of silicate weathering in nature: How strong a negative feedback on long-term accumulation of atmospheric CO₂ and global greenhouse warming? *Geology* **21**, 1059–1062.
- von Paris P., Rauer H., Grenfell J. L., Patzer B., Hedelt P., Stracke B., Trautmann T. and Schreier F. (2008) Warming the early earth—CO₂ reconsidered. *Planet Space Sci.* **56**, 1244–1259.
- Walker J. C. G. (1977) *Evolution of the Atmosphere*. Macmillan, New York.
- Walker J. C. G. (1982) Climatic factors on the Archean earth. *Palaeogeography Palaeoclimatol. Palaeoecol.* **40**, 1–11.
- Walker J. C. G. (1985) Carbon dioxide on the early earth. *Origins Life* **16**, 117–127.
- Walker J. C. G., Hays P. B. and Kasting J. F. (1981) A negative feedback mechanism for the long-term stabilization of Earth's surface temperature. *J. Geophys. Res.* **86**, 9776–9782.
- Walther J. V. and Wood B. J. (1986) Mineral-fluid reaction rates. In *Fluid-Rock Interactions during Metamorphism* (eds. J. V. Walther and B. J. Wood), pp. 194–211. Springer-Verlag, New York.
- Warfvinge P. and Sverdrup H. (1992) Calculating critical loads of acid deposition with PROFILE—a steady-state soil chemistry model. *Water, Air and Soil Pollut.* **63**, 119–143.
- West A. J., Galy A. and Bickle M. (2005) Tectonic and climatic controls on silicate weathering. *Earth Planet. Sci. Lett.* **235**, 211–228.
- White A. F. (1995) Chemical weathering rates of silicate minerals in soils. *Rev. Mineral.* **31**, 407–461.
- White A. F. and Blum A. E. (1995) Effects of climate on chemical weathering in

- watersheds. *Geochim. Cosmochim. Acta* **59**, 1729–1747.
- White A. F., Blum A. E., Bullen T. D., Vivit D. V., Schultz M. and Fritzpatrick J. (1999) The effect of temperature on experimental and natural chemical weathering rates of granitoid rocks. *Geochim. Cosmochim. Acta* **63**, 3277–3291.
- White A. F., Schulz M. S., Vivit D. V., Blum A. E., Stonestrom D. A. and Anderson S. P. (2008) Chemical weathering of a marine terrace chronosequence, Santa Cruz, California I: Interpreting rates and controls based on soil concentration–depth profiles. *Geochim. Cosmochim. Acta* **72**, 36–68.
- Wilhelm E., Battino R. and Wilcock R. (1977) Low-pressure solubility of gases in liquid water. *Chem. Rev.* **77**, 219–262.
- Williams J. Z., Bandstra J. Z., Pollard D. and Brantley S. L. (2010) The temperature dependence of feldspar dissolution determined using a coupled weathering–climate model for Holocene-aged loess soils. *Geoderma* **156**, 11–19.
- Willienbring J. K. and von Blackenburg F. (2010) Long-term stability of global erosion rates and weathering during late-Cenozoic cooling. *Nature* **465**, 211–214.
- Wolf E. T. and Toon O. B. (2010) Fractal organic hazes provided an ultraviolet shield for early Earth. *Science* **328**, 1266–1268.
- Yang J., Hu Y. and Peltier W. R. (2012) Radiative effects of ozone on the climate of a Snowball Earth. *Clim. Past* **8**, 2019–2029.
- Yang L. and Steefel C. I. (2008) Kaolinite dissolution and precipitation at 22 °C and pH 4. *Geochim. Cosmochim. Acta* **72**, 99–116.
- Yapp C. J. and Poths H. (1996) Carbon isotopes in continental weathering environments and variations in ancient atmospheric CO₂ pressure. *Earth Planet. Sci. Lett.* **137**, 71–82.
- Yokota K., Kanzaki Y. and Murakami T. (2013) Weathering model for the quantification of atmospheric oxygen evolution during the Paleoproterozoic. *Geochim. Cosmochim. Acta* **117**, 332–347.
- Yokoyama T. (2013) Characterization of the reaction and transport properties of porous rhyolite and its application to the quantitative understanding of the chemical weathering rate. *Geochim. Cosmochim. Acta* **118**, 295–311.
- Young G. M., von Brunn V., Gold D. J. C., and Minter W. E. L. (1998) Earth's oldest reported glaciation: Physical and chemical evidence from the Archean Mozaan Group (~2.9 Ga) of South Africa. *J. Geol.* **106**, 523–538.
- Zhang X. and Zindler A. (1993) Distribution and evolution of carbon and nitrogen in Earth. *Earth Planet. Sci. Lett.* **117**, 331–345.

VI. General conclusions

In this thesis, I developed three weathering models for the estimation of P_{CO_2} and P_{O_2} from paleosols and that of P_{CO_2} in a theoretical framework. I applied the first two models to eight Neoproterozoic-Paleoproterozoic paleosols and five Paleoproterozoic paleosols to estimate P_{CO_2} and P_{O_2} , respectively.

In the model to estimate P_{CO_2} from paleosols, I considered the mass balance of elements between rock and water phases, charge balance in porewater and the thermodynamics of the weathering secondary-minerals. The model reproduced observed modern soil P_{CO_2} values when applied to modern weathering profiles. The rate expression of weathering derived from the model was consistent with those in the laboratory and filed in the literature, from the viewpoints of the dependency of the weathering rate on P_{CO_2} and the apparent activation energy. Thus, I concluded that the model is robust and valid to estimate P_{CO_2} from modern- and paleo-weathering profiles. Application of the model to Neoproterozoic-Paleoproterozoic paleosols requires the local temperatures at which the paleosols were weathered. I estimated the local temperatures of the paleosols mainly by the relationships between solute concentration and temperature in the literature. Within the constrained local temperatures, P_{CO_2} levels in the Neoproterozoic-Paleoproterozoic were estimated: $10^{-1.6}$ – $10^{-0.8}$ atm at ~2.77 Ga, $10^{-1.6}$ – $10^{-0.1}$ atm at ~2.75 Ga, $10^{-1.3}$ – $10^{-0.8}$ atm at ~2.46 Ga, $10^{-2.0}$ – $10^{-1.2}$ atm at ~2.15 Ga, $10^{-2.2}$ – $10^{-0.7}$ atm at ~2.08 Ga and $10^{-2.1}$ – $10^{-1.2}$ atm at ~1.85 Ga. The estimated P_{CO_2} levels were higher than previously thought and high enough to maintain the average global surface temperature of the Earth above the freezing point of water in the Neoproterozoic-Paleoproterozoic except for the wide-spread glaciation periods. Furthermore, the P_{CO_2} estimates suggested a gradual decrease in P_{CO_2} in long term in the Neoproterozoic-Paleoproterozoic. Based on the estimates from the paleosols along with implications from the other geological records like MIF-S, I concluded that the multiple glaciations at ~2.9 and ~2.4–2.2 Ga might be differently triggered: the Pongola glaciation by CH_4 accumulation, the Ramsey Lake and Bruce glaciations by the collapse of both CO_2 and CH_4 and the Gowganda glaciation by the collapse of both CO_2 and CH_4 or only CO_2 .

To estimate P_{O_2} from paleosols, the relationship between P_{O_2} and Fe(II) oxidation rate is essential. I conducted Fe(II) oxidation experiments under low O_2 conditions (P_{O_2}

$<10^{-3}$ atm) to establish the relationship. The experiments were conducted in a glove box at $\sim 10^{-5}$ – $\sim 10^{-4}$ atm of P_{O_2} and pH 7.57–8.09. The obtained data, combined with the data of Sugimori et al. (2011) at $\sim 10^{-3}$ –0.2 atm of P_{O_2} , lead to a comprehensive understanding of the relationship between O_2 and the Fe(II) oxidation rate over a wide range of P_{O_2} , $\sim 10^{-5}$ atm $< P_{O_2} < 0.2$ atm. I found that the rate law changes with P_{O_2} level; when $P_{O_2} = \sim 6 \times 10^{-3}$ –0.2 atm, the rate law is essentially the same as that originally derived by Stumm and Lee (1961), whereas the oxidation reactions were found to obey a hitherto unknown rate law at 10^{-5} – 6×10^{-3} atm of P_{O_2} where the rate is proportional to $[O_2]^{0.58}$. The mechanism causing this change in rate order with respect to O_2 was possibly attributed to the change of the dominant oxidation pathway from O_2 to the steadily produced H_2O_2 with a minor contribution from O_2^- .

Then, I developed a weathering model that considers steady-state weathering and essentially calculates the ratio of the precipitated Fe(III)-(oxyhydr)oxides from dissolved Fe(II) to the total dissolved Fe(II) during weathering (ϕ), as a function of P_{O_2} . The Fe(II) oxidation kinetic expression was adopted from the above experimental results and then modified by the kinetic data in the literature to include the effects of P_{CO_2} and pH on Fe(II) oxidation. The input parameters, pH of porewater, P_{CO_2} , water flow rate, temperature and O_2 diffusion into soil at the time of weathering, which significantly affect the P_{O_2} estimates, were scrutinized so that the model can give robust estimates of P_{O_2} . I adopted the parameter values of P_{CO_2} and pH specific to the paleosols given by the above P_{CO_2} estimation model. The water flow parameter, k_f , was estimated from the mass balance of Si, the relationships between weathering fluxes and runoff, and the relationships between hydraulic conductivity and k_f , for each Paleoproterozoic paleosol. The temperatures specific to the paleosols at the time of weathering were from those given by the above P_{CO_2} estimation model while the effects of diffusion of O_2 into soil were assumed in a reasonable range. Using the constrained values of the above parameters for the Paleoproterozoic paleosols, the model calculated P_{O_2} levels for each paleosol: $10^{-6.7}$ – $10^{-5.4}$ atm at ~ 2.46 Ga, $10^{-5.2}$ – $10^{-3.2}$ atm at ~ 2.15 Ga, $10^{-3.9}$ – $10^{-1.2}$ atm at ~ 2.08 Ga and more than $10^{-4.6}$ – $10^{-2.5}$ atm at ~ 1.85 Ga. These constraints on P_{O_2} indicate that the gradual rise of oxygen in the Paleoproterozoic is likely in long term, as suggested by Murakami et al. (2011). Comparison of the calculated P_{O_2} levels to the estimates of P_{O_2} in the literature suggests that a drastic rise of oxygen would not have occurred at ~ 2.4 Ga, supporting a slightly rapid rise of oxygen at ~ 2.4 Ga and a gradual rise of oxygen in the Paleoproterozoic in long term.

In addition to the constraints on P_{CO_2} and P_{O_2} in the Precambrian from paleosols, I discussed the effects of atmospheric composition (CO_2 as well as CH_4 and O_2) on the apparent activation energy of silicate weathering in a theoretical framework, and suggested quantitative patterns of atmospheric evolution as well as surface-temperature variation in the Precambrian.

From the relationships in the apparent activation energy between different scales (mineral reaction to total elemental-loss and weathering flux), the apparent activation energy of weathering flux of silicates was estimated as a function of the temperature dependence of P_{CO_2} ($\Delta H'_{\text{CO}_2}$). The estimated apparent activation energies were related to the flux of total cations by silicate weathering (F_{CO_2}) by introducing the compensation law and the general rate law for silicate weathering flux, leading to the establishment of the relationships between $\Delta H'_{\text{CO}_2}$, temperature (T) and F_{CO_2} . Based on the relationships between $\Delta H'_{\text{CO}_2}$, T and F_{CO_2} , I discussed the effects of atmospheric CO_2 , as well as those of CH_4 and O_2 , on the silicate weathering, and their implications for the atmospheric compositions and surface temperatures in the Precambrian Earth.

The effects of CO_2 on silicate weathering were discussed based on the relationships between $\Delta H'_{\text{CO}_2}$, T and F_{CO_2} and the greenhouse effect of CO_2 . In the global-scale weathering, the greenhouse effect of CO_2 represents $\Delta H'_{\text{CO}_2}$. I calculated the ratio of the change in F_{CO_2} to the corresponding change in P_{CO_2} as an indicator of the feedback of silicate weathering on CO_2 using the greenhouse effects of CO_2 in the literature. The calculation revealed that when $P_{\text{CO}_2} > 10^{-0.5}$ atm, the feedback is negative and independent of both temperature and P_{CO_2} . On the other hand, when $P_{\text{CO}_2} < 10^{-0.5}$ atm, the feedback is almost P_{CO_2} -independent but temperature-dependent; at high ($> \sim 30$ °C) and low ($< \sim 30$ °C) temperatures, the feedback is positive and negative, respectively. Thus the conditions of $P_{\text{CO}_2} < 10^{-0.5}$ atm and $> \sim 30$ °C are unstable; with a slight change in CO_2 , the conditions change immediately into either the conditions of $P_{\text{CO}_2} > 10^{-0.5}$ atm or those of $P_{\text{CO}_2} < 10^{-0.5}$ atm and $< \sim 30$ °C. In the conditions of $P_{\text{CO}_2} < 10^{-0.5}$ atm and $< \sim 30$ °C, the feedback is not only negative but also becomes more negative as temperature decreases. Thus, global glaciations hardly occur in the conditions of $P_{\text{CO}_2} < 10^{-0.5}$ atm and $< \sim 30$ °C. The stable conditions at low temperatures with $P_{\text{CO}_2} < 10^{-0.5}$ atm against glaciations may explain the stable climates in the Precambrian excluding the periods of the glaciations, especially the stable climate in the Mesoproterozoic.

I considered the effects of CH_4 on weathering by calculating the feedback indicator with the relationships between $\Delta H'_{\text{CO}_2}$, T and F_{CO_2} and the greenhouse effects of CH_4 in the literature. With limited ratios of CH_4/CO_2 ($< \sim 0.15$ and $> \sim 0.03$), positive

feedback operates at low temperatures ($< \sim 5$ °C). Therefore, when the conditions of ~ 0.03 — ~ 0.15 of CH_4/CO_2 and $< \sim 5$ °C of temperature are satisfied, global glaciations can occur. The emergence of CH_4 with the limited ratios of CH_4/CO_2 may explain the glaciation in the Mesoarchean.

The change in P_{O_2} affects the apparent activation energy of weathering flux of silicates directly by involving oxidation reactions in weathering. When P_{O_2} increases from extremely low levels to $\sim 10^{-6}$ – 10^{-3} atm, F_{CO_2} can increase at low temperatures due to the change in the apparent activation energy. Thus, I concluded that oxygen increase is one of the possible triggers of global glaciations, which may explain the glaciations in the Paleoproterozoic.

I finally calculated the P_{CO_2} and temperature transitions in the Precambrian, confirming that CO_2 was the dominant greenhouse effect gas through the eon. The calculated P_{CO_2} and temperature suggest that the Precambrian Earth can have been at > 0 °C only with CO_2 and that the Hadean-Archean might have been hot. The estimates of P_{CO_2} are consistent with those calculated by the other weathering model based on paleosol data, further supporting the argument.

As a summary, the present constraints on the Precambrian atmosphere suggest that (i) CO_2 decreased gradually through the Precambrian in long term, with P_{CO_2} high enough to allow the existence of liquid water through the eon only by itself, (ii) O_2 increased gradually in the GOE in long term, (iii) the emergence of CH_4 and the increase in O_2 could have triggered the global glaciations in the Precambrian, and (iv) the Hadean-Archean might have been hot. The findings in this thesis will serve for a better understanding of the evolution of atmosphere in the Precambrian.

Acknowledgements

I would like to thank my supervisor, Professor T. Murakami, for his guidance, advice and permission to use all apparatus in his laboratory. I also would like to thank the members of SES seminar, especially Professor T. Kogure and Professor Y. Suzuki, for useful and inspiring discussions. The chief examiner, Professor T. Kogure, and the examiners, Professors H. Kagi, T. Murakami, Y. Suzuki and E. Tajika offered me thoughtful reviews of this thesis, which improved the manuscript.